Spaceborne monitoring of high temperature volcanic thermal features: studies using the ERS Along Track Scanning Radiometer

Thesis

UNRESTRICTED

Spaceborne monitoring of high temperature volcanic thermal features : studies using the ERS Along Track Scanning Radiometer

A thesis presented for the degree of Doctor of Philosophy

Martin John Wooster

BSc (Hons) Bristol, MSc London

Date of submission: 27 November 1997
Date of award: 6 April 1998

1997

Department of Earth Sciences, The Open University

ProQuest LLC.
789 East Eisenhower Parkway
P.O. Box 1346
Ann Arbor, MI 48106 – 1346

To Mum and Dad, Andrew and Siri.

Abstract

Satellite-based instruments have long been suggested as suitable for monitoring thermal phenomena occurring at the surface of active volcanoes. Past studies using data from high spatial resolution instruments indicated the effectiveness of this technique, but such data are expensive, time-consuming to obtain, and offer a poor temporal resolution. This thesis uses data from the European Remote Sensing satellites' Along Track Scanning Radiometer (ATSR) to analyse infrared thermal emittance from a variety of volcanic thermal features at low spatial resolution (1 km^2) but high temporal resolution (~ 3 days), with data from vegetation fires also being investigated. I calibrate the (previously uncalibrated) 1.6 μm channel of ATSR-1, and go onto show how nighttime data in this waveband can be used to characterise emittance from high temperature surfaces, even if these are significantly smaller than the ATSR pixel size.

Procedures are developed to detect hotspots in ATSR data, filter out cloud contaminated observations, and quantitatively analyse the measurements of infrared thermal flux. ATSR time-series datasets are then used to study thermal emittance from active lava domes at Lascar Volcano (Chile) and Unzen Volcano (Japan), with volcanological interpretations being made from the observed variations in radiance. At

both volcanoes the dominant source of nighttime shortwave infrared thermal flux is found to be high temperature surfaces heated by fumarolic degassing. During the monitoring period, decreases in shortwave infrared flux indicate an increased hazard at Lascar, such a change indicating blockage of the degassing system and an increased likelihood of a major pressure-driven explosive event. The reverse is found to be true at Unzen, where increases in shortwave infrared flux are found to be generally related to increases in magma supply (both being positively correlated with the flux rate of magmatic gas) and so to an increased frequency of hazardous pyroclastic flow from the growing dome.

ATSR time-series studies of active lava flows at Fernandina Volcano (Galápagos Islands) and Mount Etna (Sicily) indicate that such data can also be used to document the thermal evolution of a developing lava flow field. Though necessitating assumptions regarding the flow-field thermal structure, ATSR-based estimates of the area of emplaced lava compare favourably with those obtained using higher spatial resolution imagery. For the 1991 - 1993 Etna flow, the estimates of flow surface temperature and area are used to investigate the importance of the various heat loss mechanisms. Results indicate that radiative losses dominate, but that basal conduction is also highly significant.

The Moderate Resolution Imaging Spectrometer (MODIS) of NASA's Earth Observing System (EOS) will soon provide a new source of multi-waveband, high temporal resolution data, available to the general volcanological and remote sensing community via the EOSDIS data network. I recommend that consideration be given to nighttime operation of the MODIS shortwave infrared channels, since studies using ATSR suggest that these data have considerable potential for the thermal monitoring of active volcanoes.

Acknowledgements

The work contained within this thesis is a product of Natural Environment Research Council (NERC) studentship (GT12/94/ATSR2/37) and European Space Agency ERS Investigatorship UK101. Additional moneys were kindly provided by the Natural Resources Institute (NRI) under the NERC Co-operative Awards in Sciences of the Environment (CASE) scheme. Thanks go to all of these, and to my managers at NRI (Jane Rosenberg, Jim Williams, Chris Sear) for encouraging my decision to undertake this research.

Throughout the project I have received invaluable advice and excellent supervision from Dave Rothery (OU) and Chris Sear (NRI), my strongest thanks go to them both. I have also greatly benefited from interaction with other members of the Volcanology and Geophysics group at the OU, most notably Peter Francis, Steve Blake, Hazel Rymer and John Murray, and from IP-Lab discussions with Steve Drury. I must also thank the staff of NRI's Environmental Science Department for pleasant times in Chatham, and for the trip to Nicaragua funded by the Department for International Development. Andy Lloyd, John Taylor, John Holbrook, Rita Quill and Janet Dryden of the OU Department for Earth Sciences provided countless instances of practical support, but the greatest contribution in

this area came from Dick Carlton.....the long suffering system manager. Dick thinks he has seen the last of those copious ATSR data files....little does he realise MODIS will be worse....

Without support (and data !) from the Rutherford Appleton Laboratory ATSR project, this Ph.D. would not have been possible. I am indebted to all at RAL who provided me with assitance. Chris Mutlow, Albin Zavody and Phil Watts were most enthusiastic supporters and providers of information, and were also good companions for the ERS symposium. Dave Smith, John Delderfield, Paul Bailey and Jack Abolins also gave valued advice, and the ATSR Core Group generously granted all of my data requests. I must also thank John Wright for getting ATSR re-tasked over Hawaii....pity it was cloudy most of the time (that's IR radiometry for you !). Perhaps my greatest thanks go to Nigel Houghton and his data processing team of Ben Thomas, Mark Kwiatkowski and Mila de Vere. They never failed to help me in gathering my data and made efforts that surely went above and beyond the call of duty.

I enjoyed the company of my fellow remote sensing students. Andy Harris, Anthony Denniss and Robert Wright all provided good company and suggestions at various stages, and Mark Davies wowed me with his media-friendly skills. My good friends at various London institutions all showed that any PhD problems were not a unique OU experience. The NERC Equipment Pool for Field Spectroscopy were mightily generous in their loan of an ASD Fieldspec, and more generous in their reaction to learning it had broken. Dave Pieri (JPL) and Peter Mouginis-Mark and team (University of Hawaii) are thanked for their hospitality, as are the staff of the Hawaii Volcanoes Observatory and the Hawaii Volcanoes National Park. I promise that I will look out for bicycle racks the next time I am parking a hire car...

The ATSR data used in this work are courtesy of ESA/RAL/BNSC/NERC, whilst SPOT images of Fernandina Volcano were provided via a collaboration with the NASA Earth Observing System Volcanology Team (PI Peter Mouginis-Mark). OPS data were supplied under the terms of a JERS-1 verification project (NASDA J-0107). Painstaking and extremely helpful reviews of the papers in this thesis were variously provided by Peter Mouginis-Mark (University of Hawaii), Lori Glaze (NASA Goddard Spaceflight Centre), John Fink (Arizona State University), Vince Realmuto (Jet Propulsion Laboratory), Paul Delaney (U.S. Geological Survey), Clive Oppenheimer (Cambridge University), Tim Corsica (University of Miami) and a number of anonymous reviewers. I am grateful for all their suggestions. In addition to staff at RAL, a number of engineers provided information on the various remote sensing instruments used in this study. William Barnes of the NASA Goddard Spaceflight Centre provided information on MODIS, whilst Yukio Mukai of the Remote Sensing Technology Centre (RESTEC) of Japan provided information on OPS.

The work described in Chapter 6 was carried out with Takayuki Kaneko of the University of Tokyo. Thanks go to the Ministry of Education, Science and Culture (Japan) who made it possible for Dr Kaneko to carry out work in the UK, I look forward to future collaborations with him. A number of other Japanese scientists contributed information to this chapter, most notably S. Takana (RESTEC), K. Umakoshi (Shimabara Earthquake and Volcano Observatory), J. Hirabayashi (Kusatsu-Shirane Volcano Observatory), S. Nakada (University of Tokyo) and H. Sato (Kobe University).

Final thanks go to my wife Siri for supporting me throughout this work.

Table of contents

List of figures

List of tables

Co-author contribution to published manuscripts

Chapter/Appendix	Content and co-author contribution
1	***Review and project aims.*** No co-author contribution.
2	***ATSR background.*** No co-author contribution.
3	***ATSR data calibration***. No co-author contribution.
4	***Lascar Volcano.*** Advice on data analysis ~ 10%.
5	***Unzen Volcano***. Background information on Unzen eruption, initial interpretation of TM and thermal video data of lava dome temperatures ~ 30%.
6	***Geometric considerations.*** Advice on data presentation ~ 10%.
7	***Fernandina.*** Advice on data analysis and interpretation ~ 15%.
8	***Validation.*** No co-author contribution.
9	***Cooling mechanisms.*** Advice on conductive cooling model and thermal budget methodology ~ 20%.
10	***Conclusion.*** No co-author contribution.
A	***IDL routine.*** No co-author contribution.
B	***Split window variance ratio.*** No co-author contribution.
C	***Radiative losses.*** No co-author contribution.
D	***Indonesian fires.*** Background information to Indonsian forestry situation, development projects and provision of HRPT imagery ~ 15%
E	***Automatic hotspot discrimination.*** No co-author contribution.

Chapter 1.

Techniques used in satellite monitoring of high temperature volcanic phenomena and the aims of the current project

---

1.1. Background

The 1980s were the worst decade for volcanic disasters this century, with 24000 - 28000 fatalities each associated with two particularly devastating eruptions, that of El Chichón (Mexico, 1982) and Nevado del Ruiz (Columbia, 1985). Such tragedy clearly shows that active volcanoes continue to represent extreme hazards, despite advances in the science of volcanology and in the technology available for ground-based monitoring of pre-eruptive volcanic phenomena (McGuire *et al.*, 1995). This is particularly true in developing countries, where the presence of highly fertile volcanic soils often leads to large populations close to active volcanoes (Clarke, 1991). It is these countries where the logistical, political and budgetary constraints may be so severe as to prevent the adequate

implementation of traditional high technology ground based-volcano monitoring systems (Stoiber and Willams, 1990).

Further to the above difficulties, there is the problem of the sheer number of potentially active volcanoes whose monitoring needs to be addressed. The Catalogue of Active Volcanoes (CAVW, 1951-1975) documents over 500 volcanoes that have had recently dated eruptions. On average, more than 50 eruptions occur annually. Little wonder that volcanic activity occurring in relatively unpopulated areas receives scant attention, despite the probability that the phenomena exhibited at these sites may assist the understanding of volcanoes and eruptive phenomena as a whole (Mouginis-Mark, 1995). As Mouginis-Mark *et al.* (1989) point out, The National Academy of Science Committee for the International Decade for National Disaster Reduction (IDNDR) has determined that 'identification and global mapping of all active and potentially active volcanoes is an important science objective for the decade' (National Academy of Sciences, 1987). With such a huge number of potentially active volcanoes, traditional forms of monitoring require assistance if all these targets are to be kept under surveillance. Thermal monitoring of volcanic surface temperature is one method by which this may be achieved.

1.2. Monitoring the temperature of active volcanoes

1.2.1. The relevance of thermal monitoring

To be of most use any thermal monitoring must be directed at phenomena that are relevant to internal (magmatic) activity, since it is this activity which ultimately controls the character and eruptive nature of a volcano. Since magma is hot most thermal monitoring programs are aimed at detecting surface or near-surface thermal manifestations of this internal heat source, with an obvious target for such monitoring being the volcanic

fumarole, a vent through which volcanic gases are emitted. These gases are primarily comprised of elements and compounds that have previously been dissolved in the volcanic magma, partly by virtue of the high pressures experienced at depth. Water vapour and carbon dioxide are the commonest volatiles, followed by compounds of chlorine, flourine and sulphur. Since the majority of fumarolic gases have their source within the magma of the volcano, their temperature may provide information on internal magma movements, or on related changes in the thermal structure of the volcano (Suwa and Tanaka, 1959). Fumaroles may have temperatures anywhere between a few tens of degrees above ambient, to near magmatic temperatures in excess of 800 °C. Prior to many volcanic eruptions, the temperature of fumaroles have been observed to vary, quite considerably in some cases. Moxham (1971), Francis (1979), Stoiber and Williams (1990) and Connor *et al.* (1993) each outline a number of examples. Whilst the individual temperature of a fumarole may not provide particularly useful information, other than confirming the presence of a magma body at depth, data on fumarole temperature change may allow much more detailed conclusions to be drawn.

One example of an internal activity that may greatly affect fumarole temperature is the ascension of a new magma body from depth. The decreasing pressure may cause an increased concentration of magmatic volatiles to come out of solution, with a consequent increase in the temperature of the vented gases and in the rocks surrounding the surface fumaroles (Suwa and Tanaka, 1959). However many other factors, for example rainfall variations, may also affect fumarole temperatures and so thermal monitoring is ideally performed on a very regular basis so that truely volcanogenic changes can be better identified (Connor *et al.*, 1993).

Volcanic fumaroles often occur on lava domes, these being mounds of highly viscous magma piled up around an active volcanic vent. Lava domes expand by magma being squeezed out of open fissures, or by inflation caused by a supply of magma to the dome interior. These two processes are termed, respectively, exogenous and endogenous growth (Willams, 1932) and they may proceed for many years at a single location, forming a lava dome many hundreds of meters in diameter. Figure 1.1 shows a thermal image of the summit lava dome that began to form soon after the 1980 explosive eruption of Mount St. Helens Volcano, USA (Fink *et al.*, 1989). Dome growth proceeded until 1986 and, though these data were taken in 1988, hot areas associated with the continued release of fumarolic gases can still be clearly seen.

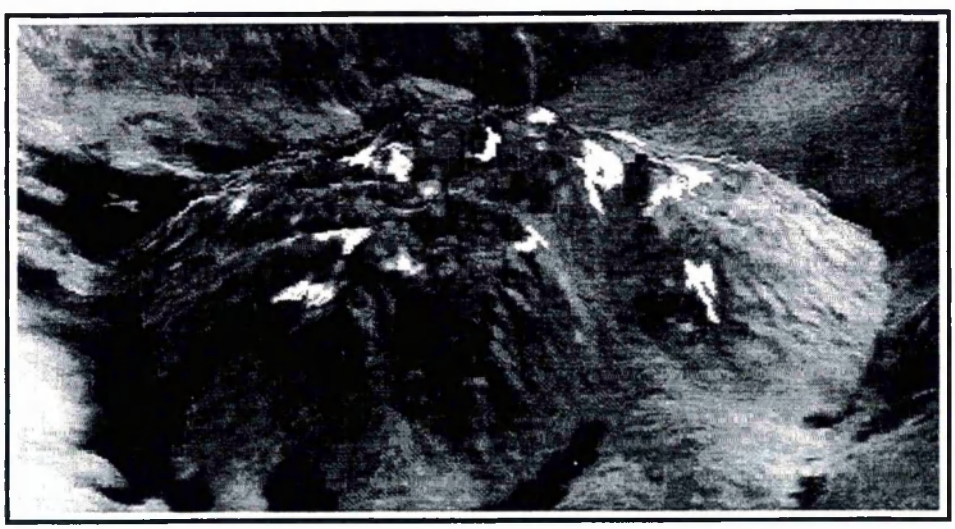

Figure 1.1. A perspective view of the Mount St. Helens lava dome, created by registering data from the airborne Thermal Infrared Multspectral Scanner (TIMS) to a 1:4000 scale digital elevation model. The dome volume is 7 x 10^7 m^3, with fumarolically heated areas highlighted using the TIMS thermal data (Friedman and Realmuto, in press).

Though the surface temperature of an active lava dome is usually fairly low, the interior is often held at a very high temperature due to the excellent insulating properties of the outer chilled crust. Pyroclastic flows of ash, rock and volcanic gases are generated

by explosive activity on the lava dome, caused either by the collapse of a dome segment exposing hot magma to atmospheric pressure, or by the explosive release of pent-up magmatic or meteoric water (Blake, 1990). These pyroclastic flows are extremely hot and travel at very high speeds, making them amongst the most destructive and hazardous of all volcanic phenomena. The 1995 - 1997, and currently ongoing, crisis of Soufriere Hills volcano, Monserrat is an example of lava dome growth accompanied by frequent, highly destructive, pyroclastic flow generation (McGuire *et al.*, 1997).

Though temperature data are clearly relevant to the monitoring of a number of volcanic processes, as with other volcano monitoring techniques they are best suited to analysis alongside additional information on, for example, seismic activity and gas concentration (Rothery, 1992; McGuire *et al.*, 1995). Additionally, though not directly relevant to the science of volcano monitoring and eruption prediction, it is pertinent to mention that temperature data are also important in the study of active lavas. The thermal properties of a lava flow surface may directly impact upon its longevity and flow length, making surface temperature information invaluable for use in models of lava flow motion (e.g. Crisp and Baloga, 1990; Dragoni, 1989).

1.2.3. *In situ* measurements of temperature

Volcanic temperature monitoring has most often been performed using simple thermocouple devices, or in some cases glass thermometers, placed into the body to be investigated, for example the water of a crater lake (e.g. Alcaraz and Cardoso, 1969), the mouth of a degassing fumarole (e.g. Fisher, 1957) or even an actively flowing lava (e.g. Tanguy and Biquand, 1967). To be of most use such measurements require frequent visits to the volcano so that a suitable time-series dataset can be obtained, it being the trends in temperature that are often the most informative. These visits are obviously time

consuming and potentially dangerous. It can also be difficult to standardise the measurement conditions of each visit. Some limited success has been obtained with the automated telemetry of fumarole temperature data (e.g. Moxham *et al.*, 1972; Connor *et al.*, 1993), but these systems have often been disabled by corrosion of the measurement devices, lightning strikes to the telemeter aerial or any one of a host of other environmental hazards present on active volcanoes.

1.2.4. Remote measurements of temperature

In the 1960s and 1970s thermal remote sensing of volcanic activity was identified as a suitable method of reducing the time, risk and logistical difficulty involved in making *in situ* temperature measurements of volcanic phenomena (Moxham, 1971). The theoretical basis of the remote measurement of temperature is the Planck Equation, which governs the relationship between the temperaure (T) of a body and the spectral radiance (L) emitted from it at a particular wavelength (λ) :

$$L(\lambda,T)=\frac{2hc^2}{\lambda^5(\exp(\frac{hc}{\lambda kT})-1)} \qquad (1.1)$$

where λ is wavelength (m)

T is temperature (K)

L is spectral radiance ($W/m^2/sr/m$)

h is Planck's constant (6.6×10^{-34} Ws^2)

k is the Boltzmann constant (5.67×10^{-8} $W/m^2/K^{-4}$)

c is the velocity of light in a vacuum (3×10^8 m/s)

Figure 1.2 shows the general form of the Planck function, and indicates that emitted spectral radiance increases with temperature over the entire wavelength range. The figure also demonstrates that the hotter the blackbody, the shorter the wavelength of peak thermal emittance, this being one manifestation of Wein's law. Exceptionally hot bodies will emit significant amounts of radiation at even visible wavelengths, i.e. they will begin to glow. This phenomena was the basis of the first instrument used to measure volcanic surface temperatures remotely, namely the optical pyrometer. Gray and Müller (1974) describe the workings of this instrument and an example of its use is given by Calvari *et al.* (1994), who used the device to confirm the temperature of an Etnean lava channel as 850 - 1080 °C. Though pyrometers have proved their value in such studies, their use is restricted to very high temperature sources since only these emit significantly at visible wavelengths.

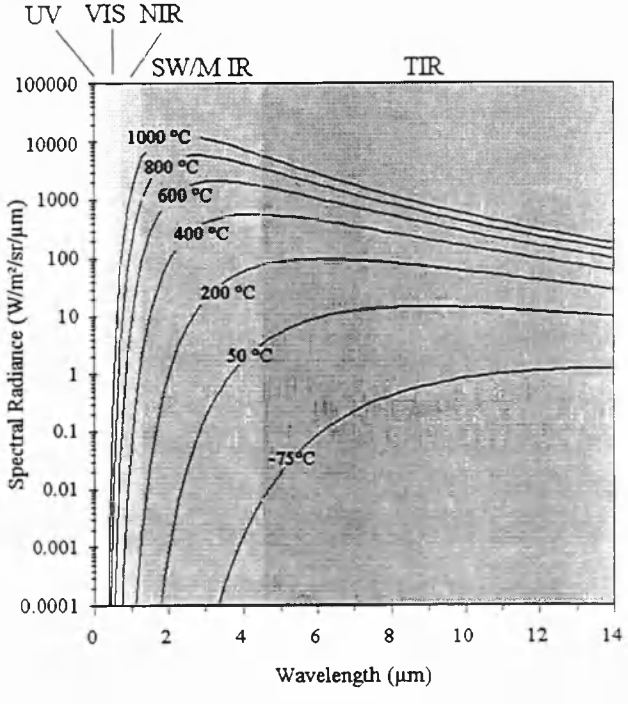

Figure 1.2. Blackbody radiances according to Planck's function, shown over ultra violet, visible, near infrared, shortwave/middle infrared and thermal infrared wavelengths.

In order to measure the temperature of cooler surfaces remotely, the use of longer wavelengths must be employed. The development of such infrared radiometers was a significant advance since, as analysis of Figure 1.2 indicates, by carefully choosing the infrared region in which to observe, the entire range of ambient to magmatic surface temperatures can be covered. Moxham (1971) describes the early radiometers, whilst Oppenheimer and Rothery (1989) describe the use of two modern hand-held devices, operating at 0.8 - 1.1 μm and 8 - 14 μm respectively. The first can be used to measure temperatures in the range 600 to 3000 °C, whilst the second operates in a -50 to 1000 °C temperature range. These and similar instruments have been used to measure the temperature of a wide variety of volcanic surfaces and can reduce hazards and ease logistics by allowing measurements to be made from distances of up to several kilometres (e.g. Lange and Avent, 1975). Aircraft-mounted thermal infrared scanners, usually working at 8 - 14 μm or some similar wavelength range, were also found to be of use in remotely delineating volcanic thermal anomalies (e.g. Shillin and Komarov, 1968; Moxham, 1970; Ehara *et al.*, 1975; Perry and Crick, 1976), though the costs involved in providing the necessary frequency of observation means that routine airborne monitoring is unlikely to be available in developing countries (Francis, 1979).

Following from the infrared techniques employed during ground-based and airborne remote sensing surveys, infrared observations made from Earth orbiting satellites were suggested as a suitable data source with which to adapt such methods to a wider spatio-temporal context (Moxham, 1971; Francis, 1979). The repetitive nature of satellite observations was seen as a great resource for the routine monitoring of volcanic thermal activity, and for the documentation of effusive volcanic activity occurring in otherwise unobserved areas (Francis, 1979; Rothery *et al.*, 1988; Mouginis-Mark *et al.*, 1991b).

Furthermore in the 1970s it was conceivable that the cost of satellite operation and launch would be continually borne by the U.S. Government (National Research Council, 1995), making it likely that satellite-derived infrared imagery would be significantly cheaper than that obtained by mounting specialist airborne campaigns.

1.3. Spaceborne thermal observations of active volcanoes

1.3.1. The early days

The first thermal infrared images of the Earth from space were obtained in August 1964 by the Nimbus I meteorological satellite, operated by the National Aeronautics and Space Administration (NASA). The High Resolution Infrared Radiometer (HRIR) onboard Nimbus I possessed a thermal infrared channel centred at 3.8 μm, with a nadir spatial resolution of around 6 km. It was not long before HRIR data were put to a volcanological use, demonstrating that the active Kilauea volcano on the Big Island of Hawaii had a higher thermal radiance than its quiescent neighbour, Mauna Loa (Gawarecki *et al.*, 1965). Interestingly the study showed the crucial value of nighttime data taken in the absence of solar reflected radiation, something that I have confirmed during the current project. Thermal data from a second imaging satellite, Nimbus II, was also used to observe volcanic activity, this time the ongoing eruption of Surtsey that formed a new island off the Icelandic coast between 1963 and 1967 (Friedman and Williams, 1968).

1.3.2. Detecting new volcanic eruptions

The 1970s eruptions in the Galápagos archipelago were the first situations in which satellite remote sensing demonstrated its value for detecting ongoing eruptive activity, prior to traditional ground based observations. By this time the US National Oceanic and

Atmospheric Administration (NOAA) were operating a series of meteorological satellites carrying the Very High Resolution Radiometer (VHRR), providing visible (0.6 - 0.7 μm) and thermal infrared (10.5 - 12.5 μm) observations at around 1 km spatial resolution. The plume from the 1977 eruption of Fernandina was observed in VHRR data obtained from the NOAA 2 satellite, 24 hours before the eruption was noticed by the inhabitants of neighbouring islands (Simkin and Kreuger, 1977). Two and a half years later a new plume from Sierra Negra was also noted on VHRR imagery, leading to the immediate request for acquisition of a Landsat MSS scene of the area, subsequently obtained on 19 November 1979 (SEAN, 1979; Rothery *et al.*, 1988). Though MSS was initially designed and built with a thermal infrared channel, this failed soon after launch and was not available at the time of the Sierra Negra investigation. Nevertheless, the 80 m spatial resolution MSS data did show signs of thermally emitted radiance, but in the red (0.6 - 0.7 μm) and near infrared (0.7 - 0.8 μm and 0.8 - 1.0 μm) channels traditionally used to record solar reflected radiation. Surface temperatures at the eruption site were so high that significant levels of thermally emitted visible wavelength radiation were reaching the MSS instrument, 900 km above the Earth. Calculations indicated that the equivalent MSS pixel brightness temperatures were between 640 and 1040 °C for a 3 pixel wide region, covering a 10 km distance from near the summit down towards the coast (Rothery *et al.*, 1988). This was a clear indication of a major lava flow, showing near magmatic surface temperatures for a considerable distance.

The devastating 1980 eruption of Mount St Helens provided further evidence of the role that thermal remote sensing could play in volcano monitoring. Scientists were alerted to the possibility of a forthcoming eruption by changes in a variety of geophysical phenomena, with the result that a high intensity monitoring campaign was instigated at the

volcano (Lipman *et al.*, 1981). This campaign included data aquisition by airborne thermal infrared scanners, these revealing a few hotspots along the flank of the main stratocone. A flank collapse in this area on 18 May 1980 preceded a catastrophic explosive eruption of great magnitude, with the GOES geostationary meteorological satellite obtaining an unprecidented view of the spreading eruption cloud (Short, 1982). Later thermal observations by the orbiting Heat Capacity Mapping Mission (10.5 - 12.5 μm, 600 m spatial resolution) highlighted the early emplacement of a lava dome within the newly created amphitheatre (Short, 1982).

1.3.3. Improved thermal observations from space : The AVHRR

Following on from the 1970s and early 1980s successes at detecting and monitoring new volcanic activity using satellite observations of eruption plumes, routine observation of such features is now part of operational activity at the NOAA National Environmental Satellite, Data Services Division (National Oceanic and Atmospheric Administration, 1987; Stephens, 1993). This project uses data from the improved VHRR instrument, the Advanced Very High Resolution Radiometer (AVHRR), first flown onboard TIROS-N in 1978. The AVHRR still had a nominal spatial resolution of just over 1 km, but had an increased number of spectral channels (Table 1.1).

Of particular interest to those interested in the satellite monitoring of volcano surface temperatures was the incorporation of a new AVHRR middle infrared (3.7 μm) waveband, since thermal emittance at this wavelength changes rapidly with temperature (Figure 1.3). Theoretically it should be easier to detect surface temperature changes using observations made at 3.7 μm rather than those made at longer thermal infrared wavelengths.

Channel	Wavelength Range (μm)	Spectral Region
1	0.55 - 0.90 0.58 - 0.68*	Visible Red*
2	0.73 - 1.10	Near Infrared
3	3.55 - 3.93	Middle Infrared
4	10.5 - 11.5	Thermal Infrared
5*	11.5 - 12.5*	Thermal Infrared*

*Table 1.1. The channels of the AVHRR instrument, carried onboard the NOAA Polar Orbiting Environmental Satellites (NOAA/POES) from 1978 to the present. * indicates a channel available on the AVHRR/2 only, operational from 1981 onwards.*

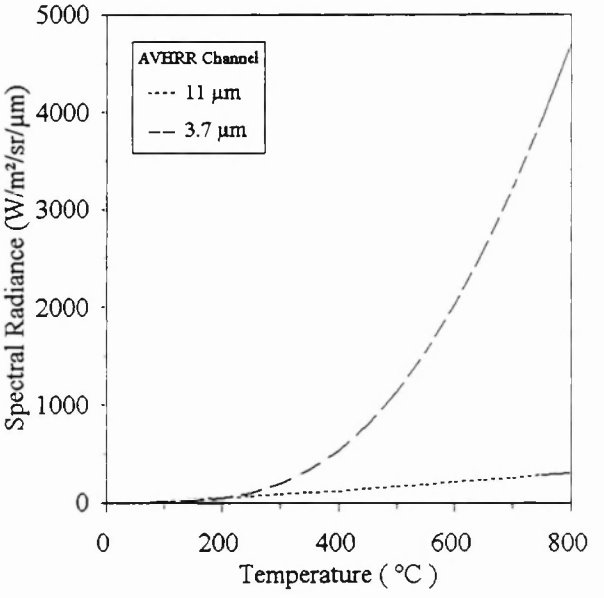

Figure 1.3. The relationship between spectral radiance and blackbody temperature for the AVHRR 3.7 and 11 μm wavebands.

Dozier (1981) first pointed out the possibility of using AVHRR 3.7 μm data to detect high temperature Earth surface features of subpixel resolution. Since high

temperature sources emit so strongly at 3.7 μm, a hot source covering even a very small fraction of the 1 km² AVHRR field of view will cause a much more significant rise in 3.7 μm channel pixel radiance or brightness temperature than in the corresponding 11 μm channel measurement (Figure 1.4). Dozier (1981) further suggested that comparison of the 3.7 μm and 11 μm data could be used to confirm the subpixel nature of the heat source since, if the entire ground surface were at a uniform temperature, the atmospherically corrected 3.7 μm and 11 μm brightness temperatures should be almost identical. If this were not the case then the heat source is likely to be of subpixel size.

Matson and Dozier (1981) first used the Dozier (1981) technique to observe and map the location of industrial gas flares, but it was not long before volcanoes were again targeted as potential sources of study. Weisnet and D'Aguanno (1982) studied AVHRR 3.7 μm data of the Mount Erebus lava lake (Antartica) whilst Scorer (1986; 1987) made repeated AVHRR observations of hotspots at Mount Etna (Sicily). Oppenheimer (1989) attempted a more wide ranging and quantitative study of volcanic signals in AVHRR data, utilising imagery of the Erebus, Stromboli, Vulcano and Etna volcanoes. That study concluded that AVHRR data were not really suited to the quantitative thermal monitoring of volcanoes due, in part, to the excessive pixel size when compared to the thermal features of interest. Though it was relatively easy to detect an active volcanic hotspot with AVHRR, it was believed that variations in the pixel brightness temperature could not be unambiguously attributed to volcanic change since the spatial resolution of the measurements was so poor. Furthermore the AVHRR 3.7 μm channel was plagued by noise problems, and hotspot signals often appeared 'smeared' over many pixels due to the large pixel overlap associated with off-nadir parts of the AVHRR scan (Oppenheimer, 1989; Breaker, 1990).

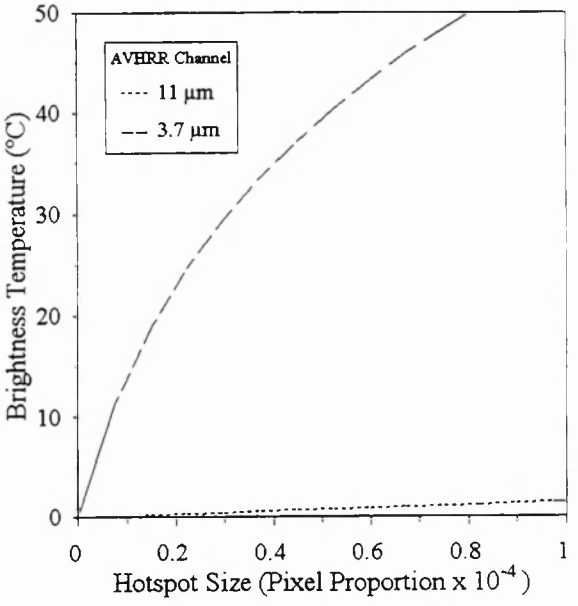

Figure 1.4. AVHRR 3.7 and 11 μm channel pixel brightness temperatures for a modelled dual thermal component situation. The modelled pixel has a background temperature of 0 °C and contains a subpixel-sized hotspot at 500 °C. The whole-pixel brightness temperature is plotted for situations where the hotspot comprises between 0 and one thousandth of the pixel area. As the hotspot size increases, the 3.7 μm brightness temperature increases sharply whilst the 11 μm brightness temperature increases only slowly. Thus the 3.7 μm measurement is seen to be much more sensitive to the presence of subpixel sized hotspots than the longer wavelength observations.

1.3.4. A new dawn : Landsat Thematic Mapper

Gloom at the initially unpromising nature of quantitative volcanic studies using AVHRR was tempered by the fact that new investigations using data from the Landsat Thematic Mapper (TM) showed significantly greater promise. As detailed in Table 1.2. TM operates in six wavebands covering the visible, near infrared and shortwave infrared region at 30 m spatial resolution, with an additional thermal infrared channel operating at 120 m spatial resolution (Engel and Weinstein, 1983). Francis and Rothery (1987) first analysed TM data of Lascar Volcano (Chile) and found that certain summit pixels were anomalously radiant in both the thermal and shortwave infrared wavebands, suggesting the

presence of a very high temperature source within Lascar's active crater. A similar signature was also found in TM data of Erta 'Ale volcano (Ethiopia), where Le Guern *et al.* (1979) and previous researchers had documented the presence of a long duration active lava lake.

TM Channel	Wavelength Range (μm)	Spectral Region	Spatial Resolution (m)
1	0.45 - 0.52	Blue	30
2	0.52 - 0.60	Green	30
3	0.63 - 0.69	Red	30
4	0.76 - 0.90	Near Infrared	30
5	1.55 - 1.75	Shortwave Infrared	30
6	10.4 - 12.5	Thermal Infrared	120
7	2.08 - 2.35	Shortwave Infrared	30

Table 1.2. The channels of the Thematic Mapper (TM) instrument, carried onboard Landsats 4 and 5 from 1972 to the present.

The spatial resolution of the TM sensor appears much better matched to the unambiguous identification of change in a volcanic heat source than does that of AVHRR, making the possibility of quantitatively monitoring such phenomena from space apparently much more likely. The Francis and Rothery (1987) study highlighted the fact that the temperatures derived from the anomalous TM band 5 pixels were consistently 50 - 100 °C higher than those from the corresponding TM band 7 pixels. This was initially attributed to the preferential absorption of longer wavelength (TM band 7) radiation by gaseous volatiles in the active crater, but this explanation was reconsidered when Rothery *et al.*

(1988) found similar results at yet another active volcanic site, namely Mount Erebus (Antarctica).

In a similar manner to the situation depicted in Figure 1.4, it was realised that the differential TM band 7 and 5 brightness temperatures could be generated if the hottest volcanic surfaces occupied only a small fraction of the sensors field of view, with the remainder of the 30 m pixel being at a much lower temperature. Rothery *et al.* (1988) realised that a dual component thermal structure was likely to describe many volcanic surface phenomena quite well, citing the example of fumarole fields, where small patches of rock are heated to a high temperature by escaping magmatic gas, and convecting lava lakes, where hot cracks expose the molten material beneath the relatively cooler solidified crust. This work went on to adapt the Dozier (1981) subpixel analysis technique to the TM shortwave infrared wavebands, using the method to estimate the approximate size and temperature of the subpixel volcanic hotspots at Lascar, Erta 'Ale, and Mount Erebus volcanoes, and also the temperature distribution on the 1979 Sierra Negra flow imaged by Landsat MSS. The methodology became known as the 'dualband technique' and adaptations of it have since been applied to many TM datasets in order to derive the temperature and area of many different volcanic surface phenomena, for example hot cracks and cooler crust on active lava flows (e.g. Pieri *et al.*, 1990; Oppenheimer, 1991; Flynn *et al.*, 1994, Andres and Rose, 1995) and lava lakes (e.g. Oppenheimer and Francis, 1997), and thermally anomalous regions of active lava domes (e.g. Glaze *et al.*, 1991b; Oppenheimer *et al.*, 1993; Andres and Rose, 1995) and fumarole fields (e.g. Gaonac'h *et al.*, 1994).

Despite the assumption of only two surface temperature components, one limitation of the dualband technique (Equations 1.2 and 1.3) is that there are more unknowns than data with which to solve them :

$$R_5 = P_h L_5(T_h) + (1 - P_h) L_5(T_c) \quad (1.2)$$

$$R_7 = P_h L_7(T_h) + (1 - P_h) L_7(T_c) \quad (1.3)$$

where R_5 is the atmospheric and emissivity corrected radiance in TM band 5 ($W/m^2/sr/\mu m$)

R_7 is the atmospheric and emissivity corrected radiance in TM band 7 ($W/m^2/sr/\mu m$)

P_h is the proportion of the TM pixel covered by the hot temperature component

$L_5(T)$ is the radiance emitted in TM band 5 by a body at T Kelvin ($W/m^2/sr/\mu m$)

$L_7(T)$ is the radiance emitted in TM band 7 by a body at T Kelvin ($W/m^2/sr/\mu m$)

T_h is the temperature of the hot component (K)

T_c is the temperature of the cool component (K)

Two ways of dealing with this indeterminacy evolved, (i) assume the temperature of the hot component, usually invoked in cases where it is believed to be magmatic, or (ii) estimate the temperature of the cooler component from neighbouring pixels that are believed to have a uniform thermal structure. In this way the temperature and size of the remaining thermal component can be solved using Equations 1.2 and 1.3, either graphically or numerically (Rothery *et al.*, 1988; Oppenheimer *et al.*, 1991). Once solutions have been determined, an adaptation of the Stefan-Boltzman equation, obtained by integrating the Planck function with respect to wavelength, can be used to calculate the total power emitted by each surface temperature component (Equation 1.4). Such a

technique has been used for estimating the thermal budgets of a number of active volcanoes (e.g. Glaze *et al.*, 1989a), though when used only with data from the TM shortwave infrared wavebands it does not properly take account of heat emitted by the cooler volcanic surfaces.

$$M = A\varepsilon\sigma T^4 \qquad (1.4)$$

where M is the total radiant exitance from the area (W)

A is the area of the thermal component (m^2)

σ is the Stefan-Boltzmann constant (5.67×10^{-8} $W/m^2/K^4$)

T is the surface temperature of the thermal component (K)

ε is the wavelength integrated emissivity of the surface

Despite the advances brought about by dualband analysis of TM data, many impediments remained to the use of such data for routinely monitoring changes in volcanic thermal features. These are discussed further in, for example, Rothery *et al.* (1992) and Oppenheimer (1993) but include (i) frequent saturation of the most radiant pixels in TM bands 5 and 7, thus providing only a lower limit on the level of emitted radiation, (ii) uncertainties in the corrections made for solar reflected radiation in daytime TM scenes and the requirement for special scheduling if nighttime TM data are to be obtained, (iii) the relatively infrequent repeat cycle of Landsat TM, once by day and once by night every 16 days, (iv) difficulty in obtaining TM datasets whose quantitative fidelity has not been corrupted by geometric resampling, and (v) the significant time delays and monetary costs involved in purchasing TM imagery from commercial data providers. Such restrictions limited most TM studies of active volcanoes to analysis of the unsaturated pixels present

in just one or two scenes, though a few notable exceptions included analysis of significantly longer time-series (e.g. Oppenheimer *et al.*, 1993; Oppenheimer and Francis, 1997).

1.3.5. A return to AVHRR

The rapid growth in TM based studies vastly improved the outlook for the routine thermal monitoring of volcanic activity using satellite remote sensing. It was clear that if suitable data could be made available both frequently and cheaply, then such methods could usefully supplement more traditional geophysical monitoring techniques at many active volcanoes, and could provide useful observations at sites where no current monitoring program existed. To tackle the issues of data cost and timeliness, some researchers returned to investigate further the potential of AVHRR since this sensor continued to offer frequent data that could be received locally at no cost to the user. Since AVHRR's low spatial resolution had previously been highlighted as a significant disadvantage for its use in volcanic thermal studies (Oppenhiemer, 1989), the new investigations initially concentrated on the largest volcanic thermal features, namely active lava flows. Mouginis-Mark *et al.* (1991a) showed how local reception of AVHRR data at Honolulu could be used to monitor the distribution of active Kilauea lava on the neighbouring Big Island of Hawaii, whilst a later study by Harris *et al.* (1995d) used archived AVHRR data collected by the University of Dundee to retrospectively document the thermal signature of the 1984 Krafla lava flow (Iceland). The success of these investigations led to further volcanological use of AVHRR, with the Alaska Volcano Observatory making use of locally received AVHRR data for the routine monitoring of potential volcanic hotspot sites in the North Pacific Ocean region (Dean *et al.*, 1996).

However, despite the renewed success of these AVHRR volcanological investigations, problems with the quantitative use of the instrument remain. In addition to the problems of poor spatial resolution, already noted by Oppenheimer (1989), Setzer and Verstraete (1994) and Harris *et al.* (1995c) highlighted the saturation problems of the AVHRR 3.7 μm channel. The saturation brightness temperature of this channel is 49 - 58 °C, depending upon the exact NOAA satellite in question (Robinson, 1991), and the intense radiance emitted by very hot bodies in this waveband means that even relatively small volcanological heat sources are likely to lead to pixel saturation (Figure 1.5). Nevertheless, Harris *et al.* (1997) were able to use combined AVHRR 3.7 and 11 μm observations of the 1991 - 1993 Etna flow to document accurately the spatio-temporal evolution of the flow field and to estimated a variety of time-variant flow parameters, though the saturation problems make the accuracy of estimation somewhat difficult to quantify. Despite this the work has made it clear that low spatial resolution datasets have value for the monitoring of volcanic thermal phenomena, though quantitative use of the AVHRR 3.7 μm data, which is potentially the most useful for the observation of subpixel sized hotspots, remains hampered by many of the factors originally highlighted by Oppenhiemer (1989).

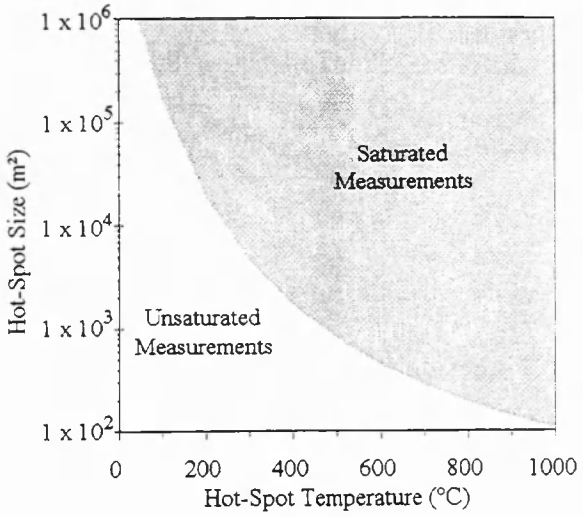

Figure 1.4. The AVHRR 3.7 μm channel saturation envelope for observations of subpixel sized hotspots. For this modelled blackbody example the saturation temperature was set to 50 °C, with an ambient background temperature of 10 °C. Increases in the ambient background temperature make the 3.7 μm observations more prone to saturation since thermal emission from the background will be increased.

1.4. The current project

It is now over 30 years since the first thermal observations of active volcanism were made from space and, since that time, a wide range of volcanic studies have made use of such information. However none of the remote sensing instruments used in these investigations has been designed for the purpose of volcano monitoring and, unsurprisingly, each has its limitation when used for this purpose. Though a dedicated satellite and instrument package designed specifically for the purpose of volcano monitoring has been proposed (Pieri and Glaze, 1989), the costs involved probably make such a development unlikely, at least in the short term. Rather than the development of a specialist 'volcano monitoring' satellite, the immediate future of spaceborne volcano remote sensing depends upon continuing to make best use of multi-purpose satellite remote sensing data.

The purpose of the current work is to investigate the potential of a relatively new remote sensing instrument, the Along Track Scanning Radiometer (ATSR), for the thermal observation of high temperature volcanic phenomena. ATSR has been designed with the specific purpose of measuring global sea surface temperature by making measurements of ocean emitted radiance in a series of infrared wavebands (Delderfield *et al.*, 1985). However, from its vantage point onboard the European Remote Sensing (ERS) satellite, ATSR also observes each of the world's terrestrial volcanoes. The spatial resolution of ATSR is almost identical to that of AVHRR, but the instrument incorporates a number of new features that make it of potentially greater use for the monitoring of volcanic thermal activity. These include the presence of a shortwave infrared (1.6 μm) waveband, similar to band 5 of Landsat TM. This project was established to investigate whether this enhanced spectral capability, coupled with the instruments frequent repeat cycle, make data from ATSR a useful tool for the thermal study of active volcanoes, both in terms of detecting and monitoring new eruptions and in the analysis of thermal emissions from persistently active sites. An ideal, though not necessarily realistic, result would be obtained if ATSR were found to offer quantitative data of a value somewhat comparable to that obtained from TM, but at a temporal frequency and cost more similar to that obtained from AVHRR.

The ATSR is, in fact, a series of instruments planned to operate over at least a 15 year period in order to determine the existence and extent of climate change related sea surface temperature variations (Delderfield *et al.*, 1985; Holdaway, 1993; Stricker *et al.*, 1995). This means that any potential volcanological use of ATSR need not be confined to the period of operation of the first instrument, launched onboard ERS-1 in 1991. Furthermore, ATSR shares some spatial resolution and infrared waveband characteristics

with the Moderate Resolution Imaging Spectrometer (MODIS), which is to be flown on each of the forthcoming NASA Earth Observing System (EOS) platforms (Ardanuy *et al.*, 1991). The first EOS launch is scheduled for 1988 and EOS will operate as part of NASA's Mission to Planet Earth program for the next 15 years (Asrar and Jon Dokken, 1993). One of the 28 interdisciplinary science projects selected by NASA as part of the EOS project is the NASA EOS Volcanology Investigation. This investigation aims to address two themes, (i) an understanding of the evolution of volcanic landforms and volcanic hazards, and (ii) the role that volcanism plays in modifying local and hemispheric climate (Mouginis-Mark *et al.*, 1991b). It has been proposed that MODIS data can potentially contribute to this work by acting as a thermal alarm for the detection of new volcanic eruptions (Mouginis-Mark *et al.*, 1991b; Flynn and Mouginis-Mark, 1995). In order to minimise errors of commision, such an alarm system will require the use of techniques capable of discriminating between volcanic hotspots and those caused by non-volcanic activity, for example vegetation fires. It is also possible that MODIS-based measurements of volcanic thermal emittance may provide data useful to a variety of volcano monitoring situations. An additional aim for this project is therefore to provide an early indication of areas where thermal measurements from MODIS may be of use to volcanological monitoring and investigation.

1.5. Structure of the thesis

In accordance with preferred policy at the Open University Department of Earth Sciences, much of the work carried out for this thesis has been published in refereed journals, with the relevant chapters being presented in this format. Some repetition is thus inevitable, but it means that any chapter can be read without reference to others.

Following this review (Chapter 1), I present the background to the ATSR instrument and data products (Chapter 2), followed by description of the various procedures used to obtain accurately calibrated ATSR thermal channel data, and details of the work I conducted to calibrate the ATSR shortwave infrared channels (Chapter 3). I follow this with two detailed studies of ATSR infrared radiance time-series of active lava domes at Lascar Volcano, Chile (Chapter 4) and Unzen Volcano, Japan (Chapter 5). Consideration is given to the effect of viewing geometry on the retrieved radiances, highlighting the implications for volcanic thermal monitoring using MODIS (Chapter 6). I then go onto analyse ATSR time-series datasets from active lava flows at Fernandina Volcano, Galápagos Islands (Chapter 7) and Mount Etna, Sicily (Chapter 9), interspersed with a chapter dealing with validation of the analytical techniques used (Chapter 8). A summary of the overall research, a set of conclusions and suggestions for further related work are then provided, including any immediate implications for the thermal monitoring of volcanoes using MODIS (Chapter 10).

The Appendices to this thesis detail background and additional information on a variety of techniques used during the course of the research (Appendices A - C), along with an additional brief study of the 1997 Indonesian fires using data from the AVHRR (Appendix D). In the final appendix (Appendix E), I briefly outline the issues involved in the satellite-based detection and discrimination of Earth surface hotspots, and provide suggestions for how these problems may be addressed in any automated system.

Chapter 2.

The ERS Along Track Scanning Radiometer and associated data products

---

2.1. Introduction

The driving force behind the design of the Along Track Scanning Radiometer (ATSR) was the requirement to measure long-term global sea surface temperature (SST) to better than 0.5 °C accuracy in order meet the exacting data requirements of the World Climate Research Program (WCRP) in investigating the nature and effect of any currently-operating global climate change (Houghton and Morel, 1983). ATSR was a direct response to a European Space Agency (ESA) Announcement of Opportunity that requested proposals for instruments that could complement those already planned for the first European Remote Sensing Satellite (ERS-1) and that could make use of surplus payload and power capacity on the spacecraft. ATSR was proposed and developed by a scientific consortium led by the Rutherford Appleton Laboratory (Principal Investigator Prof. D. Llewellyn-Jones) and including University of Oxford's Department of Atmospheric, Oceanic and Planetary Physics, University College London's Mullard Space

Science Laboratory, The U.K. Meteorological Office, the French Centre de Recherches en Physique de l'Environment and CSIRO's Division of Atmospheric Research.

Reflecting the primary mission of SST measurement, ATSR was initially designed with three wavebands in the thermal infrared. These wavebands were centred at 3.7, 11 and 12 μm and were very similar to those of the long-standing Advanced Very High Resolution Radiometer (AVHRR), which is also used to routinely measure global SST but to an accuracy somewhat lower than that required by the WCRP (Kidwell, 1995).

In order to improve upon the accuracy of the AVHRR SST measurements, a number of novel features were included in the ATSR design. These include (i) a conical scanning mechanism that allows the instrument to view the Earth's surface through two different atmospheric path lengths and thus improve the atmospheric corrections used to estimate SST, (ii) a Stirling cycle cooler that maintains the infrared focal plane assembly at around 80 K in order to minimise detector noise, and (iii) a precision onboard blackbody calibration system whose characteristics are well understood and continually monitored during instrument operation. Relatively late in the design stage a fourth infrared channel, centred in the shortwave infrared region (1.6 μm), was added to the design of the first generation ATSR (ATSR-1) in order to improve cloud detection during daytime SST determination.

ATSR-1 was launched from French Giuana on board an Ariane 4 rocket on 17 July 1991. By that time the second generation ATSR was already being devised, with the same primary scientific mission of monitoring global SST. However, design changes to ATSR-2 allowed a number of new features to be incorporated into the instrument, most notably

three new spectral channels in the visible and near-infrared, primarily for the monitoring of vegetation. ATSR-2 was launched onboard ERS-2 on 21 April 1995.

Delderfield *et al.*, (1985), Tinker *et al.*, (1985), Mason (1991), Read *et al.*, (1992), Prata *et al.*, (1990), Roberts and Petkovic, (1993) and Stricker *et al.*, (1995) provide further information on the design, engineering and operating characteristics of both ATSR instruments. The remainder to this chapter will further detail (i) the ATSR viewing geometry characteristics that have specific relevance to the project aim of monitoring high temperature Earth surface features, and (ii) the various ATSR data formats that are available, outlining the advantages and disadvatages each format offers for such studies.

2.2. The ATSR viewing geometry

ATSR's ability to sense the radiation emitted from an Earth location at two different viewing angles, and thus atmospheric pathlengths, makes possible a direct measurement of the pathlength dependence of the received radiation (Delderfield *et al.*, 1985). This is the fundamental feature of the ATSR that significantly enhances capabilities for correcting the radiance measurements for the effects of the intervening atmosphere. To facilitate this dual-viewing geometry the ATSR utilises a conically scanning plane inclined mirror to reflect Earth-emitted radiation onto the primary paraboloid mirror and from there into the focal plane assembly containing the detector system. Full rotation of the scan mirror takes 150 msec and the forward tilting of the scan cone gives views of the Earth through two viewing apertures, one at nadir and one at around 47 ° to nadir (Figure 2.1).

The data recorded by the instrument during the two Earth surface views have widely differing zenith angles. Data from the forward-view scan has a zenith angle of 53 -

55 °, whilst that from the nadir-view scan has a zenith angle of 0 - 22 °. As a direct result of this viewing geometry, the centre of the forward- and nadir-view scans is separated by around 915 km on the Earth surface (Figure 2.2).

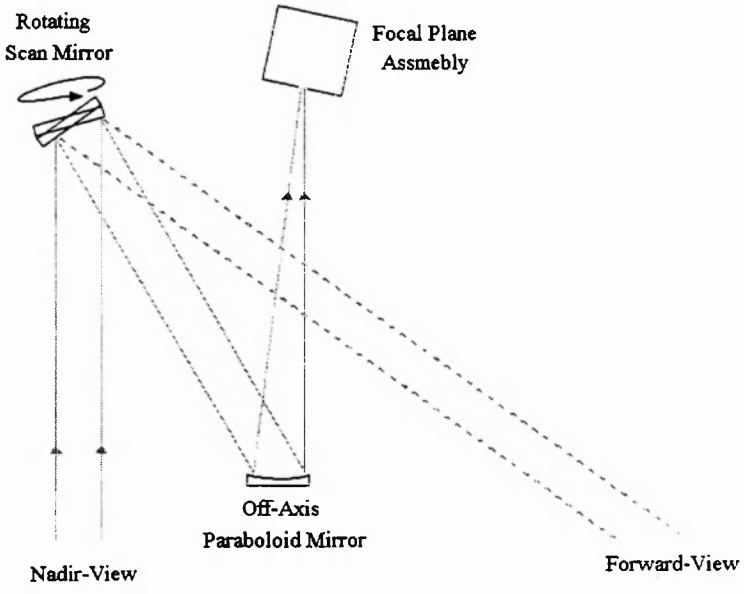

Figure 2.1. Schematic of the ATSR fore-optics, indicating how rotation of the scan mirror provides observations in both the nadir- and forward-view directions.

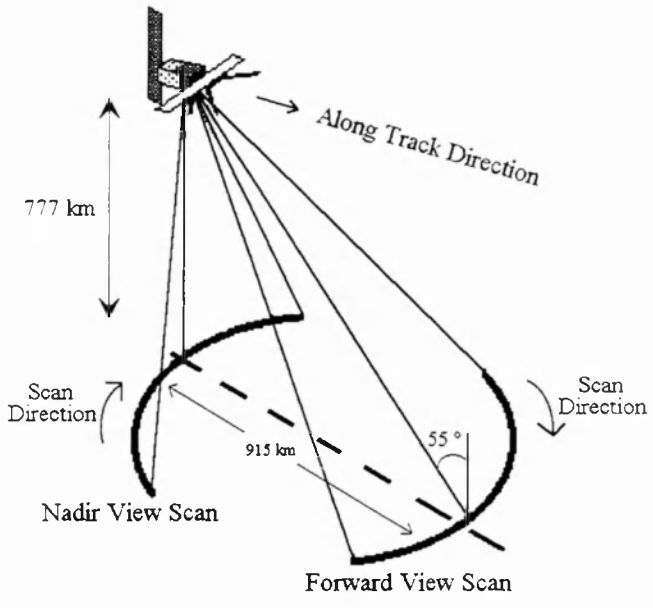

Figure 2.2. The viewing configuration of the ATSR instrument, mounted on board the orbiting ERS spacecraft. Earth surface data are obtained during both the forward- and nadir-views, with the instrument detectors viewing the internal calibration targets between each forward- and nadir-view scan.

2.3. ATSR pixel measurements

A cooled field stop of size 0.695 mm square is positioned at the focus of the instrument to define the ATSR instantaneous field-of-view (IFOV). The projection of the IFOV is different in the forward- and nadir-view scans because of the varying view geometry. At the centre of the nadir-view the IFOV projection is 1 km x 1 km, increasing to 2.82 km x 1.60 km at the centre of the forward-view (Mason, 1991). Since the ERS satellites traverse a ground-equivalent distance of 1 km during each full rotation of the scan mirror, successive swaths of forward- and nadir-view data are displaced by 1 km on the ground. This provides negligible along-track IFOV overlap at the centre of the nadir-view scan, but substantial along-track IFOV overlap at the centre of the forward-view scan.

The effect of the differing pixel size and overlap in the ATSR forward- and nadir-views can be seen clearly in Figure 2.3, which shows subscenes covering the Oman test-site that was later used as a calibration target for this channel (Chapter 3). For ease of comparison, data from both views have been geometrically co-registered using nearest neighbour resampling. Ground features are noticeably more distinct when imaged in the nadir-view than in the forward-view. The increased atmospheric path length in the forward view, up to 60% greater than that in the nadir-view, does not account for these differences since the shortwave infrared waveband is relatively insensitive to the absorbing effects of the atmosphere. Rather the increase in clarity when moving from the forward- to the nadir-view is due to the decreased pixel size and overlap.

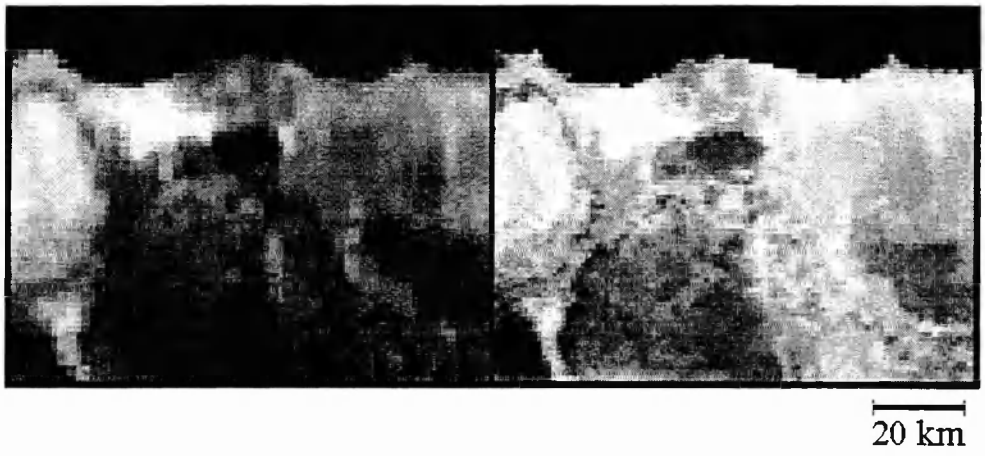

Figure 2.3. Subscenes extracted from (a) forward-view and (b) nadir-view ATSR-1 1.6 μm data of the Omani coastal region, obtained at 6:48 and 6:50 GMT respectively on 3 July 1992. The data from each view have been co-located for ease of comparison.

2.4. Spatio-temporal characteristics of dual-view ATSR data

The Earth surface projection of the forward- and nadir-view scans is 500 km wide, with both scans being centred on the sub-satellite track (Figure 2.2). Full rotation of the

scan mirror takes 150 msec, during which time the output from each of the channel detectors is passed to one of two integrator circuits that are reset 2000 times during the scan. This gives a 75 μsec integration period for each pixel measurement, with the two integrators used alternately to avoid any problems with 'dead time' during the observations (Godsalve, 1995). Each of the onboard calibration targets is the subject of 16 of these pixel measurements, with a further 371 pixels corresponding to Earth surface observations made in the forward-view and 555 pixels corresponding to Earth surface observations made in the nadir-view. The remainder of the 2000 pixels are unused and therefore not transmitted. Figure 2.4 shows an example of temporally contemporaneous forward- and nadir-view Earth surface data, recorded during 512 full ATSR scans

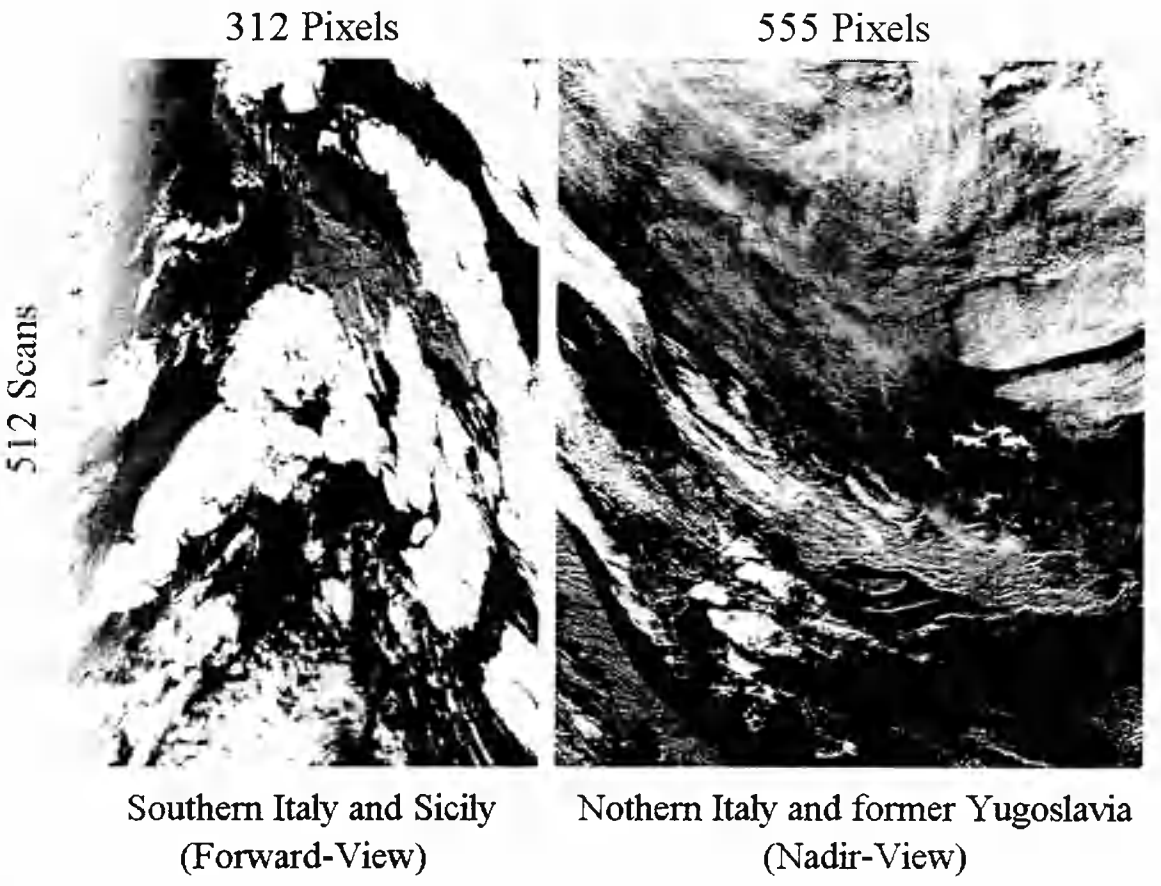

Figure 2.4. ATSR 1.6 μm image data from 512 forward- and nadir-view scans of the Earth surface taken at around 01:21 GMT on 6 January 1992, as ERS-1 passed over former Yugoslavia, the Adriatic sea and the northern coast of Italy during a descending node (daytime) pass. The contemporaneous 1.6 μm forward- and nadir-view observations are illustrated.

As the data of Figure 2.4 indicate, whilst ERS-1 passed over former Yugoslavia, the Adriatic sea and the northern coast of Italy, ATSR imaged these areas in the nadir-view. At the same time the instrument observed the toe of Italy, the Mediterranean Sea and the Island of Sicily in the forward view, each scan line of forward-view data being about 915 km forward of the sub-satellite point in the along-track direction. Figure 2.4 also indicates a number of notable features of the 'raw' ATSR data product, namely (i) the reduced number of image pixels in the forward-view compared to that in the nadir-view, (ii) the 'curved' nature of the geometric distortion in the forward-and nadir-view image

data, and (iii) the left-right inversion of the data in the forward-view due to the clockwise rotation of the scan mirror and the north-south motion of the satellite during the daytime pass (Sicily is actually east of the toe of Italy).

Because the principal aim of the dual-path viewing geometry of ATSR is to obtain observations of the same ground location through two different atmospheric path lengths, the spatially coincident forward- and nadir-view data from the same ERS orbit must be identified during data processing. Assuming all pixels are at sea level, a particular ground location imaged along the sub-satellite track in the forward-view at time t seconds and during scan number n will be imaged in the nadir-view at time $(t + 137)$ seconds during scan number $(n + 915)$. Away from the sub-satellite track the situation is more complex, but detailed orbit and scan models can be used to identify the spatially coincident pixels in both views (Prata *et. al*, 1990; O'Brien and Prata, 1990). Figure 2.5 shows forward- and nadir-view data of the area surrounding Sicily, taken during the same ERS-1 orbit as the data shown in Figure 2.4. Any particular pixel imaged in the nadir-view has a corresponding pixel, centred on approximately the same ground location, imaged in the forward-view. The Rutherford Appleton Laboratory ATSR Data Processing scheme, encouragingly termed SADIST (Synthesis of ATSR Data into Sea-surface Temperatures), uses a linked orbit and scan model to identify these corresponding pixels and, where appropriate, uses dual-view measurements in the ATSR thermal channels to retrieve SST for each cloud-free, non-land pixel (Zavody *et al.*, 1994).

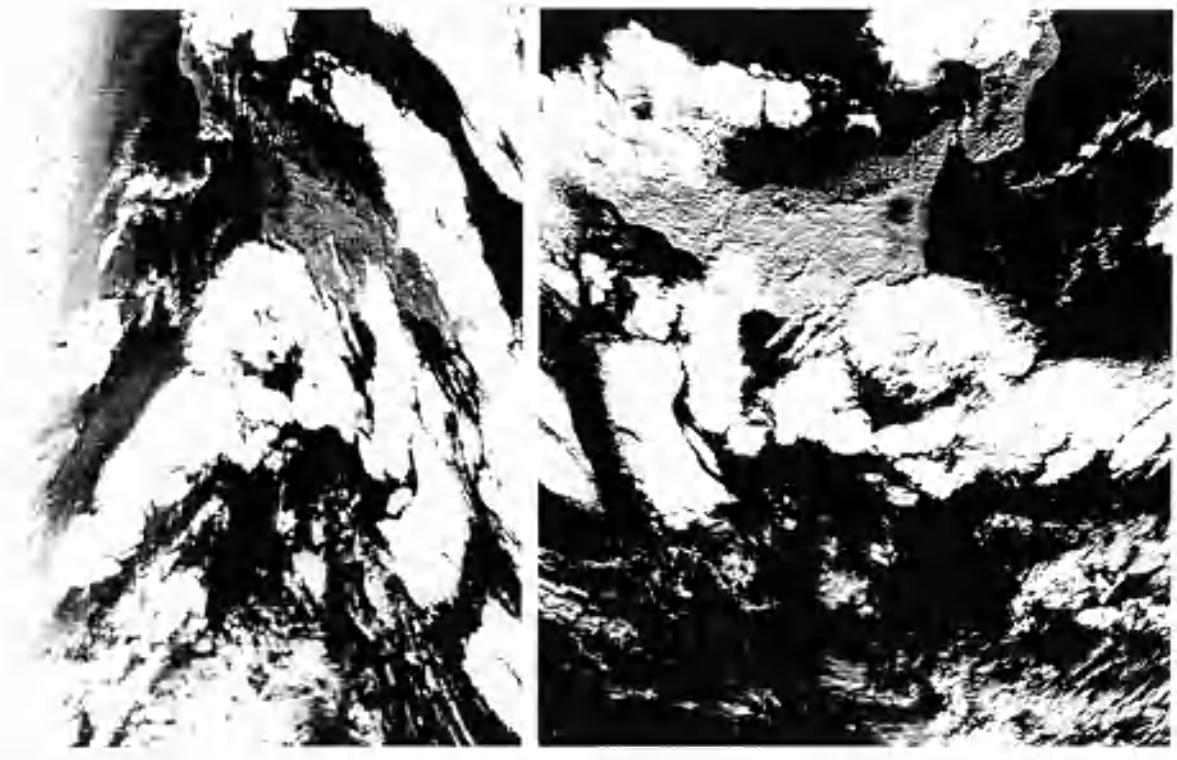

(a) (b)

Figure 2.5. The 'raw' ATSR 1.6 μm image data covering approximately the same ground area during a single ERS orbit made on 6 January 1992. (a) shows the forward-view data, which is that shown in Figure 2.3, whilst (b) shows the nadir-view data of the same area, taken approximately 137 seconds later. Differences in the geometry, number of pixels and left-right orientation of data in the two views are clearly evident.

2.5. ATSR data products

SADIST can provide ATSR data in a variety of formats, each with particular attributes that may or may not be useful to the prospective user. Bailey (1994; 1995) provides comprehensive details on each of the data products. Only brief details are provided here. The lowest level ATSR data product obtainable from SADIST is the so-called COUNTS product. COUNTS products retain the spatio-temporal characteristics of the original 'raw' ATSR data, so that data taken in the forward- and nadir-view is temporally but not spatially coincident. The data of Figure 2.3 were extracted from a

single COUNTS product and these data retain the curved nature of the original scans. For each individual pixel, the COUNTS product stores the value of digital count recorded from each of the operating ATSR spectral channels. The COUNTS product also stores data from the onboard thermal channel calibration system and these data can be used to convert the thermal channel digital counts into estimates of incoming spectral radiance. These calibration issues are further discussed in Chapter 3.

In order for users to easily combine spatially-coincident information from both ATSR views, corresponding pixels in the forward- and nadir-view data must be co-located. This attribute is available from the ATSR Brightness Temperature (BT) data product, where data from the corresponding forward- and nadir-views has been reprojected to a 512 x 512 pixel grid that is orientated parallel to the sub-satellite track. In the BT data product, image pixel (x,y) in the forward-view scene has the same ground location as image pixel (x,y) in the nadir-view scene. For pixels at sea level this statement is true to an r.m.s. accuracy of around one pixel (Bailey, 1994), though for pixels above sea level the accuracy is somewhat less. The BT thermal channel data are also calibrated into units of pixel brightness temperature, hence the name of the data product. Again, this calibration is further discussed in Chapter 3. Figure 2.6 shows data from an ATSR BT product of Sicily, produced from the 'raw' ATSR data shown in Figure 2.5. This is the BT product version of the COUNTS data product shown in Figure 2.4. Unlike the COUNTS product the BT image does not retain the original spatio-temporal characteristics of the ATSR scans, rather the forward- and nadir-view data are spatially co-registered, making it easy to identify corresponding pixels within the two views.

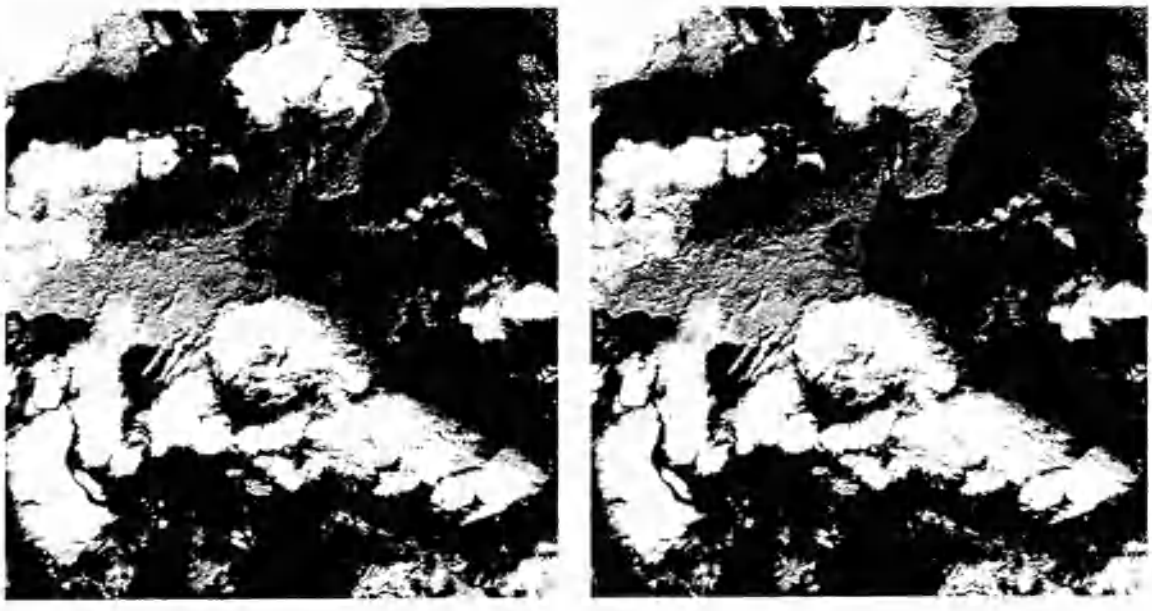

(a) (b)

Figure 2.6. 1.6 μm channel image data extracted from an ATSR BT product of 6 January 1992. The quantitative data are those shown in Figure 2.5, but in this case the forward- and nadir-view images appear almost identical since data from both scenes have been geometrically resampled to the same 512 x 512 pixel grid during SADIST data processing. Detailed examination of the two views would, however, reveal differences in image clarity similar to those observed in Figure 2.2.

2.6. ATSR data products for use in hotspot studies

Because the ATSR BT products include information on the latitude and longitude of each pixel centre, and because the curved nature of the scan geometry has been corrected for during the SADIST geolocation procedure, it is generally much easier to locate a geographic site of interest in the BT product than it is in the corresponding COUNTS product. For this reason many studies using ATSR benefit from utilising BT rather than COUNTS products, even if they only use nadir-view data. However, when using data that has been geographically resampled, care must be taken that the quantitative value of the information has not been altered during the resampling process. This is

particularly important for hotspot studies since the area of interest may cover only a few pixels whose radiance values must be accurately recorded.

To confirm that the SADIST nearest neighbour resampling scheme did not quantitatively alter the data, the BT and COUNTS product versions of the same ATSR scene were compared. Nighttime (ascending node) ATSR-1 data of the 1991 - 1993 Mount Etna lava flow (Chapters 8 and 9) were used since initial investigations showed this hotspot feature affected a relatively large number of ATSR pixels. Since the resampling scheme used by SADIST is applied equally to pixels from all wavebands, the relationship between the COUNTS and BT data products was tested using data from a single channel only. The 1.6 μm channel was selected since data from this waveband is stored as a simple digital count in both the COUNTS and BT product formats, data from the thermal channels being stored in radiance and brightness temperature units respectively (Chapter 3). During data processing SADIST applies a simple linear conversion (Equation 2.1) between the 1.6 μm digital count data of the two data formats (Albin Zavody, personal communication 1996) and so the inverse relationship was applied before data analysis began.

$$BT_{16}=2.5\,(COUNTS_{16} - 101) \qquad (2.1)$$

where BT_{16} is the 1.6 μm channel digital count in the ATSR-1 BT product

$COUNTS_{16}$ is the 1.6 μm channel digital count in the ATSR-1 COUNTS product

Figure 2.7 shows the ATSR 1.6 μm nadir-view data obtained at Mount Etna during the nighttime ERS-1 pass of 3 January 1991. For ease of comparison the 10 x 10 pixel

subscenes are all orientated so that the northern-most pixels are at the top of the image, and the western-most pixels are at the right of the image. Figure 2.7 (a) shows the data extracted from the COUNTS product, (b) the data extracted from the BT product, and (c) the data extracted from the BT product that have been subsequently resampled to a regular latitude/longitude grid with a pixel spacing equivalent to 1 km on the ground. The resampling of the Figure 2.7 (c) data was performed using the computer code shown in Appendix A, which makes use of the latitude/longitude information embedded in the BT data product.

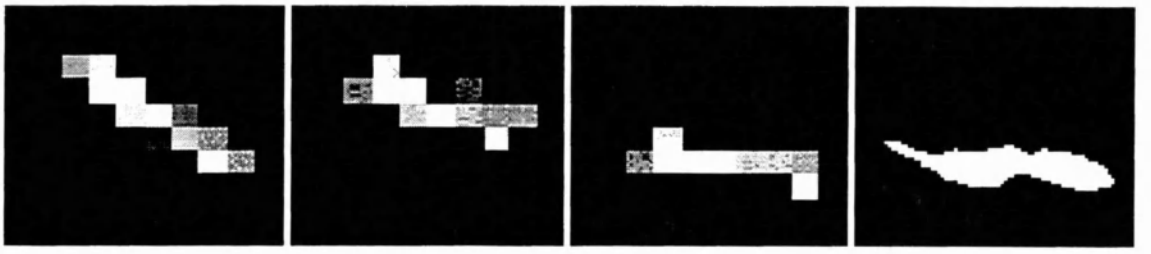

(a) (b) (c) (d)

Figure 2.7. (a), (b) and (c) are nadir-view ATSR-1 1.6 μm subscenes of the 1991 - 1993 Mount Etna lava flow, each produced from nighttime (ascending node) data obtained at 01:20 GMT on 3 January 1992 and displayed using identical histogram stretches of the digital count data. (a) shows the COUNTS product data, (b) shows the BT product data, and (c) shows the BT product data resampled to a regular latitude/longitude grid. Figure 2.6 (d) shows the outline of the Etna lava flow obtained from geocoded daytime Landsat Thematic Mapper data of 2 January 1992.

The outline of the flow obtained from geocoded Landsat TM data [Figure 2.7 (d)] indicates the generally west - east path of the lava, this pattern being accurately represented by the resampled ATSR BT product data of Figure 2.7 (c). The agreement

between these data confirms the correctness of the locational information stored within the BT data product, these data being used to perform the resampling. As expected, the 10 x 10 pixel subscenes extracted from the original COUNTS and BT products, Figures 2.7 (a) and (b) respectively, do not accurately represent the shape or orientation of the lava flow. This is because these data are displayed on pixel grids that are determined by the motion of the ATSR scan mirror and/or the ERS satellite, and not by the actual ground locations of the observed pixels. When using ATSR data to determine the shape of hotspot features it is therefore important that the original data be resampled to a regular latitude/longitude array prior to analysis.

Quantitatively comparing the original and the resampled BT data products, Figure 2.7 (b) and Figure 2.7 (c) respectively, reveals that two of the original BT product pixels do not appear in the resampled data. Instead these pixel values are replaced by second copies of pixels whose ground locations more closely match those of the output grid location. Quantitative analysis of the resampled data of Figure 2.7 (c) thus produces different results than identical analysis applied to the original BT data and should therefore be avoided. However, the original BT data are themselves resampled versions of the data present in the COUNTS product. The quantitative consistency between the original COUNTS and BT data products therefore required investigation.

Comparing the data of Figure 2.7 (a) and Figure 2.7 (b) showed that the digital count values of all radiant pixels in the COUNTS product were accurately represented in the BT product. This consistency is due to the fact that the output BT product pixel grid used by SADIST is determined by the sampling characteristics of ATSR and by the orbital motion of the ERS satellite. The sampling interval therefore matches that of the original pixel measurements, thus avoiding the problems that occur when the output grid is

determined by geographical location alone, as is the case for the Figure 2.7 (c) data.

Despite this finding however, care must still be taken, especially when considering BT data obtained in the ATSR forward-view. This is because the BT output pixel grid is substantially undersampled in the forward-view, there being 337 measurements for 512 output pixel locations (Figure 2.5). In this case, SADIST fills unpopulated BT pixel locations in the forward-view by copying values from the spatially nearest neighbour. These 'cosmetically filled' pixels are, however, easily identifiable since SADIST negates the 12 μm brightness temperature value. The 'cosmetic filling' technique is also used in the nadir-view since a few nadir-view output BT pixels also remain unpopulated after the SADIST geolocation procedure (Bailey, 1994). It is therefore important that, prior to quantitative studies of BT product radiance and/or brightness temperatures, pixels with a negative 12 μm brightness temperature are discounted from the analysis. Provided this procedure is carried out, hotspot studies can make use of the ATSR BT products that confer significant advantages when compared to the alternative COUNTS product data. It is these ATSR BT product data that I utilise in the subsequent studies of Earth surface hotspots.

Chapter 3.

ATSR data calibration

Adapted from material published in the following manuscripts :

Wooster, M. J. (1995), Proc. of the 21st Remote Sensing Society Conference, 520-527.

Wooster, M. J. (1996), International Journal of Remote Sensing , 17, 1069-1074.

RAL (in press), ATSR 1.6 μm Channel Data Calibration Report - Results of User Studies.

3.1. Introduction

Both ATSR-1 and ATSR-2 possess channels in the shortwave infrared (1.6 μm), middle infrared (3.7 μm) and longwave infrared (11 and 12 μm) regions of the electromagnetic spectrum. The 3.7, 11 and 12 μm channels are collectively referred to as the thermal channels since they are principally designed to record thermal radiance emitted from the Earth's surface. In contrast the primary purpose of the shortwave infrared channel is to record levels of solar reflected radiation during daytime observations, and it may therefore be referred to as a 'visible' channel. ATSR-2 possesses three additional visible channels centred at 0.55, 0.66 and 0.87 μm (Read *et al.*, 1992), but these

wavelengths are too short to be relevant to hotpsot studies. The spectral response functions of the corresponding channels of ATSR-1 and ATSR-2 are closely matched and are shown in Figure 3.1. The ATSR instruments can record data from any of these channels at 12 bit resolution, though not all channels are continuously recorded at full radiometric precision due to the limited bandwidth available for data transmission (Mason, 1991; Bailey, 1995).

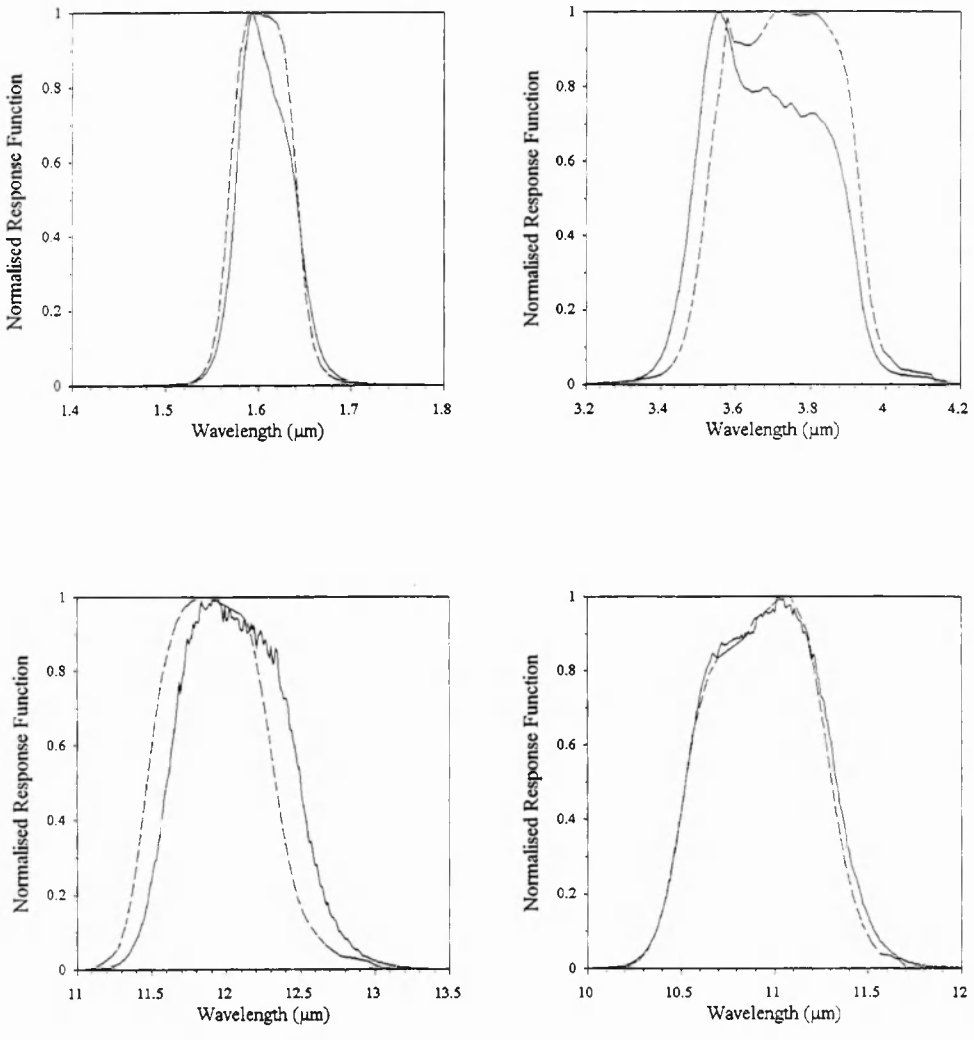

Figure 3.1. Clockwise from top left, the normalised spectral response functions of the 1.6 μm, 3.7 μm, 11 μm and 12 μm channels of ATSR-1 (dashed line) and ATSR-2 (solid line).

In order to use ATSR data quantitatively, it is necessary for the 'raw' digital count data to be converted into physical units, normally values of incoming spectral radiance. This conversion is easily made once the general relationship between output digital count and incoming spectral radiance is known for each channel, i.e. the channel is calibrated. The purpose of this chapter is to detail the calibration procedures used when analysing data obtained by the ATSR-1 and ATSR-2 sensors. Section 3.2 describes how I calibrated the (previously uncalibrated) 1.6 μm channel of ATSR-1, whilst Section 3.3 outlines how I tested and improved the calibration of the 1.6 μm channel of ATSR-2. Finally, Section 3.4 describes the techniques I used to obtain measurements of incoming spectral radiance from data obtained in the ATSR thermal channels.

3.2. Calibration of the ATSR-1 shortwave infrared channel

3.2.1. Introduction

The shortwave infrared (1.6 μm) channel was a relatively late addition to the design of ATSR-1, principally incorporated to aid daytime cloud detection during the estimation of sea surface temperature (Tinker *et al.*, 1985). The channel does not benefit from any pre-launch calibration or onboard calibration mechanism. This is a deficiency since radiance estimates at 1.6 μm would be useful in many terrestrial ATSR applications and would greatly assist ATSR-1/ATSR-2 time-series analyses, the ATSR-2 instrument having an onboard calibration system covering this spectral region (Read *et al.*, 1992).

Here I outline how I achieved an approximate digital count to spectral radiance calibration for the ATSR-1 1.6 μm channel using near-contemporaneous data from the Optical Sensor (OPS) onboard the Japanese remote sensing satellite JERS-1 (Fuyo-1), the OPS being the spaceborne sensor with a 1.6 μm channel whose bandpass is most similar

to that of the ATSR-1. The resultant calibration allows estimates of 1.6 μm spectral radiance and/or reflectance to be produced from ATSR-1 forward- and nadir-view digital count data.

3.2.2. Methodology

The JERS-1 OPS instrument is a 6-bit, 7 spectral channel visible and shortwave infrared radiometer with a spatial resolution approximating 18 x 24 m (Nishidai *et al.*, 1994). OPS digital count data can be calibrated into units of incoming spectral radiance by applying published coefficients, previously derived using contemporaneous imagery from the OPS and NASA's AVIRIS (Airborne Visible Infrared Imaging Spectrometer) sensor (Green *et. al.*, 1993; Shimada and Nakai, 1993). By obtaining ATSR-1 1.6 μm data of an area for which calibrated 1.6 μm OPS data are available, it is possible to make a cross-comparison between these datasets and thus establish an ATSR-1 digital count to spectral radiance calibration equation.

OPS and ATSR-1 data of the Omani coast were used in the cross-calibration study since the region was (i) composed of large uniform areas of differing 1.6 μm reflectance, (ii) largely devoid of vegetation, (iii) relatively low lying for maximum accuracy of ATSR geo-location and, (iv) minimally affected by cloud cover. Additionally, local knowledge of the area was good and the remotely sensed data were of high quality, with the OPS 1.6 μm image showing none of the periodic noise that has affected certain OPS scenes (Nishidai *et al.*, 1994). The OPS scene was acquired at 6:56 GMT on 25 June 1992, whist the ATSR-1 data were obtained at 6:50 GMT on 17 June and 3 July 1992. The ATSR data were obtained in both COUNTS and BT format, the two standard data product formats produced by SADIST, the Rutherford Appleton Laboratory ATSR data processing scheme (Bailey, 1994).

The BT format image has a specific latitude/longitude location associated with each ATSR pixel, with additional data theoretically allowing the ground location of each pixel centre to be determined to an accuracy of 0.0625 km, though this accuracy is unlikely to be achieved in practice (Shin *et al.*, 1997). These data were used to calculate the ground location of five separate and differently reflecting pixels in the central region of the 17 June 1.6 μm nadir-view ATSR image, each pixel being surrounded by large, near uniform areas of reflectance in this waveband. The corresponding five pixels, i.e. those with the nearest ground location to these original five, were then located on the 3 July ATSR scene. The digital count values from all ten pixels, the five on 17 June scene and the five near-spatially coincident on the 3 July scene, were recorded from the appropriate BT product files. The corresponding COUNTS product digital counts were calculated from these data using the inverse of Equation 3.1. Next the OPS 1.6 μm image statistics of these ten ground areas were extracted by first re-projecting the OPS scene to a latitude/longitude grid using a 1:100000 map and 13 ground control points (rms error = 5.5 OPS pixels), and then extracting the statistics of the ten 1 km² areas that were precisely located at the positions of the ten chosen ATSR pixels. For this work the ATSR ground resolution was taken as a simple 1 km x 1 km square, though this is a simplification of the actual case (Godsalve, 1995). Around each of the chosen locations the variance in OPS 1.6 μm digital count was minimal over many kilometres, thus making negligible any inaccuracies induced by errors in the ATSR/OPS co-location procedure.

The location of maximum surface reflectance used in the calibration is shown in Figure 3.2. This location is covered with an area of highly reflecting sediment deposit. Figure 3.3 similarly shows the location of minimum ground reflectance used in the study. Once the OPS and ATSR image statistics of all ten ground locations had been extracted,

areas of water in the Gulf of Oman were used to obtain two minimum reflectance points for the calibration. These statistics were taken from all spatially coincident ATSR/OPS offshore areas that were unaffected by suspended sediment or sunglint. Finally, nighttime ATSR data were used to find the BT and COUNTS product value corresponding to zero radiance in the 1.6 μm waveband, the so called 'dark current' of this channel.

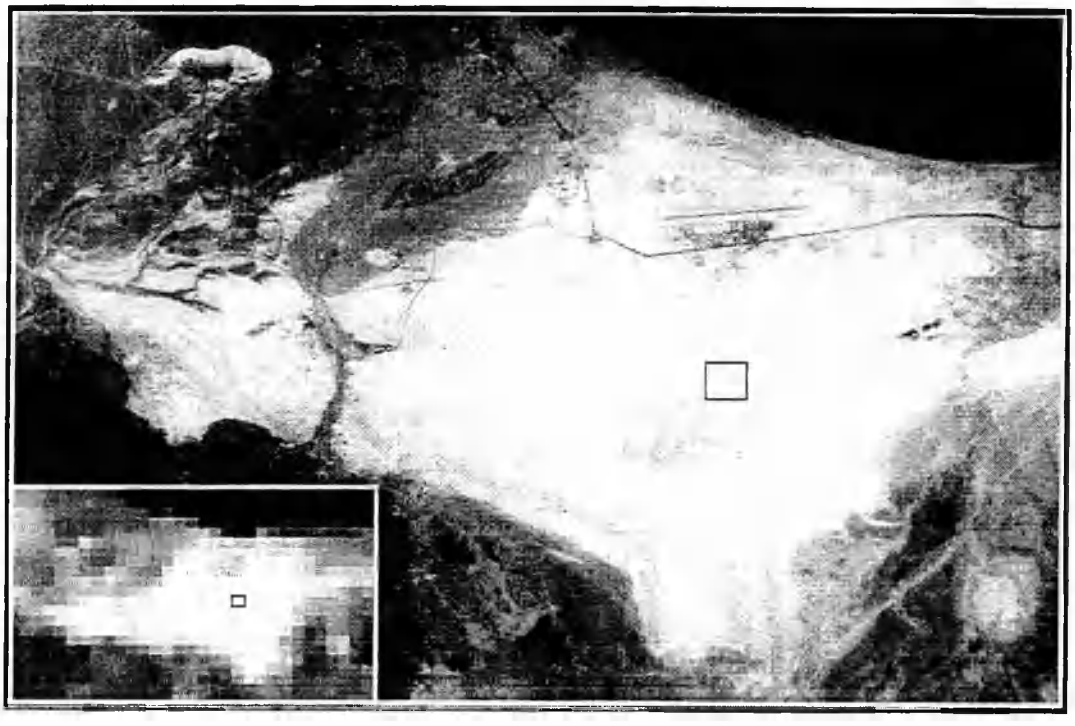

Figure 3.2. The area of maximum reflectance used in the study. The location of the ATSR pixel is outlined in the 17 June ATSR-1 1.6 μm BT data product (insert), with the corresponding 1 km² area delimited on the 25 June 1.6 μm OPS subscene (main picture). Note Seeb International Airport (top) for scale.

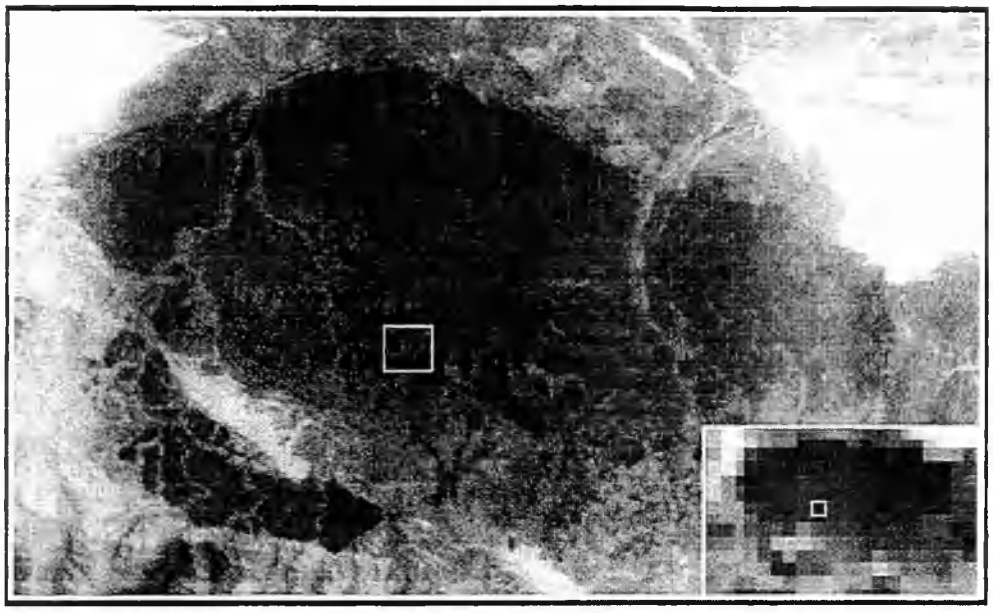

Figure 3.3. The area of minimum reflectance used in the study. The location of the ATSR pixel is outlined in the 17 June ATSR-1 1.6 μm BT data product (insert), with the corresponding 1 km² area delimited on the 25 June 1.6 μm OPS subscene (main picture).

3.2.3. Data Analysis

The ATSR and OPS image statistics were related to each other by assuming the percentage spectral reflectance (Equation 3.1) of each ground location should be identical in both the ATSR and OPS data. Errors due to this assumption were believed small since (i) the ATSR-1 and OPS 1.6 μm channel bandwidths are similar (Figure 3.2) and laboratory spectra showed that the spectral reflectance of each substrate varied by less than 2% within these wavebands (Anthony Denniss, personal communication 1995), (ii) LOWTRAN 7 (Kneizys *et al.*, 1988) predicted that the slight image-to-image variation in viewing zenith angle would introduce errors of less than 1% for a mid-latitude summer atmosphere and any particular aerosol model, (iii) variations in actual substrate reflectance due to temporal change and the changes in viewing geometry were believed small and, (iv) atmospheric change between the dates of the OPS and ATSR images was believed

minimal due to similar weather conditions. Any errors due to assumptions (ii) to (iv) would manifest themselves as differences between the statistics of the near-contemporaneous points in the ATSR dataset and should thus appear during data analyses.

$$Rf_{16} = \frac{100\pi d^2 R_{16}}{E_{16} os\theta} \tag{3.1}$$

where Rf_{16} is the top-of-atmosphere spectral reflectance in the 1.6 μm waveband (%)

d is the Sun-Earth distance (astronomical units)

E_{16} is the extraterrestrial solar irradiance in the 1.6 μm waveband (W/m²/μm)

θ is the solar zenith angle

R_{16} is the spectral radiance recorded in the 1.6 μm channel (W/m²/sr/μm)

Assuming the top-of-atmosphere spectral reflectances recorded in the ATSR and OPS 1.6 μm channels should be identical for a single ground location, rearrangement of Equation (3.1) can be used to obtain an estimate of the incoming spectral radiance that would be expected in the ATSR 1.6 μm channel (R_{atsr}) given a set of viewing conditions and the value of radiance recorded in the corresponding OPS channel (R_{ops}):

$$R_{atsr} = \left(\frac{E_{atsr} \cos\theta_{atsr} d_{ops}^2}{E_{ops} \cos\theta_{ops} d_{atsr}^2} \right) R_{ops} \tag{3.2}$$

Figure 3.4 shows the spectral response functions of the ATSR and OPS 1.6 μm channels and the incoming solar irradiance data taken from Arvensen *et al.* (1969). The spectral response functions of each detector have been linearly resampled to the 0.005 μm

spacing of the solar irradiance data and the values of E_{atsr} and E_{ops} were determined as 250.73 and 235.25 W/m²/μm respectively. Based on the radiances obtained from the OPS data, Equation 3.2 was then used to calculate the spectral radiance that would be expected in the ATSR-1 1.6 μm channel at each pixel location at the actual time of the ERS-1 overpass. This radiance was then related to the actual ATSR digital count value obtained for that location from both the COUNTS and BT data product files.

3.2.4. Results and discussion

The resulting relationship between the ATSR-1 digital count values and the estimated incoming spectral radiance is shown in Figure 3.5. The single linear fit (r^2 = 0.99) of points from both ATSR image dates validates assumptions (ii) to (iv) and indicates that the ATSR-1 1.6 μm channel is linear in its response to incoming radiation.

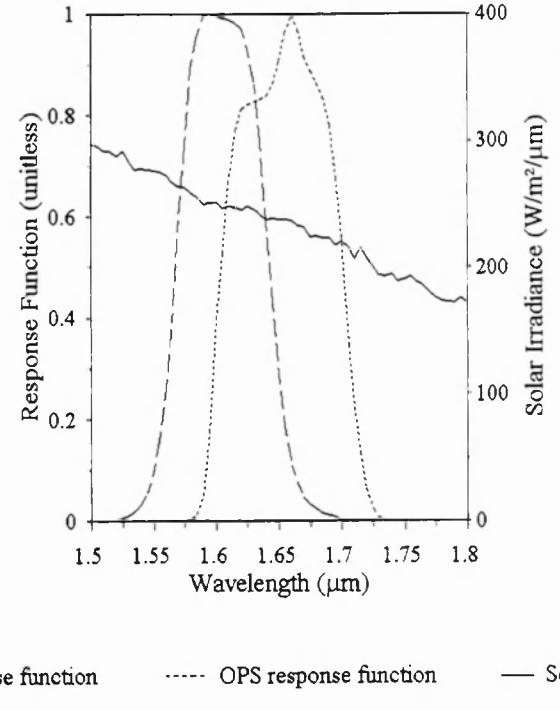

Figure 3.4. The normalised spectral response functions of the 1.6 μm channels of ATSR-1 and OPS (l.h.s. y-axis), along with the extraterrestrial solar irradiance (r.h.s. y-axis).

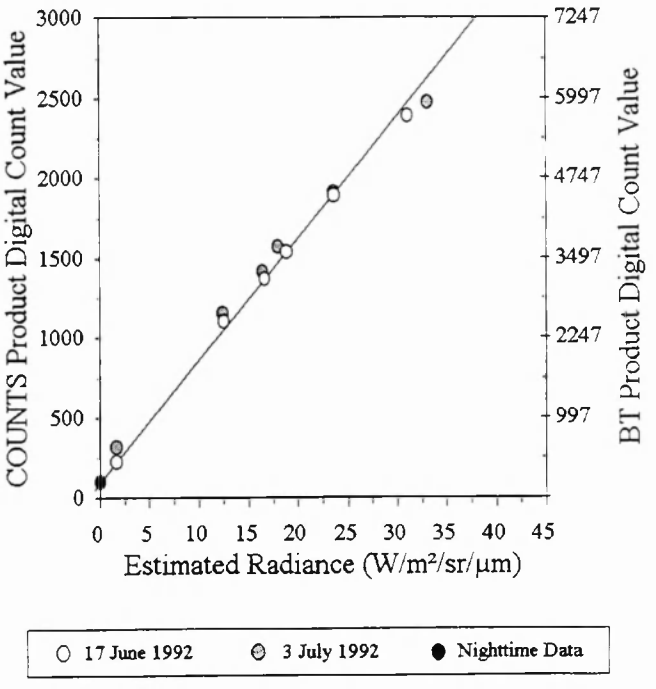

Figure 3.5. The relationship between incoming spectral radiance in the ATSR-1 1.6 μm channel, estimated using OPS data and associated calibration coefficients (Shimada and Nakai, 1993), and the digital count recorded in the COUNTS and BT product files. The least squares linear best fit to the data (Equations 3.3 and 3.4) is also shown.

From the data of Figure 3.5 we obtain two linear equations that relate the ATSR-1 1.6 μm channel COUNTS and BT product values to the incoming spectral radiance :

$$\textit{1.6 μm spectral radiance (W/m²/sr/μm)} = 0.01321\ (COUNTS_{16}) - 1.33 \qquad (3.3)$$

$$\textit{1.6 μm spectral radiance (W/m²/sr/μm)} = 0.00528\ (BT_{16}) \qquad (3.4)$$

where *COUNTS* is the 1.6 μm channel digital count recorded in the COUNTS product

BT is the 1.6 μm channel digital count recorded in the BT product

(The standard error on the linear regressions being 0.95 W/m²/sr/μm)

The derivation of Equations 3.3 and 3.4 is reliant upon on the accuracy of the OPS calibration coefficients of Shimada and Nakai (1993). Since these have not yet been widely utilised by the remote sensing community, a secondary technique for OPS data calibration was sought so that our ATSR calibration results might be confirmed using an alternative methodology. A suitable method was found using the results of Malila (1995), who derived a methodology for simulating Landsat Thematic Mapper (TM) digital count data from uncalibrated OPS digital counts, based upon a simple linear scaling :

$$DC_{tm} = 1.8588(DC_{ops}) - 19.68 \qquad (3.5)$$

where DC_{tm} is the simulated TM band 5 (1.6 μm) digital count value

DC_{ops} is the OPS band 5 (1.6 μm) digital count value

By applying Equation 3.5 to the OPS digital count data obtained from the calibration sites, and applying the long-standing TM calibration methodology of Markham and Barker (1987) to the resultant dataset, simulated TM band 5 (1.6 μm) spectral reflectance estimates for the ten 1 km² areas used in the cross-calibration were produced. These statistics were then used to calculate a new ATSR-1 1.6 μm calibration relationship, shown as Figure 3.6.

The linear relationships of Equations 3.3 and 3.4 have been superimposed on Figure 3.6, along with the least squares linear best fit to these new data. The similarity in these two sets of equations is evident from the figure, and from the equation coefficients themselves :

1.6 μm spectral radiance ($W/m^2/sr/\mu m$) = 0.01266 ($COUNTS_{16}$) - 1.28 (3.6)

1.6 μm spectral radiance ($W/m^2/sr/\mu m$) = 0.00506 (BT_{16}) (3.7)

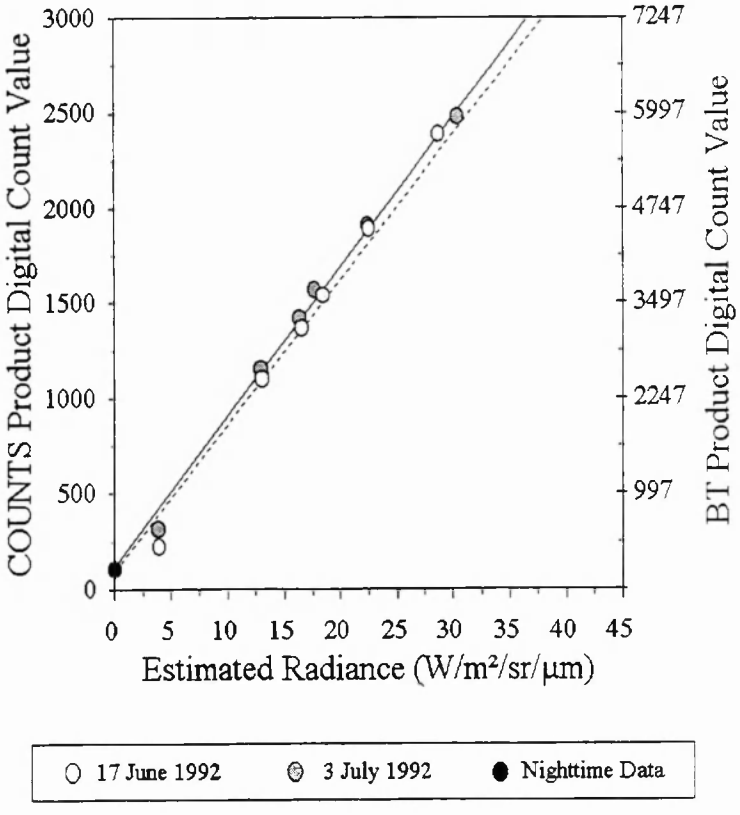

Figure 3.6. The relationship between incoming spectral radiance in the ATSR-1 1.6 μm channel, estimated using simulated Landsat TM band 5 (1.6 μm) data and associated calibration coefficients (Markham and Barker, 1987), and the digital count recorded in the ATSR-1 COUNTS and BT data product files. The linear best fit to the data is shown as the broken line (Equations 3.6 and 3.7), with Equations 3.3. and 3.4 shown as the solid line.

The closeness of Equations 3.3 and 3.4 to Equations 3.5 and 3.6 indicates that the OPS calibration coefficients of Shimada and Nakai (1993) are providing realistic values of

top-of-atmosphere radiance and reflectance, comparing well to those produced using the more widely used TM coefficients of Markham and Barker (1987). The slight difference in gain and offset between Equations 3.3 and 3.4 and Equations 3.6 and 3.7 may be due to residual errors in the OPS data calibration or in the application of Malia's (1995) TM simulation methodology to our OPS data. Malila's study was performed only three months before the December 1993 failure of the OPS shortwave infrared instrument, possibly during a period of increased sensor degradation.

The values of spectral radiance obtained from Equations 3.3 and 3.4 can be converted into estimates of spectral reflectance using Equation 3.1. The result indicates that ATSR-1 can be used to estimate the top-of-atmosphere spectral radiance in the 1.6 μm channel up to a saturation point of around 53 $W/m^2/sr/\mu m$, equivalent to a nominal lambertian spectral reflectance of 66%.

3.3. Calibration of the ATSR-2 shortwave infrared channel

3.3.1. Introduction

Stricker *et al.* (1995) provide detailed information on the design changes made between ATSR-1 and ATSR-2, one of the major ones being that the second generation instrument possesses three additional visible channels in the optical and near-infrared region of the electromagnetic spectrum. The existence of these new visible channels affects the 1.6 μm observations since ATSR-2 does not include the mirror used to reflect radiation into the 1.6 μm detector of ATSR-1. Rather it possesses a dichroic beam splitter that allows the visible and near-infrared beam to pass out of the infrared focal plane assembly and into a new visible focal plane assembly that houses the detectors for the 0.555, 0.659 and 0.865 μm channels. These new channels are allied to an onboard visible

channel calibration mechanism, the so-called VISCAL unit, that allows the output digital count data to be calibrated into units of top-of-atmosphere surface reflectance (Read *et al.*, 1992). Data from this VISCAL unit are of relevance to shortwave infrared studies, since VISCAL observations are also available for the ATSR-2 1.6 μm channel.

The ATSR-2 VISCAL unit contains an opal diffuser which is illuminated by the sun during certain parts of the ERS-2 orbit. Calibration observations of this diffuser panel are made close to the time of local satellite sunset and, during these observations, solar radiation is reflected from the diffuser and onto the detectors in the visible focal plane. These observations provide a measure of the visible channel detector output for 100% incoming extraterrestrial solar radiation. These data can be used to calibrate the visible channel Earth surface observations into units of top-of-atmosphere percentage reflectance. In practice the Rutherford Appleton Laboratory ATSR project use the VISCAL observations to produce a set of calibration coefficients for each visible channel and these are made available to ATSR-2 data users. Multiplication of the ATSR-2 visible channel digital count values (obtained from the ATSR-2 BT data products) by these calibration coefficients converts the measurements into top-of-atmosphere percentage reflectances. The visible channel calibration coefficients are updated from VISCAL observations on a near-daily basis so that variations in solar output, Sun-Earth distance and detector responsivity do not significantly affect the resultant reflectance estimates.

During the ATSR-2 commissioning phase it was found that the calibrated 1.6 μm data provided top-of-atmosphere reflectances that were somewhat low in comparison to those expected (Phil Watts, personal communication 1996). The problem was specific to the 1.6 μm channel, the calibrated 0.555, 0.659 and 0.865 μm observations being of the correct magnitude. Since shortwave infrared observations of high temperature surfaces

require accurately calibrated 1.6 μm data, any errors in the calibration of the ATSR-2 1.6 μm channel required further investigation. It was felt especially important to compare near-contemporaneous 1.6 μm channel output from ATSR-1 and ATSR-2 since time-series analysis covering the operation of both these instruments would require them to be accurately cross-calibrated. Fortunately, during the 1995 ERS Tandem Mission both ERS satellites were flown in near-identical orbits that differed by a single day, thus allowing near-contemporaneous ATSR-1 and ATSR-2 observations of the same ground locations to be intercompared.

3.3.2. Methodology

The initial task was to determine whether any major degradation of the ATSR-1 1.6 μm sensor had taken place since the calibration of that channel in June - July 1992. To evaluate this the reflectances of a series of homogeneous areas were monitored over the 1992 - 1995 period. If atmospheric and surface cover variations are assumed negligible, then any major temporal variation in the retrieved surface reflectances may be due to ongoing sensor degradation. For the reasons outlined in Section 3.2.3, I chose to perform the study using data from the same Oman region as was used for the calibration of the ATSR-1 1.6 μm channel.

Twelve ATSR-1 scenes were obtained for approximately equally spaced dates between the end of 1992 and mid-1995. Four of the chosen scenes proved to be severely cloud contaminated, but the remainder were almost cloud free. This gave eight new ATSR-1 scenes plus the two 1992 ATSR-1 scenes used in the original 1.6 μm calibration of Section 3.2. The five ground locations used in the initial ATSR-1 calibration were chosen as test sites, along with three new ground locations of an equally homogeneous nature (Figure 3.7). Equation 3.1 was used to calculate the top-of-atmosphere 1.6 μm

reflectances but, because of variations in the pixel latitude/longitude centres between each image, the reflectance of each test-site was taken as the mean of that obtained from a 3 x 3 pixel area.

Once I had assessed the degradation in the ATSR-1 1.6 μm detector, near-contemporaneous ATSR-1 and ATSR-2 observations of the same ground locations were obtained in order to perform a 1.6 μm channel intercomparison. Two ATSR-2 scenes covering the Oman test sites (Figure 3.7) were obtained for this purpose, taken on 1 and 4 July 1995, each of these being just one day later than the corresponding ATSR-1 scene. Assuming the ATSR-1 1.6 μm channel has been accurately calibrated using the results of Section 3.2 and those of the sensor degradation study, this methodology also provides a check for the VISCAL calibration of ATSR-2 1.6 μm channel.

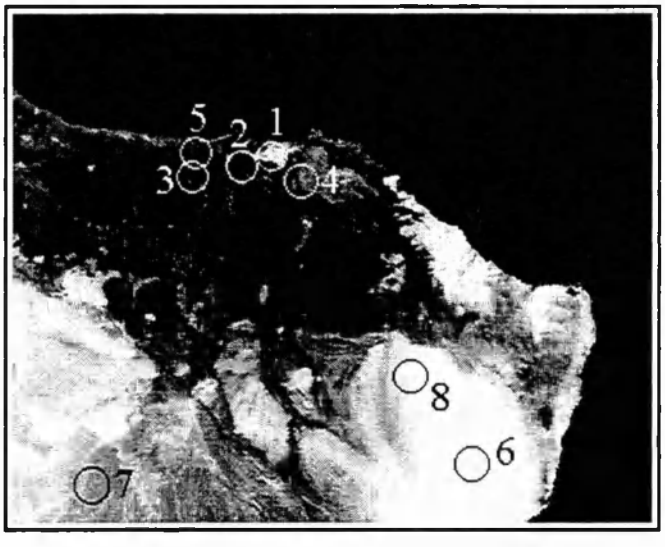

Figure 3.7. The eight ground locations of varying surface reflectance used in the ATSR-1 / ATSR-2 1.6 μm channel intercomparision. Locations 6 - 8 were specific to this study, whilst locations 1 - 5 were also used in the original calibration of the ATSR-1 1.6 μm channel (Section 3.2). Surface reflectance measurements were taken as the mean of a 3 x 3 pixel grid lying at the centre of the circled area.

3.3.3. Results and discussion

Figure 3.8 shows the retrieved top-of-atmosphere ATSR-1 1.6 μm reflectances for four of the chosen ground locations highlighted in Figure 3.7. The least squares linear best fits to the data are also shown, these indicating a small decreasing trend in retrieved reflectance over the three year period. The surface reflectances obtained at the other four locations also follow this trend, but are not reproduced on Figure 3.8 for the sake of clarity.

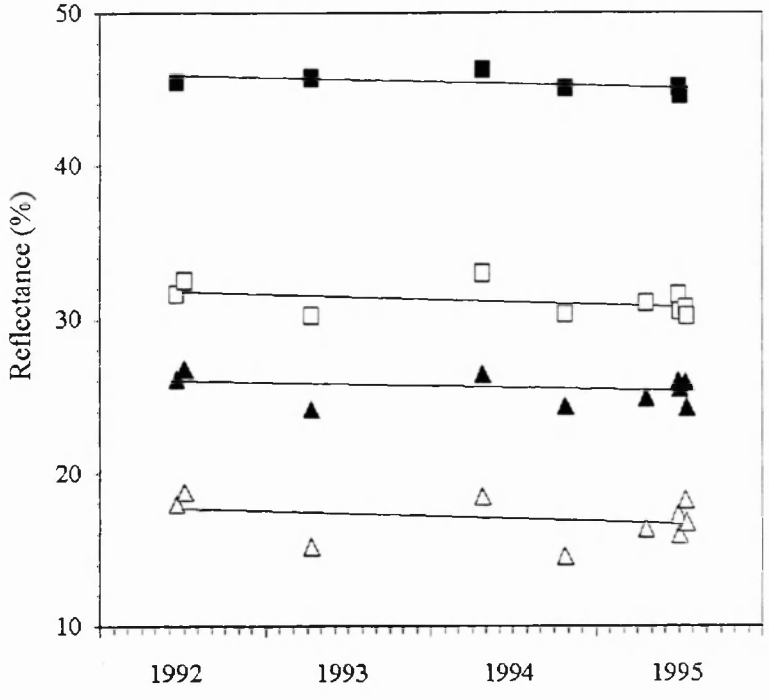

Figure 3.8. The top of atmosphere 1.6 μm reflectances obtained from ATSR-1 observations of four of the ground locations shown in Figure 3.7 (Δ = location 2, □ = location 4, ▲ = location 5 and ■ = location 8). The least squares linear best fits to the data are also shown, these having an average root mean square deviation of 1.2 % reflectance units.

The decreasing reflectance trend observed in Figure 3.8 can be explained by degradation of the ATSR-1 1.6 μm detector over the four year period. Atmospheric and surface cover variations would not be expected to consistently produce such a trend. The

potential sensor degradation was quantified using the method of Kaufman and Holben (1993), i.e. by calculating the changes in the gain parameter of Equation 3.4 that would be required to keep the observed top-of-atmosphere reflectances constant over time. For this purpose the reflectances calculated from the initial June and July 1992 ATSR-1 images were taken as the true values (prior to any sensor degradation), with the new gain parameter calculated for each subsequent image and each ground location using :

$$gain = \left(\frac{Rf_{true} E_{1.6} \cos\theta}{100\pi d^2} \right) \frac{1}{BT_{16}} \tag{3.8}$$

where *gain* is the new gain appropriate to that date (W/m²/sr/μm per BT count)

Rf_{true} is the true top of atmosphere 1.6 μm percentage spectral reflectance

Results from Equation 3.8 were used to calculate the least squares linear best fit relationships between the calculated gain and the scene date for each of the eight ground locations shown in Figure 3.7. Though any degradation in the 1.6 μm detector would not necessarily be linear, such an assumption is sufficient for this study. The calculated linear relationships provide a measure of the apparent rate of change of gain with time, with a mean value of (1.9 ± 0.8) x 10^{-7} W/m²/sr/μm per BT 1.6 μm digital count per day. This rate equates to a (5 ± 2)% change in gain of the ATSR-1 1.6 μm channel over the four years since the end of the ATSR-1 commissioning phase, much less than the 10% and 20% gain changes respectively reported for the visible and near infrared channels of the AVHRR sensor onboard NOAA-9 over the three year post-launch period (Kaufman and Holben, 1993). The fact that the Stirling-cycle cooler on ATSR-1 enabled the 1.6 μm detector to be operated at around 80 K for much of the time (Tinker *et al.*, 1985) is likely

to have contributed to the minimal level of sensor degradation evidenced in the dataset. The visible and near-infrared channels of AVHRR do not benefit from such a system and would thus be expected to degrade more rapidly in orbit.

Comparison of the ATSR-1 dataset with near-contemporaneous reflectance measurements obtained from ATSR-2 provides evidence to support the claim of errors within the ATSR-2 1.6 μm channel VISCAL calibration. Figure 3.9 shows results obtained from two of the highest reflectance areas of Figure 3.7.

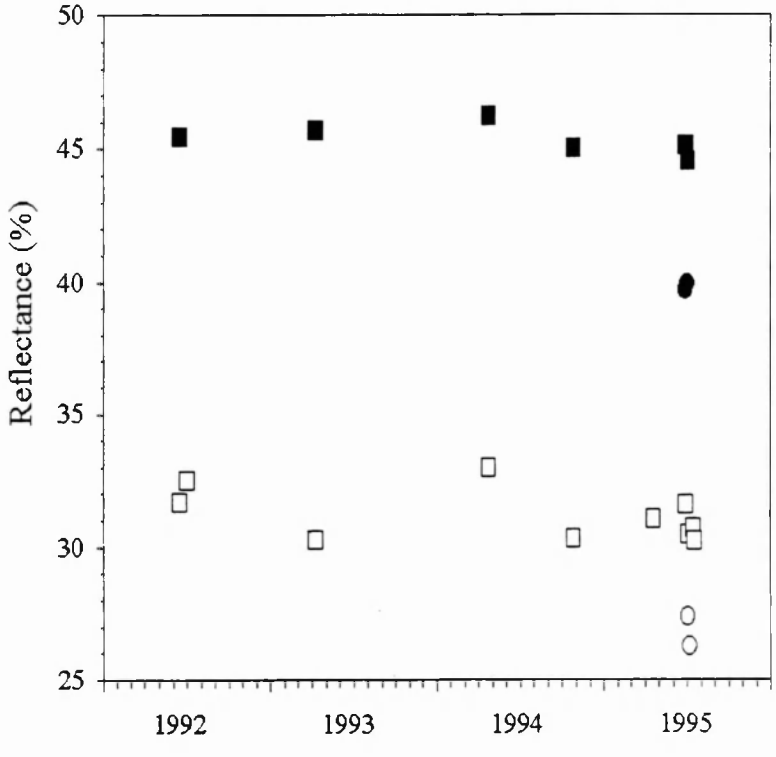

Figure 3.9. The top of atmosphere 1.6 μm reflectances obtained at locations 8 and 2 of Figure 3.7 using ATSR-1 observations made between June 1992 and July 1995 (■ = location 8 and □ = location 2) and ATSR-2 observations of 1 and 4 July 1995 (● = location 8 and ○ = location 2). The ATSR-2 observations provide reflectances that are noticeably lower than those retrieved by ATSR-1. Note the expanded scale with respect to Figure 3.8.

It is clear that the ATSR-2 observations provide surface reflectances somewhat lower than those retrieved by ATSR-1. Analysis of data from each of the test areas highlighted in Figure 3.6 indicates that the 1.6 μm top-of-atmosphere reflectances retrieved by ATSR-2 are (21 ± 4)% lower than those retrieved from ATSR-1. Studies using a variety of alternative post-flight calibration methodologies for this channel report calibration errors of a similar magnitude (RAL, in press), namely between 20% and 30%. Correcting the ATSR-2 shortwave infrared radiance estimates by the derived error factor allows for a more accurate estimation of the arriving infrared energy within this waveband, and also for more meaningful analyses of time-series data covering the operation of both the ATSR-1 and ATSR-2 instruments.

3.4. Calibration of the ATSR thermal channels

3.4.1. Introduction

The 3.7, 11 and 12 μm channels of the ATSR instruments are allied to a precise onboard calibration mechanism that is significantly enhanced over those in previous spaceborne thermal remote sensing systems (Tinker *et al.*, 1985). The ATSR thermal channel calibration mechanism works by allowing the detectors to view internal black body targets between each forward- and nadir-view scan. There are two such targets whose emissivities are known to high accuracy. One blackbody floats at the temperature of the ATSR fore-optics enclosure (~ 265 K) and the other is heated with constant power to around 305 K, providing a temperature range close to that of the observed Earth surface brightness temperatures (Mason, 1991). Each ATSR-1 thermal channel can record energy levels equating to pixel brightness temperatures of between 197 and 320 K. The 11 and

12 μm channels of ATSR-2 also possess this same dynamic range but the saturation brightness temperature of the 3.7 μm channel has been slightly reduced to 312 K.

The ATSR detectors view the calibration blackbodies through the optical chain that is also used to view the Earth, taking 16 digital count measurements of each calibration target during each rotation of the scan mirror. The temperature of each blackbody is monitored using an array of platinum resistance thermometers and these data, combined with knowledge of the blackbody emissivities and the spectral response functions of the thermal channel detectors (Figure 3.1), allows the integrated radiance emitted by each calibration target within each thermal channel to be accurately determined. Combining these calculated radiances with the digital count data recorded during each blackbody view allows the linear relationship between incoming radiance and output digital count to be determined for each ATSR thermal channel. This is done for each scan, with relationships calculated for both odd and even pixels since these measurements are made using different integrating circuits which have slightly different characteristics. These linear calibration relationships are stored as a value of slope (radiance per count) and intercept (radiance at zero count) in the COUNTS products discussed in Chapter 2 (Bailey, 1994; Bailey, 1995).

3.4.2. Calculation of thermal channel spectral radiances

The ATSR COUNTS products provide the digital count recorded by the instrument for each pixel, along with the slope and intercept values appropriate to each thermal channel, each scan line and each odd/even pixel number. Application of the slope and intercept values to the digital count data (Equation 3.9) provides a measure of the incoming radiance at that pixel location in each thermal channel :

$$R_i = \frac{slope_i(COUNTS) + intercept_i}{A_i \Omega_i Z_i} \tag{3.9}$$

where i is the ATSR channel number

R_i is the spectral radiance arriving at the ATSR detector (W/m²/sr/μm)

$slope_i$ is the slope parameter from the COUNTS product (W/count)

$intercept_i$ is the intercept parameter from the COUNTS product (W)

$A_i\Omega_i$ is the throughput for scene radiation falling on the detectors (m²/sr)

Z_i is the area under the response function of channel i (μm)

Values of Z_i were obtained from application of Equation 3.10 to the data shown in Figure 3.1, whilst values of $A_i\Omega_i$ were obtained from Mason (1991) and from the Rutherford Appleton Laboratory ATSR project (A. Zavody, personal communication 1995).

$$Z_i = \sum_{q=1}^{n} \Delta\lambda_i R_q(\lambda) \tag{3.10}$$

where $\Delta\lambda_i$ is the wavelength increment between measurements of spectral response (μm)

$R_q(\lambda)$ is the normalised spectral response at measurement location q (unitless)

n is the number of locations at which the channel spectral response was measured

Though application of Equation (3.9) gives a reasonable estimate of the radiance arriving at the ATSR thermal channel detectors for any particular output digital count, the

absolute accuracy is dependent upon the detector system having a truly linear response to incoming radiation. For the 3.7 μm channel, which uses an Indium Antimonide detector, the response is almost linear and so this assumption is valid for our purposes (Mason, 1991). However the 11 and 12 μm detectors are constructed from n-doped mercury cadmium telluride, which has a significantly non-linear response. This means that application of Equation 3.9 to the 11 and 12 μm digital count data obtained from the COUNTS product provides spectral radiance estimates slightly lower than those which were actually arriving at the detectors. The degree to which the incoming radiance is underestimated is dependent upon the brightness temperature of the target pixel, reaching a maximum of around 5% at the upper end of the target pixel temperature range (Mason, 1991). Since the main application of ATSR data is the estimation of accurate surface brightness temperatures, and hence accurate sea surface temperatures, the effects of this detector non-linearity were carefully investigated and characterised during pre-flight testing (Mason, 1991). Corrections for the non-linearity were then incorporated into the look-up-table relationships used in the ATSR data processing chain that converts COUNTS product pixel radiances into values of surface brightness temperature in the BT data product (Zavody *et al.*, 1994). ATSR BT products that record values of pixel brightness temperature are therefore correctly representing the amount of radiance arriving at the 11 and 12 μm detectors. COUNTS products that, indirectly, store values of incoming radiance are actually under-representing these values since the non-linear corrections have not been applied to these data.

3.4.3. Extracting thermal channel radiances from the BT data products

Since the ATSR BT products incorporate a variety of useful information that the COUNTS products do not (Chapter 2), it was desirable to use these BT data routinely for

our investigations. When values of incoming spectral radiance were required, these can be back-calculated from the 3.7, 11 and 12 μm brightness temperatures using :

$$R_i = \frac{\sum_{q=1}^{n} L(\lambda,T).\Delta\lambda_i.R_q(\lambda)}{\sum_{q=1}^{n} \Delta\lambda_i.R_q(\lambda)} \qquad (3.11)$$

where i is the ATSR channel number

R_i is the value of incoming spectral radiance ($W/m^2/sr/\mu m$)

T is the pixel blackbody temperature (K)

$L(\lambda,T)$ is the Planck function radiance ($W/m^2/sr/\mu m$)

Since the non-linearity of the 11 and 12μm detectors has already been taken account of in the calculation of pixel brightness temperature (Zavody *et al.*, 1994), use of Equation 3.11 should provide a correct measure of the infrared spectral radiance (R_i) arriving at the thermal channel detectors, the values being noticeably larger than those provided by Equation 3.9. I demonstrate this by analysing the COUNTS and BT data products of the same ATSR scene, in this case data of the north African coast obtained during the nighttime ERS-1 pass of 12 January 1991. This region contains a number of offshore oil and natural gas extraction platforms that combust excess gas as high temperature flares. ATSR pixels containing these flares are readily identified by the increased thermal channel brightness temperatures when compared to the surrounding sea surface, making it possible to locate the exact same ground pixel in both the BT and COUNTS data products. Flare pixels from three locations were identified and the

corresponding thermal channel radiances were calculated from the COUNTS product (using Equation 3.9) and the BT product (using Equation 3.11), the results being shown in Table 3.1.

	3.7 μm Radiance ($W/m^2/sr/\mu m$)		11 μm Radiance ($W/m^2/sr/\mu m$)		12 μm Radiance ($W/m^2/sr/\mu m$)	
Flare Pixel	COUNTS Product	BT Product	COUNTS Product	BT Product	COUNTS Product	BT Product
1	0.312	0.313	7.667	7.906	7.245	7.403
2	0.279	0.280	7.679	7.896	7.240	7.393
3	0.298	0.299	7.664	7.889	7.245	7.403

Table 3.1. The thermal channel spectral radiances of three ATSR image pixels containing offshore gas flares, calculated from both COUNTS and BT data products. The ATSR data were obtained during an ascending (nighttime) ERS-1 pass covering the Lybian coast on 12 January 1991.

The data of Table 3.1 indicate that, as expected, the 11 μm and 12 μm spectral radiances calculated from the BT data product are consistently higher than those calculated from the corresponding COUNTS data product. In this case the radiance difference is 2 - 3 %, equating to a brightness temperature difference of around 1.8 K at 11 μm and 1.4 K at 12 μm. These differences reflect the 11 and 12 μm non-linear corrections that are applied to the BT but not the COUNTS data products. Table 3.1 also shows that the 3.7 μm channel radiances are almost identical when calculated from either data product, reflecting the lack of a significant non-linear correction factor for this channel.

Studies requiring accurate values of arriving thermal flux within the 11 and 12 μm channels must calculate these parameters from the ATSR BT product or, alternatively,

must apply corrections to the radiance values obtained from the COUNTS product data. Since the BT products contain useful geocoding information which does not result in the corruption of the 'raw' pixel data (Section 2.6) the ATSR BT product is preferable for use in hotspot studies.

One further test was made to ensure the accuracy of Equation 3.11 in calculating the values of incoming 11 and 12 μm spectral radiance from the BT data products. During the initial pre-flight testing of ATSR-1, Mason (1991) produced a table giving a set of surface brightness temperatures covering the expected 200 - 320 K temperature range, along with the corresponding spectral radiances in the 11 and 12 μm wavebands of ATSR-1. Comparison of these radiance data with those calculated using Equation 3.11 provides excellent agreement, within 0.15%.

3.5. Summary and conclusions

This chapter has detailed how accurate measurements of incoming spectral radiance can be produced from measurements made in the ATSR thermal channels. Additionally, a post-flight calibration has been derived for the shortwave infrared channel of ATSR-1 and the apparent error in the onboard shortwave infrared calibration of ATSR-2 has been quantified. In subsequent chapters these techniques are used to obtain estimates of incoming spectral radiance in the ATSR shortwave, middle and thermal infrared channels, these being used in a variety of data analyses. Many of these analyses involve numerically modelling the ground-pixel thermal structure and include calculation of the radiant flux emitted in each ATSR waveband for a particular blackbody surface temperature. Such fluxes are simply calculated by integrating the Planck function over the spectral response function of the particular ATSR channel of interest. This is

accomplished using Equation 3.11 and replacing the pixel blackbody temperature (T) with the thermodynamic temperature of the emitting surface. In addition to its use with ATSR thermal channel data, Equation 3.11 is also valid for modelling high temperature radiant emission in the shortwave infrared (1.6 μm) waveband.

Chapter 4.

Thermal monitoring of Lascar Volcano, Chile using infrared data from the Along Track Scanning Radiometer: a 1992 - 1995 time-series

---

M. J. Wooster and D. A. Rothery

Bulletin of Volcanology (1997), 58, 566-579.

4.1. Abstract

Lascar Volcano (22° 22'S, 67°44'W) is the most active volcano of the central Andes of northern Chile. Regular documented observations began in 1984 and activity since that time has been characterised by periods of lava dome growth and decay within the active crater, punctuated by explosive eruptions. We present here a technique for monitoring the high temperature activity within the active crater using frequent measurements of emitted shortwave infrared radiation made by the spaceborne Along Track Scanning Radiometer (ATSR). ATSR is an instrument of low spatial resolution which shares certain characteristics with the MODIS instrument, planned for use as a

volcano monitoring tool in the NASA EOS Volcanology Interdisciplinary Science Investigation. We present a comprehensive time-series of over 60 cloud- and plume-free nighttime ATSR observations for 1992 - 1995, a period during which Lascar experienced its largest historical eruption. Variations in short wavelength infrared flux relate directly to changes in the high temperature surfaces within the active crater. From these data, interpretations are made that supplement published field reports and which document the presence and status of the lava dome during periods where direct, ground-based, observations are lacking.

Our data agree with less frequent information collected from sensors with high spatial resolution, such as the Landsat Thematic Mapper (Oppenheimer *et al.,* 1993) and are consistent with field observations and models that relate subsidence of the dome to subsequent explosive eruptions (Matthews *et al.,* 1997). Most obviously, Lascar's major April 1993 eruption follows a period in which the magnitude of emitted shortwave infrared radiation, measured at a wavelength of 1.6 μm, fell by 90%. At this time subsidence of the 1991 - 1992 lava dome was reported by field observers and this subsidence is believed to have impeded the escape of hot volatiles and ultimately triggered the eruption (Smithsonian Institution, 1993a). Extrapolating beyond the period for which field observations of the summit are available, our data show that the vulcanian eruption of 20 July 1995 occurred after a period of gradually increasing short wavelength infrared flux throughout 1994 and a more rapid flux decline during 1995. We attribute this additional, otherwise undocumented, cycle of increasing and decreasing shortwave infrared thermal flux as most likely representing variations in degassing through fumaroles contained within the summit crater. Alternatively it may reflect a cycle of dome growth and decay. The explosive eruption of 17 December 1993 appears to have followed a similar, but

shorter, variation in shortwave infrared flux and we conclude that large explosive eruptions are more likely when the 1.6 μm signal has fallen from a high to a low level.

The ATSR instrument offers low cost data at high temporal resolution. Despite the low spatial detail of the measurements, ATSR-type instruments can provide data that relate directly to the status of Lascar's lava dome and other high temperature surfaces. We therefore suggest that such data can assist with predictions of eruptive behaviour, deduced from application of physical models of lava dome development to this and other similar volcanoes.

4.2. Introduction

4.2.1. Lascar Volcano

Lascar is the most active volcano of the central Andes of northern Chile (Oppenheimer *et al.*, 1993). The volcano is located at 22° 22' S, 67° 44' W, 34 km from the village of Toconao (Figure 4.1) and possesses a single active crater at 5450 m altitude. Lascar's activity is characterised by continuous fumarolic degassing, punctuated by occasional vulcanian explosive eruptions. The majority of these eruptions are rather small and create ash columns extending up to a few kilometres above the summit. However, on a number of occasions larger eruptions have taken place. Most notable are the events of 16 September 1986, 20 February 1990 and 18 - 20 April 1993, when eruption columns rose 10, 14 and 20 km respectively above Lascar's summit. Each led to ashfall many hundreds of kilometres away from the volcano. The September 1986 eruption was the first obvious sign of magmatic activity at Lascar for over twenty years, though retrospective study of Landsat Thematic Mapper data reveals the presence of a hot feature, now accepted to have been a lava dome, within the active crater since at least December

1984 (Francis and Rothery, 1987; Rothery *et al.*, 1988; Glaze *et al.*, 1989a; Glaze *et al.*, 1989b). The April 1993 eruption is the largest so far, causing ash to fall on Buenos Aires 1500 km downwind. The same event also produced pyroclastic flows that travelled 7.5 km down the slopes of the volcanic complex.

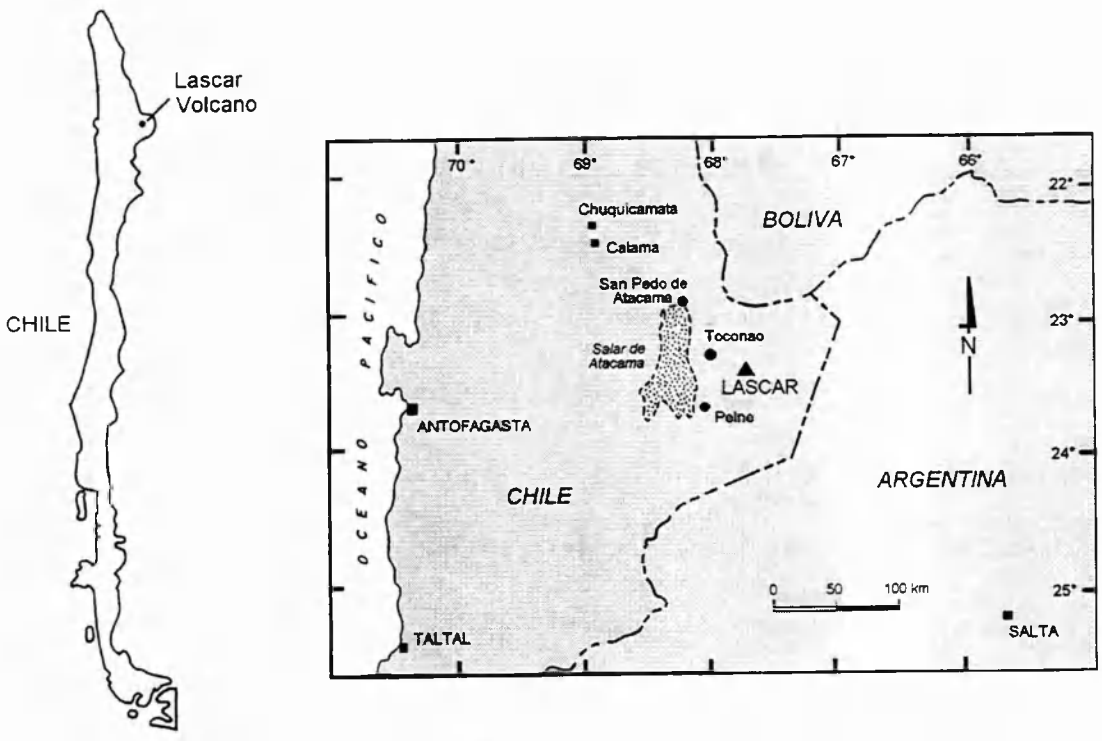

Figure 4.1. The location of Lascar Volcano in northern Chile.

Lascar's eruptive activity was first related to the growth and deflation of a lava dome by Oppenheimer *et al.* (1993). However, being rather remote, Lascar is not routinely monitored. Infrequent visits to the summit and some temporary seismographic monitoring comprise the majority of observations. In addition to these studies, occasional reconnaissance flights by the Chilean Air Force have provided a useful photographic record of summit conditions. Matthews *et al.* (1997) provide further discussion on the general geologic characteristics of Lascar volcano.

4.2.2. Previous satellite observations of Lascar

Satellite remote sensing studies of Lascar's active crater were first made at a spatial resolution of 30 x 30 m, using data from the Landsat Thematic Mapper (TM) instrument (Francis and Rothery, 1987; Rothery *et al.,* 1988; Glaze *et al.,* 1989a; Glaze *et al.,* 1989b). Radiance measurements in the shortwave infrared region were available from TM band 5 (1.6 μm) and TM band 7 (2.25 μm) and anomalies in these data indicated the presence of a high temperature feature, now accepted to have been a lava dome, within the active crater of the volcano. Use of multitemporal TM data allowed the evolution of shortwave infrared radiance to be studied and related to changes in summit activity. Oppenheimer *et al.* (1993) used TM images from fifteen dates to document the summit activity between 1984 and 1992, later supplementing this with a February 1993 measurement (Smithsonian Institution, 1993a). Figure 4.2 shows this TM 1.6 μm spectral radiance time-series, along with the ATSR 1.6 μm data that will be discussed later. The TM data indicate that the levels of thermally anomalous 1.6 μm radiance fell dramatically prior to the major eruptions of September 1986 and April 1993, which leads to the conclusion that major changes in surface temperature preceded both these events. It is also possible that a fall in shortwave infrared radiance occurred prior to the February 1990 eruption but this cannot be confirmed because of a long data gap between November 1987 and October 1989.

In March 1990, thermal measurements were made in the field to supplement those made using Landsat TM. These measurements indicated that the broad area of the dome surface had a temperature of 100 - 200 °C but that smaller areas, believed to be heated by the escape of magmatic gases, had temperatures greater than 900 °C (Oppenheimer *et al.*, 1993). We suppose that any restriction in degassing may be expected to lead to cooling of these high temperature surfaces, and thus to a fall in emitted shortwave infrared radiance.

Deflation of the lava dome has been proposed as a mechanism that would restrict the escape of hot gases through the bulk of the dome (Oppenheimer *et al.*, 1993) and, on this basis, Oppenheimer *et al.* (1993) concluded that Lascar experienced at least two cycles of lava dome extrusion and decay between 1984 and 1993, these being separated by the large explosive eruption of September 1986.

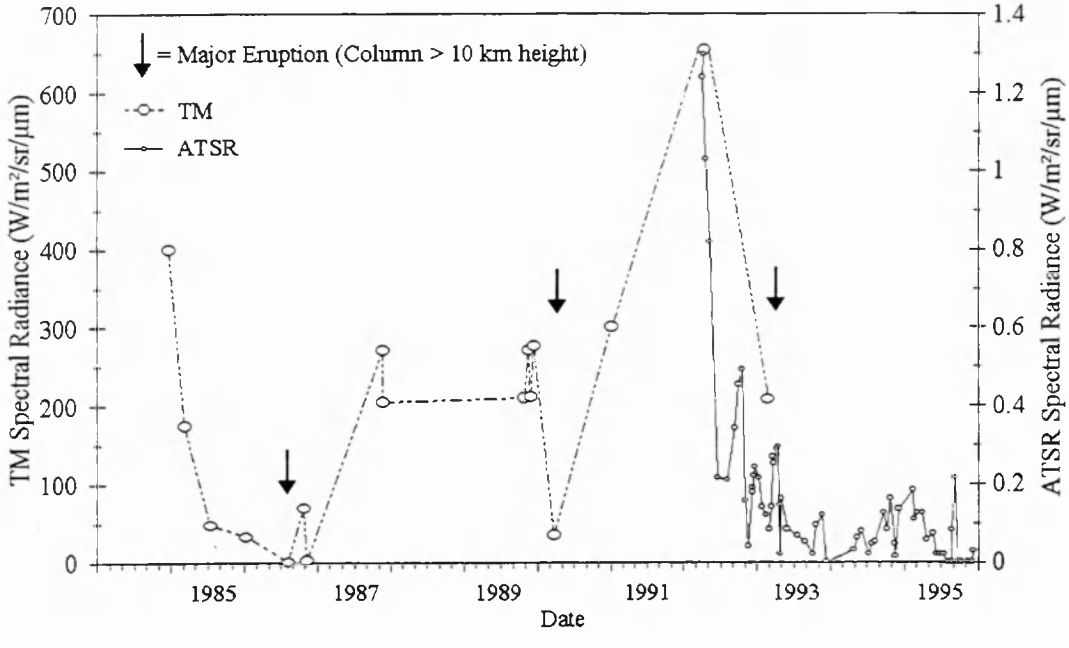

Figure 4.2. Total 1.6 µm spectral radiance of thermal origin recorded at Lascar Volcano by the TM and ATSR sensors. The vertical axes are scaled to equalise the peak values of spectral radiance recorded by each sensor. A notable decrease in the spectral radiance recorded by TM is evident prior to the September 1986 and April 1993 major explosive eruptions. The decrease prior to the April 1993 event is also mirrored by the ATSR 1.6 µm data. The two year TM data gap between 1987 and 1989 precludes the detection of any similar decrease in radiance prior to the February 1990 eruption. TM data are from Oppenheimer et al. (1993) and Smithsonian Institution (1993a).

4.2.3. Linking remotely sensed observations to pre-eruptive change

The information derived from Landsat TM has contributed to the development of a physical model that relates the extrusion and decay of the lava dome to the magmatic gas parameters that are believed to control the volcano's explosive activity (Matthews *et al.*,

1997). The model treats the magma within the eruptive conduit as a permeable magmatic foam. As degassing proceeds, the magma vesicularity is reduced and the magma becomes less permeable to the flow of gas. Degassing also reduces the total volume occupied by the magma, resulting in subsidence of the lava dome surface. This may further restrict degassing by blocking the fracture system through which the gas permeates. Fumaroles distant from the collapse zone may allow the continued escape of some gas, but if this is not sufficient to relieve the increasing pressure an explosive eruption may occur. Matthews *et al.* (1997) have calculated that complete degassing of the foam layer would take between 13 and 330 days, depending on the porosity of the magma.

The Matthews *et al.* (1997) model provides a physical mechanism that can be used to link observed decreases in shortwave infrared thermal flux, caused by decreases in magmatic gas flux, to eruptive events driven by rising internal pressure. We conclude that the decreases in shortwave infrared flux, shown in the TM data of Figure 4.2, indicate the onset of a phase of increasing internal pressure that ultimately led to major explosive eruptions many months after the shortwave infrared radiance began to fall.

This finding suggests that shortwave infrared monitoring could be a valuable means for detecting certain pre-eruptive changes at Lascar. Unfortunately, routine monitoring of the volcano using Landsat TM is made impractical by high data costs, limited data availability and long delivery times, these problemes being discussed in detail by Rothery *et al.* (1992). TM data cost upwards of US $2000 per scene and, though Landsat passes over Lascar once by day and once by night every 16 days, cloud cover can obscure the lava dome during the overpass and make the data worthless for thermal analysis. Furthermore the collection of nighttime TM data, which is the most valuable for quantitative thermal studies, is not routine and must be scheduled well in advance of the

satellite overpass. Oppenheimer *et al.* (1993) provide further frank discussion on these limitations, which restrict the 1984 - 1993 TM time-series shown in Figure 4.2 to just 16 scenes, the majority of which are daytime data. Nevertheless, we believe that the Lascar time-series still remains the most comprehensive published TM dataset available for any active volcano, though the TM scenes are not evenly distributed over the 1984 - 1993 period. The two year gap between November 1987 and October 1989, when no suitable data are available, has already been noted. To be more appropriate for time-series monitoring, spaceborne radiance data needs to be inexpensive and must be available at a temporal frequency closer to the 13 day minimum degassing timescale calculated by Matthews *et al.* (1997). The purpose of our study was to determine whether volcanologically useful shortwave infrared radiance infrormation can be provided by remotely sensed data whose spatial resolution is low, but which satisfy the desired characteristics of low cost and high temporal frequency.

4.2.4. New observations of Lascar at low spatial and high temporal resolution

The spatial resolution and temporal frequency of spaceborne remote sensing devices are, in practice, inversely related (Lillesand and Kiefer, 1991). It is thus possible to improve temporal coverage by taking measurements at a lower spatial resolution, though obviously at the expense of spatial detail. A new generation of low spatial resolution remote sensing systems will soon be operating as part of the American and European contributions to NASA's Earth Observing System (Ardanuy, 1991; Holdaway, 1993). These sensors will possess an increased number of shortwave and thermal infrared spectral channels and, provided that useful data can be obtained at these lower spatial resolutions, such instruments will offer the possibility of operational volcanic shortwave infrared monitoring at a high temporal frequency. To determine whether such data is, in

fact, suitable for this application we analyse a time-series of low spatial resolution infrared radiance measurements of Lascar Volcano, made by the ERS Along Track Scanning Radiometer (ATSR). ATSR shares certain spatial resolution and waveband characteristics with the Moderate Resolution Imaging Spectrometer (MODIS), which is a primary instrument within the NASA EOS Volcanology Interdisciplinary Science Investigation (Mouginis-Mark *et al.*, 1991b) and is due to be launched on the EOS-AM platform in 1998. In addition to providing useful science results in their own right, studies using ATSR should provide an indication of the potential MODIS offers for the future of volcanological remote sensing.

4.3. Background

4.3.1. The Along Track Scanning Radiometer

The Along Track Scanning Radiometer (ATSR-1) was first launched on the European Remote Sensing Satellite (ERS-1) on July 17, 1991. The second generation instrument (ATSR-2) was launched on ERS-2 on 21 April, 1995. Chapter 2 and Delderfield *et al.* (1985) give a good introduction to the special capabilities of the ATSR instrument, and only a brief outline is provided here.

ATSR was designed to record global sea surface temperatures by making measurements of ocean emitted radiance in three thermal infrared wavebands and through two different atmospheric path lengths. The ATSR's three longer wavelength infrared channels are centred on the same wavelengths (3.7, 11 and 12 μm) as those of the more familiar Advanced Very High Resolution Radiometer (AVHRR), which has previously been used to study the characteristics of volcanic ash plumes (e.g. Matson, 1984; Prata, 1989; Holasek & Rose, 1991; Wen & Rose, 1994) and lava flows (Mouginis-Mark *et al.*,

1991a; Harris and Rothery, 1995b; Harris *et al.*, 1995d). The spatial resolution of the ATSR is also similar to that of AVHRR, approximating 1 km^2 in the nadir-view (on which we concentrate in this study) and 4.5 km^2 in the forward-view. However, ATSR differs significantly from AVHRR in that it possesses an additional short wavelength infrared channel, centred at 1.6 μm. This waveband was included to assist daytime cloud detection but, fortuitously, it enables monitoring of thermally emitted shortwave infrared radiation at a high temporal frequency, albeit at much reduced levels of spatial detail when compared to the 30 m pixel size of bands 5 and 7 of Landsat TM.

An indication of the spatial resolution of ATSR's measurements can be gained by examining data from a high spatial resolution sensor, in this case the OPS instrument carried by the JERS-1 Satellite. OPS is a visible and shortwave infrared radiometer that makes spectral radiance measurements in 8 wavebands, each at a slightly higher spatial and spectral resolution than Landsat TM (Nishidai, 1993). Figure 4.3 shows a daytime subscene of Lascar's active crater, recorded by the OPS on 22 April 1993. Images from two channels are shown, with each image pixel corresponding to a ground area of around 18 x 24 m. In both images the majority of pixels appear moderately bright due to solar radiation reflected by the crater and its surroundings. However, the 1.6 μm image contains a grouping of anomalously bright (highly radiant) pixels at the centre of the active crater, these corresponding to high temperature areas of the lava dome surface which are emitting significantly at 1.6 μm (Denniss *et al.*, 1996). Evidence that this is not simply an area of high surface reflectance comes from the lack of a corresponding anomaly in the 0.56 μm channel. This image would show any surface reflectance variation but the wavelength is too short for the lava dome to be emitting significantly in this channel. A 1 km x 1 km box (the nominal size of the ATSR nadir-view measurements) has been overlain on the

1.6 μm scene to illustrate the spatial resolution of the ATSR pixel measurements. In reality, the crater is unlikely to be centred within a single ATSR observation and may affect up to four neighbouring measurements, from which the relevant volcanic signal must be extracted.

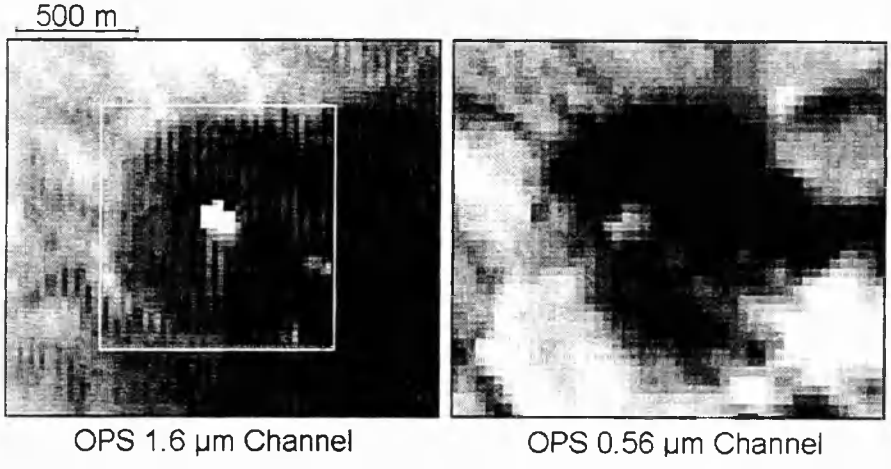

Figure 4.3. A daytime subscene of Lascar's active crater, taken by the JERS-1 OPS instrument on 22 April 1993. The bright grouping of pixels in the 1.6 μm image, not evident at 0.56 μm, corresponds to an area of thermal emittance associated with high temperature regions of the summit lava dome. A 1 km x 1 km box is overlain on the 1.6 μm image to indicate the nominal size of the ATSR nadir-view observations.

The 1.6 μm channel of ATSR-1 was uncalibrated prior to launch but Wooster (1996) has shown that its response to incoming radiation is linear, and has calibrated the data so that accurate measurements of spectral radiance can be obtained. Our investigations have shown that, for the purposes of this study, the response of the 1.6 μm channel has not varied significantly since launch, though the background noise level does vary a little between each scene. ATSR-2 incorporates an onboard calibration mechanism for the 1.6 μm waveband that allows continuous monitoring and calibration of the channel response (Read *et al.*, 1992). Both ATSR instruments incorporate a sensitive calibration and recording mechanism for the longer wavelength infrared wavebands, allowing infrared

brightness temperatures to be measured to accuracies of around 0.05 K (Delderfield *et al.*, 1985; Smith *et al.*, 1994).

4.3.2. Thermal emittance at 1.6 μm and 11 μm

The emissivity of andesitic lava, such as that comprising Lascar's dome, is greater than 85% in each of the ATSR's three thermal infrared wavebands (Salisbury & D'Aria, 1992; 1994). Our measurements, made using a visible and shortwave infrared spectrometer and the techniques outlined in Salisbury & D'Aria (1992), show that the emissivity of andesite at 1.6 μm is greater than 92%. The lava dome is thus expected to be an efficient emitter of infrared radiation throughout the spectral region of interest, as are most other rocks.

Examination of high spatial resolution imagery (e.g. Figure 4.3) indicates that during daytime observations signals in ATSR's 1.6 μm channel will be dominated by solar reflected radiation. We therefore use data from nighttime observations only, thus ensuring that all radiance measurements relate directly to thermal radiation emitted from surfaces at elevated temperatures, in accordance with the Planck function :

$$L(\lambda,T) = \frac{c_1}{\lambda^5 (\exp(\frac{c_2}{\lambda T}) - 1)} \qquad (4.1.)$$

where λ = Wavelength (m)

T = Temperature (K)

$L(\lambda,T)$ = Spectral Radiance ($W/m^2/sr/m$)

c_1 and c_2 are constants (1.18×10^{-16} Wm^2 and 1.44×10^{-2} mK, respectively).

Multiplication of the output of Equaton 4.1 by 10^6 provide spectral radiances in the more familiar units of W/m²/sr/μm. Over any particular temperature range, Equation 4.1 can be approximated by a simple non-linear function of the type shown in Equation 4.2 :

$$L_\lambda(T) = aT^b \qquad (4.2.)$$

where a and b are constants dependent upon the temperature range chosen.

Over the range of geothermal temperatures expected (~ 300 - 1000 °C), the spectral radiance emitted at 1.6 μm ($L_{1.6}$) is approximately proportional to the tenth power of the temperature (Figure 4.4). Thus levels of 1.6 μm spectral radiance emitted from the hottest parts of the lava dome surface will be high and should be detectable by ATSR even if, as expected, these hottest surfaces only fill a very small fraction of the sensor's 1 km² field of view. Figure 4.4 also indicates that even relatively small amounts of cooling in the hottest areas will lead to significant falls in the spectral radiance emitted at 1.6 μm, making such changes potentially detectable by ATSR. Furthermore, the levels of shortwave infrared thermal flux emitted by surfaces below about 300 °C are considerably weaker than those emitted at near-magmatic temperatures, making measurements in the ATSR 1.6 μm channel insensetive to variations in low temperature regions of the dome surface, or in the still colder ambient background. The results indicate that, provided that the broad surface temperature of the lava dome does not rise significantly above the 100 - 200 °C level recorded by Oppenheimer *et al.* (1993), the signals recorded in the ATSR 1.6 μm channel should relate directly to the surface area and temperature of material visible to the sensor that is heated magmatically or by magmatically driven fumaroles.

Over the 300 - 1000 °C temperature range, the thermal radiance emitted at 11 μm only varies with the square of temperature (Figure 4.4). The 11 μm signal recorded by ATSR will therefore be dominated by surfaces presenting large areas to the sensor, principally broad areas of the lava dome and the ambient background. If the highest temperature areas are of the relatively small sizes observed by Oppenheimer *et al.* (1993) then these surfaces will make relatively little contribution to the overall 11 μm signal.

In the same temperature range, the thermal emission at 3.7 μm is proportional to T^4. However, recording of the 1.6 μm and 3.7 μm channels on ATSR-1 is mutually exclusive, making 3.7 μm data of Lascar's hotspot available from the ATSR-2 scenes only.

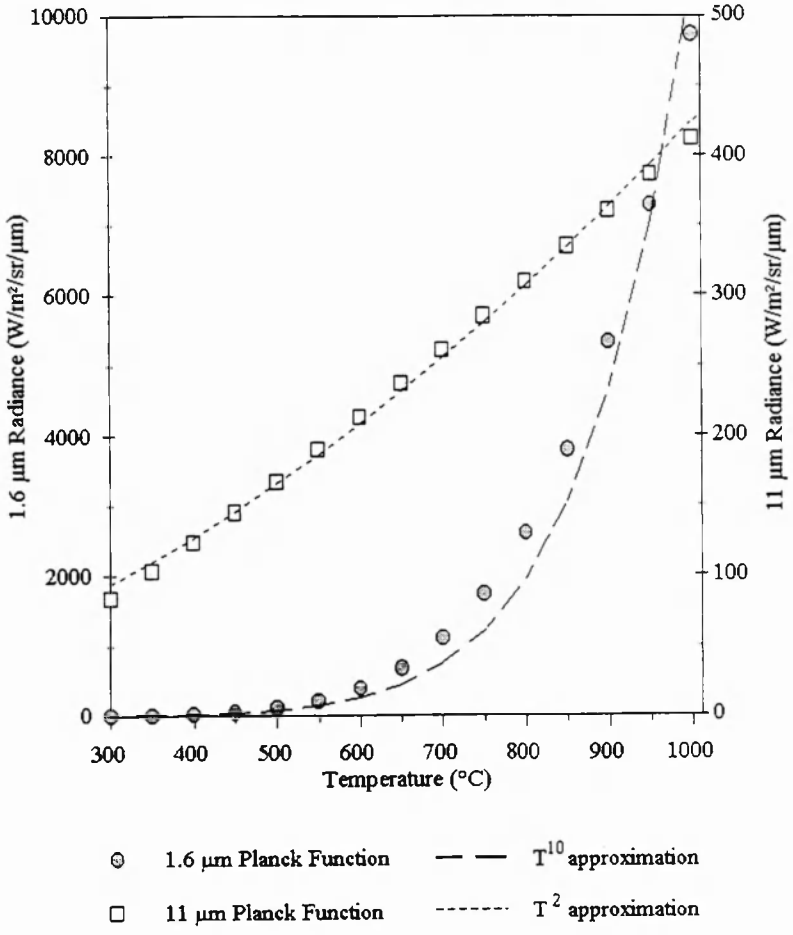

Figure 4.4. The relationship between emitted infrared spectral radiance and brightness temperature for the ATSR 1.6 μm and 11 μm channels, calculated using the Planck function (Equation 4.1). The dashed lines show the relationships obtained if the Planck function is approximated by Equation 4.2.

4.4. Methodology

4.4.1. Dataset

ATSR data of northern Chile were were obtained from the ATSR data archive held at the Rutherford Appleton Laboratory (UK). We examined 96 ascending node (nighttime) scenes, these being recorded between April 1992 and December 1995. Each scene covers a 512 x 512 km region containing the site of Lascar volcano and the data volume exceeds two scenes per month, potentially providing information at a temporal

frequency close to the minimum degassing timescale recognised by Matthews *et al.* (1997). The majority of the data are from ATSR-1, with a small number of 1995 ATSR-2 scenes. Fortuitously, the first year of full ATSR operation was immediately prior to the large April 1993 eruption of Lascar and therefore contains the dates of the final TM observations reported by Oppenheimer *et al.* (1993) and Smithsonian Instituion (1993a). This allows us to compare the high and low spatial resolution datasets obtained during this important period of activity at the volcano.

4.4.2. Data extraction

Geocoding of ATSR data products is automatically performed by the ATSR data processing system developed by the Rutherford Appleton Laboratory (Zavody *et al.*, 1994). The procedure tags each ATSR pixel with a latitude and longitude location and these data are intended to facilitate easy location of geographical areas within the scene. However, ATSR data processing is geared towards the retrieval of sea surface temperature and so the geocoding procedure assumes that each pixel is at mean sea level. This causes significant geolocation errors over high elevation targets such as Andean volcanoes. Our trigonometric calculations show that the error in geolocation due to Lascar's 5600 m altitude should be a maximum of 0° 02' (about 2 km) in the nadir-view and 0° 05' in the forward-view, the exact value being dependent upon the location of the volcano within the ATSR scan. To locate Lascar accurately within each ATSR scene we designed an automated software routine that pre-selects a 0° 05' area of latitude and longitude, centred on the true latitude/longitude of the volcano, and then searches for the highest 1.6 μm signal in both the nadir- and forward-view data. The selected locations are then taken to be the actual site of Lascar, there being no other major high temperature radiance sources in close proximity to the volcano. The signal in each of the available ATSR wavebands

was then extracted for a 5 x 5 pixel grid centred on the chosen location, allowing the local ambient background emittance in each thermal infrared waveband to be quantified. The noise statistics for the 1.6 μm channel were computed using a larger 50 x 50 pixel area. Using this technique, data from all 96 scenes are extractable within a few minutes.

Figure 4.5 shows a plot of the 1.6 μm data for a 20 x 20 pixel area of a nadir-viewing ATSR-1 scene recorded at 01:36 GMT on 29 September 1992. High temperature surfaces within the active crater have caused the 1.6 μm signal to become elevated above the noise that characterises the remainder of the subscene. In this case the summit activity has affected two neighbouring ATSR pixels, this being a function of the area covered by the lava dome and the exact geographical location and overlap of the ATSR measurements. In accordance with the technique of Oppenheimer *et al.* (1993) we used the total 1.6 μm signal of volcanic origin in our analysis, obtained by summing the anomalous radiance of all pixels more than 2σ above the background noise level. Since each ATSR radiance measurement is constructed by integrating the received signal for a 75 μsec period, summing the signal from neighbouring pixels is equivalent to increasing the integration period and is thus consistent with the physical principles of the instrument. We note that the trend in this summed value followed that of the most radiant shortwave infrared pixel.

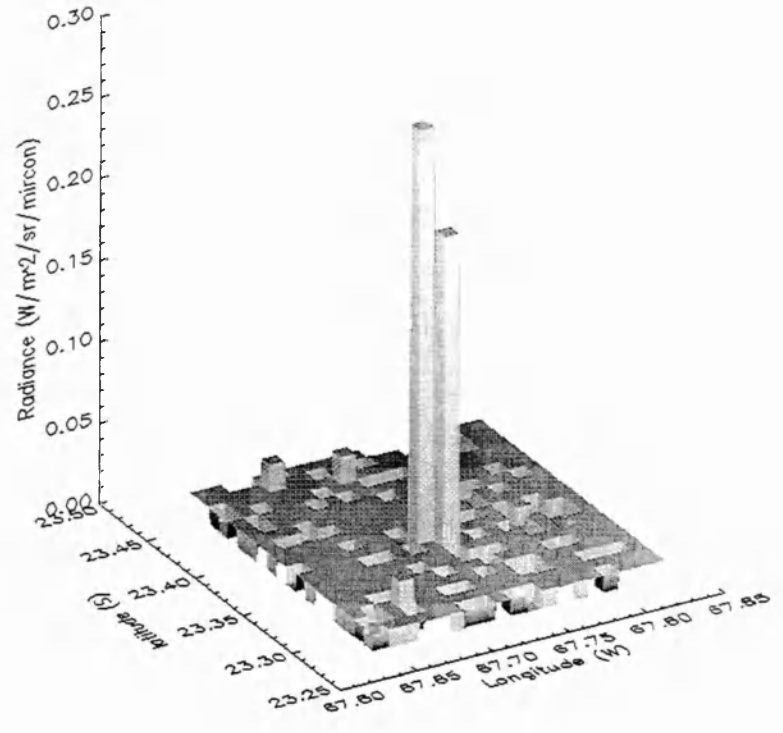

Figure 4.5. A subset of the nighttime 1.6 μm nadir-view data recorded by ATSR at 01:36 GMT on 29 September 1992. In the absence of solar radiation the majority of the pixels are characterised by detector noise but, at the location of Lascar Volcano, a strong 1.6 μm signal is present.

4.4.3. Cloud detection

The presence of cloud over the active crater will affect signals in all ATSR channels. It was therefore vital for us to identify data that were affected by cloud if the temporal analysis were to be solely representative of changes in the volcano's summit activity. Where large cold cloud bodies occurred over Lascar, anomalously low 11 μm brightness temperatures were recorded, about 10 K below the 257 - 272 K temperature range that characterised a cloud free crater. Data that showed 11 μm brightness temperatures below 250 K were therefore rejected from the study. This initial test for gross cloud cover eliminated 27 ATSR scenes from the analysis, indicating that cloud obscuration is a significant factor even at Lascar, which is likely to be less affected by

cloud cover than most other volcanoes since it resides in a region of extremely low rainfall.

Subpixel cloud cover is more difficult to detect than gross cloud cover but, since such clouds could possibly mask from view any thermal anomalies in the active crater, it was important to determine the occasions on which subpixel clouds occurred at the summit. Additionally, the volcanic plume from Lascar could itself mask the surface and so instances of excessive plume strength must also be identified. A standard method for detecting subpixel clouds in AVHRR data is to analyse the variation in 11 μm brightness temperature within a 3 x 3 pixel grid (Saunders, 1986). If the variation is greater than a pre-determined threshold then the area is flagged as cloudy. However, the widely varying elevation and ambient land temperatures around Lascar, and the presence of summit thermal anomaly, prevented this test being applied successfully to our ATSR data. We therefore developed new cloud tests, specific to the case of subpixel cloud detection at Lascar and other, similar, volcanoes. These tests relied on characterising the radiances observed at the summit pixel and comparing these with those observed in the rest of the time-series. The principal characteristics of Lascar in the 69 scenes that had been screened for gross cloud cover was an 11 μm brightness temperature greater than that of the immediately neighbouring pixels and a 1.6 μm signal elevated more than 2σ above the background noise level. Five scenes lacked a summit anomaly in both these channels and these scenes were rejected from the study. We were confident that, in these cases, the ATSR was not viewing the hot surfaces within the active crater, probably because of complete obscuration by subpixel cloud or plume.

In three ATSR scenes an anomaly existed at 11 μm but not at 1.6 μm. A likely explanation of this is a decrease in the temperature of the lava dome surface, below that at

which detectable amounts of shortwave infrared radiance is emitted. These scenes were therefore retained in the study. However, since the 1.6 μm signal is more affected by scattering from water droplets than the 11 μm signal (Zavody *et al.*, 1994), this situation could also arise if small amounts of plume were present in the crater.

In two scenes an anomaly existed at 1.6 μm but not at 11 μm. The sensitivity of 1.6 μm signals to scattering processes suggests that radiance from the lava dome was not being significantly scattered by clouds or plume and so these scenes were also retained. The low 11 μm measurements may be attributable to cooling of large areas of the dome surface, whilst some smaller surfaces remained at high temperature, or to the presence of a subpixel, high level (cold) cloud within the ATSR field of view. The presence of such a subpixel cloud would lower the pixel 11 μm brightness temperature but, provided the hottest surfaces of the lava dome remained unobscured, would leave the 1.6 μm signal relatively unaffected.

Once all cloud detection tests had been completed, a total of 64 scenes remained for further analyses, these spanning the period 7 April 1992 - 6 December 1995. It was expected that any cloud contaminated data that had escaped positive identification may subsequently reveal itself as a conspicuous departure away from the prevailing radiance trends in the dataset.

4.4.4. Non-volcanic sources of radiance variation

Apart from cloud contamination the two primary processes that may cause variations in the observed radiance, but that are not associated with changes in the volcanic surfaces, are the varying viewing geometry and changes in the intervening atmosphere. Throughout the dataset Lascar was observed with a zenith angle of 12 ± 5° in

the ATSR nadir-view. We calculate that this viewing geometry is sufficiently near-vertical that the whole of the lava dome would have been in view (unshielded by the crater walls) in each image. This is not the case for the forward-view data, taken at 55° from zenith, and (as expected) in most cases no 1.6 μm signal is evident in the forward-view. We have therefore concentrated on information contained within the nadir-view ATSR scenes. Researchers intending to use MODIS data for volcanic studies should note that towards the scan edges, MODIS will have a viewing geometry comparable to that of the ATSR forward-view. This suggests that only data from the near nadir portion of the MODIS scan will be reliable for documenting activity within deep volcanic craters. Chapter 6 discusses this finding in more detail.

With regard to atmospheric variations, before interpreting the nadir-view data it was important to quantify the amount of shortwave infrared signal variation that could be due solely to variations in local atmospheric transmission. The high elevation of Lascar means that its summit lies well above the bulk of Earth's atmospheric water vapour, and therefore above the main region of infrared absorption. Nevertheless, some atmospheric absorption of the emitted radiation is inevitable and we estimated the magnitude of this using the LOWTRAN 7 radiative transfer code (Kneizys *et al.,* 1988). Summer and winter atmospheric profiles for Lascar's latitude and elevation were obtained from Houghton (1986) and were used with LOWTRAN 7 to determine the atmospheric transmission over each of the ATSR wavebands and for each of the viewing geometries used. Assuming a standard concentration of tropospheric aerosols, atmospheric transmissivity varied between 0.97 and 0.98 for the 1.6 μm channel, between 0.94 and 0.96 for the 3.7 μm channel and 0.96 and 0.97 for the 11 μm channel. This absorption will be countered by a small but variable amount of atmospheric thermal emittance within the 11 μm and 3.7 μm

wavebands, and a small amount of path radiance due to scatter in the 1.6 μm band. Thus, the atmospherically induced variability in the received radiances is low, a few percent at most for the 1.6 μm channel. Our analysis does not allow for the variable effects of volcanogenic aerosols and gases within the active crater. However, when we compare ATSR 1.6 μm measurements made only a few days apart, we see very few outliers of the sort that we would expect if these were major factors. This also suggests that residual cloud-contamination was not a significant problem in the cloud-cleared ATSR dataset.

4.5. Results

4.5.1. The area and temperature of the lava dome surface

Figure 4.6 shows the 1992 - 1993 time-series of ATSR 1.6 μm spectral radiance measurements. The 1992 lava dome that is responsible for this varying 1.6 μm signal was first seen during an overflight in March 1992. Photographs taken at that time indicate that the area occupied by the lava dome was about 2.5% of the ATSR 1 km^2 field of view, with the remainder being ambient background (Smithsonian Institution, 1992a). Adapting the relations derived by Dozier (1981) and Rothery *et al.* (1988), Equation 4.3 can be used to predict the radiance (R_i) that would have been recorded in each of the ATSR wavebands if the ATSR field of view (FOV) contained a lava dome having n different temperature components :

$$R_i = \tau_i \varepsilon_i \sum_{k=1}^{n} P_k L_i(T_k) + Ra_i^{\uparrow} + \tau_i \frac{(1-\varepsilon_i)}{\pi} Ra_i^{\downarrow} + \tau_i \varepsilon_i Rb_i \qquad (4.3.)$$

Where i is the ATSR waveband of interest

R_i is the spectral radiance recorded in waveband i (W/m^2/sr/μm).

$L_i(T)$ is the Planck function integrated over waveband i.

T_k is the temperature of the k^{th} temperature component of the lava dome (K).

P_k is the fraction of the FOV covered by the k^{th} component of the lava dome.

ε_i is the spectral emissivity of the surface integrated over waveband i.

τ_i is the atmospheric transmission for waveband i.

$Ra_i^{\uparrow}$ is the upwelling atmospheric radiation for waveband i, (W/m^2/sr/μm).

$Ra_i^{\downarrow}$ is the downwelling atmospheric radiation for wavelength i, (W/m^2/sr/μm).

Rb_i is the spectral radiance emitted in waveband i by the ambient background contained within the FOV (W/m^2/sr/μm). Rb_i is zero for the 1.6 μm channel.

As indicated previously, the emissivity of the dome and surrounding surfaces is known to an adequate precision, and the atmospheric parameters are estimable using LOWTRAN 7. By rearranging Equation 4.3 and incorporating the Smithsonian Institution (1992) value for dome area, we used the recorded values of 1.6 μm and 11 μm spectral radiance to determine the different thermal components of the lava dome surface. Since ATSR-1 provides data in two distinct wavebands, Equation 4.3 may be solved for n = 1 or n = 2, i.e. the lava dome having one or two distinct thermal components. Rothery *et al.* (1988), Glaze *et al.* (1989a) and Oppenheimer *et al.* (1993) all assumed this thermal

distribution when analysing TM data of Lascar and Oppenheimer *et al.* (1993) previously validated the assumption with field measurements of the post-February 1990 dome.

Using the value of 1.6 μm spectral radiance recorded at the start of April 1992 (1.3 W/m²/sr/μm), Equation 4.3 provides results that are consistent with either of two end-member models: (i) the whole of the dome surface approximating a single temperature component of around 425 ± 25 °C, or (ii) the dome being composed of two distinct temperature components, small areas (0.2 - 2 % of the dome surface) at magmatic temperatures of 700 - 1000 °C, with the remaining majority area at a temperature too low to emit significantly at 1.6 μm (i.e. < 300 °C).

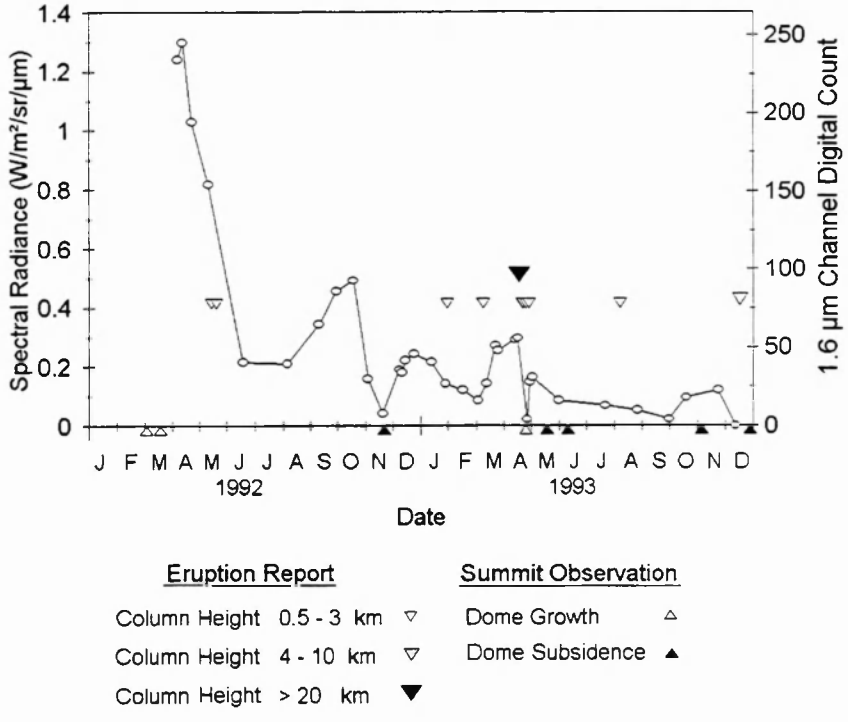

Figure 4.6. The 1.6 μm spectral radiance of volcanogenic origin detected at Lascar in 1991 and 1992 using data from the ATSR-1. All measurements are from the nadir-viewing ATSR scan and are recorded in the absence of solar radiation (01:20 - 01:50 GMT).

An indication of the actual situation was gained by analysing the 11 μm brightness temperature difference between the 'summit' pixel and its immediate neighbours. Throughout April, May and June 1992 the summit exhibited an almost constant 5.5 ± 0.5 K anomaly in the 11 μm brightness temperature data (Figure 4.7). If end-member model (i) were true, Equation 4.3 indicates that an 11 μm brightness temperature anomaly of around 25 - 30 K would have been recorded, clearly much larger than that observed. We therefore conclude that the more appropriate model is that of end-member (ii), with small fractions of the dome at near-magmatic temperatures and the broad area at a relatively low temperature. We can estimate the temperature of this broad area by assuming the remainder of the FOV was occupied by surfaces at the ambient background temperature of -7.5 °C, this value being taken from the 11 μm measurements neighbouring the summit crater. Taking into account the relatively minor 11 μm signal supplied by the very small high temperature fractions, we estimate that the broad area of the dome had a surface temperature of 90 - 130 °C (Equation 4.3), which is within the range of field measurements reported by Oppenheimer *et al.* (1993). Changes in the 1.6 μm signal should therefore be independent of low temperature variations in the broad area dome surface and this result validates our proposed methodology for detecting change in the high temperature areas using measurements at 1.6 μm.

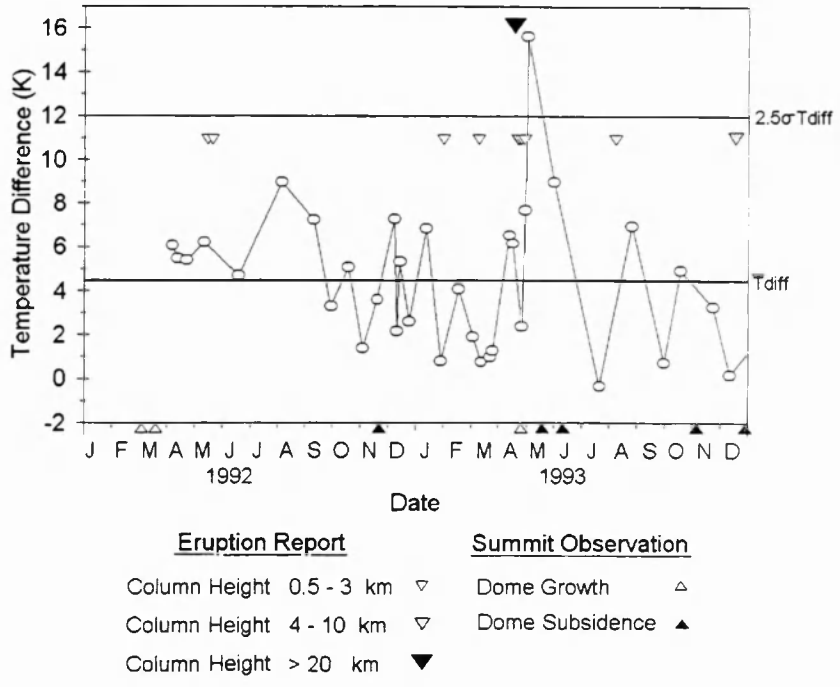

Figure 4.7. The brightness temperature difference between the Lascar 'summit' pixel and it's immediate neighbours, recorded in the nadir-viewing 11 μm channel of ATSR-1 in 1992 and 1993. The mean and 2.5σ levels are also shown and all measurements are taken in the abscence of solar radiation, between 01:20 and 01:50 GMT. The hot pyroclastic flow, produced during the eruption of 20 April 1993 (Figure 4.10), caused the 11 μm anomaly to rise above the mean + 2.5σ level.

4.5.2. Variations between April 1992 and April 1993

Figure 4.2 shows the complete set of ATSR 1992 - 1995 nadir-view 1.6 μm observations, together with the TM 1.6 μm time-series data. The difference in the TM and ATSR spatial resolutions makes the magnitude of the radiances detected by each sensor widely different. To facilitate comparison we have scaled the vertical axes to equalise the peak values of radiance recorded by each sensor. Significantly, we find that the drop in shortwave infrared radiance that is recorded by data from the final two Landsat TM scenes (15 April 1992 and 24 February 1993) is confirmed by data from 18 ATSR scenes covering the same period. This indicates that the ATSR is providing data of a similar

quantitative value to Landsat TM, but at a temporal interval that allows major shortwave infrared radiance variations to be confirmed by a time-history of measurements.

The TM data of Figure 4.2 indicate that levels of 1.6 μm spectral radiance had dropped to 30% of the 15 April 1992 value by 24 February 1993. In fact this is a minimum estimate of the radiance decrease since a large proportion of the April 1992 TM pixels are saturated and provide only a lower limit on the amount of energy arriving at the sensor within that waveband. The unsaturated ATSR measurements suggest a much larger decline in shortwave infrared radiance over this period and this is believed to be a more reliable guide to the magnitude of the change.

Figure 4.6 shows the 1992 - 1993 ATSR 1.6 μm time-series in more detail, with information from all available field reports overlain. The ATSR data actually demonstrate a 90% decrease in recorded shortwave infrared spectral radiance over the April 1992 - February 1993 period, with the major change occurring between April and June 1992. This rapid three month fall indicates that the size or temperature (or both) of the hottest summit areas decreased considerably. A possible mechanism for this change is subsidence of the lava dome, blocking the passage of hot magmatic gases through the dome structure. However, it was not until November 1992 that the summit was visited and subsidence of the dome was actually reported (Gardeweg *et al.*, 1993). This is six months after the ATSR data indicate a significant change in summit condition. Further evidence for a link between subsidence, gas flow/pressure and cooling may be provided by the small eruptions of 15 and 21 May 1992 (Figure 4.6) since these events may indicate an attempt to relieve rising internal gas pressure within the volcano.

After the steep April - May 1992 decrease in shortwave infrared signal, the ATSR data indicate fluctuating levels of 1.6 μm spectral radiance until the major April 1993

eruption. The period of these fluctuations is around 90 - 120 days and they suggest regular low frequency changes in the highest temperature summit conditions, possibly related to periodic fluctuations in degassing. The relatively smoothly varying 1.6 μm signal contrasts with the widely fluctuating 11 μm measurements made over the same period (Figure 4.7). The variability of the 11 μm anomaly is due, in part, to variations in the area and temperature of the ambient background contained within the summit pixel. Variations in these parameters, which do not affect the 1.6 μm signal, make it difficult to isolate the 11 μm component relating to physical changes within the summit crater. Though the 11 μm data are of limited use, they do reveal a decreasing trend over the April 1992 - April 1993 period, suggesting that the broad surface of the dome was cooling throughout this time.

4.5.3. The April 1993 Eruption

18 April 1993 marks the beginning of the largest historical eruption of Lascar volcano and the 1.6 μm data recorded around this event are shown in more detail in Figure 4.8. This eruption coincided with a local maximum in recorded 1.6 μm signal, which had been oscillating since the major decrease of April - June 1992 (Figure 4.6). The activity was characterised by pyroclastic flows and eruption columns extending up to 25 km altitude. In the few weeks immediately prior to the April 1993 eruption ATSR provides no evidence of a significant change in state of the volcano, rather we point to the scale of shortwave infrared radiance decrease between April 1992 and April 1993 as evidence of significant pre-eruptive changes occurring over a longer timescale. If the rapid April - June 1992 decrease in 1.6 μm radiance is due to a restriction in magmatic gas flow then the restriction appears to have remained in place until the April 1993 eruption. This may indicate that the internal pressure of the volcano was increasing for the 10 month

period since June 1992, and this long duration may be partly responsible for the anomalously large magnitude of the eruption.

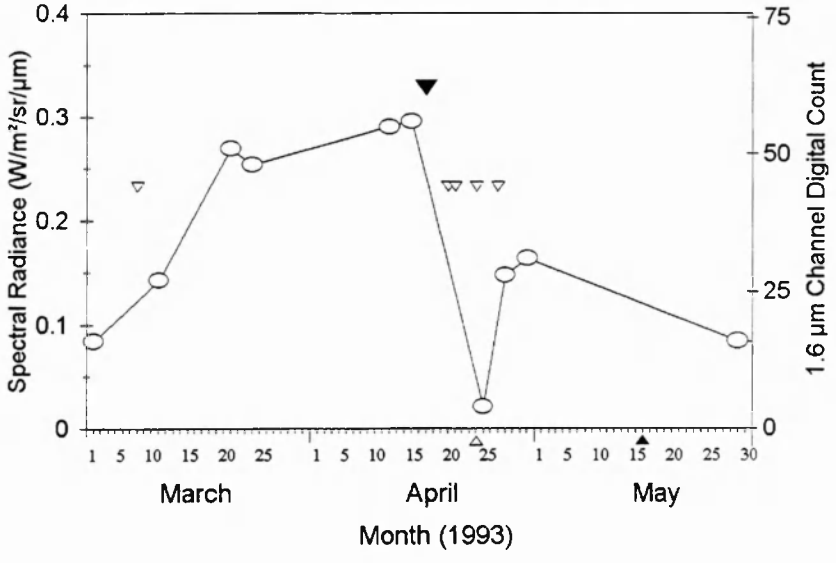

Figure 4.8. The 1.6 µm spectral radiance of volcanogenic origin detected at Lascar by ATSR-1 for the period surrounding the April 1993 eruption, the largest in the recorded history of the volcano. All measurements are nadir-viewing and recorded in the absence of solar radiation (01:20 - 01:50 GMT). Eruptions are inidcated by triangles, with the key being the same as that shown in Figures 4.6 and 4.7.

Figure 4.9 reproduces the daytime ATSR 11 µm scene recorded at 13:40 GMT on 20 April 1993. This image clearly shows the two eruption columns produced that morning. At the time of the ERS-1 overpass the initial column, which was reported to be at greater than 15 km altitude, had drifted 400 km NE of Lascar and had a minimum cloud top temperature of -68 °C. The second column, formed just 20 minutes before the image was aquired, was reported to have reached a slightly lower altitude (Smithsonian Institution, 1993a) but possessed a colder cloud top temperature of -80 °C. We presume that this discrepancy is due to the effects of undercooling on the second plume (Woods *et al.*, 1995). The earlier plume is likely to have equilibriated to the ambient air temperature

and may also have had time to retreat to its neutral buoyancy height by the time this image was recorded (Woods and Kienle, 1994).

Partial collapse of the second eruption column produced the farthest-reaching pyroclastic flows, travelling 7.5 km NW of the volcano. These are clearly visible in the magnified insert on Figure 4.9. Pyroclast surface temperatures cannot be accurately determined since, at this short time after emplacement, the hot surfaces are causing the 11 μm waveband to reach its 320 K saturation limit. However, it is simple to differentiate the pyroclastic deposits from active lava in the ATSR data. The former do not have surface material at or near magmatic temperatures and therefore do not show a thermal signal in the 1.6 μm channel.

Figure 4.7 shows that the emplacement of the pyroclastic flow was the only event associated with a significant rise in the 11 μm brightness temperature anomaly, above the 2.5 σ level. We therefore suggest that routine monitoring of this parameter could provide a method of detecting pyroclastic flow emplacement at this and other remote volcanoes. Appendix E deals with these matters more fully.

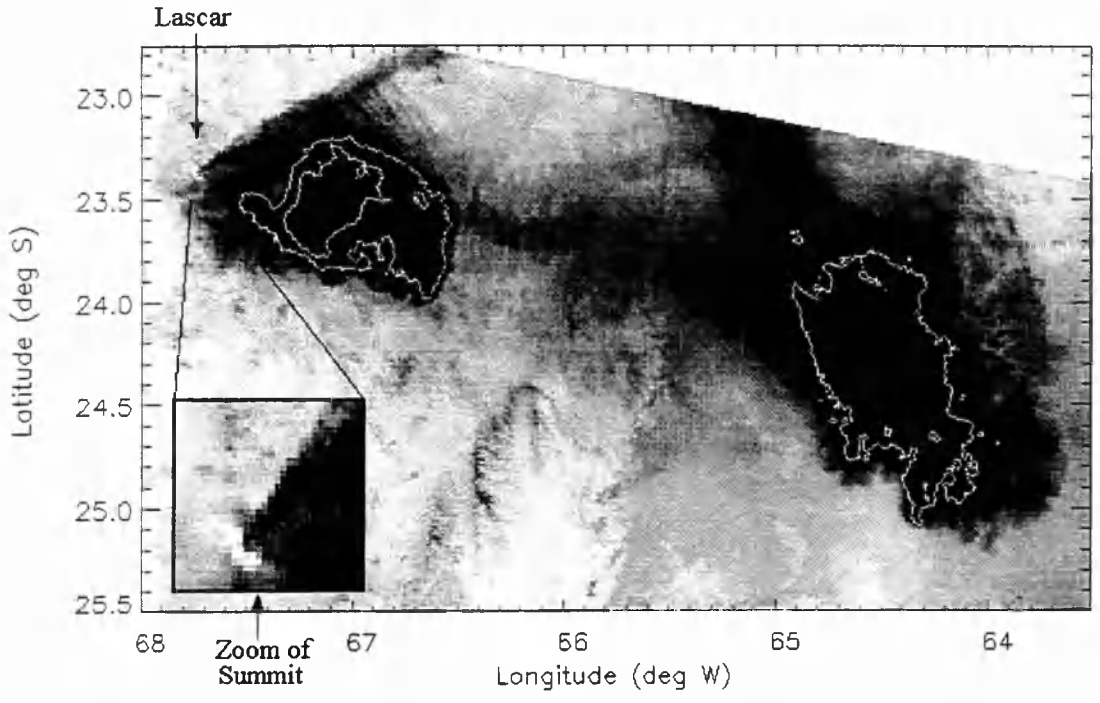

Figure 4.9. The daytime ATSR 11 μm nadir-view scene recorded at 13:40 GMT on 20 April 1993, the date of the largest historical eruption of Lascar Volcano. This image clearly shows the two eruption columns produced on the morning of that day, with contours at -70 °C and -50 °C overlain. The insert shows the recently emplaced pyroclastic flow deposit which saturated the 11 μm channel measurements.

4.5.4. Variations between April 1993 and April 1994

Lascar's eruptive activity began to subside after 20 April 1993. Observers reported generally weak columns, barely rising above the crater rim, and small explosions on 22, 23, 26 and 29 April, whose incidence is indicated on Figure 4.8. ATSR data recorded on 28 April show a minimal 1.6 μm signal, though aerial photographs taken on the 26 April show a new lava body occupying a much larger portion of the crater than did the previous dome. The new lava dome was around 380 m in diameter and 120 m thick, three times thicker than the previous dome structure (Smithsonian Institution, 1993c). The dome was reported to have grown in less than 40 hours between 24 and 26 April and contained a funnel shaped indentation, possibly a result of 26 April explosion (Smithsonian Institution,

1993b). Since a new lava dome was present in the crater at the time, which we expect would emit some shortwave infrared flux, it seems probable that the ongoing eruptive activity and plume filled nature of the crater was responsible for the low 1.6 μm signal recorded on 28 April. The explosion on 29 April may have damaged the structure of the dome still further but ATSR data recorded on 30 April and 3 May, after explosive activity had ceased, show that a substantial 1.6 μm signal had been re-established. This indicates the presence of a high temperature thermal anomaly but the signal level amounted to only a tenth of the maximum spectral radiance produced by the smaller 1991 - 1992 dome.

Aerial observations on 19 May indicated that the dome had started to subside and the increasing subsidence is tracked by a regular decrease in 1.6 μm spectral radiance, reaching a local minimum on 30 September 1993 (Figure 4.6). An eruption is reported to have occurred sometime in August 1993, probably a result of the continuing dome collapse (Smithsonian Institution, 1994a). By 5 November, observations made from the crater rim indicated that the collapsed area had reached a depth of 50 - 100 m below the surface of the dome (Smithsonian Institution, 1993c). However, the increase in 1.6 μm spectral radiance observed during October and November indicates that high temperature thermal activity may, in fact, have been intensifying, though the absolute magnitude of the radiances remained low. This contradicts the observations of April - June 1992, when dome subsidence was paralleled by a sharp fall in 1.6 μm signal, and suggests an alternative mechanism was operating. The post-April 1993 lava dome is estimated to be three times thicker than the previous lava body (Smithsonian Institution, 1993c), and it is possible that the thickness of this dome structure made it difficult for hot gases to escape from below. Ground observations and certain of the Landsat TM data suggest that when dome deflation occurs limited degassing continues from fumaroles on the crater floor

(Oppenheimer *et al.*, 1993; Smithsonian Institution, 1992c; Smithsonian Institution, 1993c). We suggest that these fumarolically heated areas may be the source of much of the shortwave infrared radiance seen in October - November 1993. The relatively small magnitude of the emission, when compared to that seen in April 1992, may also indicate a change in shortwave infrared radiance source. On 12 December the shortwave infrared signal fell to zero, indicating that, whatever the source, degassing within the crater had most likely become restricted. Five days later, two large explosive eruptions occurred that produced columns rising up to 8 km above the summit. The fall in shortwave infrared radiance may be linked to this subsequent eruptive event, though the magnitude of both phenomena was much smaller than that occurring between April 1992 and April 1993.

No ATSR observations exist for four months after the December eruption since, during this period, ERS-1 underwent a temporary orbit shift and was unable to image Lascar Volcano. However a report of a summit visit on 19 February 1994 indicates that the post-April 1993 dome, and surrounding areas of the crater floor, had almost completely subsided into a deep hole centred on the active vent. Certain fumarole temperatures neighbouring this area were observed to be > 230 °C and there were warnings that another eruption was expected in the near future (Smithsonian Institution, 1994a). These warnings were made on the grounds that degassing was constrained by large scale subsidence of the system through which gas flow was previously channelled. These conditions were believed to be similar to those observed in previous eruptive cycles (Smithsonian Institution, 1994a). However, for the next five months no explosive activity was reported by local observers, indicating that the internal pressure inside the volcano may have risen throughout this period.

4.5.5. Variations between April 1994 and July 1995

In 1994 - 1995 only two reported visits were made to the volcano. Remote monitoring of the shortwave infrared signal therefore provides information on othewise undocumented changes at the volcano. After the shortwave infrared radiance minimum immediately before the December 1993 eruption, the recorded signal is seen to rise in consecutive measurements recorded in April, May and June 1994 (Figure 4.10). The shortwave infrared radiance dropped at the start of July 1994, just prior to a period of renewed vulcanian activity that generated plumes rising 4 km above the crater. Shortwave infrared radiance remained low during this event, probably because of scattering by plumes, and then rose until mid-September, fell slightly in October, and peaked at the beginning of November. Small phreatic eruptions occurred between 13 and 19 November 1994, causing eruption plumes up to 3 km high (Smithsonian Institution, 1994c). The shortwave infrared signal decreased during these events but, since it returned to pre-November levels after the cessation of activity, we believe the lowering may again have been related to radiance scattering by eruption products. A summit visit in late November 1994 showed that the central hole in the crater floor had deepened and no lava dome was present (Smithsonian Institution, 1995f). Again, the most likely interpretation for the 1.6 μm signal is radiance from fumarolically heated surfaces away from the subsidence area. Even when it had recovered from the November 1994 minimum, the magnitude of the 1.6 μm radiances remained much lower than the maximum levels recorded in April 1992.

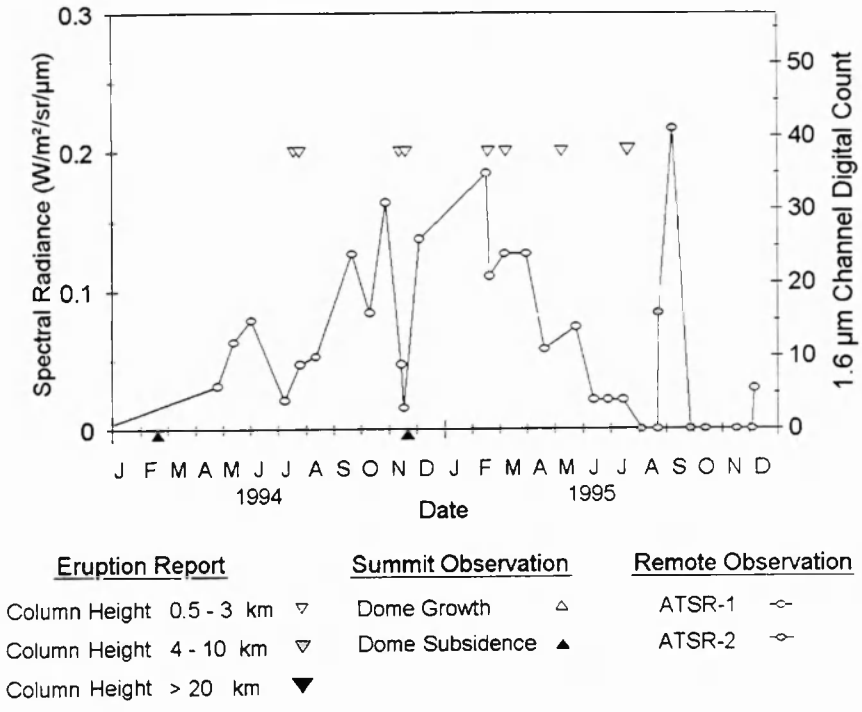

Figure 4.10. The volcanogenic radiant flux detected in the 1.6 µm channel of ATSR-1 (clear datapoints) and ATSR-2 (opaque datapoints) for the years 1994 and 1995. All measurements are nadir-viewing and recorded in the absence of solar radiation (01:20 - 01:50 GMT). Note the expanded vertical scale compared to Figure 4.6.

The shortwave infrared signal remained at a relatively constant level until February - March 1995, when a general decline began. This decline may indicate the onset of decreasing gas flux through the crater floor fumaroles. There were small ash eruptions between 18 February and 10 March and three small explosive eruptions on 10 May 1995 (Smithsonian Institution, 1995f). The shortwave infrared signal reached very low levels in June and mid-July and these data suggest that the eruptions did not allow an increase in the subsequent rate of degassing, and in consequence surface temperatures remained low. If this mechanism is correct then the general decline in radiance since February - March 1995 would indicate that gas pressure below the crater floor may have been increasing for up to 6 months. As a possible consequence of this, 20 July saw at least one, possibly two,

larger vulcanian events, with plumes reported at altitudes of 6 - 9 km (Smithsonian Institution, 1995g).

As stated above, we prefer to interpret the 1994 - 1995 trends in 1.6 μm spectral radiance as due to variations in degassing from crater floor fumaroles. However, we cannot rule out the alternative possibility that this represents another (otherwise undocumented) cycle of dome growth and collapse. If this were the case, then the late November 1994 field observation of a hole in the crater floor, which coincides with a brief dip in the eighteen month rise-and-fall in shortwave infrared themal flux, must again represent only a temporary situation, caused by the destruction of a dome in the preceding November eruptions. In this scenario, a new dome would have regrown after November and then began to subside in February/March, causing the decreasing trend in emitted shortwave infrared flux.

4.5.6. Variations between July 1995 and December 1995

After the July 1995 eruption, levels of recorded shortwave infrared spectral radiance fell to zero and remained so until August and September, when data indicate renewed onset of high temperature activity (Figure 4.10). These observations were made with the ATSR-2 instrument and so 3.7 μm measurements are available in addition to those at 1.6 μm. The 3.7 μm brightness temperatures for the two readings in August and September are 20 K above all other ATSR-2 3.7 μm datapoints, in one case the measurement reaching the 320 K saturation temperature. This coincident rise in 1.6 μm and 3.7 μm signals confirms that these data relate to a temporary increase in high temperature summit activity which, as expected, we do not observe in the highly variable 11 μm signal (Figure 4.11). The 1.6 μm and 3.7 μm radiance levels fell again without any reported eruptions, and levels of observed 1.6 μm radiance remained negligible until a

small rise in our last observation, recorded on 6 December 1995. The most recent reported visit was made on 6 February 1996 (Matthews *et al.*, 1997) when the 1993 dome was seen to have been completely absent, leaving a deep pit with four fumarolic jets around its rim. We suppose that variations in degassing through these jets was responsible for the rises in shortwave infrared thermal flux levels seen in September and December 1995 though, in this case, these variations do not appear to have signified pre-eruptive events.

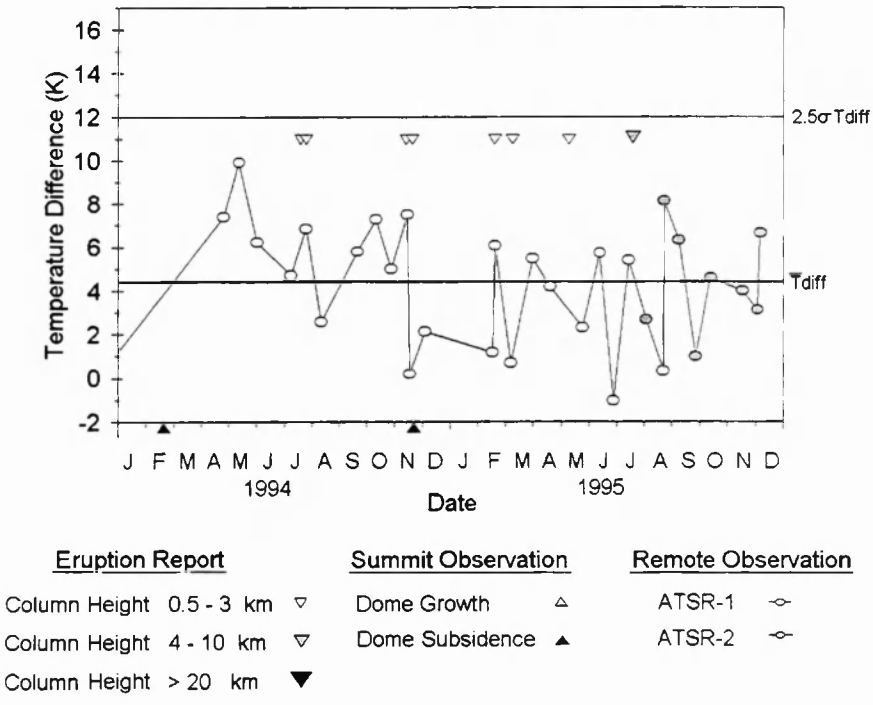

Figure 4.11. The brightness temperature difference between the Lascar 'summit' pixel and its immediate neighbours, recorded in the 11 μm channel of ATSR over the years 1994 and 1995. All measurements are nadir-viewing and recorded at night (01:20 - 01:50 GMT). The mean and 2.5σ levels are also shown.

4.6. Conclusions

This study has shown that measurements of volcanogenic shortwave infrared (1.6 μm) spectral radiance can be made using low spatial resolution satellite based

instruments such as the Along Track Scanning Radiometer. The nighttime 1.6 μm signal is derived exclusively from high temperature areas, and so is not affected by changes in the ambient temperature or in surfaces having temperatures much below 300 °C. The information can therefore be interpreted as relating to changes in the hottest surfaces on the volcano. At Lascar Volcano, large explosive eruptions appear more likely when the 1.6 μm signal has fallen from a high to a low level. The 11 μm data is less useful, since it is difficult to isolate the signal caused by changes in the hottest areas of the summit.

The low spatial resolution of the ATSR 1.6 μm measurements ensures that the sensor does not become saturated, whereas the high temporal resolution (gained at the expense of spatial detail) allows a more comprehensive dataset to be collected than is possible with Landsat TM. The closely spaced nature of the time-series also assists in identifying temporary excursions in the data that are attributable to accumulations of volcanogenic gases, aerosols or plume. New cloud detection tests, specific to the volcanic conditions encountered, allowed cloud-contaminated data to be removed from the analysis.

At Lascar Volcano, our observations of variations in the levels of emitted 1.6 μm spectral radiance are consistent with observations made using high spatial resolution data (Oppenheimer *et al.*, 1993; Smithsonian Institution, 1993a) and with field observations of dome growth and subsidence (Gardeweg *et al.*, 1993). Such data can therefore assist predictions of eruptive behaviour deduced from the application of models of lava dome growth to this and other, similar, volcanoes. We suggest that the magnitude of the April 1993 eruption may be related to the long interval between the initial decrease in radiance and the major eruptive event, this allowing internal pressure inside the volcano to reach uncharacteristically high levels. After the major eruption of April 1993, the 1.6 μm flux

never regained its April 1992 levels. This may be due to the relative thinness of the 1992 lava dome or perhaps indicates that anomalously high pressures existed within the volcano even prior to the 1993 dome subsidence, these high pressures causing fumarolic emission and heating that was more intense than that exhibited during later degassing episodes.

In addition to the April 1992 - April 1993 activity, we observed a cycle of increasing shortwave infrared thermal flux during 1994, and flux decline during the first half of 1995, for which more direct observations are lacking. We suggest that this cycle is related to variations in gas flow through fumaroles on the crater floor and we observe that these variations are followed by a major explosive event. However, we cannot discount the possibility that this cycle represents an otherwise unobserved cycle of dome growth and collapse. A briefer and lower amplitude cycle is observed between October and December 1993 and this is also followed by a relatively large eruption. Our most recent data confirm field observations that, by October 1995, Lascar had entered a phase characterised by weak degassing.

The analytical techniques developed during this study will be applicable to the monitoring of certain volcanic targets using shortwave infrared radiance data from the low spatial resolution MODIS sensor and the forthcoming Advanced ATSR instrument, both due for launch in the late 1990s. However, lack of information in the ATSR forward-view indicates that care must be taken to ensure that only data having the appropriate viewing geometry (usually near nadir-viewing) is used in such studies.

Chapter 5.

Satellite thermal analyses of lava dome effusion at Unzen Volcano, Japan.

M. J. Wooster and T. Kaneko

Journal of Geophysical Research (Accepted for publication, October 1997)

5.1. Abstract

This paper presents analyses of high- and low-spatial resolution infrared remote sensing data of the 1992 - 1994 lava dome growth episode of Unzen Volcano (Japan). The primary aim is to determine whether such data can indicate trends in the rate of magma supply to the dome since this is one of the principal factors controlling the frequency of pyroclastic flow. Frequent, low-spatial resolution infrared spectral radiance measurements were obtained by the Along Track Scanning Radiometer (ATSR), operating onboard the ERS-1 satellite. These data correctly delimit the two discrete phases of magma supply to the dome and, during phase 1, the shortwave infrared spectral radiance data are found to be strongly correlated with ground-based estimates of lava effusion rate. The correlation is, however, significantly weaker during phase 2. Analysis of high spatial resolution data

from airborne and satellite based systems allows us to determine the principal source of shortwave infrared flux as fumarolically heated dome surfaces, these being significantly hotter than the actively growing lava lobes. Variations in the shortwave infrared signal observed by ATSR are, therefore, directly attributed to fluctuations in the size and temperature of the fumarolically heated area. These fumarolic variations are largely dependent upon the flux rate of magmatic gas, which in turn is partly dependent upon the rate of magma supply. Gas fluxes were monitored throughout the eruption using COSPEC measurements of SO_2 concentration and these data indicate that the relationship between fumarolic discharge and the effusion rate of lava was relatively stable during phase 1 but highly variable during phase 2. Additionally we note that the fumarolic vents were noticably smaller during phase 2. We suggest these variations as an explanation for the strong correlation observed between the emitted shortwave infrared flux and the effusion rate of lava during phase 1, and the altered and significantly weakened correlation observed during phase 2. A previous study of the phase 1 Unzen eruption used high-spatial resolution infrared spectral radiance data obtained by the Landsat 5 Thematic Mapper (TM). As a result of the current investigation we show that the relationship between lava effusion rate and the thermally anomalous area recorded by TM is substantially improved when analysis is confined exclusively to the western dome. Thermal radiance from this area was primarily determined by levels of fumarolic emission, which we understand to be well correlated with the effusion rate of lava, and is believed to have been relatively unaffected by variations in the surface activity of the lava lobes which, at this time, were present solely on the eastern dome. As a result of this study we conclude that appropriate analysis of high- and low-spatial resolution shortwave infrared remote sensing data may assist in elucidating trends in lava supply at volcanoes exhibiting similar dome growth episodes to that experienced at Unzen.

5.2. Introduction

After 198 years of dormancy Unzen Volcano began erupting in November 1990, developing a summit lava dome in May 1991. The dome continued to grow for the next four years, primarily in an E-W direction, with lava effusion rates monitored by trigonometric surveys and helicopter inspections of the summit (Nakada and Shimizu, 1995). Collapses from the growing lava dome generated around 10,000 pyroclastic flows, these being most frequent when lava effusion rates were high (Sato *et al.*, 1992). Despite the evacuation of up to 12,000 local inhabitants, one of the largest pyroclastic flows (length 4.3 km) caused 43 fatalities on 3 June 1991. The relationship between the growth rate of the lava dome and the frequency of pyroclastic flow highlights the importance of monitoring the rate of magma supply, though doing so accurately presents numerous logistical and physical problems.

Studies have already demonstrated that newly active lava domes can be detected through use of low-spatial resolution shortwave infrared spectral radiance data (Wooster and Rothery, in press). Appendix E.3 shows the example of the 1991 dome of Galeras Volcano (Columbia), where measurements of thermal flux made by ATSR correctly indicate the arrival of the new dome within the volcanic complex. Chapter 4 further demonstrated the ability of such data to delimit changes in the thermal status of a persistently active dome, namely that at Lascar Volcano (Chile). The results of the Lascar study also indicated that significant changes in emitted shortwave infrared spectral radiance, most probably related to large-scale variations in degassing through the dome structure, preceded vulcanian explosive eruptions. Since Lascar is a remote and largely unmonitored volcano only qualitative field reports were available to compare with data obtained by remote sensing methods. By constructing a similar time-series for Unzen Volcano the infrared radiance data can be analysed alongside a variety of quantitative *in situ* measurements, including data on the rate of magma supply to the growing dome. This

allows for a better assessment of the value of the remote sensing technique and, in particular, for an investigation into how trends in the observed thermal signal relate to variations in the rate of magma supply and lava dome expansion. An understanding of these relationships would strengthen efforts to use such data in the monitoring of other volcanoes exhibiting similar episodes of lava dome growth.

5.3. Background to the 1990 - 1995 Unzen Eruption

Unzen Volcano (32 ° 46 ' N, 130 ° 17 ' E, elev. 1360 m) is situated on the Shimabara Peninsula of the island of Kyushu, the southern-most of the four principal islands of Japan. The volcano was formed around 500 ka in the Unzen volcanic graben and erupts predominantly dacite magma (Ohta, 1984). Historical eruptions occurred in 1663 and 1792, with eruption products characterised by thick lava flows and domes (Nakada and Fujii, 1993). In the latter eruption collapse of a parastitc edifice caused the death of 15,000 local inhabitants. Unzen was selected for study as a 'Decade Volcano' during the International Decade of Natural Disaster Reduction (National Academy of Sciences, 1987).

The 1990 - 1995 activity of Unzen Volcano began with phreatic and phreatomagmatic eruptions in November 1990. A new lava dome began to grow at the summit of Mount Fugen, one of the Unzen volcanic peaks, in May 1991 (Figure 5.1). Lava effusion rates were highest (~ 4 x 10^5 m^3/day) during the initial stages of dome growth and this activity formed three lava lobes on the western summit region before effusion rates began to fall and the site of lava effusion switched to the eastern summit in September 1991. For the remainder of phase 1 the western dome was solely associated with fumarolic activity related to the degassing of magma in the conduit, prior to its exogenous extrusion at the eastern dome location (Figure 5.2). Six additional lava lobes were formed on the eastern dome before effusion rates dropped to near-zero levels in January 1993 (Nakada and Shimizu, 1995).

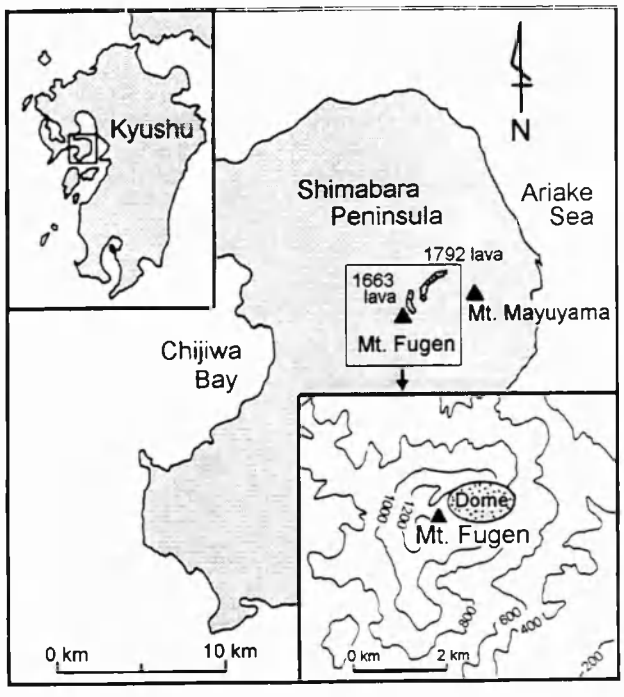

Figure 5.1. The location of Unzen Volcano, historical lava flows, and the 1991-1994 active lava dome at the summit of Mount Fugen. Adapted from Hirabayashi et al. (1995).

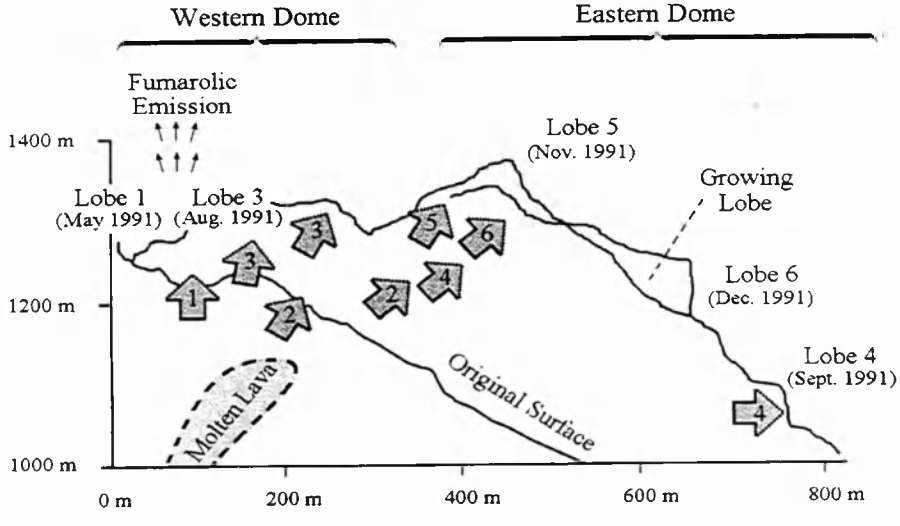

Figure 5.2. Cross section of the Mount Fugen summit, indicating the supply of magma and date of lava lobe emergence. Lobes 1, 2 (subsequently buried) and 3 emerged in the western dome, whilst lobes 4, 5 and 6 emerged through an inclined conduit in the eastern dome. Volcanic gases continually discharged from vents in lobe 3. The situation depicted is that which existed at the end of phase 1. The maximum inclination of the dome faces was around 35 ° from the horizontal. Figure adapted from that in Nakada (1992).

Phase 2 of magma supply commenced in February 1993 (Nakada, 1992) with an increase in lava effusion (to around 2 x 10^5 m^3/day) and increases in earthquake and pyroclastic flow frequency. The actively growing area of the lava dome also returned to the western dome region. The phase 2 activity was characterised by exogenous growth until November 1993, when endogenous growth began to dominate (Nakada *et al.*, 1995). Four additional lava lobes were formed during the phase 2 activity, lobe numbers 10, 11, 12 and 13. A typical lobe, active for several months, was around 300 - 400 m long, 200 - 300 m wide and 50 - 100 m thick (Nakada *et al.*, 1995). By the summer of 1994 effusion rates had again fallen to relatively insignificant levels, with the cessation of all activity in 1995 (Nakada and Shimizu, 1995).

5.4. Methodology

5.4.1. Measuring thermal emittance using the ERS-1 ATSR

The principal remote sensing dataset used in this study was obtained by the ERS-1 Along Track Scanning Radiometer (ATSR-1), full details of which are given in Chapters 2 and 4.3. The ATSR-1 instrument uses a single pre-amplifier for the 1.6 μm and 3.7 μm channels and these measurements are therefore mutually exclusive. Switchover is controlled by a signal thresholding system that operates on a pixel-by-pixel basis (Tinker *et al.*, 1985). In standard operating mode the 3.7 μm data are recorded unless a significant signal (above the detector noise level) is sensed in the 1.6 μm channel. However the 3.7 μm channel failed in May 1992 and 1.6 μm data have been collected continuously since that time.

Nighttime data from ATSR were used to measure variations in the spectral radiant energy being emitted from surfaces at the summit of Unzen Volcano. The amount of thermal radiation being emitted by these surfaces varies in accordance with the Planck function, which is adapted here to include the emissivity (ε) of the surface (Equation 5.1).

At night the radiance recorded at the Unzen dome can be considered as an area-weighted sum of the individual thermal components that fill the ATSR field-of-view (Equation 5.2).

$$L(\lambda,T) = \varepsilon\lambda \frac{C_1}{\lambda^5 (\exp(\frac{C_2}{\lambda T}) - 1)} \tag{5.1}$$

where λ is wavelength (m)

T is temperature (K)

L is spectral radiance ($W/m^2/sr/m$)

C_1 and C_2 are constants (1.19×10^{-16} Wm^2 and 1.44×10^{-2} mK, respectively)

$$R_i = \varepsilon_i \tau_i [\sum_{k=1}^{n} P_k L_i(T_k) + (1 - \sum_{k=1}^{n} P_k) L_i(T_b)] + Ra_i^{\uparrow} + \tau_i (1/\pi)(1-\varepsilon_i) Ra_i^{\downarrow} \tag{5.2}$$

where i is the ATSR waveband of interest

L_i is the recorded infrared spectral radiance ($W/m^2/sr/\mu m$)

n is the number of discrete thermal components on the active volcanic surface

$L_i(T)$ is the Planck function radiance ($W/m^2/sr/\mu m$)

Tk is the surface temperature of the k^{th} thermal component

Pk is the fraction of the ATSR field of view covered by the k^{th} component

ε_i is the spectral emissivity of the surface and τ_i is the atmospheric transmission

$Ra_i^{\uparrow}$ is the upwelling atmospheric radiance reaching the sensor ($W/m^2/sr/\mu m$)

$Ra_i^{\downarrow}$ is the downwelling atmospheric radiance reaching the ground ($W/m^2/sr/\mu m$)

T_b is the temperature of the ambient background (K)

Measurements by Salisbury and D'Aria (1994) and Urai and Isobe (1995) indicate that the emissivity of the Unzen dacite is around 0.85 for each of the ATSR wavebands, making it an efficient emitter of infrared radiation. For nighttime shortwave infrared measurements, $Ra_{1.6}^{\uparrow}$, $Ra_{1.6}^{\downarrow}$ and $L_{1.6}(T_b)$ are effectively zero, whist results from the LOWTRAN 7 radiative transfer model (Kneizys *et al.*, 1988) place $\tau_{1.6}$ at greater than 0.95 at the latitude and height of Unzen. For the 3.7 μm, 11 μm and 12 μm wavebands, τ_i, $Ra_i^{\uparrow}$, $Ra_i^{\downarrow}$ and $B_i(T_b)$ are non-negligible and vary on a diurnal and seasonal basis.

By examining the Planck function relationship between blackbody temperature and radiant flux for each of the ATSR wavebands (Figure 5.3) we can infer that the signal recorded in each channel is likely to be dominated by a different thermal component of the lava dome surface. The highly non-linear 1.6 μm curve, with increasing steepness at higher temperatures, indicates that measurements at this wavelength are likely to be dominated by thermal emission from the highest temperature surfaces, even if these surfaces cover only a small fraction of the sensor field of view. In contrast the near-linearity and gentle slope of the 11 μm Planck function suggests that this signal is likely to be dominated by emission from surfaces that present the largest area within the field-of-view. The 3.7 μm signal is also likely to be dominated by radiation from the hottest surfaces but, in contrast to measurements at 1.6 μm, surfaces at ambient and near-ambient temperatures will also emit significantly within this waveband.

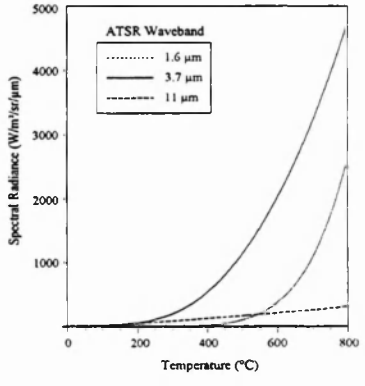

Figure 5.3. The relationship between emitted infrared spectral radiance and surface brightness temperature for the ATSR 1.6 μm, 3.7 μm and 11 μm channels, calculated using the Planck function (Equation 5.1).

5.4.2. ATSR data extraction and analysis

All relevant ascending-node (nighttime) ATSR-1 data of the Shimabara Peninsula were obtained from the end of the ERS-1 commissioning phase (December 1991) until July 1994. Orbital calculations indicate that nighttime ATSR data of the area should be obtained on a three-day basis, though shifts of the ERS-1 orbit decreased this frequency somewhat. A subset of the 1.6 μm and 11 μm data from a single ATSR scene are shown as Figure 5.4.

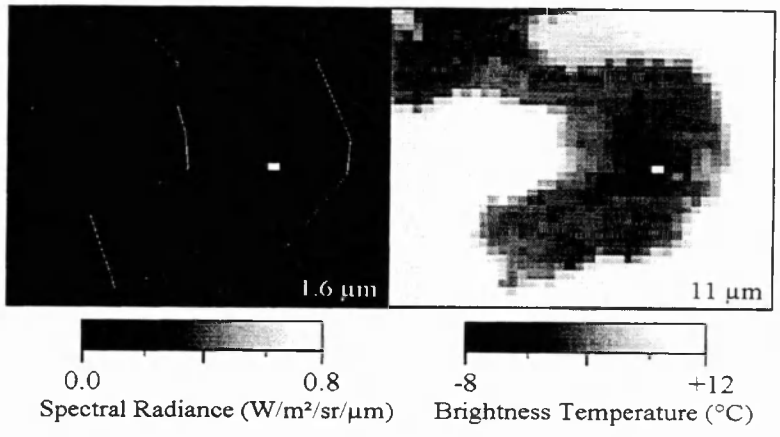

Figure 5.4. ATSR 1.6 μm and 11 μm data for the Shimabara Peninsula, obtained at 13:10 GMT on 24 December 1992. The location of the Mount Fugen lava dome is clearly indicated in both wavebands but no other area shows a significantly elevated surface temperature. The 1.6 μm signal is below the detection limit at all other locations within the subscene and a coastal outline has been superimposed on this image for ease of reference.

For each of the 159 images obtained, a subscene covering Mount Fugen was extracted using the automated methodology developed by Wooster and Rothery (1997b) and outlined in Section 4.4.3. The extracted data were subject to a number of screening techniques aimed at removing cloud-contaminated data from the analysis,. It was observed that the sub-tropical location and relatively low elevation of Mount Unzen caused the cloud-free summit pixel to consistently possess an 11 μm brightness temperature greater than 0 °C. Gross cloud cover lowered the brightness temperature below this threshold and 75% of scenes were removed on this basis, these images also

showing no 1.6 μm signal at the location of Unzen. The fact that the volcano was obscured by cloud during the majority of the ERS-1 passes indicates the importance of obtaining data at a high temporal frequency, something that is best achieved by a low-spatial resolution instrument. The ATSR scenes that did not exhibit gross cloud cover at the volcano location were subject to the subpixel cloud tests described in Section 4.4.3, the two scenes that failed these tests also being removed. Finally, visual analysis of the remaining 11 μm images identified two scenes on which large plumes originated from the volcano. Such plumes are likely to have impeded the instrument's view of the summit and these data were also discarded.

Of the remaining 31 scenes, which had a viewing zenith angle to the volcano of 8.7 ° ± 0.5 °, no cloud or plume was detectable on or near Unzen Volcano. Since Mount Fugen was the only high temperature heat source in the vicinity of Unzen, the ATSR pixel corresponding to the summit was identified on the basis of the most radiant 1.6 μm measurement, the level of high temperature activity being sufficient to turn on recording of this channel as illustrated in Figure 5.4. Subsequent to the May 1992 failure of the 3.7 μm channel, geographical overlap of the ATSR instantaneous field-of-view (Godsalve, 1995) caused certain pixels neighbouring the most radiant to also record a 1.6 μm signal. Scenes recorded after this date had the total 1.6 μm signal calculated by summation of the signal from all pixels radiant at 1.6 μm.

Variations in the longwave infrared signal were quantified by extracting the 11 μm brightness temperature of Mount Fugen. To facilitate quantitative comparisons with the remotely sensed data, the lava effusion rate estimates obtained by the Joint University Research Group (JURG) and the Geographical Survey Institute (GSI) were linearly interpolated to the relevant ERS-1 overpass dates.

5.5. Results

5.5.1. ATSR time-series data

Figure 5.5 (a) shows the variation in total 1.6 μm spectral radiance, subsequent to the 3.7 μm channel failure in May 1992, whilst Figure 5.5 (b) shows the 1.6 μm signal recorded at the summit pixel for the whole of the time-series. Trends in these two parameters are virtually identical, with a Pearsons product moment linear correlation coefficient (r) of 0.95, as would be expected since the relationship between them is principally a function of the geographical overlap of the ATSR pixels (Godsalve, 1995). Figure 5.5 (c) shows the original lava effusion rate data collected by the JURG and the GSI. Though noise inherent in these magma flux data are relatively high, up to around ±50% error on the measurements, the data do clearly indicate the two phases of magma supply identified by the Smithsonian Institution (1994b), with a transition date in January-February 1993. These two phases are also well delineated by the sharp rise in ATSR 1.6 μm spectral radiance soon after the onset of phase 2. Additionally, the phase 1 fall in shortwave infrared spectral radiance correctly parallels the fall in lava effusion rate, with inspection of Figure 5.6 (a) suggesting that the relationship between these two variables is approximately linear. Calculation of the Pearson Product Moment linear correlation coefficient (r) provides a value of 0.80, which is significant at the 95% confidence level and indicates that there is only a 0.05% chance that the relationship between these data is, in fact, randomly generated. This degree of correlation is all the more convincing given the relatively high degree of noise within the dataset. During 1992 four different lava lobes were active on the eastern dome, with active lobe transitions in March, August and December 1992. During phase 1 the positive relationship observed between lava effusion rate and shortwave infrared flux appears unaffected by these changes in active lava lobe.

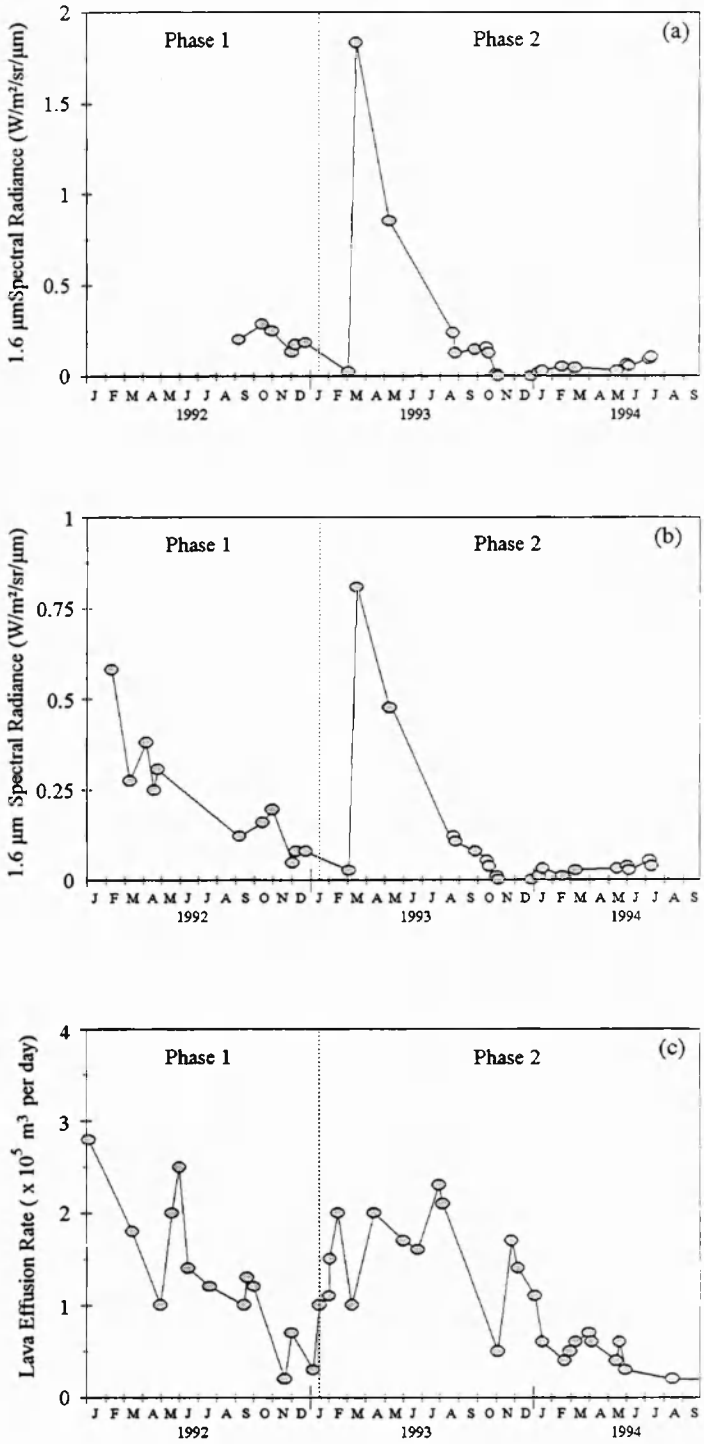

Figure 5.5. (a) The summed value of 1.6 µm spectral radiance recorded at Mount Fugen, (b) the summit pixel 1.6 µm spectral radiance and (c) the effusion rate of lava. Effusion rate data were collected by the Joint University Research Group and the Geographical Survey Institute, error on the measurements is estimated to be ±(0.3 - 1.0) x 10^5 m^3/day.

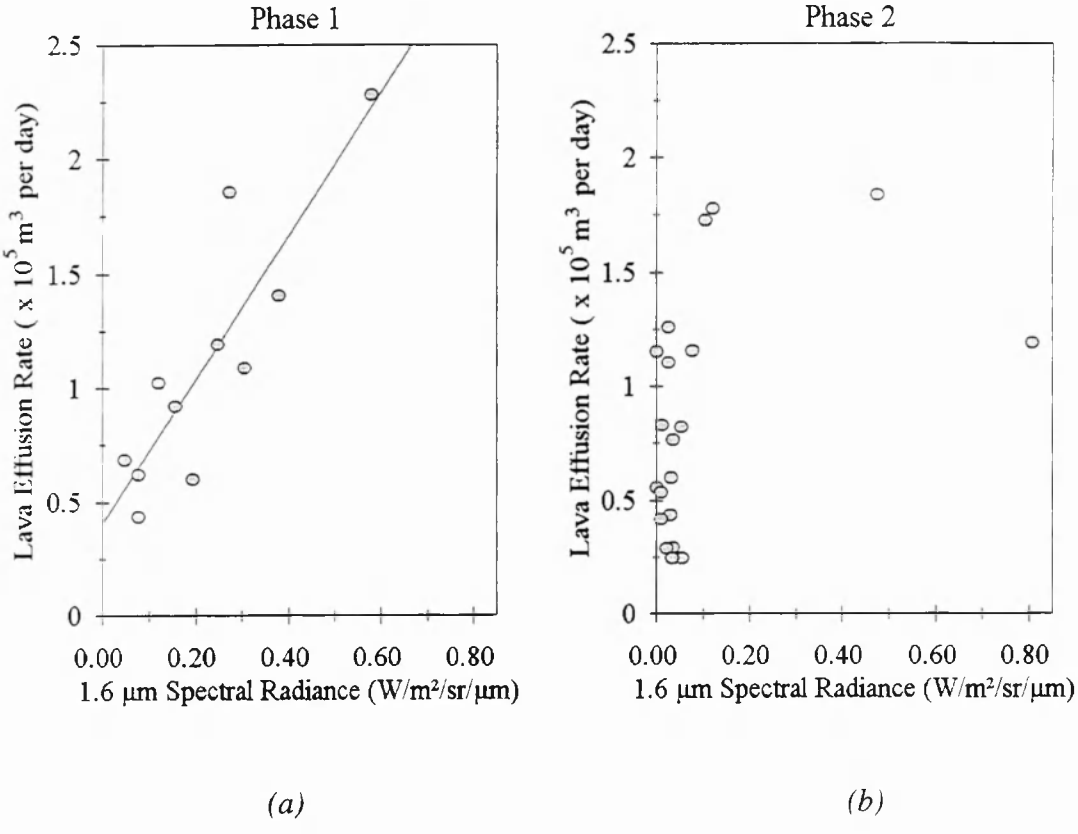

Figure 5.6. (a) The phase 1 and (b) phase 2 relationships between the shortwave infrared (1.6 μm) spectral radiance of the Mount Fugen summit pixel and the contemporaneous lava effusion rate, interpolated from the data collected by JURG and GSI.

In contrast to the strong correlation found during phase 1, the shortwave infrared spectral radiance and effusion rate datasets of phase 2 show somewhat different patterns (Figure 5.6). At the start of phase 2 there is a rapid increase in effusion rate as new lava is supplied to the dome. Initially there is a corresponding increase in shortwave infrared flux (April and May 1993), but these two most radiant points lie off the trend of the remaining phase 2 data (Figure 5.6 [b]). Calculation of the non-parametric Spearman rank correlation coefficient (r_s) gives a value of 0.33 for the entire phase 2 dataset, which is not significant at the 95% confidence level. The phase 2 changes in effusion rate are comparable in magnitude to those exhibited during phase 1 but, apart from the two most radiant points,

there is relatively little change in the level of recorded shortwave infrared flux. This finding weakens the argument for a direct link between these two variables, though the strong correlation found during phase 1 implies that they are somehow related. Furthermore, the fact that the phase 1 and 2 data plot in systematically different regions of the Figure 5.6 graphs suggests that a fundamental difference in activity may exist between these two phases.

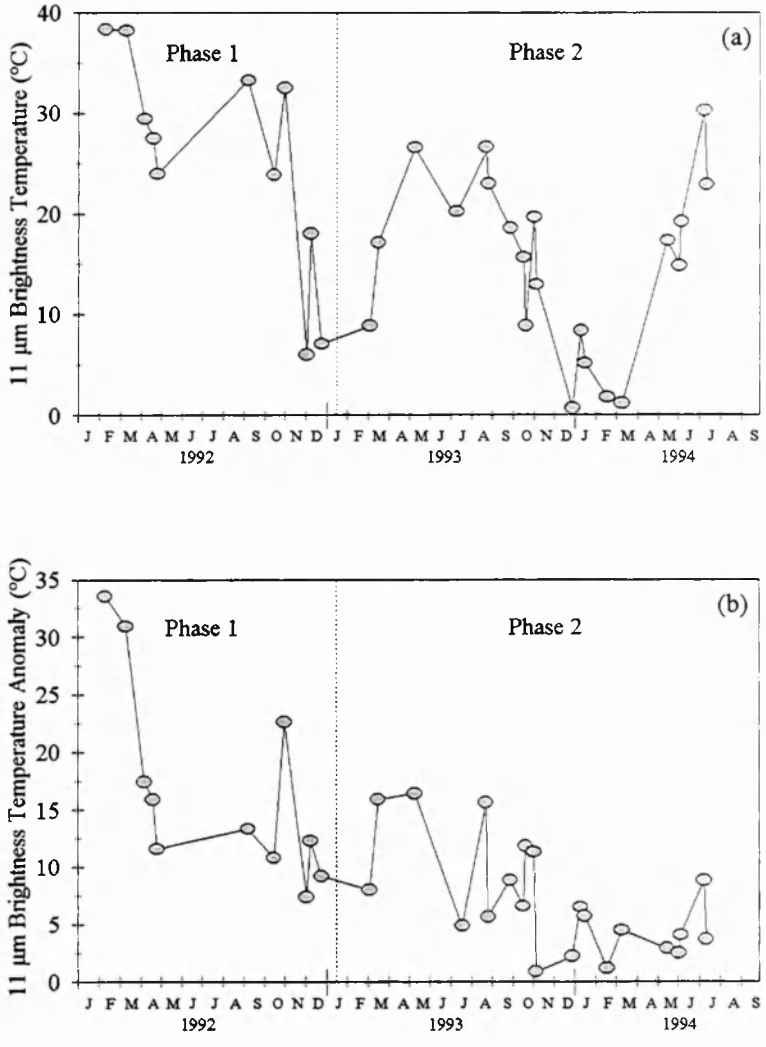

Figure 5.7. (a) The 11 μm brightness temperature data of Mount Fugen and (b) the 11 μm temperature anomaly, calculated to lessen the effects of seasonality within the dataset.

In contrast to the shortwave infrared data, which are unaffected by changes in ambient background and atmospheric emission, the longwave infrared (11 μm) brightness temperature data of Mount Fugen show a clear seasonal trend (Figure 5.7 [a]). To lessen the effects of seasonality we calculated the brightness temperature difference between the summit pixel and the neighbouring non-thermally anomalous pixels. Figure 5.7 [b] shows the resulting time-series, with a noisy but approximately monotonic decrease in the brightness temperature anomaly throughout the eruption. Unlike the 1.6 μm time-series, there is no clear delineation of phases 1 and 2 of magma supply in the 11 μm data. This difference in response is best explained by examining the source of the radiant energy recorded in these two wavebands.

5.5.2. Origin of the longwave infrared signal observed by ATSR

The near-linear, gently sloping relationship between emitted longwave infrared (11 μm) spectral radiance and temperature (Figure 5.3) means that trends in the 11 μm anomaly are likely to be generally representative of changes in the broad-area surface temperature of the summit, the hottest components being too small in area to be highly significant at this wavelength. A more detailed interpretation is hampered by the fact that all observed surfaces contribute some signal at this wavelength, as does the intervening atmosphere. The Figure 5.7 (b) data indicate a generally decreasing broad-area summit temperature over the period. This maybe explained by the observed thickening, and therefore cooling, of the lava dome carapace as the eruption proceeded (Nakada *et al.*, 1995).

5.5.3. Origin of the shortwave infrared signal observed by ATSR

Unlike the longer wavelength measurements, the short wavelength data are independent of changes in the ambient background temperature and are only weakly affected by local atmospheric variations. Furthermore the highly non-linear nature of the

1.6 μm Planck function (Figure 5.3) suggests that the majority of the shortwave infrared flux is likely to originate at the hottest surfaces of the lava dome. To determine these locations we use high spatial resolution imagery of the summit.

Figure 5.8 shows the band 5 (1.6 μm) data from a daytime Landsat TM scene of 4 December 1991, with an outline of the lava dome overlain. The TM data indicate that at this time two distinct areas are thermally anomalous at 1.6 μm, the actively growing eastern dome and the fumarolically active western dome (Umakoshi *et al.*, 1992).

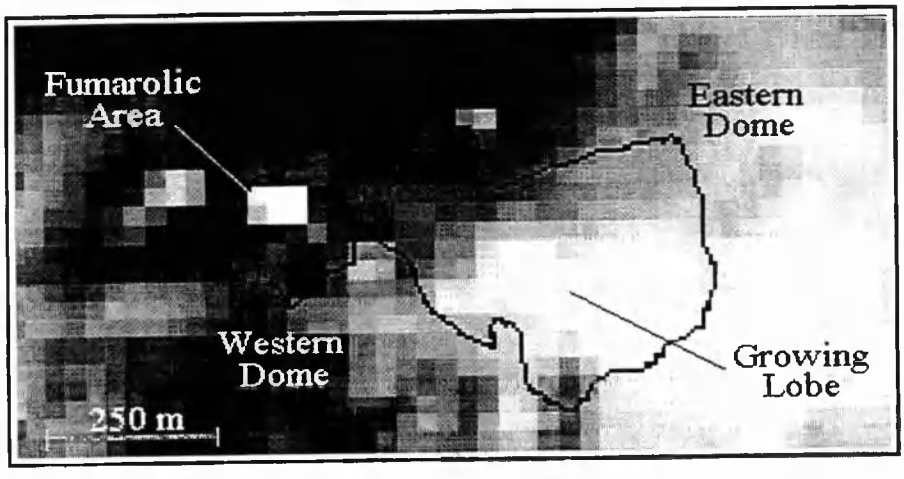

Figure 5.8. Daytime Landsat TM band 5 (1.6 μm) image of Mount Fugen, collected on 4 December 1991. An outline of the lava dome as observed on 5 December 1991 by Nakada (1992) is overlain. Pixel size is 30 m x 30 m. The majority of the observed radiance is due to solar reflected radiation, however two areas of the summit are sufficiently hot to be emitting detectable levels of 1.6 μm thermal flux. These thermally anomalous areas are the most radiant (brightest) pixels in the image. At this time lobe 3 of the western dome was the site of intense degassing activity and an area of thermally anomalous pixels is centred on these fumarolic vents. Lobe 4 of the eastern dome was actively growing, with a series of thermally anomalous pixels indicating the high temperature zone surrounding the lava effusing vent.

Either of the two thermally anomalous sites highlighted in Figure 5.8 may have provided the dominant source of shortwave infrared thermal flux but, unfortunately, the daytime TM data of Figure 5.8 cannot be used to estimate actual surface temperatures

since the high levels of solar reflected radiation, and the geographic resampling strategy used by the data provider, have corrupted the thermal signal (Rothery *et al.*, 1988). Rather we use surface temperature measurements extracted from thermal infrared video data of the summit. These data are of sub-meter spatial resolution and were collected during 1991 and early 1992 using a helicopter-mounted infrared camera system, equipped with a variable gain facility to avoid sensor saturation (Umakoshi *et al.*, 1992). Table 5.1 indicates the principal surface temperature components that were consistently present during the infrared camera surveys. In addition to these persistent temperatures, the crack at the centre of the lava effusing vent (eastern dome) was observed to have a maximum temperature of 540 °C (area ~ 250 m^2) on one particular day, but this temperature fell rapidly immediately away from the vent location. Similarly, immediately after a collapse event newly exposed surfaces were sometimes observed to have temperatures greater than 400 °C, however rapid radiative cooling quickly returned them to a temperature close to that of the broad-area dome surface (K. Umakoshi, unpublished data, 1992). In contrast to these transient temperature increases on the eastern dome, the high temperatures associated with fumarolic heating on the western dome were consistently found over large areas. Maximum temperatures of 658 °C and 626 °C were recorded near the steam and gas vents of the western dome in October 1991 (Umakoshi *et al.*, 1992).

Dome Site	Temperature Component	Minimum Temperature (°C)	Maximum Temperature (°C)	Estimated Area (m^2)
Eastern Dome	Broad Area Surface	50	150	50000
Eastern Dome	Lava Effusing Vent	150	350	100 to 300
Western Dome	Large Fumaroles	400	800	1000
Western Dome	Small Fumaroles	300	500	500

Table 5.1. The typical range of surface temperatures observed during the surveys of Umakoshi et al. (1992). Data were taken repeatedly during surveys carried out between September 1991 and January 1992 (phase 1 period), when lava effusion was occurring at the eastern dome and the western dome was the site of high temperature (~ 800 °C) fumarolic gas emission. Approximate size of thermal features was calculated from infrared and colour photography, with additional information provided by K. Umakoshi (personal communication, 1997).

Combining the data of Table 5.1 with knowledge of the 1.6 μm Planck function (Figure 5.3) leads to the deduction that fumarolically heated areas of the western dome, primarily those surrounding the two large (~ 20 - 50 m diameter) vents of lobe 3 (Figure 5.2), were the dominant source of shortwave infrared thermal flux during this period. Estimates using Equation 5.2 indicate that the 1.6 μm spectral radiance contribution from this area may have been an order of magnitude greater than that from the actively growing lava lobes on the eastern dome. This supposition is supported by nighttime TM data of the Mount Fugen summit, collected on 15 October 1991. These data indicate that, at this time, the source of at least 70% of the total spectral radiance emitted from the dome in TM band 5 was the western dome fumarole area. Saturation of the TM sensor over certain of these fumaroles prevents a more accurate determination. Urai and Isobe (1995) further analysed this TM imagery using the dual-band technique of Rothery *et al.* (1988), which aims to convert the band 5 (1.6 μm) and band 7 (2.2 μm) spectral

radiance data of each pixel into an estimate of the subpixel surface temperature structure. Figure 5.9 shows a histogram of Urai and Isobe's (1995) surface temperature results, which confirm the evidence obtained from the thermal infrared video surveys. When compared to the actively growing eastern dome, the fumarolically active western dome shows significantly more pixels having a very high surface temperature component. These results confirm that thermal emittance from high temperature fumarolically heated surfaces is likely to have been the dominant source of shortwave infrared thermal flux recorded by ATSR. The large scale fumarolic vents of the western dome, which were associated with the highest surface temperatures (Figure 5.9), persisted throughout phase 1. From January 1992 onwards some small scale fumarolic activity was also intermittently observed in regions of the eastern dome (Earthquake Research Institute, unpublished data 1992) and it is possible that these areas may have provided a lesser, secondary source of fumarolically derived shortwave infrared thermal flux.

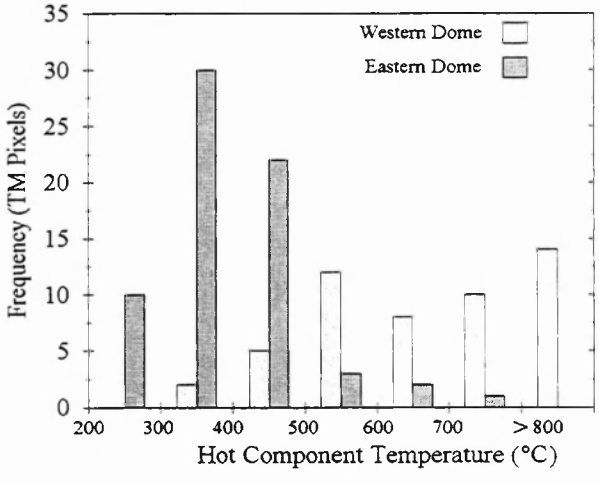

Figure 5.9. The subpixel surface temperatures obtained from dual-band analysis of nighttime Landsat TM data of the Mount Fugen lava dome, collected on 15 October 1991. The data indicate that the fumarolically heated western dome possessed significantly higher surface temperatures, distributed over a wider area, than did the actively growing eastern dome. Sensor saturation prevented solutions for eleven pixels in the image, band 5 (1.6 μm) saturation occurring only over areas of the western dome. Each TM pixel corresponds to a 30 m x 30 m area of ground. Data were adapted from that reported by Urai and Isobe (1995).

5.5.4. Variations in magmatic degassing

Our analyses have determined that the level of shortwave infrared thermal flux observed by ATSR is directly linked to the extent of fumarolic heating on the dome surface. Any correlation between the shortwave infrared spectral radiance and lava effusion rate datasets is secondary in nature and is dependent upon the exact relationship between the surface fumaroles and the internal magmatic activity. Our data (Figure 5.6) indicate that the correlation between lava effusion rate and shortwave infrared thermal flux is strong during phase 1 but weak during phase 2, and this change may be explained by variations in the degassing regime operating during each phase. From measurements made in May - December 1992, Hirabayashi *et al.* (1995) showed that the discharge of total gaseous volatiles was an average of 7700 ton/day, and they monitored variations in this rate using correlation spectrometer (COSPEC) measurements of SO_2 flux between 1991 and 1994. Averages of these data were subsequently used to estimate changes in the amount of SO_2 gas released per unit of erupted magma. These data are shown in Figure 5.10 and they indicate that the SO_2/magma ratio was approximately constant during phase 1, though it became highly variable during phase 2. This implies that, during phase 1, an approximately linear relationship existed between the flux rates of magmatic gas and of magma, which we suggest explains the strong correlation between the fumarolically driven shortwave infrared signal and the lava effusion rate data of this phase (Figure 5.6 [a]). Modelling studies would be necessary to further investigate the exact nature of the relationship between the flux rates of magmatic gas and the temperature and area of the fumarolically heated surfaces visible to the sensor. Nevertheless, the fact that the shortwave infrared signal appears dominated by thermal emission from fumaroles also provides an explanation for the apparent insensitivity of this signal to changes in the actively growing lava lobe, these occurring throughout 1992.

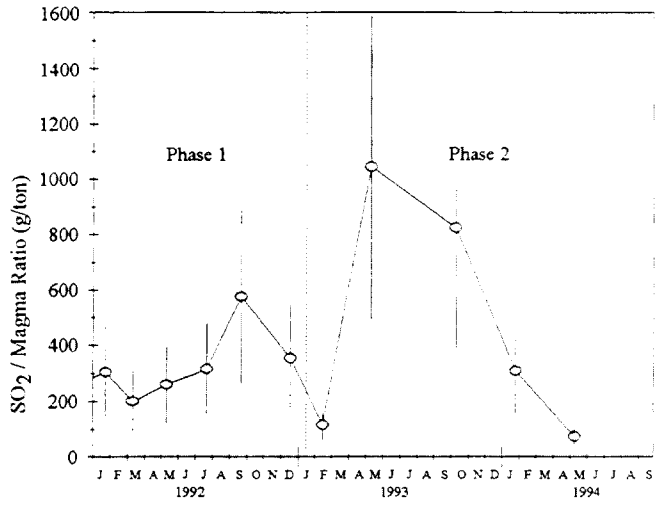

Figure 5.10. Temporal variation in the ratio of SO_2 discharge to magma effusion rate. Data taken from Hirabayashi et al. (1995), with each SO_2 flux measurement calculated from the mean of 16 - 60 COSPEC scans.

As already noted, during the phase 2 activity the SO_2/magma ratio appears significantly less stable than during phase 1 (Figure 5.10). This weakening of the gas/magma relationship would also be expected to weaken the connection between the amount of fumarolic heating, on which the 1.6 μm signal is dependent, and the rate of magma supply. This may explain the poor correlation between the lava effusion rate and shortwave infrared flux data of phase 2. Additionally, the start of phase 2 coincides with the return of lava effusion to the western dome area and the growth of lobe 10 at the site of the largest active fumaroles. The two large fumarolic vents of lobe 3 were seen to be absent during phase 2, degassing proceeding through a series of smaller fumaroles and cracks. Since the growth of lobe 10 appears to have impeded the previous gas pathway it is possible that degassing was reduced for a period. The SO_2 flux data of Hirabayashi *et al.* (1995) indicate that degassing was low during the first month of phase 2, even though lava effusion was relatively high (Figure 5.5c). These data lead to the calculation of a low SO_2/magma ratio early in phase 2 (Figure 5.10) and may explain why the first ATSR measurement of this phase shows a low 1.6 μm signal (Figure 5.5 [b]), since fumarolic

heating would be expected to be reduced by a restriction in degassing. It is possible that the restricted degassing led to the temporary confinement of gas within the edifice. In this case the sharp rise in shortwave infrared thermal flux seen in late-March and May 1993, and corresponding to the two outliers in Figure 5.6 (b), may be related to anomalously high levels of surface heating caused by release of this confined gas. The high SO_2/magma ratio observed at this time (Figure 5.10) supports this argument. An alternative explanation for the high radiances observed in late-March and May 1993 is that fresh lava was being directly observed by the sensor. However the periods of exogenous growth that preceded and followed these early phase 2 observations did not lead to similarly high 1.6 μm measurements, suggesting this explanation is invalid. Exogenous growth was also reported at the start of phase 2 (Nakada *et al.*, 1995), when the shortwave infrared signal is observed to be very low.

We have already stated that phases 1 and 2 show consistently different relationships between the level of recorded shortwave infrared spectral radiance and the rate of lava effusion (Figures 5.6 [a] and 5.6 [b]). Apart from the high values recorded in March and May 1993, the levels of shortwave infrared flux observed in phase 2 are persistently low when compared to those observed during phase 1. Since the shortwave infrared signal appears dominated by thermal emission from fumarolically heated surfaces, this difference may be explained by the original volatile content or efficiency of degassing being lower for phase 2 magma than for phase 1. However, unless SO_2 content is not representative of overall volatiles, this explanation does not agree with the data of Hirabayashi *et al.* (1995) which indicate the SO_2/magma ratio was highest during phase 2. A more probable explanation is that the efficiency of thermal transmission between the fumarolic gas and the surrounding rock surface was lower during phase 2 than during phase 1, probably due to the change in the site of active lava effusion. This explanation is supported by the knowledge that the large gas vents active in phase 1 were replaced with a series of smaller vents and cracks during phase 2. It is likely that this change in fumarole structure and geometry was responsible for the altered relationship between gas flux and

the nature of the fumarolically heated surfaces observed by ATSR. The small vents may be expected to have provided a reduction in this area, thus leading to the lower levels of emitted shortwave infrared thermal flux observed for the majority of this phase.

5.5.5. Re-interpretation of nighttime TM time-series of Unzen dome growth

Knowledge gained during this investigation allows for a re-interpretation of the TM time-series data previously used to study phase 1 of the Unzen eruption. Nine night-time TM scenes covering the period October 1991 - November 1992 were analysed by Urai and Isobe (1995). For certain of the scenes, sensor saturation prevented accurate determination of infrared thermal flux and so results were based on the total number of thermally emitting pixels within each band 5 (1.6 μm) image, this variable being broadly representative of the overall size of the summit thermal anomaly. Whilst features such as the May - June increase in magma supply are apparently identified by these data (Figure 5.11 [a]), Urai and Isobe (1995) found a generally poor relationship between this variable, which is associated with both fumarole and lava lobe activity, and the lava effusion rate (Figure 5.11 [b]). However our study has determined that the rate of lava effusion is likely to be better correlated with thermal variations associated exclusively with fumarolic activity, rather than with the overall size of the summit thermal anomaly. For each of the TM scenes we therefore calculated the number of thermally anomalous band 5 pixels in the western dome region (outlined in Figure 5.8), this being the dominant fumarolically active area throughout phase 1. The resultant dataset is plotted as Figure 5.11 (c) and it is clear that the decreasing trend in effusion rate (Figure 5.11 [b]) is more closely matched by the similarly decreasing size of the western dome fumarolically heated area (Figure 5.11 [c]) than by the overall size of the summit thermal anomaly (Figure 5.11 [a]). By concentrating analysis on the western dome fumaroles the TM data are therefore shown to be of value for determining trends in lava effusion, though in this case they appear little better than the more frequent, and considerably cheaper, low spatial resolution data provided by ATSR.

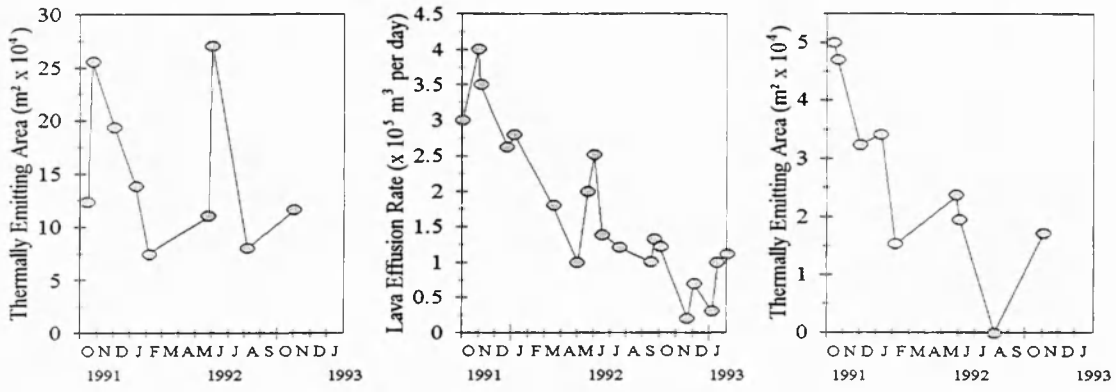

(a) *(b)* *(c)*

Figure 5.11. (a) Hot-area change at Mount Fugen, calculated from band 5 (1.6 μm) nighttime Landsat Thematic Mapper data collected during phase 1 activity. (b) Variation in the effusion rate of lava between October 1991 and November 1992 (detail extracted from Figure 5.6 [c]) (c) Hot-area change of the western dome (fumarole area) of Mount Fugen, calculated with the Landsat TM data used for Figure 5.11 (a).

5.6. Discussion

The results of this study have indicated that appropriate analysis of low- and high-spatial resolution shortwave infrared remote sensing data can be used to determine trends in the surface heating regime of the 1991 - 1994 lava dome of Unzen Volcano. It is likely that adaptations of this technique may be used to investigate actively growing lava domes at other terrestrial volcanoes. In situations similar to phase 1 of the Unzen activity, where trends in magmatic degassing and surface heating appear directly related to variations in magma supply, remotely monitoring levels of thermally emitted shortwave infrared flux may provide an additional method of determining trends in the growth rate of active domes. By providing low cost data at a high temporal frequency, instruments similar to ATSR can supply frequent time-series information that is impractical to obtain using higher resolution sensors. We note that the availability of such data is set to increase with the 1998 launch of the NASA EOS satellite carrying the Moderate Resolution Imaging Spectrometer (MODIS) instrument (Ardanuy *et al.*, 1991). Since this satellite also carries

the high spatial resolution ASTER instrument, we expect that dual use of these new datasets will significantly widen the applicability of the techniques presented here.

5.7. Conclusion

Between 1991 and 1994 a lava dome grew at the summit of Unzen Volcano, causing frequent pyroclastic activity. We show that the two phases of dome growth are well delineated by low spatial resolution shortwave infrared flux data taken by the ERS-1 Along Track Scanning Radiometer. During phase 1 of the eruption a highly significant correlation exists between the level of recorded shortwave infrared flux and the rate of lava effusion, with a weaker correlation found during phase 2. Analysis of high spatial resolution remotely sensed data allows us to determine the dominant source of 1.6 μm flux as fumarolically heated surfaces of the lava dome, other dome surfaces possessing temperatures that were generally too cool to be highly significant at shortwave infrared wavelengths. The shortwave infrared signal is therefore found to be directly related to the level of fumarolic emission, which itself is related to the rate of magma supply. COSPEC data of the eruption indicate that the relationship between fumarolic gas flux and the effusion rate of lava was relatively stable during phase 1 and significantly more variable during phase 2, with only smaller fumaroles active during phase 2. This explains why the lava effusion rate and shortwave infrared flux data appear well correlated during phase 1, but poorly correlated during phase 2. The identification of a positive correlation during phase 1 allowed us to re-interpret the Landsat TM time-series data of this phase, previously studied by Urai and Isobe (1995). By confining TM data analysis to the fumarolically heated western dome we found a highly significant relationship between the thermally anomalous area and the rate of lava effusion. This relationship was considerably weakened when the eastern dome area of actively growing lava lobes was included in the analysis.

Chapter 6.

Geometric considerations for the remote monitoring of volcanoes: studies of lava domes using ATSR and the implications for MODIS

M. J. Wooster, D. A. Rothery and T. Kaneko

International Journal of Remote Sensing (Accepted for publication, December 1997)

6.1. Abstract

The Moderate Resolution Imaging Spectrometer (MODIS), an instrument on NASA's proposed Earth Observing System (EOS), will supply low-spatial resolution infrared radiance data that may be used to thermally monitor active volcanoes. MODIS uses a ± 55° scan angle to provide a wide (2330 km) swath and thus frequent temporal coverage. This geometry means that zenith angle and pixel area will vary greatly across the swath. The Along Track Scanning Scanning Radiometer (ATSR), currently operating on the ERS-1 and ERS-2 satellites, provides near-contemporaneous low-spatial resolution infrared radiance data at two widely differing zenith angles. I compare dual-viewing

geometry ATSR data for two subpixel sized volcanic (lava dome) hotspots in order to investigate geometric effects on the retrieved radiances. The effect of pixel size increasing with zenith angle is shown to be counteracted by increasing pixel overlap, theoretically providing comparable thermal-anomaly signals from the two ATSR views. This is shown to be the case at Unzen Volcano (Japan) but not at Lascar Volcano (Chile), where the lava dome is contained within a summit crater and geometric shielding of hot-surfaces is shown to be significant at high zenith angles.

6.2. Introduction

Satellite remote sensing provides a potential methodology for routinely monitoring the thermal output of active volcanoes. At sites possessing active lava domes such data may provide evidence of dome growth or subsidence, factors that may be related to the liklihood of future explosive eruptions (Oppenheimer *et al.*, 1991). Low spatial resolution infrared radiance data from the ERS Along Track Scanning Radiometer (ATSR) have been used to study variations in the thermal emittance from active domes at Lascar Volcano, Chile (Chapter 4) and Unzen Volcano, Japan (Chapter 5). These studies concentrated on shortwave infrared (1.6 μm) spectral radiance data from the ATSR nadir-view scan. However the conical scanning mechanism of ATSR allows a second (forward-view) 500 km swath of data to be imaged during each rotation of the scan mirror (Prata *et al.*, 1990). Data from the two swaths provide near-contemporaneous observations of the same ground locations but at widely differing zenith angles (Figure 6.1). In order to investigate the effects of viewing geometry on the observed thermal anomaly we now compare the signals retrieved from these volcanoes at the two ATSR viewing conditions. An understanding of geometric effects is important in planned studies of volcanoes using the

Moderate Resolution Imaging Spectrometer (MODIS) because this instrument observes a wide (2330 km) swath by scanning 55° either side of nadir, equivalent to a zenith angle variation of ± 65° (Salomonson, 1989). MODIS observations of infrared thermal flux are proposed for use in an automated eruption detection system, and for studies of the thermal evolution of volcanically active locations (Mouginis-Mark *et al.*, 1991b). In order to maximise the temporal coverage of cloud-prone volcanic locations, time-series volcanological studies using MODIS will need to combine data from nadir and all usable off-nadir regions of the swath. The maximum resultant zenith angle variation will be of a similar magnitude to that between the ATSR forward- and nadir-views, making ATSR a useful indicator of the geometric effects that will be of relevance to such studies.

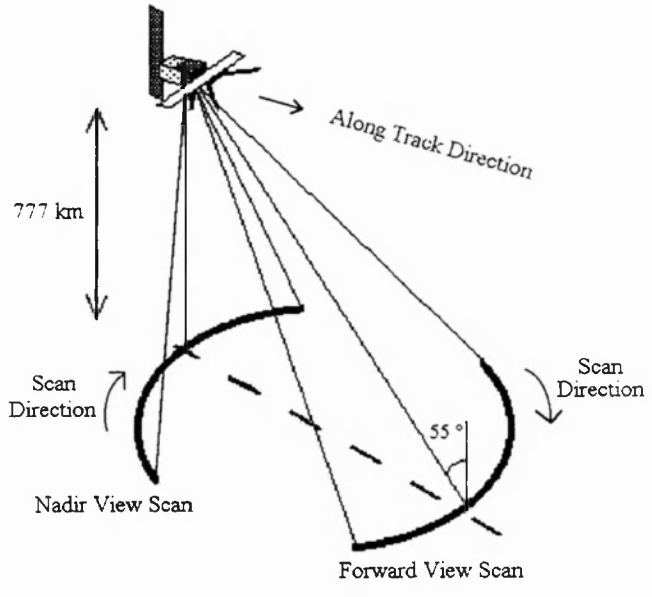

Figure 6.1. The viewing geometry of the ATSR sensor, mounted onboard the orbiting ERS satellite. Nadir-view pixels have zenith angles 0° (scan centre) - 22 ° (scan edge), the forward-view pixels have zenith angles 55 ° (scan centre) - 52 ° (scan edge). The satellite takes 137 seconds to traverse the distance between the two views.

6.3. Detail of the ATSR observation process

The instantaneous field-of-view (IFOV) of the ATSR sensor is 0.074 ° and each pixel is constructed by integration of the signal retrieved from within the IFOV over a 75 μsec period. During this integration period rotation of the instrument scan mirror causes the projection of the IFOV to just clear itself, resulting in a pixel response function profile that is an equilateral triangle. Figure 6.2 (a) illustrates the one dimensional situation for the pixels at the sub-satellite point (centre of the nadir-view scan), where the IFOV projection equates to a 1 km distance on the ground. Since each integration period is continuous with the previous, the response functions of neighbouring along-scan pixels overlap by 50% in that direction (Figure 6.2 [b]). Unless it lies exactly at a pixel centre, ground locations lying near the sub-satellite point will contribute to the signal of two neighbouring along-scan pixels, but the response function profiles of Figure 6.2 (b) indicate that any such point is always observed with a cumulative view time of 75 μsec, equating to a 100% pixel responsivity maximum if signals from all the affected pixels are considered. Pixels at the sub-satellite point have an along-track width of 1 km and, since the ERS satellite traverses a 1 km distance during complete rotation of the scan mirror, there is no along-track overlap for the nadir-view pixels at the sub-satellite point (Prata *et al.*, 1990).

Because of the large forward-view zenith angle, Prata *et al.* (1990) shows that the ATSR forward-view pixels are around 3 - 4 times larger than the corresponding nadir-view pixels. At the centre of the forward-view scan, there is a three pixel overlap in the along-track direction, in addition to the half-height along-scan overlap already described. This causes the cumulative view time for any observed ground location to be the equivalent of 3 integration periods (225 μsec). Away from the sub-satellite track ATSR

pixels get rotated with respect to the along- and across-track directions and this changes the nature of the pixel overlap around the scan (Prata *et al.*, 1990). However, Godsalve (1995) indicates that, to a first order approximation, the cumulative view time for a ground location imaged anywhere within the forward-view scan is constant at the equivalent of 3 integration periods. Similarly, for ground locations imaged anywhere in the nadir-view scan the cumulative view time is always equivalent to that of a single integration period.

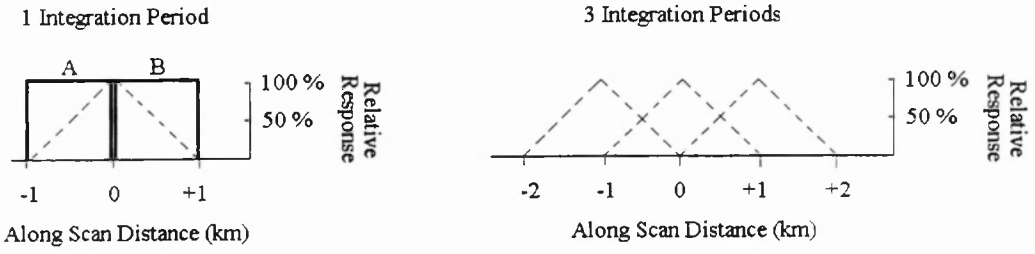

(a) *(b)*

Figure 6.2. (a) During a single 75 μsec integration period the projection of the ATSR IFOV (——) advances from A to B, a distance of 1 km at the sub-satellite point. The resulting pixel has a triangular response function (----) with a 2.0 km base and a 1 km half-width. (b) The response functions for 3 consecutive along-scan pixels. Pixels overlap at the half-height (50%) response level. Any ground location is observed in two neighbouring along-scan pixels unless it is located exactly at the pixel centre (100% response point).

6.4. Observations of volcanic hotspots at low-spatial resolution

For observations made at shortwave infrared wavelengths, negligable radiance is emitted from ambient temperature surfaces. Nighttime observations eliminate solar reflected radiation and, in such a situation, the spectral radiance (R_λ) retrieved for an ATSR or MODIS pixel containing a subpixel sized hotspot is given by :

$$R_i = \tau_i \varepsilon_i (\frac{A_h}{A}) L_i(T_h) \quad (6.1)$$

Where i is the waveband of interest

τ_i is the atmospheric transmissivity

ε_i is the surface spectral emissivity

A is the pixel area (m^2)

A_h is the hotspot area (m^2)

$L_i(T_h)$ is the Plank function radiance at temperature T_h Kelvin ($W/m^2/sr/\mu m$)

T_h is the hotspot surface temperature (K)

If measurements are taken at middle infrared or thermal infrared wavelengths then Equation 6.1 is easily adapted to include a radiance contribution from the ambient background. As discussed in Mouginis-Mark *et al.* (1994), it is easily seen than Equation 6.1 predicts a decrease in the measured radiance as pixel size increases. The widely differing pixel sizes in the ATSR forward- and nadir-views suggest that the radiance retrieved from any subpixel hotspot will be correspondingly lower when observed in the forward-view than when observed in the nadir-view. However the effect of increased pixel area in the forward-view is counteracted by the predicted tripling of the cumulative view time, making the total radiance recorded for the hotspot comparable in both views, provided the contribution from all affected pixels is considered. Figure 6.3 illustrates this effect for shortwave infrared thermal flux data of the subpixel sized fumarolic hotspot associated with the summit lava dome of Unzen Volcano (Chapter 5). Figure 6.4 shows the time-series 1.6 μm data of Unzen collected in the nadir-view (and discussed in Chapter 5), alongside the corresponding data from the ATSR forward-view. In general, the forward-view and nadir-view data show approximately the same level and

trend in 1.6 μm signal, indicating that in such a situation thermal anomaly data from almost any part of the MODIS swath could be combined to produce a high-temporal resolution time-series.

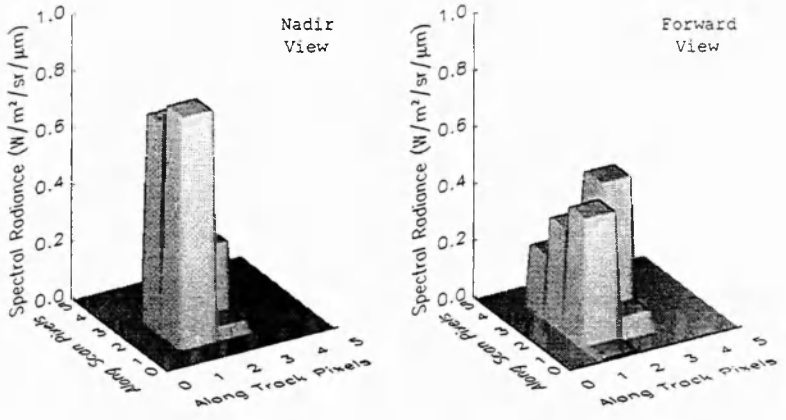

Figure 6.3. The nighttime 1.6 μm spectral radiances retrieved for Unzen Volcano, Japan at 13:10 GMT on 17 March 1993. Four pixels are radiant in the nadir-view, with total radiance 1.8 W/m²/sr/μm. Six pixels are radiant in the forward-view, with total radiance 1.6 W/m²/sr/μm. The fumarolically heated area is expected to be a relatively lambertian emitter of radiation and radiative transfer calculations indicate that differences in $\tau_{1.6}$ are likely to be less than 5% between the two views.

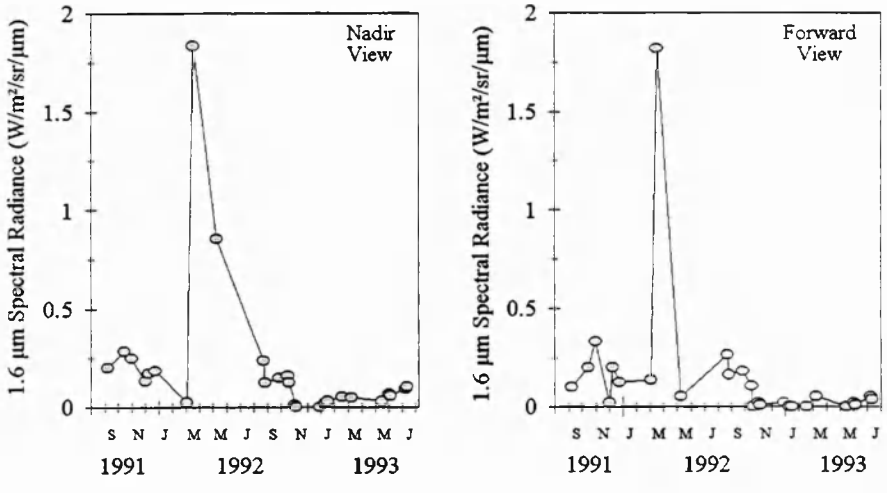

Figure 6.4. The 1.6 μm spectral radiance time-series of Unzen Volcano, obtained from totalling the signals in the ATSR forward- and nadir-views. Levels and trends in radiance are similar in both views. The notable exception is the data of May 1992, possibly because of volcanic fumes masking the signal in the forward-view.

6.6. Geometric shielding

In contrast to the summit lava dome of Unzen Volcano, the fumarolically active dome associated with Lascar Volcano is contained within a crater whose depth is significant with regard to the ATSR viewing geometry. Figure 6.5 illustrates the situation at Lascar and geometric calculations show that the dome will be partially shielded from view when :

$$\theta > \tan^{-1}\left(\frac{R_c - R_d}{D}\right) \qquad (6.2)$$

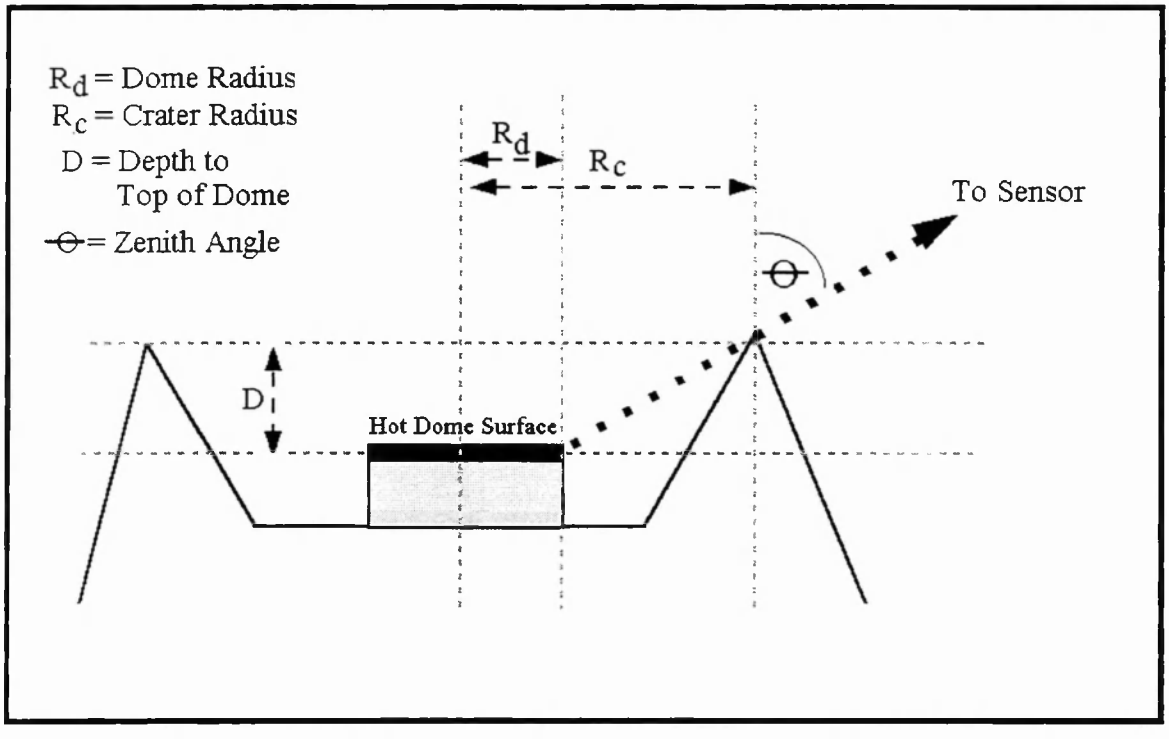

Figure 6.5. Sketch map of the lava dome contained within the summit crater of Lascar Volcano. R_C = crater radius, R_d = dome radius, θ = zenith angle. The figure is illustrative only and reflects the approximate geometry of the hot dome surface in relation to the surrounding crater walls. For simplicity I have excluded the non-active craters.

Use of Equation 6.2 with the physical dimensions of Lascar's active crater and dome (Chapter 4) indicates that geometric obscuration of the hot dome surfaces will commence at zenith angles greater than about 50°, thus affecting observations made in the ATSR forward-view. Figure 6.6 indicates the ATSR 1.6 μm time-series for Lascar and, in contrast to the un-obscured situation at Unzen, a strong radiance trend is present only in the nadir-view data (which are discussed in detail in Chapter 4), but is largely absent from data taken in the forward-view. We note that such shielding could also occur on the micro-scale if the radiance source were hot-cracks showing preferences in orientation, for example the surface of an active blocky (aa) lava flow.

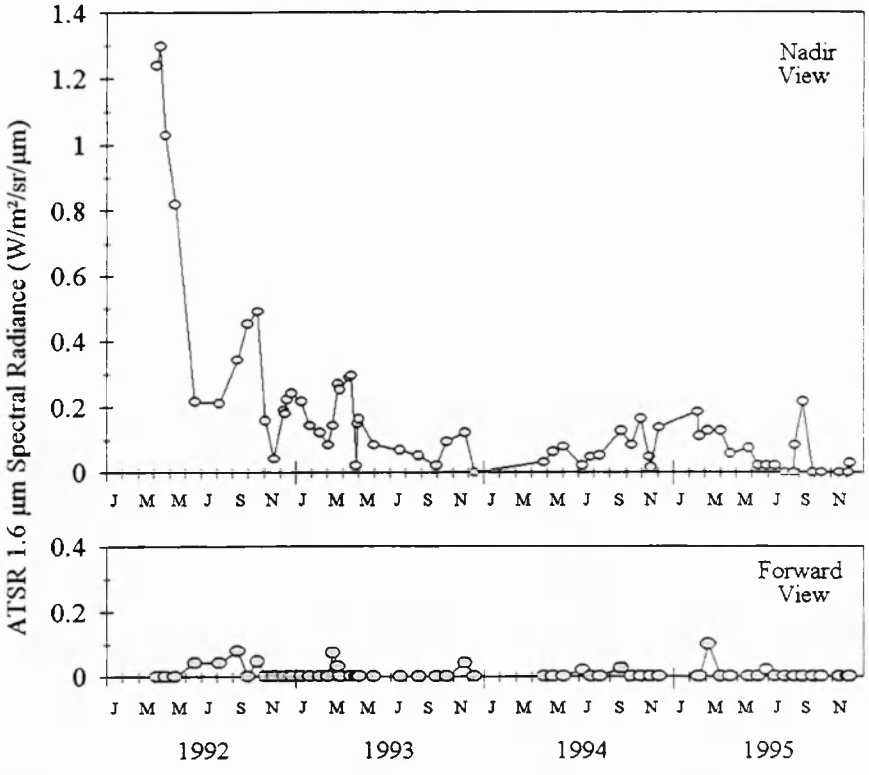

Figure 6.6. The 1.6 μm spectral radiance time-series of Lascar Volcano, obtained from ATSR forward-view and nadir-view data. Signals are negligible in the forward-view due to geometric shielding by crater walls.

6.7. Conclusions

Considerations of viewing geometry are shown to be important when observing the thermal activity within volcanic craters using low-spatial resolution sensors. Near-simultaneous ATSR forward- and nadir-view observations of the Lascar lava dome provide widely differing datasets because of geometric shielding of the thermally anomalous area by the surrounding crater walls. When using MODIS data to monitor activity within volcanic craters it is therefore unlikely that data from widely varying parts of the scan can be meaningfully compared. However a similarly sized fumarolically active lava dome, which was not contained within a crater, provides a comparable signal in both the ATSR forward and nadir views. This indicates that, in cases where geometric shielding is not a significant factor, the majority of the MODIS swath may be combined in a single time-series in order to maximise temporal coverage.

Chapter 7.

Time-series analysis of effusive volcanic activity using the ERS Along Track Scanning Radiometer : the 1995 eruption of Fernandina Volcano, Galápagos Islands.

M. J. Wooster and D. A. Rothery

Remote Sensing of Environment (1997), 62, 109-117.

7.1. Abstract

The ERS-1 Along Track Scanning Radiometer (ATSR) provides frequent shortwave and longwave infrared radiance data of every terrestrial volcanic region, at a spatial resolution of 1 km². By adopting a simplified model that assumes that any observed active lava flow is composed of two distinct thermal components, we present techniques that allow subpixel lava flow areas to be estimated from the infrared spectral radiance data obtained by ATSR. Such estimates are especially useful in documenting effusive volcanic activity occurring in remote regions, where ground observations may be sparse or lacking completely. We use a time-series ATSR dataset to document the 1995

eruption of Fernandina Volcano, an important but isolated volcanic island in the Galápagos archipelago. We estimate that the 1995 Fernandina activity generated a 6 km^2 lava flow field which involved the eruption around 20 million m^3 of magma, a similar magnitude to previously studied Fernandina eruptions. This is the first time-series analysis of an active Galápagos lava flow produced using remotely sensed data. Previous Fernandina flows have been investigated many months or years after the activity had ceased. The current and future availability of frequent, low spatial resolution infrared radiance data from spaceborne sensors such as the Advanced Along Track Scanning Radiometer (AATSR) and the Moderate Resolution Imaging Spectrometer (MODIS) should ensure that adaptations of these techniques can be used to document future volcanic eruptions occurring in similarly isolated regions.

7.2. Introduction

Infrared radiance data from Earth-orbiting satellites have long been suggested as a suitable data source for documenting remote effusive volcanic activity (Francis, 1979; Rothery *et al.*, 1988; Mouginis-Mark *et al.*, 1991). To date, the majority of investigations have been carried out using shortwave infrared radiance data collected by the Landsat Thematic Mapper (TM), which provides high levels of spatial detail but at a relatively high data cost and a low temporal frequency. A smaller number of studies have used data from the Advanced Very High Resolution Radiometer (AVHRR), but the utility of this instrument is limited since it lacks a shortwave infrared waveband. Another limitation of both TM and AVHRR data sources is that the detectors are prone to saturation over hot lava flows, restricting quantitative use of the resultant data. These limitations have

contributed to the potential of remote sensing being largely unrealised for time-series analysis of lava flow development (Rothery and Pieri, 1993).

The Along Track Scanning Radiometer (ATSR), currently operating on the European Remote Sensing Satellites ERS-1 and ERS-2, is a relatively new source of global shortwave and longwave infrared radiance data. Though it is of relatively low spatial resolution (1 km^2), ATSR provides frequent data at low cost. ATSR data have already been shown to be of value for monitoring the growth of lava domes at Lascar Volcano, Chile (Wooster and Rothery, 1997b) and Unzen Volcano, Japan (Wooster and Kaneko, in press). Here we use a time-series ATSR dataset to document the evolution of the lava flow associated with the 1995 eruption of Fernandina Volcano, Galápagos Islands. Fernandina's frequent eruptions are of great interest to volcanologists, but the remote and uninhabited nature of the island has prevented detailed investigation of previous eruptions in progress (Simkin, 1984; Munro and Mouginis-Mark, 1990). The transitory nature of the eruptive phenomena makes it imperative to use frequent, low spatial resolution measurements if adequate time-series of infrared thermal flux data are to be obtained. Here we demonstrate the utility of such data for determining characteristics of the 1995 Fernandina lava flow, and we note that the availability of such data is expected to increase with the coming launch of the Moderate Resolution Imaging Spectrometer (MODIS) on the NASA EOS-AM and EOS-PM platforms (Salomonson *et al.*, 1989) and the Advanced Along Track Scanning Radiometer (AATSR) on ENVISAT (Holdaway, 1993).

7.3. ATSR sensor characteristics

Full details of the ATSR sensor are provided in Chapters 2 and 4.3. ATSR makes spectral radiance measurements in both the longwave and shortwave infrared, with

sampling performed at 12 or 10 bit resolution depending upon the mode of instrument operation. Three longer wavebands are centered on the same wavelengths as those of the AVHRR (3.7, 11 and 12 μm), with a single shortwave infrared waveband (1.6 μm) included to allow monitoring of solar reflected radiation (Wooster, 1996). Table 7.1 indicates the spectral and dynamic range of each channel, and Figure 7.1 indicates how these fit with spectral radiant emittance over the range of natural Earth surface temperatures. Though surfaces at ambient temperatures are too cold to emit in the shortwave infrared, Figure 7.1 indicates that the ATSR 1.6 μm waveband is close to the wavelength of peak spectral radiant emittance for surfaces at magmatic and near magmatic temperatures (~ 1000 °C), making it useful for thermal studies of active lava. Studies at low spatial resolution must utilise 1.6 μm data from nighttime passes only since, during daytime observations, thermal signals at such short wavelengths are masked by solar reflected radiation.

ATSR-1 Channel	**Wavelength Range (μm)**	**Waveband Width (μm)**	**Dynamic Range ($W/m^2/sr/\mu m$)**
1.6 μm	1.57 - 1.64	0.07	0.020 - 0.53
3.7 μm	3.52 - 3.93	0.41	0.0057 - 0.98
11 μm	10.52 - 11.31	0.79	0.96 - 13
12 μm	11.47 - 12.33	0.86	1.1 - 12

Table 7.1. The four infrared channels of the ATSR-1 sensor, with wavelength range quoted at the 50% response level. Data are taken from Mason (1991).

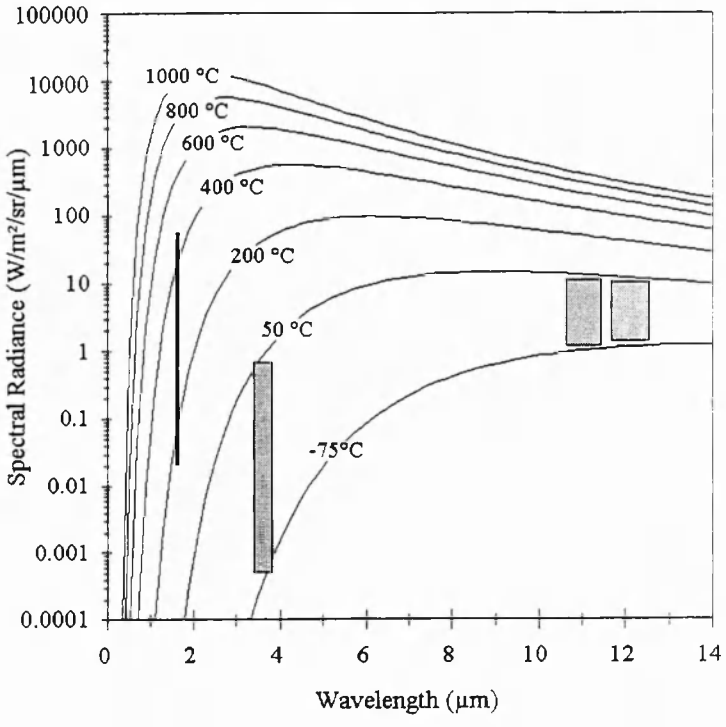

Figure 7.1. The spectral bandpasses and dynamic range of the four ATSR-1 infrared wavebands, displayed against the wavelength dependence of thermally emitted radiance according to Planck's radiation formula. The Planck curves cover the expected range of natural Earth surface temperatures (cold high clouds to recently erupted magma). The dynamic range of the AVHRR 3.7 µm channel is similar to that of the equivalent ATSR channel.

The ERS-1 ATSR (ATSR-1) uses a single preamplifier for the 1.6 µm and 3.7 µm channels, causing measurements in these two wavebands to be mutually exclusive (Tinker *et al.*, 1985). In the standard operating mode, ATSR-1 records data from the 3.7 µm channel unless the 1.6 µm signal exceeds a variable threshold, nominally set just above the 1.6 µm detector noise level of around 0.02 W/m²/sr/µm. This results in 1.6 µm data being recorded throughout daytime ERS-1 passes, but during nighttime passes only when the sensor views a surface that is hot enough to emit in the shortwave infrared. Calculations indicate that thermal emission from any active lava surface would exceed this shortwave infrared threshold and thus trigger recording of data from the 1.6 µm channel. After the

failure of the ATSR-1 3.7 μm channel in May 1992, 1.6 μm data have been recorded continuously. As outlined in Chapter 3, the ATSR-2 sensor incorporates engineering modifications that allows the simultaneous collection of both 1.6 μm and 3.7 μm data (Stricker *et al.*, 1995).

Previous AVHRR studies of subpixel sized volcanic hotspots (e.g. Mouginis-Mark *et al.*, 1994; Harris *et al.*, 1995; Harris *et al.*, 1997) have utilised 3.7 μm data since, as Figure 7.1 indicates, this wavelength is also highly sensitive to emission from hot surfaces. However, the dynamic ranges of the AVHRR and ATSR 3.7 μm channels are optimised for observations of near-ambient temperature surfaces (Figure 7.1) so that measurements of even relatively small subpixel sized hotspots are prone to saturation (Mouginis-Mark *et al.*, 1994). In contrast, the dynamic range of the ATSR 1.6 μm channel is optimised for observing high levels of solar reflected radiation, making it possible to obtain unsaturated spectral radiance measurements of nighttime thermal emission from significantly larger hotspots than is the case at 3.7 μm (Figure 7.2). Since saturation of the detectors precludes quantitative use of the 3.7 μm data, this is a major advantage of the ATSR sensor. The MODIS instrument will incorporate a low-gain 3.7 μm channel specifically to avoid saturation of 3.7 μm data over subpixel sized hotspots (Salomonson *et al.*, 1989; Ardanuy *et al.*, 1991).

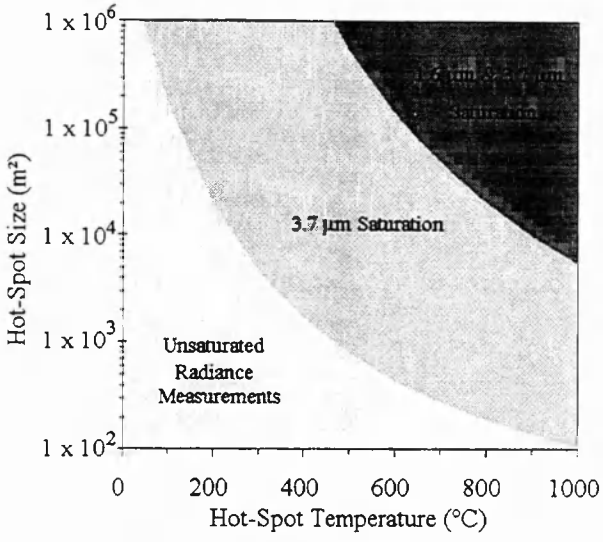

Figure 7.2. The sensor saturation envelope for observations of subpixel sized hotspots at 3.7 µm (AVHRR and ATSR-1 sensors) and 1.6 µm (ATSR-1 sensor). Observations at 1.6 µm are unsaturated over a much wider range of hotspot temperature/size combinations than observations at 3.7 µm. For this modelled example the ambient background temperature has been set to 10 °C. Increases in background temperature make 3.7 µm observations more prone to saturation (since thermal emission from the background will be increased) but will not affect the situation at 1.6 µm since this shorter wavelength is insensitive to such low temperature surfaces.

7.4. The 1995 eruption of Fernandina Volcano

Fernandina Volcano is a shield volcano in the Galápagos archipelago (Figure 7.3), having a maximum elevation of 1.5 km and possessing a large elliptical caldera almost 1 km deep and 4 km by 6.5 km across. On the evening of 25 January 1995 fishermen sailing 140 km east of Fernandina reported an ongoing eruption at the volcano. Locally-based volcanologists were able to carry out ship-board observations and ground surveys while aa lava flows were still active, these reports remaining the most comprehensive published descriptions of the activity (Smithsonian Institution, 1995a-e). The eruption is believed to have lasted for around 10 weeks duration (Smithsonian Institution, 1995d) and was initially reported to be unimaged from space due to almost continuous cloud cover in

was initially reported to be unimaged from space due to almost continuous cloud cover in the region (Smithsonian Institution, 1995a). However, examination of the 17 nighttime ATSR-1 scenes covering the relevant period indicates 8 cloud free views of the eruption, obtained on 8, 14 and 28 February, 3, 17, and 23 March, 5 and 8 April 1995. We have used these data to provide estimates of the lava flow thermal parameters, based on the levels of shortwave and longwave infrared thermal flux recorded in the affected region of Fernandina.

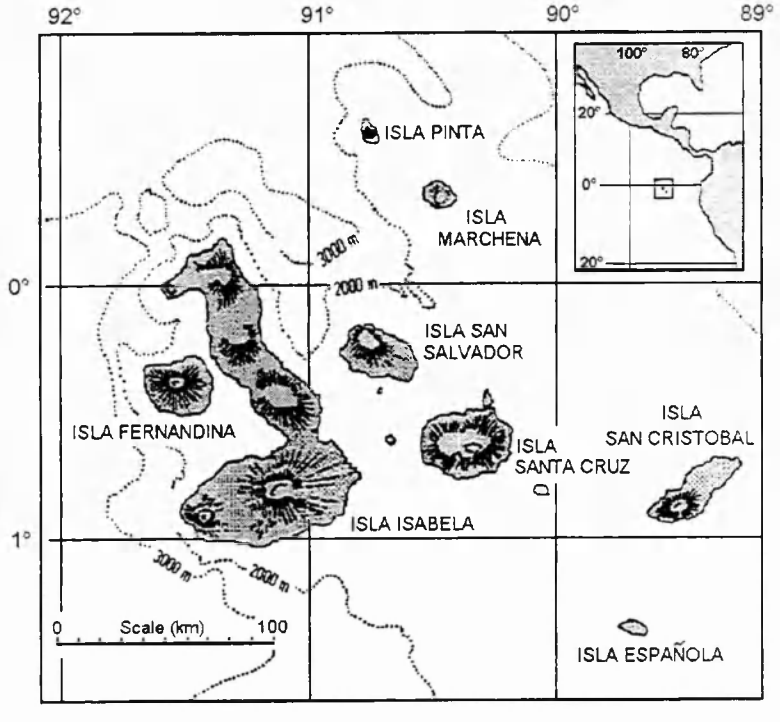

Figure 7.3. Location map of the Galápagos Islands. Isla Fernandina is a single shield volcano on the western edge of the archipelago. The map is slightly modified from that in Simkin and Howard (1970) and Rowland and Munro (1992).

7.5. Methodology: the estimation of lava flow parameters

7.5.1. A multi-component thermal model

Crisp and Baloga's (1990) lava flow model considers an active flow to be composed of two principal thermal components, namely areas of moderate temperature crust and underlying high temperature magmatic material. They assume that the majority of the active flow surface is generally comprised of the cooler crustal material, but that the hot inner core can become exposed at the surface by cracks or rifts in the crust brought about by the lava flow motion (Figure 7.4).

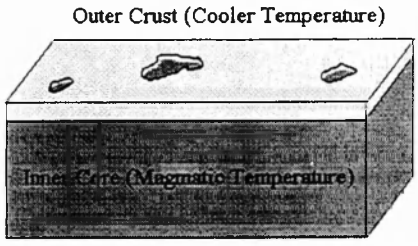

Figure 7.4. Schematic of the lava flow thermal structure propsed by Crisp and Baloga (1990). The cooler outer crust insulates a hot molten core, thus allowing the lava to continue to flow. Cracks in the crust can expose the core and thus accelerate heat loss..

Our analysis of infrared thermal flux data of the 1995 Fernandina flow follows previous high spatial resolution studies (e.g. Rothery *et al.*, 1988; Pieri *et al.* 1990; Oppenheimer, 1991; Flynn *et al.* 1994) in that assumes that real flow surfaces also conform to this dual-component thermal structure. Flynn and Mouginis-Mark (1992) used ground-based spectroradiometer measurements to validate this hypothesis on a Hawaiian pahoehoe flow field, whilst numerous observations of aa flow surfaces suggest that they do conform to a bimodal temperature distribution (e.g. Calvari *et al.*, 1994). However, when considering the radiances recorded at a 1 km² pixel, radiation from the two flow

surface thermal components must be considered alongside contributions from the atmosphere and ambient background :

$$R_i = \varepsilon_i \tau_i [P_h L_i(T_h) + P_c L_i(T_c) + P_b L_i(T_b)] + Ra_i^{\uparrow} + \tau_i (1/\pi)(1-\varepsilon_i) Ra_i \downarrow \qquad (7.1)$$

where R_i is the spectral radiance recorded in waveband i

L_i is the radiance emitted in waveband i by a blackbody at temperature T (K)

T_h, P_h are the temperature (K) and fractional area of the exposed hot core

T_C, P_C are the temperature (K) and fractional area of the cooling crust

T_b, P_b are the temperature (K) and fractional area of the ambient background

$P_b + P_h + P_c = 1$

ε_i is the spectral emissivity of the surface integrated over waveband i

τ_i is the atmospheric transmission for waveband i

$Ra_i^{\uparrow}$ is the upwelling atmospheric radiation for waveband i (W/m²/sr/μm).

$Ra_i \downarrow$ is the downwelling atmospheric radiation for waveband i (W/m²/sr/μm). (The effect of reflected downwelling atmospheric radiation can be neglected since basalt lavas have minimal reflectivities [Salisbury and D'Aira, 1992]).

For the purpose of observing high-temperature surface activity, data from the ATSR 11 μm and 12 μm channels provide almost equivalent information. We use only 11 μm data because the 12 μm channel is known to suffer from data losses at locations of very high thermal gradient (Delderfield *et al.*, 1985). The two spectral radiance measurements provided by ATSR ($R_{1.6}$ and R_{11}) are insufficient for full inversion of Equation 7.1, but previous remote sensing studies of active lava flows (e.g. Pieri *et al.*,

1990; Oppenheimer 1991; Flynn *et al.* 1994), coupled with information from lava flow models (e.g. Crisp and Baloga, 1990; Kilburn and Lopes, 1991) allow us to define a realistic range for each of the lava flow thermal parameters of the equation (Table 7.2). We combine this information with knowledge of the relationship between emitted spectral radiance and blackbody temperature for the ATSR longwave and shortwave infrared wavebands (Figure 7.4.) in order to provide a range of solutions of Equation 7.1.

	T_c	T_h	$P_h / (P_c + P_h)$
Minimum Value	70	950	1×10^{-3}
Mid-Range Value	150	1000	1×10^{-2}
Maximum Value	400	1050	1×10^{-1}

Table 7.2. The expected range of crust temperatures (T_C), exposed core temperatures (T_h) and the ratio of exposed core area to total flow area, $P_h / (P_C + P_h)$, taken from previous remote sensing studies and thermal models of active lava flows (Pieri et al., 1990; Crisp and Baloga, 1990; Kilburn and Lopes, 1991; Oppenheimer 1991; Flynn et al., 1994). The core temperature expressed here is the temperature of the internal magmatic material once it is exposed at the surface by rifting and cracking of the crust, rather than the (somewhat hotter) internal temperature of the flow.

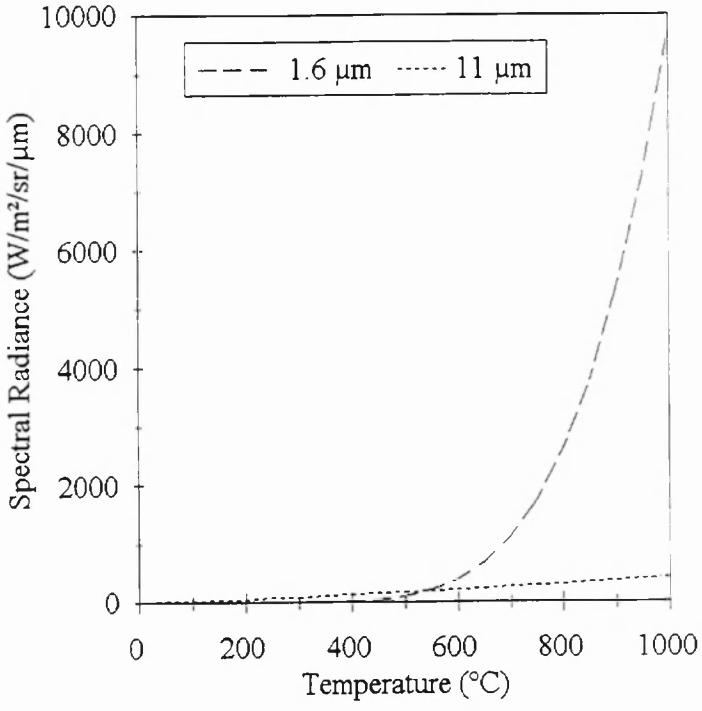

Figure 7.5. The relationship between emitted spectral radiance and surface temperature at 1.6 μm and 11 μm. At 11 μm the relationship is of shallow slope and is approximately linear over the entire temperature range. At 1.6 μm the relationship is highly non-linear, with increasing slope at higher temperatures. At 1.6 μm negligible radiance is emitted at temperatures below about 300 °C. The temperature range is that defined for active lava flows by Kilburn (1993).

7.5.2. Solutions using the longwave infrared data (11 μm)

The relative insensitivity of the 11 μm signal to changes in emitting temperature (Figure 7.4), coupled with the relatively small areas of exposed core on active lava flows (Table 7.2), ensures that the 11 μm data are dominated by radiation from the crust and ambient background surfaces. For measurements at 11 μm we can therefore simplify Equation 7.1 by assuming only two temperature components within the FOV, the crust and the ambient background. Rearrangement allows us to solve for the possible range of crust fractional areas (P_c) using the potential range of crust temperatures (T_c) listed in Table 7.2

:

$$P_c = \frac{\left(\frac{R_{11}}{\varepsilon_{11}\tau_{11}}\right) - Ra_{11}^{\uparrow} - L_{11}(T_b)}{L_{11}(T_c) - L_{11}(T_b)} \tag{7.2}$$

7.5.3. Solutions using the shortwave infrared data (1.6 μm)

Since there is no atmospheric emission at this wavelength, and by night no radiance from the ambient background (Figure 7.5), simplification and rearrangement of Equation 7.1 provides a range of exposed core fractions (P_h) based on the potential range of exposed core temperatures (T_h). The relatively minor shortwave infrared contribution from the crust is estimated using the (P_C,T_C) solutions of Equation 7.2.

$$P_h = \frac{\left(\frac{R_{1.6}}{\varepsilon_{1.6}\tau_{1.6}}\right) - P_c L_{1.6}(T_c)}{L_{1.6}(T_h)} \tag{7.3}$$

7.5.4. Application to the 1995 Fernandina dataset

To provide time-series estimates of the lava flow parameters, Equations 7.2 and 7.3 were applied to all thermally anomalous pixels within the eight cloud free ATSR scenes of the eruption. For each date, the total area of crust and of exposed core was calculated by summation of the P_c and P_h values for that scene, multiplied by the nominal ground resolution element size of the ATSR pixels (A_{GRE}). Early vents of the 1995 activity occurred high up on the flanks of the volcano, requiring an alteration in the assumed pixel area (A_{GRE}) to account for the relatively high local slope of 32° - 35°. However the volume of lava erupted in this initial flow is understood to be negligible (Rowland, 1996)

and the activity is known to have switched to vents in the shallow sloping, lower regions sometime prior to 8 February 1995, the date of the first cloud-free ATSR scene (Smithsonian Institution, 1995b). The main 1995 lava flow traversed areas with slopes $< 10°$, small enough to allow a constant value of A_{GRE} to be assumed for all affected pixels.

Estimates of the ambient background temperature (T_b) were obtained from pixels neighbouring the flow-field. Values of the surface emissivity of basalt lava ($\varepsilon_{1.6}$ and ε_{11}) were taken from Salisbury and D'Aira (1992), with estimates of the atmospheric parameters calculated using the LOWTRAN 7 radiative transfer code (Kneizys *et al.*, 1988) for a standard tropical atmosphere. Error analysis indicates that solutions of Equations 7.2 and 7.3 are most sensitive to uncertainties in the longwave atmospheric transmission parameter (τ_{11}). Since Fernandina is characterised by anomalously low equatorial rainfall conditions (Simkin, 1984) values of τ_{11} and $R^{\uparrow}_{11}$ calculated for the standard tropics may therefore be significantly in error and required independent verification. Estimates of these parameters were therefore calculated on a scene-by-scene basis using the Split Window Variance Ratio technique (SWVR) of Jedlovec (1990) and Sobrino *et al.* (1994), further outlined in Appendix B. For each scene the values of τ_{11} and $R^{\uparrow}_{11}$ calculated using the SWVR technique were within 8% of those predicted by LOWTRAN 7, (τ_{11}= 0.5, and $R^{\uparrow}_{11}$ = 4.3 W/m²/sr/μm), thus confirming the assumption of a standard tropical atmosphere as valid for the Galápagos.

7.6. Results

7.6.1. Lava flow area estimates

The first cloud-free (nighttime) ATSR data of the eruption were recorded on 8 February 1995. Figure 7.5 shows the 11 μm thermal radiance from the active lava area, superimposed on a map of Fernandina showing eruptive fissure distribution and orientation. These data indicate that the 1995 activity was confined to the southwest quadrant of the island, a region previously shown to be crossed by a number of radial fissures (Munro and Mouginis-Mark, 1990). The ATSR data immediately disprove initial reports that the eruption vent was only 2 km from the shoreline, but are consistent with rival reports of an approximately 5 km long lava flow entering the sea along a wide (~ 800 m) flow front (Smithsonian Institution, 1995a).

The results of applying Equations 7.2 and 7.3 to estimate the area of active crust and exposed core in each of the 8 cloud-free scenes of the eruption are shown as Figures 7.6 and 7.7. As the eruption progresses, the estimated area of still-active crust is seen to fall as the cooling of non-active parts of the lava surface proceeds. Furthermore, the area of exposed core is seen to diminish exponentially as the crustal surface cools and thickens, becoming less susceptible to cracking and rifting.

Our methodology estimates the maximum active area of the lava flow to be 0.4 km^2 - 5 km^2, 20 days after the start of activity (Figure 7.6). We suggest that the upper estimate is more reasonable since it assumes the crust temperature predicted to exist a few days to weeks after lava emplacement (Flynn *et al.*, 1994). Extrapolating best-fit polynomials to these data, we obtain a maximum estimate of the active area of the flow as 0.5 km^2 - 6 km^2.

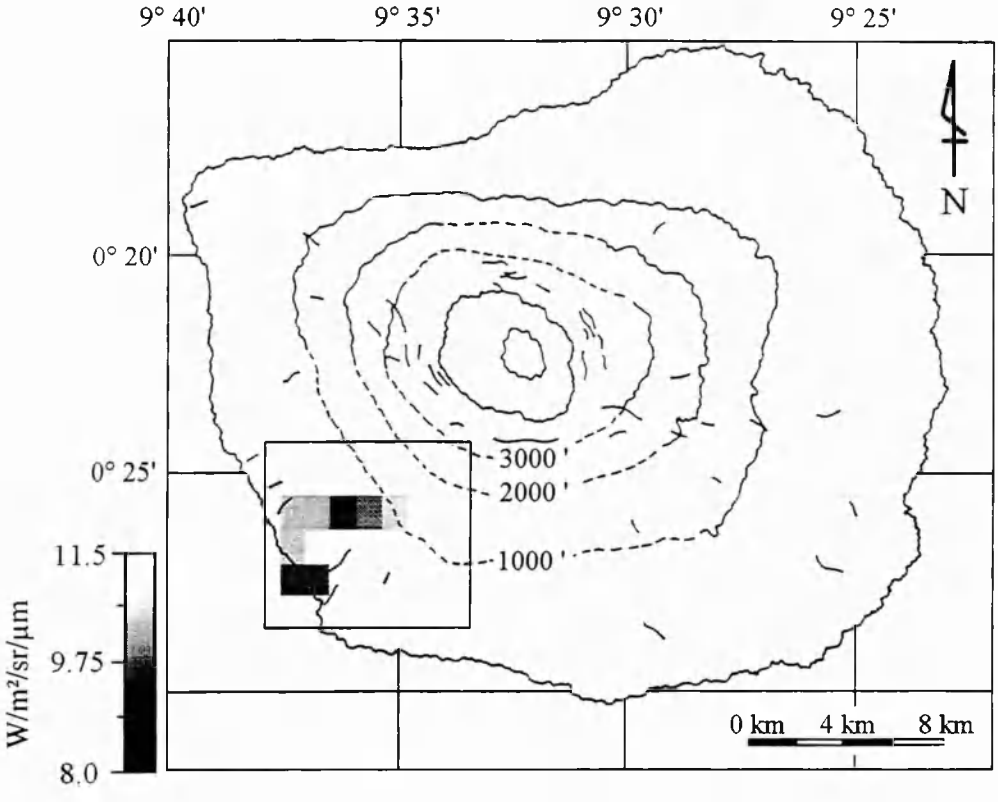

Figure 7.6. The first nighttime, cloud free ATSR 11 µm spectral radiance data of the 1995 Fernandina eruption, recorded on 8 February 1995. The data have been masked to show flow-field pixels only and have the eruptive fissure map of Munro and Mouginis-Mark (1990) superimposed. Solid contours are from stereographic analysis of large format camera images (McBirney and Williams, 1969), dashed contours are approximate and based on interpretations by Munro and Mouginis-Mark (1990). The area affected by the 1995 lava flow is box outlined for later reference. Data were geo-referenced using the latitude/longitude grid provided in the ATSR data product file (Bailey, 1994)

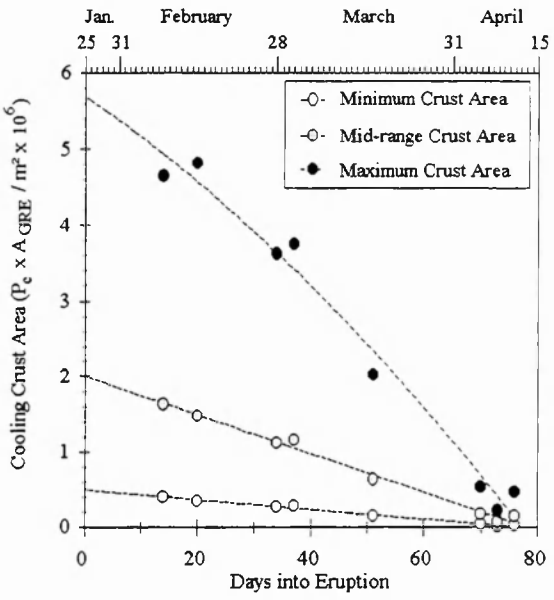

Figure 7.7. The area of cooling lava crust derived from the eight nighttime, cloud-free ATSR scenes of the 1995 Fernandina eruption, showing the minimum and maximum values permitted by solution of (2) with the range of crust temperatures (T_C) shown in Table 7.2. The best-fit polynomials to the data are also shown.

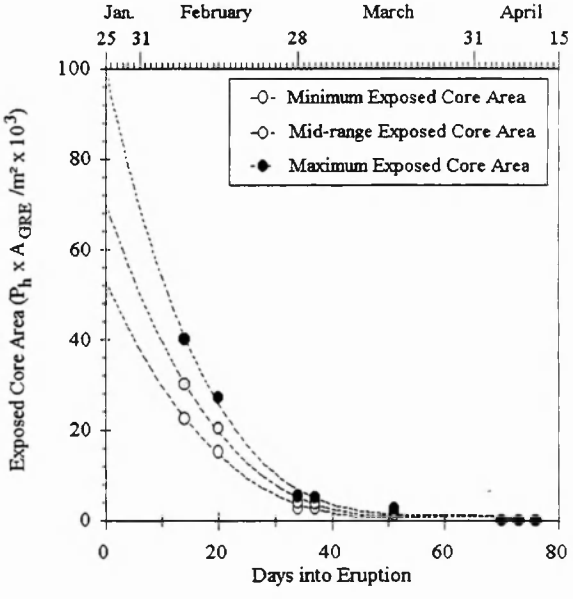

Figure 7.8. The area of exposed hot core derived from the eight nighttime, cloud-free ATSR scenes of the 1995 Fernandina eruption, showing the minimum and maximum values permitted by solution of Equations 7.2 and 7.3 with the range of crust temperatures (T_C) and exposed core temperatures (T_h) shown in Table 7.2. The best-fit polynomials to the data are also shown.

The Smithsonian Institution (1995a and 1995e) provide a map of the 1995 Fernandina flow field, produced using a number of GPS survey points. These GPS data suggest an area of 5 km^2 for the main lava flow, with an inexact area estimate of < 1 km^2 for the initial flow on the upper slopes that ceased shortly after the start of the eruption. We have mapped the extent of the post-eruption lava using panchromatic (10 m spatial resolution) and multi-spectral (20 m spatial resolution) imagery from the HRV sensor of the SPOT satellite. Comparison of pre- and post-flow SPOT scenes, recorded on 25 October 1988 and 6 July 1995, provide a total flow area of 8.2 km^2, with the area of the main flow estimated at 7.4 $km^2 \pm 5\%$. The uncertainty stems from sites where the 1995 lavas have traversed other relatively recent lava deposits, making the exact boundaries of the 1995 flow difficult to determine. Both the GPS survey and our SPOT-derived area estimates of the main 1995 flow are within 25% of the upper estimate produced using the low spatial resolution ATSR data, despite the broad assumptions made regarding the lava flow thermal structure. Multiplying the upper area estimate by the estimated mean flow depth of 3 m (Smithsonian Institution, 1995a) provides a flow volume of 2×10^7 m^3, equivalent to the mean volume of previously mapped young extracaldera flows in this region of the volcano (Rowland, 1996).

7.6.2. Flow field morphology variation

Figure 7.8 indicates how the geographical distribution and level of emitted infrared thermal flux varied throughout the eruption. These data provide evidence of gross morphological changes in the lava flow field. The data of 8 February 1995 show evidence for the presence of an open channel of lava, in that the levels of recorded 1.6 μm spectral radiance were greater than 35 $W/m^2/sr/\mu m$ in the six most radiant pixels occupying a line from vent to coast. Calculations using Equation 7.3 indicate that these levels equate to the

presence of magmatic temperature material over a 5 - 10 m wide channel for the whole of the 5 km distance. These dimensions match those given for the lava 'river' briefly described in field observations of this period (Smithsonian Institution, 1995a). The 8 February data also indicate that detectable levels of shortwave infrared thermal flux were being observed higher up the slopes of the volcano than was the case for later ATSR scenes, possibly evidence of the initial flow that was active on the higher flanks of the volcano.

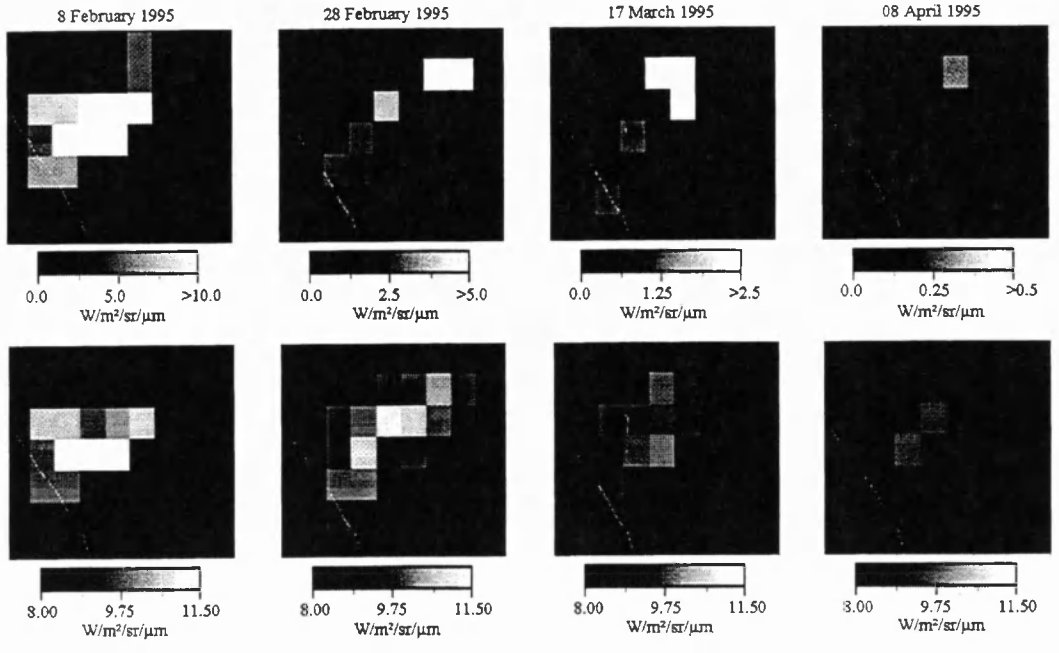

Figure 7.9. The nighttime ATSR 1.6 µm (upper row) and 11 µm (lower row) data, recorded on four dates during the 1995 Fernandina eruption. The data have been masked to show flow-field pixels only and have the coastline of Isla Fernandina superimposed. The geographical area covered by these data is that box outlined in Figure 7.5. Note the varying radiance scale used to display the 1.6 µm data.

Results shown in Figure 7.7 suggest that between 14 and 28 February 1995 there was a major decrease in the amount of surface material at magmatic temperatures. Ground observers also reported a change in character at this time, with the main lava channel

becoming blocked and smaller flow lobes developing (Smithsonian Institution, 1995a). The data of 28 February (Figure 7. 8) indicate that the number of thermally anomalous 11 μm pixels is greater than the number showing significant levels of shortwave infrared spectral radiance. This is presumably related to the rapid cooling of certain of the smaller flow lobes to temperatures too low to emit at shorter wavelengths, and the sealing of any cracks in them so that the hot inner core was no longer observed.

On 17 March the line of radiant 1.6 μm pixels extending from vent to coast, previously unbroken, appears fragmented. This indicates that lava tubes, reported in post-eruption field surveys (Smithsonian Institution, 1995e), had probably begun to form by this time. A large number of pixels still showed 11 μm anomalies, outlining the area of the still-cooling flow surface. The data of early April indicate that significant levels of shortwave infrared thermal flux existed only at the vent and near the ocean entry, further evidence of a substantial lava tube system.

The outputs of Equations 7.2 and 7.3 were used to calculate the ratio of exposed core area to crust area (Figure 7.9). This ratio falls to zero for data recorded on 8 April 1995 (day 74), indicating the termination of lava supply and the end of lava flow motion as defined by Crisp and Baloga (1990). We can therefore confirm the Smithsonian Institution (1995d) report that eruptive activity had ceased by 8 April 1995 and we note that calculated values of this exposed core/crust ratio consistently lay within the range predicted by the Crisp and Baloga (1990) lava flow model.

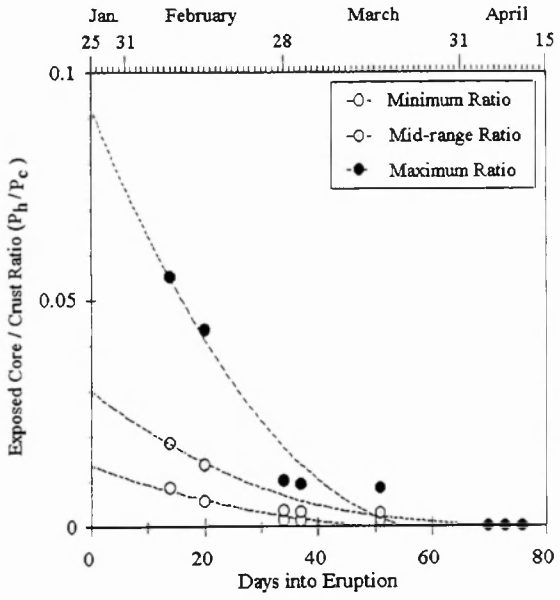

Figure 7.10. The ratio of exposed core to cooling crust for the eight nighttime, cloud-free ATSR scenes of the Fernandina eruption. The best-fit polynomials to the data are shown.

7.7. Conclusion

This study has indicated that ATSR can provide remotely sensed infrared data at a temporal frequency that is sufficiently high to enable monitoring of lava flow development. Although the spatial resolution of the observations is relatively poor (1 km^2), the wavelength characteristics are such that the spectral radiance measurements at 1.6 μm and 11 μm are unsaturated and can be used to estimate subpixel characteristics of the lava flow's thermal components. Though dependent upon the accuracy and validity of the dual thermal component lava flow model, this subpixel information can be used to estimate the approximate surface area of the active flow and, if information on likely mean flow depth is available, the total lava flow volume.

Previous Fernandina lava flows have been investigated many months (or years) after the activity has ceased. This is the first time-series analysis of an active Galápagos

lava flow produced using remotely-sensed data. The inferred structure of the 1995 flow and the values of flow area agree with the limited field observations made of this isolated volcanic eruption and also with estimates produced from post-eruption SPOT HRV imagery. We confirm the cessation date of the 1995 eruption as lying between 5 and 8 April 1995.

We suggest that low-spatial resolution sensors working simultaneously in the shortwave and longwave infrared can in future be used to provide estimates of eruption parameters for unmonitored or isolated effusive eruptions such as those occurring in the Galápagos Archipelago. Such estimates are approximations and contain implicit uncertainties due to the assumptions made about the temperature structure of the lava flow surface. We expect such uncertainties to decrease with the launch of the MODIS sensor since this instrument possesses an increased number of infrared wavebands (Salomonson *et al.*, 1989) and will observe at a temporal frequency even greater than that of ATSR (Mouginis-Mark *et al.*, 1991b).

Chapter 8.

Further validation of methods used to analyse ATSR infrared radiance data of active lava flows

8.1. Introduction

The methods used to analyse ATSR data of the lava flow associated with the 1995 eruption of Fernandina (Chapter 7) include techniques that provide areal estimates from analysis of the infrared thermal flux data. To further demonstrate and validate these methods I now apply them to (i) simulated ATSR observations of a modelled lava flow surface, and (ii) real ATSR observations of the 1991 - 1993 Mount Etna flow for which near-contemporaneous high spatial resolution observations are available. In both these situations the 'true' area of the flow is known and these studies therefore provide a useful additional method of validating the developed techniques.

8.2. Studies using simulated ATSR infrared radiance data

8.2.1. Introduction

One method of validating techniques used to retrieve estimates of Earth surface parameters from remotely sensed data is to simulate such data for a particular surface structure and then apply retrieval techniques in an effort to recover the original surface parameters. The closeness of the retrievals to the original parameters provides a method of accuracy assessment. This methodology was first used with ATSR data by Fletcher *et al.* (1995) in order to study the accuracy of subpixel surface reflectance retrievals.

Here I couple a simulated lava flow temperature surface to a model of the ATSR observation process, thus simulating ATSR infrared thermal flux observations of the flow. Estimates of the flow surface thermal component surface areas are then retrieved by applying the analytical techniques described in Sections 7.5.2 and 7.5.3 to these simulated data. These estimates can then be compared with the true parameter values contained within the original surface temperature model.

8.2.2. The temperature surface of an active lava flow

Figure 8.1 shows a simulated temperature surface for an active lava flow of length 2 km and width 100 - 400 m. The surface was created by defining the flow outline and a number of spot temperatures, and interpolating at a ground-equivalent spatial resolution of 5 m. The spot temperatures were taken from representative values published in Pieri *et al.* (1990), Crisp and Baloga (1990) and Flynn *et al.* (1994). The temperature surface has representations of cracks, fissures, open channels and skylights which expose the internal magmatic temperature (950 - 1050 °C) material. The crust temperature rises to a maximum near certain of these features but decreases rapidly with distance, reaching a minimum at the flow margins.

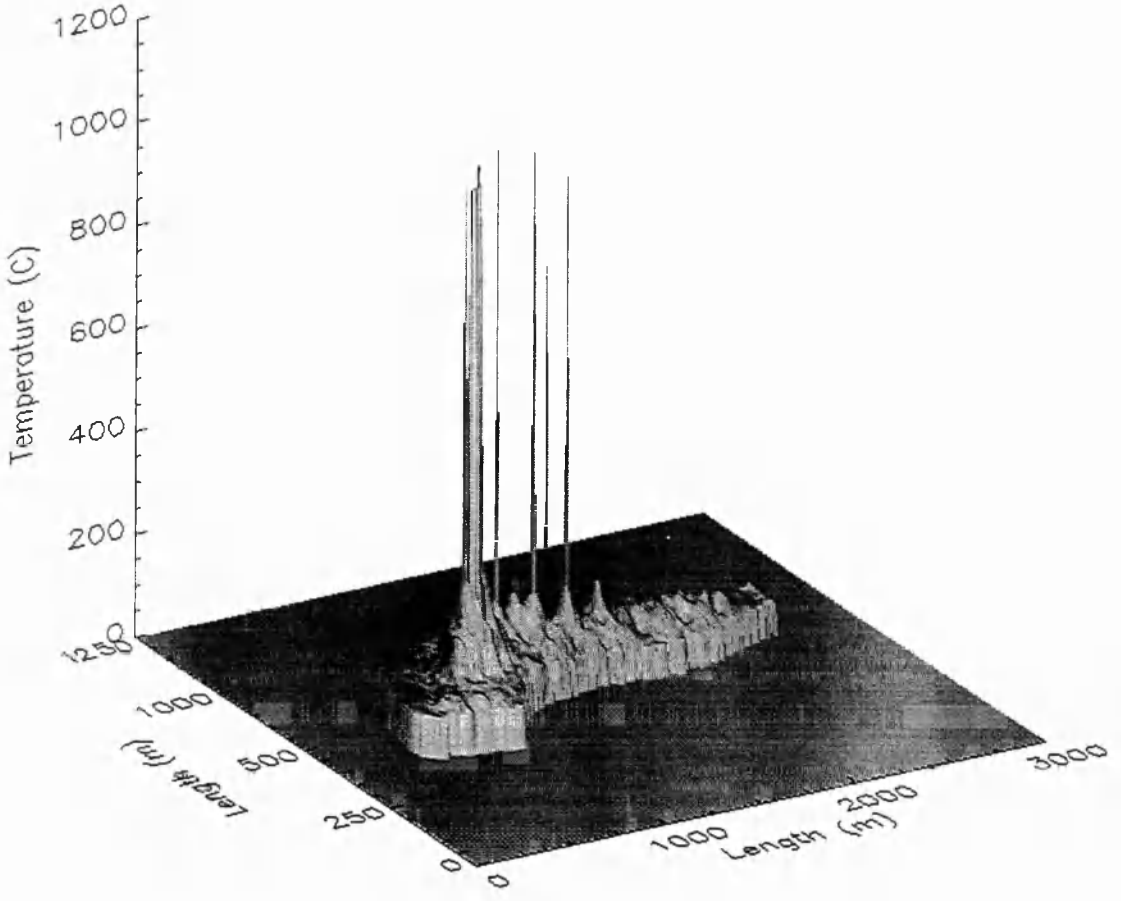

Figure 8.1. A modelled representation of the surface temperature of an active lava flow. The simulated surface is comprised of representations of cooling solidified crust and cracks, fissures and skylights that expose higher temperature (molten) material.

8.2.3. Modelling the ATSR observation process

As explained in Chapter 2, ATSR's Earth surface observations are implemented by rotation of the internal scan mirror. This rotation causes the projection of the IFOV to be swept around the scan cone on the surface of the Earth (Figure 8.2). Each ATSR ground pixel, or ground resolution element (GRE), is thus the autocorrelation of the IFOV as it is swept around the scan during the 75 μsec integration period. At the nadir point the projection of the IFOV is a 1 km x 1 km square and the 75 μsec integration period equates to a travel distance of 1 km in the along scan direction. Mason (1991) shows how the

ATSR scan geometry forms a 2 km x 1 km rectangular GRE at the center of the nadir-view and a hexagonal GRE of similar area at the edge of the nadir-view (Figure 8.2). GREs at intermediate locations have shapes between these two extremes and GREs from the forward-view show similar shape variations but are significantly larger in area (Mason, 1991). Here I concentrate on nadir-view observations since they are of a significantly higher spatial resolution and so are the most useful for the study of active lavas.

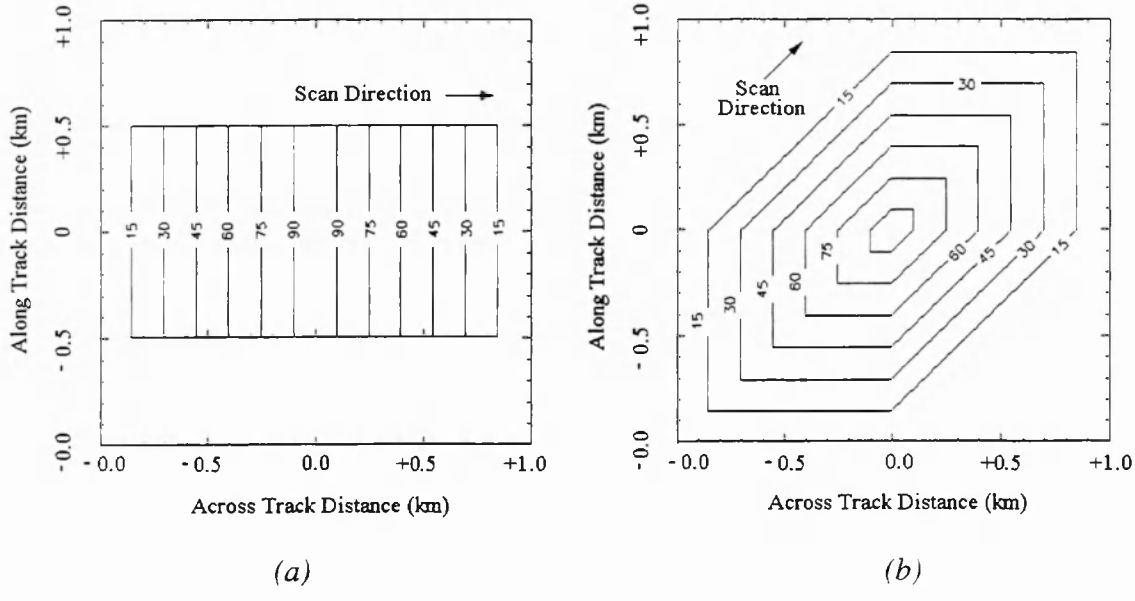

Figure 8.2. The ground resolution elements (GREs) formed by the projection of the ATSR IFOV being scanned across the Earth's surface. (a) shows the GRE at the center of nadir-view scan and (b) the GRE at the edge of nadir-view scan. The contours show the time that each surface location is viewed for, as a percentage of the 75 μsec integration period. A 15% cut off has been chosen for illustrative purposes.

In accordance with the autocorrelation function, different locations within the GRE are viewed for differing proportions of the 75 μsec integration period, as indicated by the contouring of the GREs in Figure 8.2. The time for which any particular ground site is viewed can be considered a function of (i) the number of GREs containing that site, and (ii) the location of the site within each of the GREs. The number of GREs affected by a

particular ground location is determined by the GRE overlap, which varies around the scan as outlined in Chapter 6.3. Since the scan mirror makes one complete rotation in the time the satellite takes to travel 1 km in the along track direction, the GREs at the center of the nadir-view do not overlap at all in this direction. However, at the edge of the nadir-view the GREs extend around 2 km in the along track direction (Figure 8.2) and so significant along-track overlap occurs at these edge of scan measurements. This situation is different for the along-scan direction and, since there is no 'dead-time' between pixel integration periods, all GREs overlap their along-scan neighbours by 50%, as described in Section 6.3.

Godsalve (1995) analysed the along-track and along-scan GRE overlaps in further detail and studied the overall tileing of the GREs onto the Earth surface. With respect to this process, Prata *et al.* (1990) show that the effects of Earth rotation are exactly compensated for by the 'yaw steering' of the ERS satellite, with Godsalve's (1995) research showing that, to a first order approximation, any particular point imaged during the nadir-view scan is observed for an amount of time equivalent to a single integration period of 75 μsec. This cumulative view time will be split unequally between one and up to four nadir-view GREs, depending on the exact location of the point within the scan. Again, Section 6.3 describes the particular situation for pixels at the sub-satellite point.

8.2.4. Simulating the ATSR spectral radiance measurements

The ATSR observations of the flow surface were simulated by first using the Planck function to convert the temperature map of Figure 8.1 into surfaces representing the spectral radiance emitted at 1.6 and 11 μm. The GREs of Figure 8.2 were then produced at a matching ground-equivalent spatial resolution of 5 m and convolved with the radiance surfaces to produce the simulated ATSR spectral radiance observations.

In order to produce a complete set of simulated radiance observations for each channel, the location of the GREs with respect to the flow must be varied according to the GRE recticulation process described by Godsalve (1995). Following Fletcher *et al.* (1995)

this process was simulated by relocating the GRE at the appropriate along-track and along-scan location prior to each convolution (Figure 8.3). This process was repeated until all GRE locations covering the lava flow surface had been sampled.

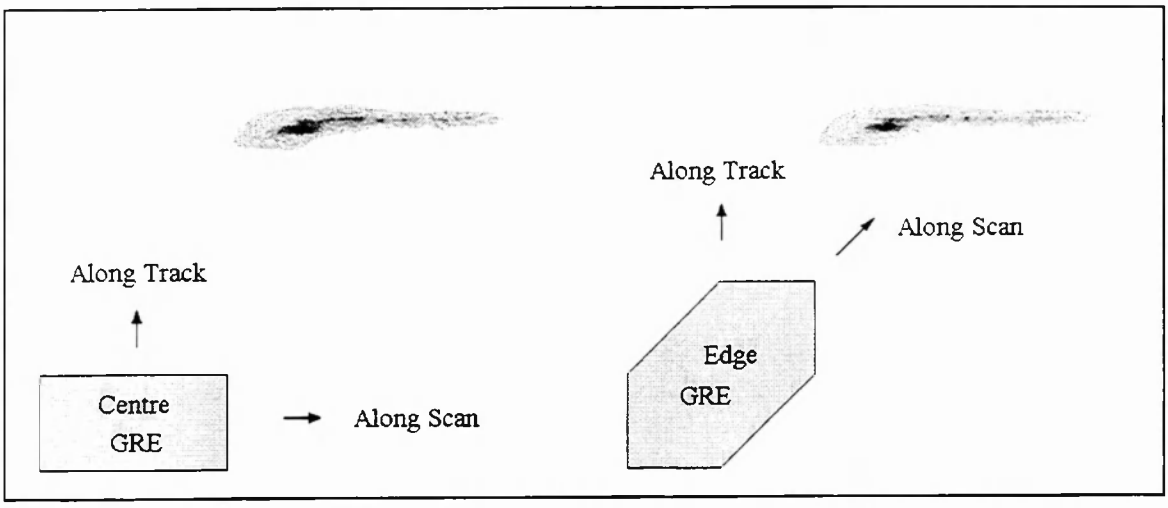

Figure 8.3. The GRE shape and appropriate along-track and along-scan directions for (a) the center, and (b) the edge of the nadir-view scan, shown in relation to the simulated lava flow surface.

The simulated ATSR observations are shown in Figure 8.4 and these indicate that different observations are obtained when the simulation is performed at the two limiting nadir-view locations, i.e. the center and edge of the scan. The differences are a result of the varying GRE shape and overlap at the two locations. In the case illustrated, at the center of the nadir-view scan the GREs affected by radiance from the flow all lie within a single scan line. In contrast, at the edge of the nadir-view scan the along-track GRE overlap causes pixels from two scan lines to be affected, however the maximum level of the recorded radiance is reduced in each channel (Figure 8.4).

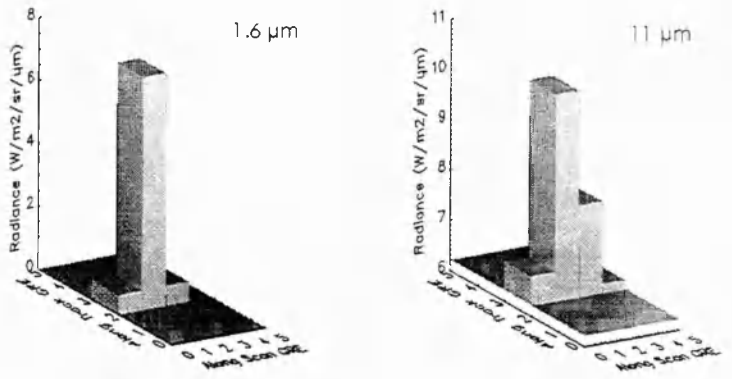

(a) Centre of nadir-view

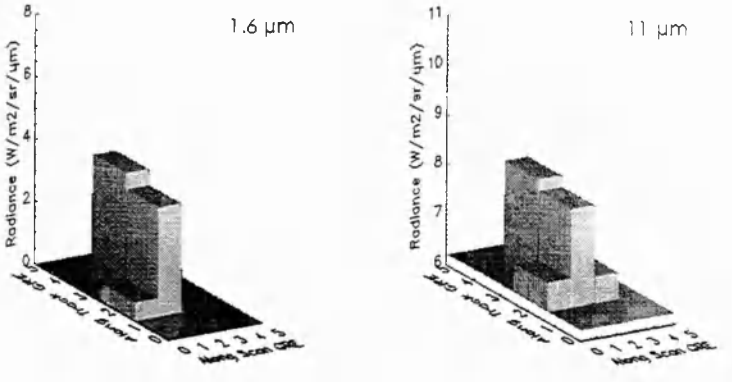

(b) Edge of nadir-view

Figure 8.4. The simulated ATSR observations of 1.6 and 11 μm spectral radiance for the temperature surface shown in Figure 8.1. The upper row shows simulated observations when the lava flow is at the center of the nadir-view scan, whilst the lower row shows the simulated observations obtained when the flow is imaged at the edge of the nadir-view scan.

8.2.5. Retrieval of the original flow parameters

Equations 7.2 and 7.3 were applied to the simulated data of Figure 8.4 in order to attempt retrieval of the original lava flow parameters, namely the area of the crust and exposed core. A transparent atmosphere and unitary emissivity were assumed in the original simulation, so these parameters were appropriately set in the retrieval equations.

The equations were applied using the range of assumed temperatures listed in Table 7.2. Results for the retrievals are shown in Table 8.1.

		Area Retrieved Using ATSR Simulation		
	'True' Areal Extent	**Minimum Estimate**	**Mid-Range Estimate**	**Maximum Estimate**
Crust (m^2)	3.9×10^5	5.6×10^4 (400 °C)	2.2×10^5 (150 °C)	5.8×10^5 (70 °C)
Exposed Core (m^2)	7.8×10^2	6.0×10^2 (1050 °C)	8.8×10^2 (1000 °C)	1.2×10^3 (950 °C)

Table 8.1. The actual parameters of the modelled lava flow surface, along with the range of estimates produced using the simulated ATSR infrared radiance data. The assumed temperatures are shown bracketed. The retrievals are summed over all affected GREs, making the results identical for observations at the center or the edge of the nadir-view scan.

Since the center and edge of scan ATSR observations are different, as illustrated in Figure 8.4, the corresponding estimates made for the areas of crust and exposed core within each affected GRE also vary. However, as in the real ATSR scan and measurement process, the simulation ensures that each location on the simulated temperature surface is 'observed' for the same total view time. Thus, as the results tabulated in Table 8.1 show, when the area estimates of crust and exposed core are summed over all affected GREs the cumulative values of these parameters are identical. This result assumes that the lava flow surfaces are not sufficiently rough to be self-obscuring at any of the viewing geometries used, though Pieri *et al.* (1990) suggest that this will be the case for most lavas.

The range of areal estimates listed in Table 8.1 correctly bound the actual parameters of the flow surface, suggesting the validity of the retreival methodology. However, as noted in Chapter 7, the crust area estimates vary by an order of magnitude

due to the wide range of potential crustal temperatures we consider during analysis (Table 7.2). When analysing real ATSR data from an eruption that has been progressing for a number of days, it is likely that majority of the active crust will lie towards the lower end of this temperature range (Flynn and Mouginis-Mark, 1992; Flynn *et al.*, 1994). If this can be confirmed then the estimated crust area (P_c) provided by Equation 7.2 may be constrained more tightly by lowering the range of crust temperatures considered.

8.3. ATSR and Landsat TM comparison study

8.3.1. Introduction

As detailed further in Chapter 9, the December 1991 - March 1993 eruption of Mount Etna (Sicily) was a long duration effusive eruption that formed an aa lava flow field covering 7.6 km². The activity was well studied on the ground and was separated into five distinct phases of activity by Calvari *et al.* (1994). Figure 8.5 shows a map of the 1991 - 1993 lava flow field, which was mainly contained within the Valle del Bove on the eastern flank of the volcano. As Pieri *et al.* (1995) report, the long duration of the eruption allowed an unusually large number of cloud free Landsat TM scenes of the active flow to be obtained. Here I present a limited analysis of two of these TM scenes, including calculations to estimate the active lava flow area. By comparing these results to information derived from near-contemporaneous ATSR data, using the techniques detailed in Sections 7.5.2 and 7.5.3, a comparison between the information derived from the high and low spatial resolution datasets can be made.

The TM and ATSR datasets used in the cross-comparison study are detailed in Table 8.2. They cover two separate phases of the 1991 - 1993 Etna eruption, both prior to and subsequent to an attempt at impeding the advance of the flow towards the town of Zafferana Etnea (Barberi *et al.*, 1993). The location of the earthern barrier that was constructed for this purpose is shown in Figure 8.5. Though this initial attempt at halting

the progress of the flow was relatively ineffectual, later attempts at flow diversion were ultimately successful in preventing the destruction of the town.

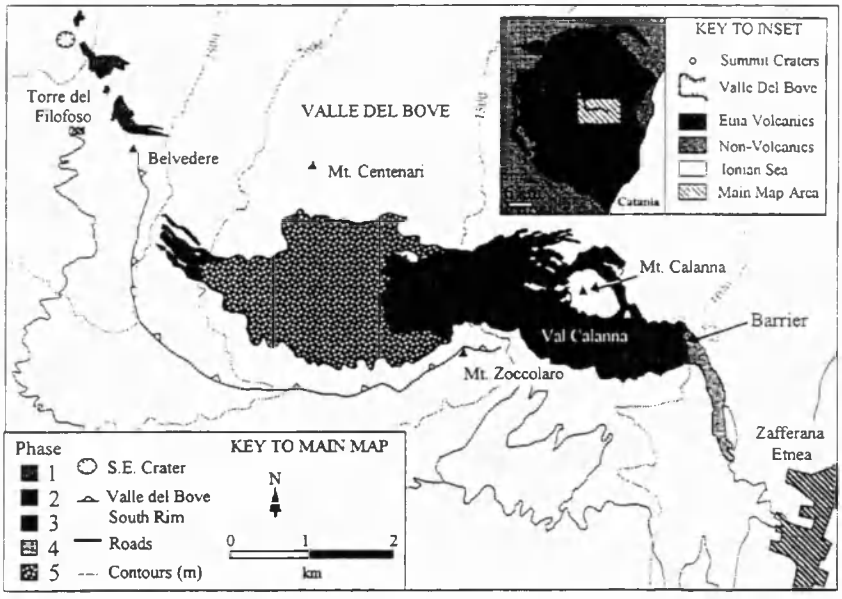

Figure 8.5. Map of the 1991 - 1993 Etna lava flow showing the lavas emplaced during each of the five eruption phases described by Calvari et al. (1994); Phase 1 (15 December 1991 - 2 January 1992), Phase 2 (3 January - 10 January 1992), Phase 3 (11 January - 7 April 1992), Phase 4 (8 April - 30 May 1992) and Phase 5 (31 May 1992 - 31 March 1993). Phase 5 lavas were emplaced in the upper flow area, covering some of the earlier phase 2 deposits. Map adapted from that in Harris et al. (1997).

Eruption Phase	**Phase 2 : Pre-Diversion (Total Flow Length 6.5 km)**			**Phase 3 : Post-Diversion (Total Flow Length 8.5 km)**		
Main activity	Open lava channel > 1 km long flowing from the erupting vent			Upper channelised flow tubed over but breakouts further down		
Sensor	ATSR	TM	ATSR	ATSR	TM	ATSR
Scene Date	31.12.91	02.01.92	03.02.92	18.03.92	22.03.92	24.03.92
Day/Night Scene	N	D	N	N	D	N

Table 8.2. Details of the six scenes used in the cross-comparison study. Each TM scene is bracketed by two ATSR scenes recorded within 54 ± 20 hrs of the TM acquisition time.

8.3.2. Visual (qualitative) comparisons

The TM band 4 (0.76 - 0.90 μm), band 5 (1.55 - 1.75 μm), band 6 (10.4 - 12.5 μm) and band 7 (2.08 - 2.35 μm) data were calibrated using the techniques outlined in EOSAT (1986) and calibration data presented in the TM header file. The data covering the Etna region were then geometrically warped to a latitude/longitude grid using nearest neighbour resampling and a 1:50000 map with 20 ground control points, the grid having a ground equivalent pixel spacing of 30 m. Figure 8.6 shows the resulting geo-referenced TM band 5 data of 2 January 1992.

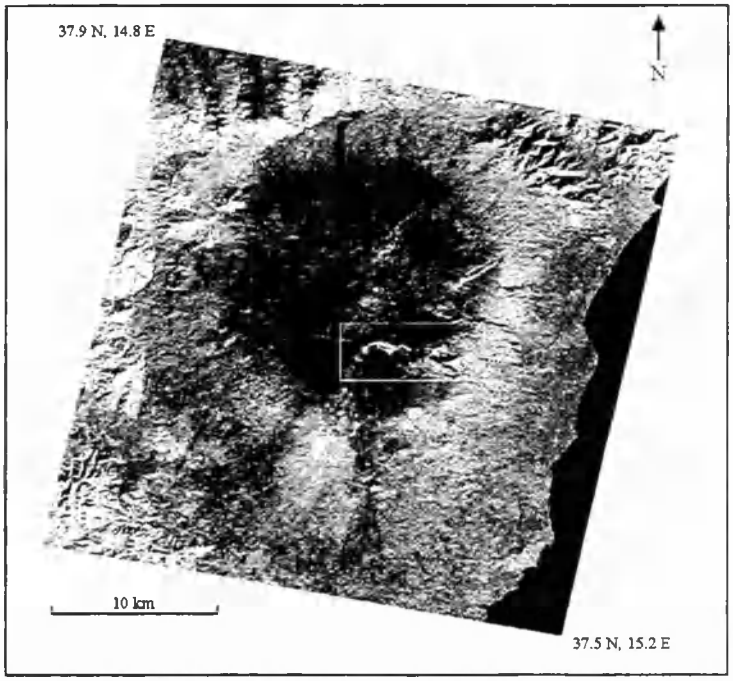

Figure 8.6. Overview of the calibrated and geo-referenced TM band 5 data of the Etna region, obtained on 2 January 1992 during phase 2 of the 1991 - 1993 eruption. Certain surfaces on the active lava flow are hot enough to be emitting significant amounts of radiation within this waveband, these showing up as highly radiant (bright) areas within the Valle del Bove of the volcano. The box outlined region corresponds to the area of the main map of Figure 8.5 and is shown in more detail in Figure 8.7.

The nadir-view ATSR data were calibrated into values of spectral radiance using the techniques outlined in Chapter 3, and were geometrically warped to the same 30 m grid as used for the TM data processing. ATSR georeferencing was performed using the

IDL routine listed in Appendix A, making use of the latitude/longitude information inherent in the BT data products. The low spatial resolution of the ATSR observations obviously resulted in large areas of the output grid having uniform pixel values since more than one thousand 30 m pixels are covered by a single ATSR nadir-view pixel. However, the geocoding to identical pixel grids allowed for easy visual comparisons between the datasets of widely differing spatial resolutions.

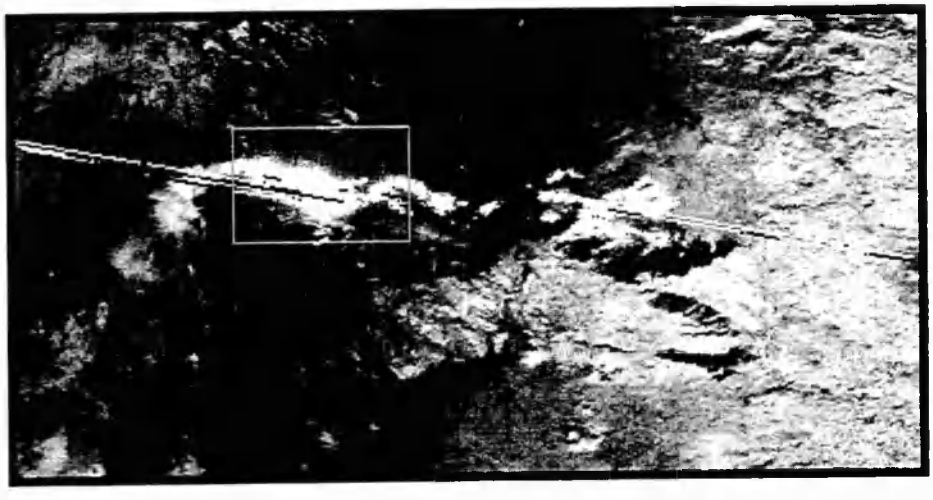

Figure 8.7. The full spatial resolution TM band 5 data corresponding to the main map area of Figure 8.5 and the area box outlined in Figure 8.6. Thermal emission from the lava flow is clearly seen within the Valle del Bove, with corrupt scan lines caused by persistent saturation of the TM sensor over the most radiant parts of the flow. The box, centred on the most radiant part of the flow, outlines the area shown in Figure 8.11.

The radiance characteristics of the active lava flow were determined in both the TM and ATSR datasets, with thresholds being set in each waveband to delineate thermally anomalous pixels. The georeferenced data from each sensor were then masked to show these thermally anomalous areas only. Figures 8.8 and 8.9 show the results of this processing for the 1.6 μm and 11 μm datasets obtained from the both TM and ATSR. Results from only a single ATSR scene for each month are shown, as the near-contemporaneous ATSR scenes show almost identical patterns.

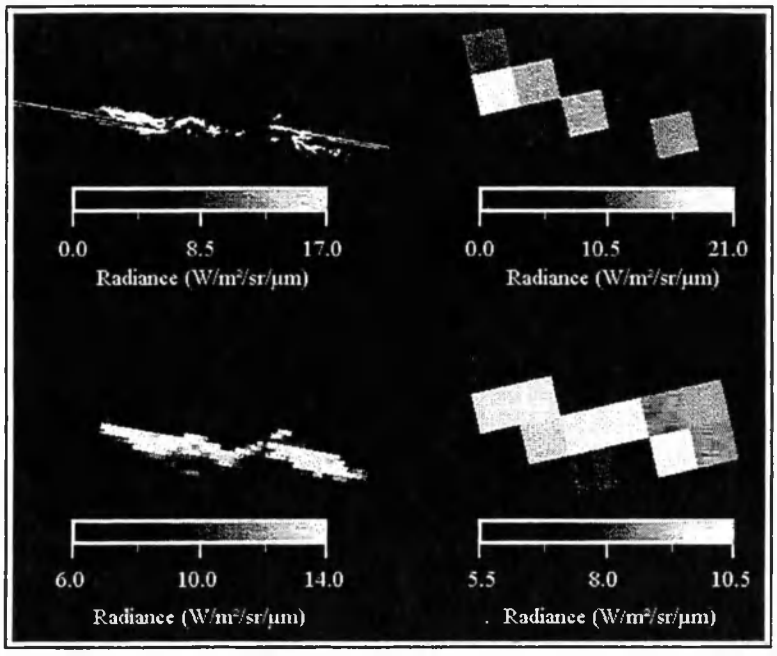

Figure 8.8. The near-contemporaneous TM (left column) and ATSR (right column) datasets of January 1992, detailed in Table 8.2. The upper row shows the 1.6 μm channel data, the lower row the 11 μm channel data. All datasets have been geometrically resampled to a common latitude/longitude pixel grid (30 m spatial resolution) and are masked to show thermally anomalous lava flow field pixels only. The TM 1.6 μm data are partially corrupted by persistently saturated measurements down-scan of the most radiant parts of the flow, these showing up as streaks in the 1.6 μm channel image.

I discuss the shortwave infrared data of both sensors first. The higher levels of 1.6 μm thermal flux recorded by ATSR in January (Figure 8.8) as compared to March (Figure 8.9) suggests that the proportion of surface material at or near magmatic temperatures decreased significantly between these dates. This is confirmed by the TM band 5 data that clearly show a far greater number of pixels radiant at 1.6 μm in January as compared to March. Between these dates the location of the most radiant area in the ATSR 1.6 μm image has also moved from near the source (west) to near the toe (east) of the flow. This change is also mirrored in the TM band 5 data and represents the tubing of the open channel that existed in the upper flow region in January 1992, but that continued to feed surface flows near the toe (Rothery *et al.*, 1992; Calvari *et al.*, 1994).

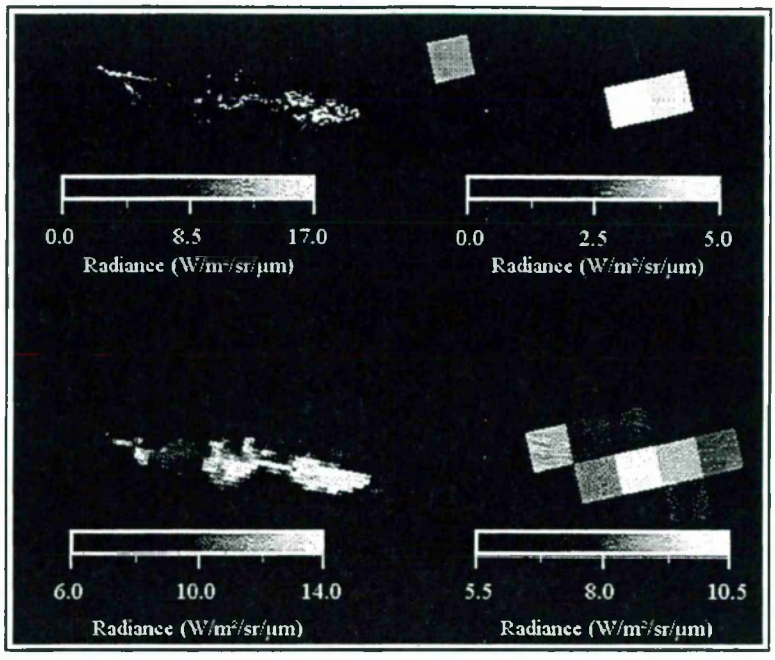

Figure 8.9. The near-contemporaneous TM (left column) and ATSR (right column) datasets of March 1992, detailed in Table 8.2. The upper row shows the 1.6 μm channel data, the lower row the 11 μm channel data. Note the change in the radiance scale used to display the ATSR shortwave infrared data when compared to that of Figure 8.8. All datasets have been geometrically resampled to a common latitude/longitude pixel grid (30 m spatial resolution) and are masked to show thermally anomalous lava flow field pixels only. The persistent down-scan saturation associated with the most radiant TM 1.6 μm pixels is much reduced when compared to that evident in Figure 8.8, being confined to a small area neighbouring the vent.

It is interesting to note that the ATSR 1.6 μm data of March 1992 show a similar pattern to that seen in the shortwave infrared ATSR data obtained towards the end of the 1995 Fernandina eruption (Figure 8.8). Both scenes indicate a near absence of radiance at the location of the lava tubes, corresponding to the lack of surface material at near-magmatic temperatures, but significant radiance at the locations of the issuing vent and at the surface flows near the toe. It is clear that the shortwave infrared radiance data provide information that is most relevant to flow surfaces at or near magmatic temperatures and that tubing over of the flow prevents such material being observed by the sensor.

In contrast to the shortwave infrared signals, the longwave infrared (11 μm) data from both sensors outlines the flow areas where surface temperatures lie significantly

above those of the ambient background, most probably by tens or hundreds of degrees Celsius (Flynn *et al.*, 1994). The TM band 6 data of January 1992 (Figure 8.8) indicate that the entire flow surface is at a highly elevated temperature, around half of all the anomalous band 6 pixels being saturated. The corresponding ATSR data of January 1992 also show the 11 μm radiances significantly elevated for the entire flow length. By March the levels of 11 μm spectral radiance recorded by ATSR are generally much lower, especially in the upper flow area. This pattern again agrees with that found from Landsat TM, with a general lowering of radiance recorded in TM band 6 between January and March 1992, again especially in the upper flow region.

8.3.3. Quantitative comparisons

The application of Equations 7.2 and 7.3 allowed quantitative estimates of the lava flow area to be produced from the ATSR data listed in Table 8.2. For the purpose of this work values of τ_{11} and $R_{11}\uparrow$ were estimated as 0.81 and 1.04 W/m²/sr/μm respectively using LOWTRAN 7 (Kneizys *et al.*, 1988) and mean winter atmospheric profile data of the Etna region (Great Britain Meteorological Office, 1962). In this case these estimates are within 5% of those produced from the ATSR BT data using the Split Window Variance Ratio technique of Jedlovec (1990).

With regard to the TM data, the total surface area of the active flow on 2 January and 22 March 1992 was calculated by counting the number of thermally anomalous TM band 6 pixels in the data of Figures 8.8 and 8.9 and multiplying by the appropriate pixel area. Taking these TM derived estimates as 'truth', it is instructive to note that the results shown in Figure 8.10 indicate that the range of area estimates derived from the near-contemporaneous ATSR data correctly bracket those derived from TM. However, it is also clear that the range of area estimates produced from each ATSR scene span almost an order of magnitude, this being a direct result of the large temperature range used in the solution of Equation 7.2. Without some additional data to further constrain the possible crustal temperature range, this level of uncertainty cannot be avoided. However, as

previously suggested, radiative cooling will most likely bring the majority of the crust to temperatures significantly less than 400 °C quite rapidly (Flynn *et al.*, 1994). With more detailed knowledge of the cooling rates of active flows, it may be possible to constrain the area estimates more tightly than has been performed during these analyses.

One further feature to note is that the active flow areas retrieved from the phase 3 data are consistently lower than those retrieved from the phase 2 data. Clearly the erupted volume had increased between the two phases, as had the planimetric flow area; though by less than 0.5 km² (Calvari *et al.*, 1994). However the results shown in Figure 8.10 do not represent the total area of erupted lava but rather the area of still active crust, i.e. that which is subtantially above the ambient background temperature. This area decreases between phases 2 and 3, most probably as a result of the rapid radiative cooling of areas of the upper flow surface that are no longer being fed by new lava (Calvari *et al.*, 1994).

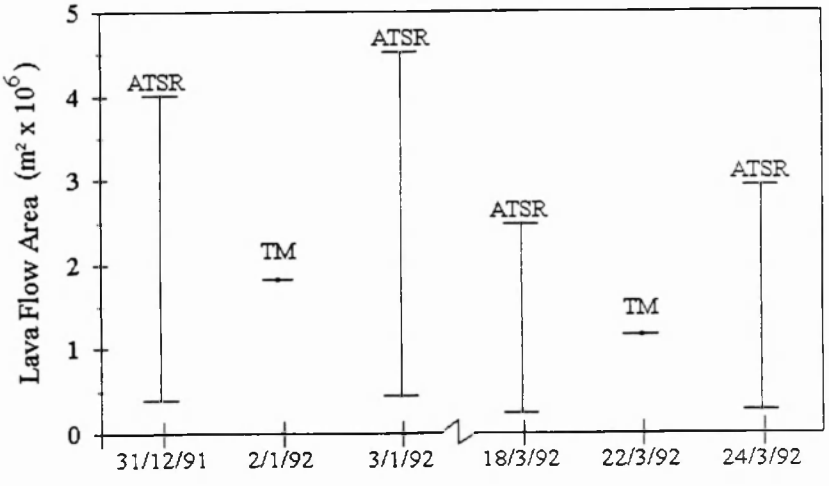

Figure 8.10. The total area of active lava derived from the four ATSR and two Landsat TM scenes obtained in December 1991 - March 1992 (Table 8.2). The range of area estimates derived from each ATSR image reflects the range of lava flow surface temperatures used in the solution of Equations 7.2 and 7.3.

In addion to providing estimates of the total lava flow area, the TM datasets can, in theory, additionally be used to estimate the area of near-magmatic material exposed at the

surface of the flow using the dualband technique of Rothery *et al.* (1988). However, application of this methodology to the January and March 1992 TM datasets was made relatively meaningless by the large scale saturation of the TM band 7 and, to a lesser extent, band 5 data. An alternative methodology was therefore applied in order to obtain an approximate measure of this parameter.

For the TM scene aquired in January 1992, the majority of surface material at or near a magmatic temperature was believed to be associated with the presence of the open lava channel, first noted in TM data by Rothery *et al.* (1992). Thermal emittance from this channel was large enough to significantly affect (but not saturate) seventy TM band 4 (0.83 μm) pixels (Figure 8.11). Therefore, for the January 1992 TM scene, the thermally anomalous band 4 data were analysed using an adaption of Equation 7.3, made appropriate to measurements in this waveband :

$$Area_h = \frac{A_{TM} \sum_{k=1}^{n} R_{thermal}}{\varepsilon_\lambda L(T_h)} \qquad (8.1)$$

Where $Area_h$ is the estimated total area of exposed core contained within the pixels (m^2)

A_{TM} is the ground equivalent area of a TM shortwave infrared pixel (m^2)

n is the number of thermally anomalous pixels in the TM band of interest

$R_{thermal}$ is the thermally anomalous radiance in that waveband ($W/m^2/sr/\mu m$)

T_h is the assumed temperature of the exposed core (°C)

$L(T_h)$ is the Planck function radiance in the waveband of interest ($W/m^2/sr/\mu m$)

ε_λ is the spectral emissivity of the surface

Since the TM data were taken during daylight hours, $R_{thermal}$ for the anomalous TM band 4 pixels was calculated using the techniques outlined in Oppenheimer (1991). This involved adjusting the signals for atmospheric and surface emissivity effects, after first

subtracting the solar reflected component which was estimated using neighbouring non-thermally anomalous pixels. Analysis of the Planck function appropriate to TM band 4 wavelengths indicates that the crustal surface would emit negligible radiance in this waveband. $R_{thermal}$ for TM band 4 can therefore be assumed to correspond solely to radiance from areas of exposed molten lava at near-magmatic temperatures, in this case that associated with the open channelised flow.

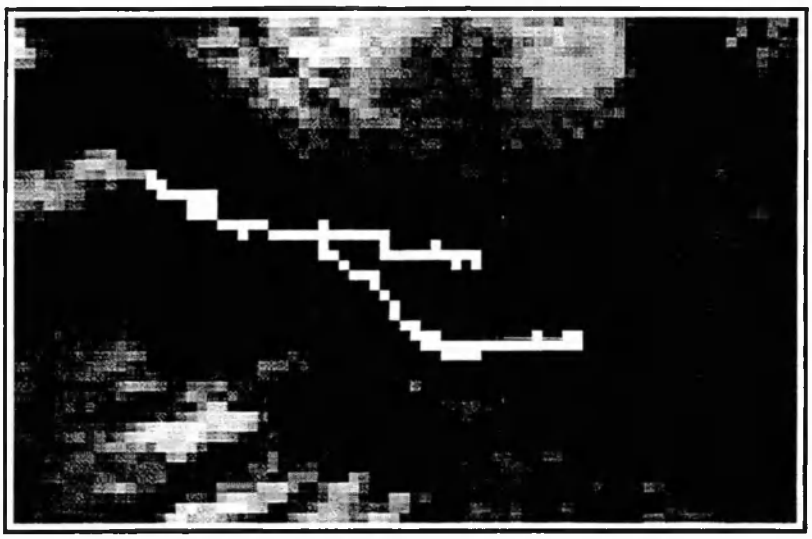

Figure 8.11. The open lava channel defined by the thermally anomalous TM band 4 pixels, shown here highlighted against the non-thermally anomalous background of this 2 January 1992 TM band 4 subscene (area box outlined in Figure 8.7). The lava effusing vent is at the left of the subscene. In contrast to the TM band 5 data (Figure 8.7), anomalous TM band 4 pixels occur only at the location of the open lava channel.

In early January 1992 the Smithsonian Institution (1992a) report that the surface temperature of the open channel was 850 - 1080 °C, measured using thermocouples and a optical pyrometer. Flynn and Mouginis-Mark (1992) report a similar temperature range for an open Kilauea lava channel. Using this temperature range and the TM band 4 data, Equation 8.1 provides an area estimate for the open channel of 1500 - 20000 m². The spatial distribution of the anomalous band 4 pixels (Figure 8.11) indicates that the channel flowed for an initial distance of 780 m, before splitting into two separate channels of

lengths 500 m and 900 m respectively. This gives a cumulative length of 2180 m for the entire channel.

Dividing the value of channel area by channel length gives a mean channel width of 1 - 9 m. The Smithsonian Institution (1992a) report the width as around 10 m, though it is not clear whether this value is appropriate to the entire channel length. Photographs in Rothery *et al.* (1992) suggests this value is of the correct magnitude and, if so, the results from TM agree provided the lower limit is taken for the lava temperature. Following the analysis of the open channel area, the wider TM dataset was then used to provide estimates of the area of near magmatic temperature material exposed over the remainder of flow field. For the January TM scene, the pixels that were thermally radiant in band 5, but not band 4, were used with Equation 8.1 to provide an estimate of this parameter outside of the open channel. These estimates were added to those of the open channel to provide an estimate of the total area of magmatic material. For the March TM scene the same procedure was applied, but data from band 5 was used alone since no thermal signals were detectable in band 4, principally due to tubing of the previously open channelised flow. This methodology assumes that radiance from the cooling crust is negligible in TM band 5, which is realistic for crust temperatures below about 300 °C. Small areas of the crust may have been at temperatures greater than this but the resultant inaccuracies will be offset by the fact that many pixel estimates of TM band 5 radiance are a minimum due to saturation in this waveband.

To provide a comparison dataset to that obtained from Landsat TM, data from the four ATSR scenes were used with Equations 7.2 and 7.3 to provide estimates of the area of near magmatic material exposed over the entire flow field. Figure 8.12 shows a comparison of the areas calculated from both the TM and ATSR datasets. The range of area estimates derived from ATSR matches quite well that obtained from Landsat TM, especially during phase 3 of the eruption (March TM scene). The slight discrepancy in the ranges calculated for phase 2 (January TM scene) may be due to the large proportion of

saturated TM band 5 pixels in the January scene (25%), compared to only 4% saturation for the TM scene obtained in March. ATSR provides non-saturated 1.6 μm channel measurements for all dates and is therefore more trustworthy as a measure of total emitted radiance in this waveband. Despite these differences, data from both sensors indicate a marked decrease in the amount of near-magmatic temperature material exposed at the surface during phases 2 and 3. It is also instructive to note the similarity of the area estimates of magmatic material derived from ATSR data obtained on near-neighbouring days. This provides an indication that these data are providing stable estimates of these parameters, and are not being unduly affected by variations in volcanogenic gas flux or other transient phenomena.

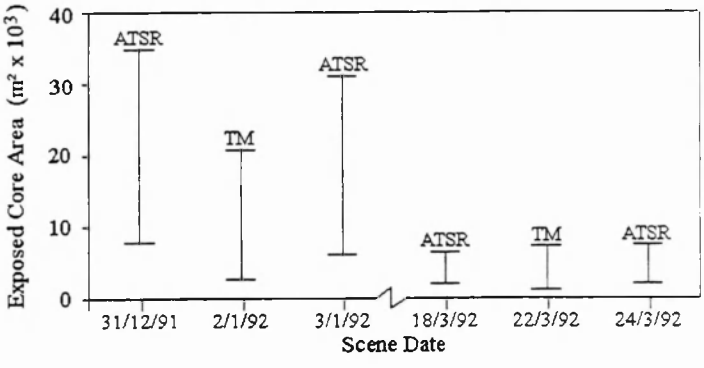

Figure 8.12. The area of exposed magmatic temperature material derived from ATSR and TM data obtained in December 1991 - March 1992 (Table 8.2).

8.4. Conclusions

Modelling of the ATSR measurement process, as applied to observations of an active lava flow, has partly validated the methodology used to determine estimates of lava flow area from low spatial resolution infrared radiance measurements. The model has indicated that such measurements are insignificantly affected by the differing viewing geometries found in the ATSR nadir-view observations, provided self obscuration of flow features is not of significance. This is expected to be the case for the near-nadir viewing

angles associated with these data, though obscuration may occur when using data from the ATSR forward-view since significantly larger viewing angles are involved (Chapter 6).

Comparison of flow area estimates made from real ATSR data of the 1991 - 1993 eruption of Mount Etna provides results that are in agreement with those derived from contemporaneous higher spatial resolution (TM) datasets. Qualitative inferences made from the ATSR data are also in agreement with those made from field reports and from TM data of phases 2 and 3 of the Etna eruption, most notably with regard to the spatial distribution of vigorous surface activity. A similar conclusion was reached by Harris *et al.* (1997) when comparing data from the AVHRR sensor with published field reports for the Etna flow. However, the principal advantage of the ATSR over AVHRR is that, by taking low spatial resolution nighttime measurements at 1.6 μm, the ATSR short wavelength data do not suffer from the saturation effects that plague the AVHRR 3.7 μm channel.

Using the unsaturated ATSR shortwave infrared data, estimates of the area of near magmatic surface temperature material can be produced since this waveband is highly sensitive to radiance from these sources, and relatively insensitive to radiance from the significantly cooler lava flow crust. When large numbers of non-saturated pixel measurements allow estimates of this parameter to be produced from TM data, these estimates have been found to be in agreement with those obtained from ATSR.

The results of these validation exercises suggest that it is appropriate to attempt to derive subpixel lava flow parameters from infrared radiance data collected by ATSR, and indeed by other low spatial resolution sensors working at suitable wavelengths. However, such techniques rely on a variety of assumptions regarding the temperature structure of the lava flow surface, most notably that it is comprised of two endmember thermal components having temperatures within known limits. Though this assumption has been tested and used by a host of previous remote sensing studies of active lava, the accuracy of the results obtained in such studies are heavily dependent on the correctness of these

assumptions. Innaccuracies can be minimised by assuming a wide range of potential crust temperatures during the analysis and using the resultant estimates as bounding cases, within which the true value should lie. If the range of temperatures assumed in these methodologies could be reduced, then the resultant area estimates could be constrained more tightly. However we must await further field studies, and improved multi-waveband and hyperspectral observations, before this can truly be the case. As Rothery and Pieri (1993) report, a number of researchers working in the area of remote sensing volcanology have as a goal the desire to obtain high-spatial resolution (5 - 10m) multispectral image data covering the entire spatio-temporal development of a lava flow at wavelengths between 2 and 10 μm, partly in order to test the validity of these multi-component thermal models. Clearly in order to obtain the high-spatial resolution and frequency of coverage such a dataset would best be obtained by a helicopter or aircraft-mounted instrument package. A combination of the NASA Thermal Infrared Multispectral Scanner (6 bands, 8 - 12 μm) and the Thematic Mapper Simulator (7 bands 0.4 - 2 μm, plus one longwave infrared channel) would appear to be suitable for the purpose, though problems with inter-instrument pixel registration and sensor saturation would need to be addressed. Rothery and Pieri (1993) report that these instruments have occasionally been deployed in Hawaii but, for the most part, logistical and technical difficulties, coupled with an under-performing Kilauea, have so far prevented the ideal dataset from being obtained. Another possibility is the relatively recent development of relatively low cost Fourier Transform Infrared Spectrometers, working between 3 and 14 μm, which is expected to lead to the development of imaging versions of these devices. Such hyperspectral instruments would also appear suitable for gathering the necessary data for invesitgating the surface temperature stucture of a developing lava flow, building upon the shortwave infrared ground-based hyperspectral work of Flynn and Mouginis-Mark (1992; 1994). Once obtained such data could clearly be used to improve the boundary conditions used in models of lava flow thermal and rheological development, as well as for the purposes of validating models surface temperature distribution.

Chapter 9.

Cooling mechanisms and an approximate thermal budget for the 1991-1993 Mount Etna lava flow

---

M. J. Wooster, R. Wright, S. Blake and D. A. Rothery

Geophysical Research Letters (Accepted for publication, October 1997)

9.1. Abstract

The 1991- 1993 eruption of Mount Etna, Sicily built a 7.2 km² aa lava flow field within the Valle del Bove of the volcano. This paper provides estimates of the power losses associated with various cooling mechanisms operating during the development of the flow field, derived from time-series analysis of nighttime satellite remote sensing data. Unlike sensors used in many previous remote sensing studies of active lava, the ERS-1 Along Track Scanning Radiometer (ATSR) provides unsaturated measurements of spectral radiance from even very hot surfaces, allowing for a more accurate solution of the lava flow endmember thermal components. We find that radiative and conductive processes dominated, with our model suggesting energy losses of similar magnitude. Radiative

losses peaked about one month into the eruption, when lava flowed in open channels. Conductive losses peaked after two months, with a marked decline caused by a significant decrease in the horizontal spreading rate of lava. By the end of the eruption the 235 x 10^6 m^3 of erupted lava is estimated to have lost only 28% of its initial thermal energy. A further 6.5 x 10^{17} J must be lost before the lava reaches ambient temperature.

9.2. Introduction

Though recent lava flow cooling models (e.g. Dragoni, 1989; Crisp and Baloga, 1990) have concentrated on radiative processes, Keszthelyi (1995) has suggested that conductive heat loss mechanisms may be equally significant in certain flow regimes. The dominance of radiative processes is highly dependent upon the amount of magmatic material exposed at a lava flow surface, with radiative losses expected to peak during episodes of persistent channelised flow. Satellite remote sensing can characterise the relative proportions of crust and exposed magmatic material at the surface of active lava (Rothery *et al.*, 1988) and a number of previous studies have calculated these parameters using Landsat Thematic Mapper (TM) data (e.g. Pieri *et al.*, 1990; Oppenheimer, 1991; Flynn *et al.*, 1994). Unfortunately the infrequent temporal coverage of Landsat, and the saturation of the TM sensor over the most radiant flow surfaces, have prevented accurate quantification of total radiative loss for an entire eruptive episode (Rothery *et al.*, 1992). Here we use data from a relatively new remote sensing instrument, the ERS-1 Along Track Scanning Radiometer (ATSR) (Prata *et al.*, 1990), to document the radiative history of the 1991 - 1993 aa lava flow field of Mount Etna (Sicily). Harris *et al.* (1997) used Advanced Very High Resolution Radiometer (AVHRR) imagery for this eruption to provide information on spatio-temporal variations in thermal flux and other parameters, but

widespread saturation of the AVHRR middle infrared (3.7 μm) channel largely prevented determination of the radiance contribution from areas at near-magmatic temperatures. However the ATSR provided frequent, dual-band (1.6 μm and 11 μm) unsaturated data for the entire eruptive episode, allowing spatio-temporal variations in total radiative power loss to be more accurately determined. Comparison with physically based estimates of heat losses due to conductive, convective and hydrologic processes allows the relative importance of these competing heat loss mechanisms to be investigated and the overall energy budget of the flow to be quantified. Such information may be of most value where the opportunity for commercial heat extraction exists, such as at the 1973 Heimaey flow field (Björnsson, 1980), or for potential volcanic hazards applications, such as lava flow diversion efforts (Barberi *et al.*, 1993).

9.3. Determination of thermal endmembers

When applying the subpixel 'dual-band' model of Rothery *et al.* (1988) to data of an active lava surface at the ATSR pixel size (1 km²), Chapter 7 showed how it is necessary to increase the number of temperature components to three, namely the area of cooling crust, hot exposed core (magmatic temperature material) and ambient background surface :

$$R_i = \varepsilon_i \tau_i \sum_{k=1}^{3} P_k L_i(T_k) + Ra_i^{\uparrow} + \tau_i (1/\pi)(1-\varepsilon_i) Ra_i^{\downarrow} \qquad (9.1)$$

Where i is the measurement wavelength (μm)

R_i is the recorded spectral radiance (W/m²/sr/μm)

P_k is the fraction of the sensor field of view covered by the k^{th} thermal component

T_k is the temperature of the k^{th} thermal component

$L_i(T_k)$ is the spectral radiance emitted by the k^{th} thermal component ($W/m^2/sr/\mu m$)

ε_i is the surface emissivity

τ_i is the atmospheric transmission

$Ra_i^{\uparrow}$ is the upwelling atmospheric radiation reaching the sensor ($W/m^2/sr/\mu m$)

$Ra_i^{\downarrow}$ is the downwelling atmospheric radiation reaching the ground($W/m^2/sr/\mu m$)

Based on solutions of Equation 9.1, Sections 7.5.2 and 7.5.3 showed how, with knowledge of the ambient background temperature, data from the 1.6 μm and 11 μm channels of ATSR can be used to characterise the two endmember thermal components of an active lava flow surface. Chapter 8 provided further validation of this technique, which was used to analyse ATSR data of the 1995 lava flow on Fernandina Volcano, Galápagos Islands in Chapter 7. When subjecting TM data of active lava flows to dual-band analysis, Oppenheimer (1991) and Flynn *et al.* (1994) assumed surface temperatures close to 1000 °C for the areas of hot exposed core. Flynn and Mouginis-Mark (1992) validated this assumption for a Kilauea lava flow. I follow by assuming the hot component temperature of the active flow lies within the range 950 °C - 1050 °C. Following the results of Flynn *et al.* (1994) I further define a 70 °C - 400 °C temperature range for the cooling crust. Using the techniques outlined in Chapter 7 (and in Wooster and Rothery [1997a]), these temperature assumptions allow Equation 9.1 to be simplified into Equations 7.2 and 7.3 and solved for the minimum and maximum areas of hot exposed core and cooler crust, with atmospheric parameters determined using the LOWTRAN 7 radiative transfer code (Kneizys *et al.*, 1988) with atmospheric profiles of the Mediterranean region.

9.4. Application to the estimation of radiative power loss

The 1991 - 1993 Etna lava flow was active within the Valle Del Bove of the volcano for 15 months between 15 December 1991 and 30 March 1993. The areal and volumetric evolution of the flow has been separated into five distinct phases by Calvari *et al.* (1994). The eruption involved the effusion of 235 x 10^6 m^3 of magma that formed an 8.5 km long lava flow field, with a mean depth of 32 m and a maximum depth of 96 m (Stevens *et al.*, 1997). During the eruption a number of attempts were made to hinder the advance of the flow towards the town of Zafferana Etnea (Barberi *et al.*, 1993), with resultant changes in the location of the most radiant surfaces well evidenced in the AVHRR 11 μm spectral radiance maps of Harris *et al.* (1997).

I obtained twenty nine cloud-free, nighttime ERS-1 ATSR scenes of Mount Etna, covering the period 16 December 1991 to 18 May 1993. The shortwave infrared (1.6 μm) data were calibrated using the relationship derived by Wooster (1996), with 11 μm data neighbouring the flow field used to determine the ambient background temperature required for solution of Equation 7.2. Following Pieri *et al.* (1990) and others, the solutions of dual-component temperature and area were used with the Stefan-Boltzmann equation to calculate the radiative power loss from the upper flow surface, the results being shown as Figure 9.1 (a). Appendix C shows this procedure in more detail. Analysis of the power loss contributions from the individual thermal end-members indicates that areas of exposed core were responsible for around 30% of the radiative losses prior to the end of January 1992. This is the result of large open lava channels that were present during phases 1, 2 and the early part of phase 3; see Figures 3 and 4 in Rothery *et al.* (1992) for examples of these open channel conditions. Calvari *et al.* (1994) report that tubing of the main channels was complete by the end of January 1992, and our results

indicate that for the remainder of the eruption radiative losses from the areas of exposed core were reduced to between 7% and 20% of the total radiative loss. We note that Pieri *et al.* (1990) found a mean value of 9% for a single date of the 1984 Etna lava flow using TM data. ATSR data taken immediately after the eruption ceased show a negligible signal at 1.6 μm, indicating that after the cessation of flow motion no magmatic temperature material remained exposed at the surface. Post-eruption radiative losses from the crust were also significantly reduced, but remained non-negligible at around 0.5×10^9 W.

9.5. Convective energy loss

Head and Wilson (1986) presented relations for deriving power losses due to free convection over an active flow field and, following their application by Oppenheimer (1991) and Harris *et al.* (1997), we use an identical strategy to estimate the convective power loss from the upper surface of the Etna flow. The results are shown as Figure 9.1 (b), with the convecting area of the flow field taken from solutions of Equation 7.2 and 7.3. If free convection were replaced by forced convection, driven by a moderate wind of 10 m/s, then Head and Wilson (1986) indicate that changes in the magnitude of the convective power loss would be insignificant with regard to our data. The relatively low values derived for the convective power loss (Figure 9.1 [b]) support the supposition of Head and Wilson (1986), in that convective losses become significant only after an initial period (in this case phases 1 to 4) where losses from the upper surface are dominated by radiation.

9.6. Conductive energy loss

Conductive losses from the base of the flow into the underlying rock are estimated by first calculating the time-invariant contact temperature between the base of the flow and the underlying surface (T_b). Turcotte and Schubert (1982) show that :

$$(T_b - T_0) / (T_m - T_0) = 1 / (1 + erf\lambda) \tag{9.2}$$

$$\varphi F \sqrt{\pi} / C_p (T_m - T_0) = e^{-\lambda^2} / \lambda(1 + erf\lambda) \tag{9.3}$$

Where C_p is the basalt specific heat capacity (1250 J/kg/K)

F is the latent heat of fusion (4 x 10^5 J/kg)

φ is the mass fraction crystallisation (0.45) (Armienti *et al.*, 1994)

T_0 is the ambient temperature (~300 K)

T_m is the eruptive temperature (~1300 K)

λ is a dimensionless scale factor and *erf* is the error function.

Evaluating the left hand side of Equation 9.3 and solving for λ gives T_b as 854 K.

Following Pitts and Sissom (1997), the conductive heat flux from the lava to the ground is given by Equation 9.4 :

$$Q / A = k(T_b - T_0) / a\sqrt{t} \tag{9.4}$$

Where Q/A is the power loss (W/m^2)

k is the thermal conductivity of basalt (3.3 J/m/s/K)

t is the time elapsed since that component was emplaced (s)

a is a constant $(\pi\alpha)^{1/2}$, where α is the thermal diffusivity of basalt (7×10^{-7} m^2/s).

Calvari *et al.* (1994) provide detailed measurements of the time-varying planimetric flow area, from which the daily increase in new lava area in contact with the ground and the subsequent time of emplacement is easily calculated. Conductive losses were calculated as a daily sum, as each day's new cold ground was overrun and as the old (previously emplaced) lava thermally decayed. In this way, use of Equation 9.4 enables the time varying conductive loss from the entire lava flow base to be estimated (Figure 9.1 [c]). The sharp peak in conductive loss at the end of January 1992 coincides with an order of magnitude decrease in the rate of change of planimetric flow area. The less dramatic break in slope in March 1993 signifies the end of lava effusion. Results from this model support the conclusions of Keszthelyi (1995), in that power losses due to basal conduction are of a similar magnitude as those due to radiation. However, I note that conduction may have been reduced somewhat if the flow base were significantly blocky. These data can be used to reject the supposition of Danês (1972), who suggested that conductive losses through the flow base can be considered negligable.

9.7. Losses Due to hydrological processes

Additional energy losses are sustained in warming, and possibly vaporising, precipitation that falls onto the flow surface. Climatic tables (HMSO, 1967) provide details of the 10 year monthly mean precipitation for the region, which show a strong seasonal cycle. Multiplying these values by the corresponding planimetric flow area and by the density of water allows the mean monthly mass of water falling on the flow to be determined. Conversion to a rate per second and multiplication by the energy required to heat and vaporise the water, assuming an initial ambient temperature given by the climate tables, allows for an evaluation of the maximum potential power loss due to hydrological processes (Figure 9.1 [d]). The levels are small but non-negligible in comparison to the other heat loss mechanisms.

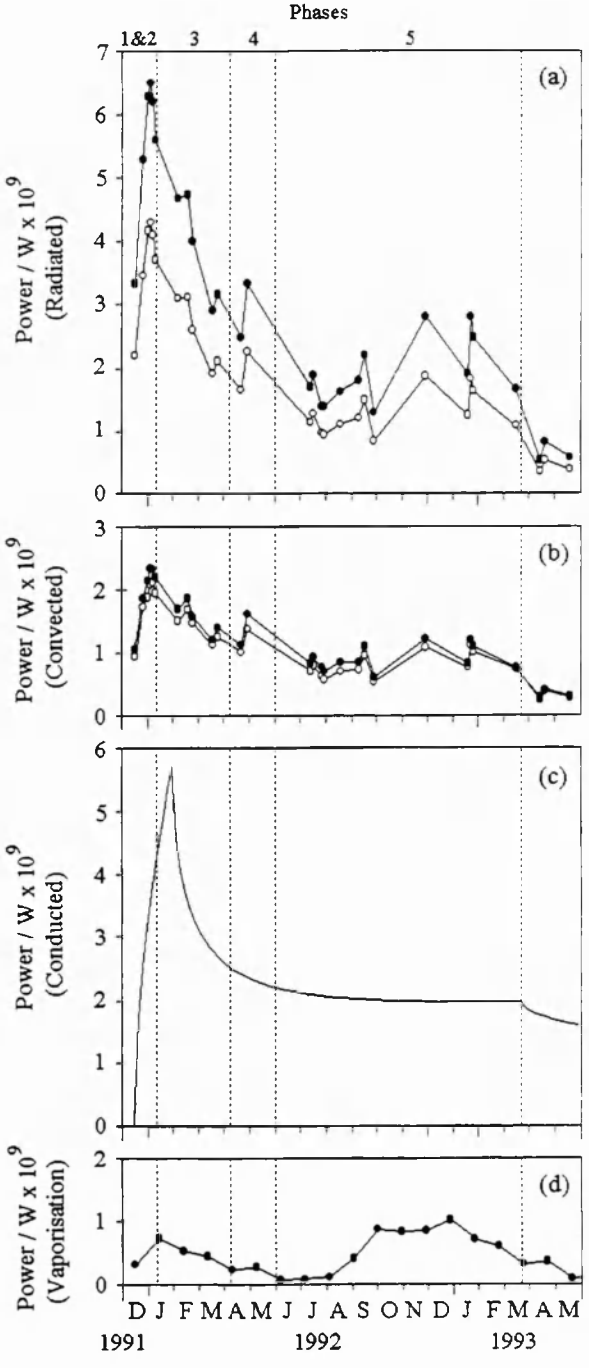

Figure 9.1. Estimated power losses during phases 1 - 5 (Calvari et al., 1994) of the 1991 - 1993 Mount Etna flow. (a) Radiative power loss from the surface of the flow, calculated from analysis of ATSR-1 nighttime imagery. The upper and lower curves give the maximum and minimum solutions obtained using the stated range of temperatures for the lava flow thermal components. (b) Power loss due to free convection from the flow surface. The upper and lower curves give the solution obtained using the maximum and minimum estimated area for the lava flow thermal components. (c) Power loss due to conduction through the base of the flow. (d) Potential maximum power loss due to vaporisation of precipitation falling onto the flow surface.

9.8. The energy balance of the 1991 - 1993 lava flow

An estimate of the time-varying lava flow energy balance is provided by differencing the thermal energy supplied and lost by the flow throughout the eruption. The supplied thermal energy ($E_{\Delta T}$), dependent upon the temperature and liquid state of the erupted volume, is given by Equation 9.5, where the volume estimates are taken from 1992 - 1993 reports in the Global Volcanism Network Bulletin and from Calvari *et al.* (1994).

$$E_{\Delta T} = \rho V(C_p \Delta T + \varphi F) \qquad (9.5)$$

where ρ is the density of lava (2600 kg/m^3)

V is the erupted volume (m^3)

$\Delta T = T_m - T_0$ (K)

A temporal profile of the thermal energy lost by the flow is given by integrating the sum of all the estimated power losses (radiation, convection, conduction and vaporisation) with respect to time (Figure 9.2). For reasons of clarity we have displayed the mean of this energy loss profile, there is a ±10% variation due to the range of values calculated for losses due to radiation and convection. Subtracting the energy lost from the energy supplied provides a profile of the lava flow energy balance, again plotted on Figure 9.2. It is clear that the rate of energy supply is considerably greater than the rate of heat loss, leading to a consistent increase in the thermal energy content throughout the eruption. Looked at in terms of percentage energy retention (Figure 9.3) we see that for the first three months of the eruption the high levels of radiative and convective loss were effective

in continuously decreasing the proportion of retained thermal energy. However, after this period decreasing power losses caused the efficiency of energy retention to stabilise at between 70% and 80%. By the end of the eruption we estimate that 6.5 x 10^{17} J of heat energy was contained within the emplaced lava (Figure 9.2).

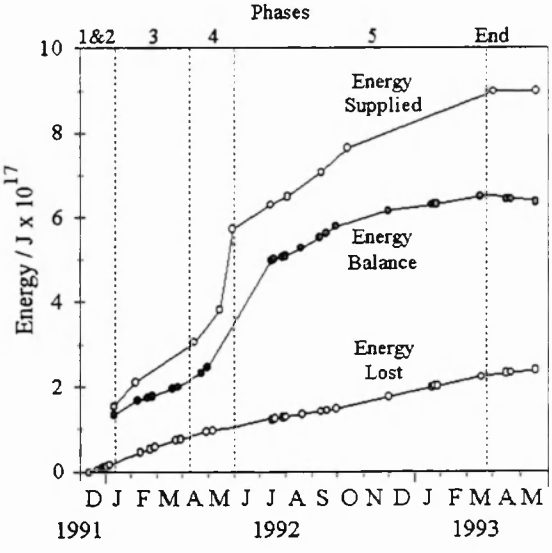

Figure 9.2. The time variant thermal energy balance of the 1991 - 1993 Mount Etna lava flow. The energy balance is the difference between the heat energy contained within the flow by virtue of its high temperature and liquid state (Energy Supplied) and the heat energy lost from the flow (Energy Lost), calculated from summation and integration of the power losses shown in Figure 9.1.

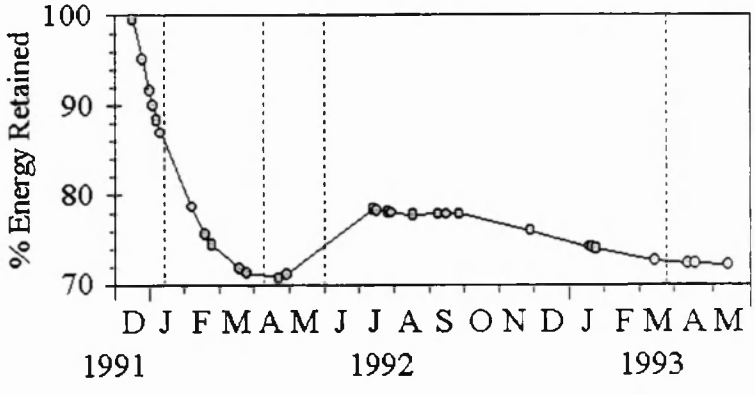

Figure 9.3. The percentage of the supplied thermal energy retained within the developing lava flow field throughout the 1991 - 1993 eruption.

9.9. Conclusion

This study highlights the advantage of using a channel at 1.6 μm, rather than 3.7 μm, to measure volcanic thermal radiance by nighttime remote sensing at low spatial resolution. Results indicate that heat loss from the 1991 -1993 Etna lava flow was dominated by radiative and conductive mechanisms, which our model suggest provided comparable energy losses. These mechanisms were most efficient during the first three months of the eruption, when open lava channels radiated strongly and horizontal spreading of the lava rapidly increased the area of magma in contact with new ground. By the end of the eruption we estimate that the flow had lost only 28% of it's thermal energy and that a further 6.5×10^{17} J must be lost before it reaches ambient temperature. We note that the thicker regions of the flow were still reported to be hot at the surface almost three years after the eruption ceased (Stevens *et al.*, 1997).

Chapter 10.

Summary, conclusions and further work

10.1 Introduction

The research work carried out for this thesis falls into three principal sections, (i) calibrating the ATSR measurements of infrared thermal flux and investigating the characteristics of the data retrieved over Earth surface hotspots, (ii) applying these data to the monitoring of infrared thermal flux at active lava domes and interpreting the results volcanologically, and (iii) using analysis of ATSR time-series data to monitor the spatio-temporal development of active lava flows and to estimate the lava flow thermal budget. Detailed results and conclusions for each of these topics are included at the end of the relevant thesis chapters. Here I briefly summarise the work once more and offer some broad conclusions drawn from the research. I then go onto present some ideas for the direction that future related research might take.

10.2. Summary of research

10.2.1. The characteristics of ATSR hotspot data

Initial research for this thesis involved using high spatial resolution data from the JERS-1 OPS sensor to develop a calibration for the (previously uncalibrated) shortwave infrared (1.6 μm) channel of ATSR-1. A calbration equation was derived and it was shown that the ATSR 1.6 μm channel is linear in its response to incoming radiation, with a saturation level of 53 $W/m^2/sr/\mu m$. Time-series reflectance measurements from the ATSR-1 1.6 μm channel were used to assess the degradation of this sensor between 1992 and 1995. Results indicated a (5 ± 2) % change in gain over the four years, with this relatively low rate of degradation being attributed to cooling of the 1.6 μm detector throughout much of the mission. After the launch of the ERS-2 in July 1995, contemporaneous ATSR-1 and ATSR-2 data were used to verify that the ATSR-2 visible channel calibration mechanism was providing an anomalously low calibration for the 1.6 μm channel reflectance measurements. A correction factor was derived using the contemporaneous ATSR-1 and ATSR-2 datasets.

The characteristics of the standard ATSR COUNTS and BRIGHTNESS TEMPERATURE (BT) data products were investigated with reference to hotspot studies. Simple modelling of subpixel volcanic hotspots indicated that nighttime ATSR data would be required to properly analyse the shortwave infrared component of the thermal signals, daytime observations being dominated by solar reflected radiation. It was apparent that the ATSR BT data contain a number of useful features that do not exist in the COUNTS data products, for example latitude/longitude information for each pixel and an inherent correction for the ATSR 11 and 12 μm detector non-linearities. Investigations of the ATSR-1 COUNTS and BT products for the same hotspot scene indicated that, despite the

geometric resampling processes undertaken during BT data processing, the quantitative fidelity of the radiances remained intact in this data product. BT products therefore offer the most convenient method of accessing ATSR data for hotspot studies. However, further investigations showed that, prior to any quantitative analyses of volcanic thermal radiance, it is vital that any 'cosmetically filled' ATSR BT product pixels are identified and discarded.

10.2.2. Studies of active lava domes using ATSR

The first volcanic phenomena studied during the course of this thesis were active lava domes. An initial study indicated that ATSR data were indeed capable of identifying the arrival of a new dome within an active volcanic crater, in this case Galeras Volcano, Columbia (Appendix E). Following this result, longer time-series ATSR datasets of active domes at Lascar Volcano (Chile) and Unzen Volcano (Japan) were studied in order to assess the quantitative value of the infrared radiance data. Nighttime data from ATSR's shortwave infrared (1.6 μm) channel proved to be of most value, being dominated by thermal emission from the hottest volcanic surfaces. Despite the hot surfaces of the domes being significantly smaller in area than an ATSR pixel, at both sites the cloud-free ATSR nadir-view data identified patterns of varying infrared thermal emittance that agreed with those obtained using much higher spatial resolution instruments. However, unlike observations made with Landsat TM the large pixel size of ATSR prevented saturation of the 1.6 μm detector, allowing a more quantitative interpretation of the derived radiances. At both volcanoes the ATSR 11 μm data were found to be less useful than the shorter wavelength measurements, it being difficult to unambiguously isolate the volcanic component of the signal.

At the Lascar and Unzen domes, analysis of the ATSR shortwave infrared time-series, combined with knowledge of the processes operating at the volcano, allowed volcanological interpretations to be made from variations in the level of emitted infrared radiation. During the monitoring period, a significant reduction in the level of shortwave infrared spectral radiance recorded at Lascar was found to be cause for concern, since it suggests blockage of the degassing system which can lead to a pressure-driven explosive eruption. This combination of ATSR and field-based observations was used to validate the newly-derived Lascar degassing model of Matthews *et al.* (1997). Most significantly a major decrease in emitted shortwave infrared thermal flux was observed nine months prior to Lascar's largest historical eruption in April 1993. The reverse finding was generally true at Unzen, where a significant increase in emitted shortwave infrared spectral radiance was generally indicative of an increase in the effusion rate of lava (since both were positively related to levels of fumarolic degassing) and in the frequency of collapse-driven pyroclastic flow. In contrast to Lascar, a significant rise in shortwave infrared thermal flux recoded at this volcano thus indicated a likely increase in hazard.

The Lascar and Unzen case studies indicate that time-series of low spatial resolution infrared radiance data can provide useful information at volcanoes exhibiting lava dome growth and/or high temperature fumarolic activity. Analyses of such time-series, combined with knowledge of the particular volcano in question, would most likely assist predictions of activity being made at other volcanoes exhibiting lava dome activity, for example Monserrat (West Indies) and Merapi (Indonesia). However, care must be taken when constructing time-series obtained from wide swath instruments (such as the AVHRR or MODIS), since comparison of data obtained in the ATSR forward- and nadir-

views shows that geometric shielding of hot surfaces can be a limiting factor at far off-nadir view angles.

10.2.3. Studies of active lava flows using ATSR

Following the studies of active lava domes I went onto analyse ATSR time-series covering the development of active lava flows at Fernandina Volcano (Galápagos Islands) and Mount Etna (Sicily). My analyses followed many previous remote sensing studies of active lava in assuming that the flow surface possessed a bimodal temperature distribution. It was shown that the ATSR longwave infrared (11 μm) data are likely to be dominated by radiation from the cooling lava crust, whilst the shorter wavelength (1.6 μm) data are likely to be dominated by radiation from areas of exposed magmatic material. Equations were derived that can be used to estimate the area of these two thermal components from the ATSR infrared radiance data, with the methodology being validated using models of the ATSR observation process and near-coincident TM and ATSR datasets.

The inferred morphological evolution of the Fernandina flow field, made by interpreting the ATSR time-series, agreed with the record provided by limited field observations of this remote eruption. An estimate of the overall area of emplaced lava also agreed with a figure produced from post-eruption SPOT HRV imagery. For the 1991 - 1993 Etna flow, the temperatures and areas retrieved using the ATSR time-series were used within models of radiative, conductive, convective and hydrologic cooling mechanisms in order to compare the importance of these various heat loss processes. Results indicated that radiative losses dominated, but that conductive processes were also highly significant. The model results suggest that these mechanisms were most efficient during the first three months of the eruption, when open lava channels radiated strongly and horizontal spreading of the lava rapidly increased the area of magma in contact with

new ground. Despite the efficiency of heat loss during these early months, analysis of the entire time-series indicated that the emplaced lava had lost only 28% of its initial thermal energy by the end of the eruption. The bulk of the lava will therefore most likely be at an elevated temperature for many years before reaching the ambient state.

These studies of active lava flows suggest that low spatial resolution sensors, working simultaneously in the shortwave and longwave infrared regions, can be used to provide estimates of eruption parameters for unmonitored or isolated effusive eruptions such as those occurring in the Galápagos Archipelago. Furthermore, such satellite data provide the only efficient means of obtaining regular information on the thermal properties of an entire lava flow surface, even one as well monitored as the 1991 - 1993 Etna flow. Though estimates made from such data are model dependent and contain many implicit uncertainties, I would expect these to decrease when satellite-based instruments having a substantially increased number of wavebands finally become available (see discussion at the end of Chapter 8.4).

10.3. Final conclusions

The primary conclusion drawn from this work is that suitable analyses of spaceborne low spatial resolution infrared radiance data can provide infromation relevant to the surface thermal manifestations of many volcanic processes. A similar conclusion was reached by Harris *et al.* (1996) when analysing AVHRR data of effusive volcanic activity. However one of the principal advantages of ATSR over AVHRR is that, by taking low spatial resolution nighttime measurements at 1.6 μm, the ATSR shorter wavelength data do not suffer from the saturation effects that plague the AVHRR 3.7 μm channel. ATSR can thus provide a more quantitatively accurate measure of the shorter

wavelength thermal emissions associated with the hottest components of the volcanic surface. Furthermore, unlike thermal signals recorded at 3.7 μm, those recorded at shorter wavelengths are insensitive to changes in surfaces having temperatures below about 300 °C. A significant change in the 1.6 μm signal can therefore be unambiguously attributed to variations in high temperature surface activity, something that may be highly significant in many volcanological situations. Use of ATSR thus allows a more quantitative approach to be taken during data analyses when compared to other currently operating low spatial resolution instruments.

In comparison to data from Landsat TM, which has dominated previous volcanic studies using thermal infrared satellite remote sensing, the low spatial resolution of the ATSR measurements ensures that the sensor does not become saturated, whereas the high temporal resolution (gained at the expense of spatial detail) allows a much more temporally comprehensive dataset to be collected. Furthermore, datasets from low spatial resolution instruments such as ATSR are, at present, available at prices that are orders of magnitude lower than those of data from higher resolution sensors. The comparatively low data volumes, and centralised data reception and processing facilities, make it feasible to use such low spatial resolution data for routine global hotspot monitoring. Such a system could, for example, provide nighttime shortwave infrared radiance data for all volcanoes identified as being radiant in this waveband. This would allow new effusive eruptions to be identified, and trends in emitted radiance to be gauged at persistently active sites. If and when a near-real time processing scheme for the Advanced ATSR (AATSR) becomes operational, I would recommend that the development of such a system be considered to complement the MODIS-based thermal alert system being planned at the University of Hawaii (Mouginis-Mark *et al.*, 1991b).

10.4. Future work

10.4.1. Initial studies

In the short term, initial work should be carried out to expand the number of volcanoes, and types of effusive volcanic activity, studied using ATSR. This will assist in advancing the utility of the low spatial resolution monitoring technique, and will also demonstrate how applicable the techniques are to a wider variety of volcanic situations. To this end I am currently obtaining ATSR-2 data of a number of new volcanic targets. These include Soufriere Hills Volcano (Montserrat), which is currently undergoing a major eruption involving the growth of a summit lava dome and the generation of frequent explosive events accompanied by pyroclastic flows. Soufriere Hills' activity was initially believed to be similar to that of the 1991 - 1994 Unzen eruption, with collapses of the growing dome generating the pyroclastic flows. Unlike phase 1 of the Unzen eruption however, reports suggest that Soufriere Hills does not possess large open fumaroles which would be a likely source of intense shortwave infrared thermal flux. Nevertheless, ATSR data of the volcano do show a sizeable shortwave infrared signal. The initial study will concentrate on identifying the likely source of this radiance, analysing the shortwave infrared time-series, and determining relationships between it and the other volcanogenic activity (e.g. dome growth rate, seismiscity and frequency of pyroclastic flow). It is proposed that the ATSR dataset will be analysed alongside complimentary data from the AVHRR and GOES meteorological satellites, these being currently investigated by another OU researcher.

The second and third newly identified volcanic targets are Erta 'Ale volcano (Ethiopia), where a long-duration lava lake has recently been studied using a variety of high spatial resolution imagery (Oppenheimer and Francis, 1997), and Masaya Volcano

(Nicaragua), where a continuously degassing vent has been active for some years and which is reported to have undergone a recent increase in activity. It will be instructive to note whether, in a similar manner as for Lascar and Unzen, the low spatial resolution data can provide high-temporal information of sufficient quality for use in monitoring the persistent activity exhibited by these volcanoes.

The fourth new volcanic target departs somewhat from the previous studies of effusive volcanism. It is Ruapehu (New Zealand), where a crater lake exists whose temperature is partly determined by the underlying magmatic activity of the volcano (Oppenheimer, 1997). Prior to it's 1995 eruption Ruapehu's water temperature reached a 13-year high, indicating that such data are a valuable resource for eruption prediction efforts. At Ruapehu the lake temperature is well monitored using ground-based techniques, though this is not the case for all such crater lakes. If low-spatial resolution satellite based instruments could be used to provide evidence of lake surface temperature change at Ruapehu, then the procedure could be adapted to other crater lakes that are at present unmonitored. Wooster *et al.* (1994) have previously used low spatial resolution data from the AVHRR to accurately measure the temperature of large tropical lakes in Africa, whilst Oppenheimer (1997) has successfully used high spatial resolution TM band 6 data to measure Ruapehu's water temperature. Despite Ruapehu's lake surface area being smaller than a single ATSR pixel, simple modelling suggests that significant changes in the water temperature should be identifiable with ATSR, particularly as the sensor possesses the so-called 'split window' channels that can be used to correct the signal for atmospheric variations (Llewellyn-Jones *et al.*, 1984). It will most instructive to determine whether ATSR can detect the increase in water temperature prior to Ruapehu's 1995 eruption.

10.4.2. Longer term: 'Mission to Planet Earth'

The NASA Earth Observing System (EOS) Volcanology Investigation (Mouginis-Mark *et al.*, 1991b) is the largest volcano remote sensing project to date and, as such, the longer-term future of spaceborne volcano remote sensing is intertwined with that of EOS and NASA's Mission to Planet Earth (MTPE). MTPE is a multi-billion dollar dedicated system of instruments, information systems and data analysis and research activities, all aimed at no smaller a task than the understanding of the Earth system as a whole. Volcanoes, being a necessary part of the Earth's geosphere and an important contributor to the Earth's biosphere, are specifically targeted for intensive study during MTPE. The NASA EOS Volcanology Investigation is the umbrella title for this activity, it being one of 28 interdisciplinary science investigations selected by NASA as part of the EOS project (Mouginis-Mark *et al.*, 1991b; Asrar and Jon Dokken, 1993).

At the core of MTPE is a flotilla of intermediate size satellites, each carrying a multitude of remote sensing instruments, which are to be operated over at least a 15 year period from 1998. These satellite and instrument packages, collectively known as the Earth Observing System (EOS), will provide the Earth remote sensing data necessary to fulfil the MTPE objectives. They will also produce by far the most comprehensive set of spaceborne Earth observation data in the history of remote sensing, these data being channelled through the EOS Data and Information System (EOSDIS) to scientific investigators world-wide (Asrar and Jon Dokken, 1993; Ardanuy *et al.*, 1991).

The Moderate Resolution Imaging Spectrometer (MODIS) is the primary EOS instrument and it will be flown on all of the principal EOS platforms (Salomonson *et al.*, 1989; Ardanuy *et al.* 1991). MODIS will make daily observations of the entire Earth surface by utilising a wide (2330 km) swath width, similar to that of the AVHRR. MODIS

observes in 36 spectral channels covering all spectral regions from visible to thermal infrared, at nadir spatial resolutions of between 250 and 1000 m. The most important bands for the thermal monitoring of volcanoes are those in the shortwave infrared (2 wavebands at 1.64 μm and 2.13 μm, 500 m spatial resolution) and those at longer infrared wavelengths (17 wavebands between 3.75 μm and 14.24 μm, 1000 m spatial resolution).

The work carried out for this thesis confirms that MODIS observations should indeed be useful for the thermal investigation of active volcanoes. It is already planned that thermal data from MODIS will be utilised in a near real-time eruption alarm system to be based at the University of Hawaii (Mouginis-Mark *et al.*, 1991b). To be most effective such a system will need to discriminate between volcanic thermal anomalies and those caused by other activity, for example the vegetation fires that are the subject of Appendix D. Following early work using Landsat TM (Flynn and Mouginis-Mark, 1995), this thesis includes suggestions of ways in which this discrimination may be achieved using low spatial resolution measurements (Appendix E). These discriminatory procedures will need further investigation once MODIS data become available.

My ATSR analyses suggest that MODIS observations may be useful for far more than simply the detection of new volcanic hotspots. I suggest that MODIS could be a valuable source of data for monitoring radiance trends at persistently active volcanic sites. This idea has already been carried forward by the University of Hawaii, who will attempt to use radiance data from MODIS in a variety of time-series studies (Luke Flynn, personnel communication 1997). Unfortunately, it appears that the MODIS shortwave infrared sensors (1.6 and 2.1 μm) will be switched off during nighttime passes. This is an unfortunate state of affairs since this thesis has clearly indicated that nighttime shortwave infrared data appear by far the most useful for volcano monitoring purposes. Furthermore,

since MODIS has two shortwave infrared channels, compared to ATSR's one, nighttime shortwave infrared data from MODIS might allow additional constraints to be placed on the nature of the highest temperature volcanic surfaces.

Despite the apparent lack of nighttime shortwave infrared data from MODIS, some comfort can be taken in the fact that the instrument possesses a low-gain 3.7 μm channel, which is specifically designed to avoid sensor saturation over hot targets. I will shortly be examining a 1995 - 1997 ATSR-2 time-series of Lascar to determine differences in the 1.6 and 3.7 μm radiance trends (provided the 3.7 μm channel is not persistently saturated). However, it seems likely that data taken at 3.7 μm will be less useful than that taken at 1.6 μm since the longer wavelength measurements are subject to variations in the ambient background. Time-series of 3.7 μm observations will therefore need to be corrected for seasonal variation, but such corrections are rather imprecise and will most likely degrade the quality of the dataset. It is currently hoped that appropriate lobbying may yet get the situation altered and allow the volcanological (and fire) community to obtain nighttime shortwave infrared data from MODIS.

In addition to MODIS, the first EOS AM platform carries another visible and infrared land imager, the high spatial resolution Advanced Spaceborne Thermal Emission and Reflectance Radiometer (Kahle *et al.*, 1991). ASTER has six shortwave infrared bands between 1.60 μm and 2.43 μm (30 m spatial resolution) and five thermal infrared bands between 8.125 and 11.65 μm (90 m spatial resolution). ASTER's shortwave infrared channels have been designed to saturate at higher pixel integrated temperatures (450 - 500 °C) than those currently available from TM bands 5 (400 °C) and 7 (275 °C), making them potentially much more useful for multi-waveband studies of high temperature phenomena. My Unzen study (Chapter 5) indicates the complementary value

of high temporal, low spatial resolution (ATSR) and low-temporal, high spatial resolution (TM and airborne) volcanic thermal datasets. The possibility for such dual-sensor studies will be greatly enhanced with the complementary operation of MODIS and ASTER on the same platform, with ASTER's advanced features making it of potentially great value for identifying the exact nature of the thermal anomalies detected by MODIS. Combined use of ASTER and MODIS seems to offer a potentially powerful new tool for world-wide monitoring of volcanic thermal phenomena.

References

Alcaraz, A. and Cardoso, M.C.T. (1969), Lake Taal. *Comvol. Lett.*, **3**, 1-4.

Andres, R.J. and Rose, W.I. (1995), Description of thermal anomalies on two active Guatemalan Volcanoes using Landsat Thematic Mapper Imagery. *Photogram. Eng. & Remote Sens.*, **61**, 775-782.

Ardanuy, P.E., Hann, D. and Salomonson, V.V. (1991), The Moderate Resolution Imaging Spectrometer (MODIS) science and data system requirements. *IEEE Trans. Geosci. Remote Sens.*, **29,** 75-88.

Armienti, P., Clocchiatti, R., D'Orazio, M., Innocenti, F., Petrini, R., Pompilio, M., Tonarini, S. and Villari, L. (1994), The long-standing 1991-1993 Mount Etna eruption: petrography and geochemisty of lavas. *Acta Volcanol.*, **4**, 15-28.

Arvensen, J.C., Griffin, R.N. and Pearson, B.D. (1969), Determination of extraterrestrial solar spectral irradiance from a research aircraft. *Applied Optics*, **8**, 2215-2232.

Asrar, G. and Jon Dokken, D. (1993), *EOS Reference Handbook.* (Washington D.C.: NASA Earth Science Support Office)

Bailey, P. (1994), *SADIST Products (Version 600).* (Didcot : Rutherford Appleton Laboratory Space Science Department).

Bailey, P. (1995), *SADIST-2 v100 Products.* (Didcot : Rutherford Appleton Laboratory Space Science Department).

Lipman, P.W., Moore, J.G. and Swanson, D.A. (1981), Bulging of the north flank before the May 18 eruption - geodetic data. In *The 1980 Eruption of Mount St. Helens*, edited by P.W. Lipman and D.R. Mullineaux, U.S.Geological Survey Prof. Paper **1250**, pp. 143-156.

Barberi, F., Carapezza, M. L., Valenza, M. and Villari, L. (1993), The control of lava flow during the 1991-1992 eruption of Mt. Etna. *J. Volcanol. Geotherm. Res.,* **56**, 1-34.

Björnsson, S. (1980), Natural heat saves millions of barrels of oil. *Atlantica & Iceland Rev.,* **18**, 28-37.

Blake, S. (1990), Viscoplastic models of lava domes. In *Lava Flows and Domes, Empacement Mechanisms and Hazard Implications*, edited by J.H. Fink, (Berlin: Springer-Verlag), pp. 89-125.

Breaker, L.C. (1990), Estimating and removing sensor-induced correlation from Advanced Very High Resolution Radiometer satellite data, *J. Geophys. Res.*, **95**, 9701-9711.

Calvari, S., Coltelli, M., Neri, M., Pompilio, M. and Sobribano, V. (1994), The 1991 - 1993 Etna eruption chronology and lava flow-field evolution. *Acta Volcanol.*, **4**, 1-14.

CAVW (1951-1975), *Catalogue of Active Volcanoes of the World, Vol. 1-22.* (Rome: Int. Assoc. Volcanol. Chem. Earth's Interior).

Clarke, M.C.G. (1991), Volcanic hazards as exemplified by the 1982 eruption of Mount Galunggung, Java. In *Geosciences and Development*, edited by D.A.V. Stow and D.J.C. Laming, AGID Report No. 14, pp. 167-178.

Connor, C.B., Clement, B.M., Xiaodan S., Lane, S.B. and West-Thomas, J. (1993), Continuous monitoring of high-temperature fumaroles on an active lava dome, Volcán Colima, Mexixo: Evidence of mass flow variation in response to atmospheric forcing. *J. Geophys. Res.*, **98**, 19713-19722.

Crisp, J. and Baloga, S. (1990), A model for lava flows with two thermal components. *J. Geophys. Res.*, **95**, 1255-1270.

Danês, Z. F. (1972), Dynamics of lava flows. *J. Geophys. Res.*, **77**, 1430-1432.

Dean, K.G., Searcy, C., Wyatt, C. George, S. and Engle, K. (1996), Monitoring volcanoes in the north Pacifc Ocean region using satellite imagery, modelling and meteorological data. *Proceedings of the Pan Pacific Hazards Conference*, Vancouver, Canada, 27 July - 4 August 1996.

Delderfield, J., Llewellyn-Jones, D.T., Bernard, R., de Javel, Y., Williamson, E.J., Mason, I., Pick, D.R., Barton, I.J. (1985), The Along Track Scanning Radiometer

(ATSR) for ERS1. *Proceedings of SPIE Instrumentation for Optical Remote Sensing from Space*, **589**, pp. 114-120.

Denniss, A.H., Harris, A.J.L., Carlton, R.W., Francis, P.W. and Rothery, D.A. (1996), The 1993 Lascar pyroclastic flow imaged by JERS-1. *Int. J. Remote Sens.*, **17**, 1975-1980.

Dozier, J. (1981) A method for the satellite identification of surface temperature fields of subpixel resolution, *Remote Sens. Environ.*, **11**, 221-229.

Dragoni, M. (1989), A dynamical model of lava flows cooling by radiation. *Bull. Volcanol.*, **51**, 88-95.

Ehara, S., Yamashita, S., Yokoyama, I. (1975), Analysis of aerial infrared imagery of volcano Mihara, Oshira Island. *Bull. Volcanol. Soc. Japan*, **20**, 108.

Engel, J.L. and Weinstein, O. (1983), Thematic Mapper: An overview. *IEEE Trans. Geosci. Remote Sens.*, **3**, 258-265.

EOSAT (1986), *Landsat Technical Notes,* **1**, Lanham, MD, 8pp.

Fink, J.H., Malin, M.C. and Anderson, S.W. (1989), Intrusive and extrusive growth of the Mount St. Helens lava dome. *Nature*, **348**, 435-437.

Fisher, N.H. (1957), Melanesia, *Catalogue of Active Volcanoes of the Word: part V.,* (Naples: Int. Volcanol. Assoc.), 105pp.

Fisher, N.H. (1958), Foreward. In *The 1951 eruption of Mount Lamington, Papua*, by G.A.M. Taylor. *Bulletin of the Autralian Bureau of Mineral Resources, Ecology and Geophysics, Australia*, **38**.

Fletcher, R., Grubb, H. and Godsalve, C. (1995), Estimating radiation balance by statistical inverion of ATSR-2 observations. *Proceedings of the 21st Annual Conference of the Remote Sensing Society*, 11 - 14 September 1995, University of Southampton, pp. 311-318.

Flynn, L. P. and Mouginis-Mark, P. J. (1992), Cooling rate of an active Hawaiian lava flow from nighttime spectroradiometer measurements, *Geophys. Res. Lett.*, **19**, 1783-1786.

Flynn, L. P. and Mouginis-Mark, P. J. (1994), Temperature of an active lava channel from spectral measurements, Kilauea Volcano, Hawaii. *Bull. Volcanol.*, **56**, 297-301.

Flynn, L. P., Mouginis-Mark, P. J. and Horton, K. A (1994), Distribution of thermal areas on an active lava flow field: Landsat observations of Kilauea, Hawaii, July 1991. *Bull. Volcanol.*, **56**, 284-296.

Francis, P.W. (1979), Infra-red techniques for volcano monitoring and prediction - a review. *J. Geol. Soc.*, **136**, 355-359.

Francis, P.W. and Rothery, D.A. (1987), Using the Landsat Thematic Mapper to detect and monitor active volcanoes: An example from Lascar volcano, northern Chile. *Geology*, **15,** 614-617.

Friedman, J.D. and Realmuto V.J. (in press), Observations of temporal variations in the radiant energy output of the Mount St. Helens dacite dome, September 22, 1989 and March 30, 1991. *Bull. Volcanol.*

Friedman, J.D. and Williams, R.S. (1968), Infrared sensing of active geologic processes. *Proceedings of the 5th Symposium on Remote Sesning*, University of Michigan, pp. 787-815.

Gaonac'h, H., Vandermeulebrouck, J., Stix, J. and Halbwachs, M. (1994), Thermal infrared satellite measurements of volcanic activity at Stromboli and Vulcano. *J. Geophys. Res.*, **99**, 9477-9485.

Gardeweg, M.C., Sparks, S., Matthews, S., Fuentealba, G., Murillo, M. and Espinoza, A. (1993), V Informe sobre el comportamiento del Volcan Lascar (II Region): Enero- Marzo 1993. Unpublished Report, Servico Nacional de Geologica y Mineria, Chile, pp. 1-14.

Gawarecki, S.J., Lyon, R.J.P. and Nordberg, W. (1965), Infrared spectral returns and imagery of the Earth from space and their application to geological problems, Scientific Experiments for Manned Orbital Flight. *American Astronaut. Soc., Science and Technology Series*, **4**, 13-133.

Glaze, L., Francis, P.W. and Rothery, D.A. (1989a), Measuring the thermal budgets of active volcanoes by satellite remote sensing. *Nature*, **338**, 135-136.

Glaze, L.S., Francis, P.W., Self, S. and Rothery, D.A. (1989b), The 16 September 1986 eruption of Lascar Volcano, north Chile: satellite investigations. *Bull. Volcanol.*, **51**, 149-160.

Godsalve, C. (1995), Bi-directional reflectance sampling by ATSR-2: a combined orbit and scan model. *Int. J. Remote Sens.*, **16**, 269-300.

Gray, W.A. and Müller, R. (1974), *Engineering Calculations in Radiative Heat Transfer.* (Oxford: Pergammn Press).

Great Britain Meteorological Office (1962), *Weather in the Mediterranean.* (London: H.M.S.O.), 362pp.

Green, R.O., Conel, J.E., Shimada, M. and Nakai, M. (1993), On-orbit calibration of the Japanese Earth Resources Satellite-1 Optical Sensor using the Airborne Visible-Infrared Imaging Spectrometer. *Proceedings of the 13th International Geoscience and Remote Sensing Symposium (IGARSS '93)*, August 1993, Tokyo, Japan, pp. 1312-1314.

Harris, A. J. L, Blake, S., Rothery, D. A. and Stevens, N. F. (1997), A chronology of the 1991 to 1993 Etna eruption using AVHRR data: implications for real time thermal volcano monitoring. *J. Geophys. Res.*, **102**, 7985-8003.

Harris, A. J. L., Swabey, S. E. J. and Higgins, J. (1995a), Automated thresholding of active lavas using AVHRR data, *Int. J. Remote Sens.*, **16**, 3681-3686.

Harris, A.J.L. and Rothery, D.A. (1995b), Thermal Monitoring of Volcanoes using data from the AVHRR. *Proceedings of the 21st Annual Conference of the Remote Sensing Society*, University of Southampton, 11-14 September 1995, pp. 528-535.

Harris, A.J.L., Rothery, D.A., Carlton, R.W., Langaas, S. and Mannstein, H. (1995c), Non-zero saturation of AVHRR thermal channels over high temperature targets: evidence from volcano data and a possible explanation. *Int. J. Remote Sens.*, **16,** 189-196.

Harris, A.J.L., Vaughan, R.A. and Rothery, D.A. (1995d), Volcano detection and monitoring using AVHRR data: the Krafla eruption, 1984. *Int J. Remote Sens.*, **16**, 1001-1020.

Head, J. W. and Wilson, L. (1986), Volcanic processes and landforms on Venus, theory, predictions and observations, *J. Geophys. Res.*, ***91***, 9407-9446.

Hirabayashi, J., Ohba T.,Nogami, K. and Yoshidi, M. (1995), Discharge rate of SO_2 from Unzen Volcano, Kyushu, Japan. *Geophys. Res. Lett.*, **22**, 1709-1712.

HMSO (1967), *Tables of Temperature, Relative Humidity and Precipitation for the World, Part III.* (London: H.M.S.O.), 153pp.

Holasek, R.E. and Rose, W.I. (1991), Anatomy of 1986 Augustine volcano eruptions as recorded by multispectral image processing of digital AVHRR weather satellite data. *Bull. Volcanol.*, **53**, 420-435.

Holdaway, R. (1993), U.K. Instruments for Mission to Planet Earth. *Space Technol.*, **13**, 561-567.

Houghton, J.T. (1986), *The Physics of Atmospheres, 2nd Edition.* (Cambridge: Cambridge University Press).

Houghton, J.T. and Morel, P. (1983), The word climate research programme. In *The Global Climate*, edited by J. T. Houghton. (Cambridge: Cambridge University Press).

Jedlovec, G.R. (1990), Precipitable water estimation from high-resolution split-window radiance measurements, *J. Appl. Meteorol.*, **29**, 863-876.

Kahle, A., Pallucconi, F. D., Hook, S. J., Realmuto, V. J. and Bothwell, G. (1991), The Advanced Spaceborne Thermal Emission and Reflection Radiometer (ASTER). *Int. J. Imag. Syst. Technol.*, **3**, 144-156.

Kaufman, Y.J. and Holben, B.N. (1993), Calibration of the AVHRR visible and near-IR bands by atmospheric scattering, ocean glint and desert reflection. *Int. J. Remote Sens.*, **14**, 21-52.

Keszthelyi, L. (1995), Measurements of the cooling at the base of pahoehoe flow, *Geophys. Res. Lett.*, **22**, 2195-2198.

Kidwell, K. (1995), *NOAA Polar Orbiter Data Users Guide.* (Washington D.C.: National Oceanic and Atmospheric Adminstration, National Environmental Satellite Data Information Service, Satellite Data Services Division).

Kilburn, C.R.J. (1993), Lava crusts, aa flow lengthening and the pahoehoe-aa transition. In *Active Lavas,* edited by C. R. J. Kilburn and G. Luongo. (London: UCL Press), pp. 263-280.

Kilburn, C.R.J. and Lopes, R.M.C. (1991), General patterns of flow field growth: aa and blocky lavas, *J. Geophys. Res.*, **93**, 721-732.

Kneizys, F., Shettle, E., Abreu, L., Chetwynd, J., Anderson, G., Gallery, W., Selby, J. and Clough, S. (1988), *Users guide to LOWTRAN 7.* Air Force Geophysics Laboratory, Environmental Research Paper 1010, Hanscom AFB, Massachusetts.

Lange, I.M. and Avent, J.C. (1975), Ground based thermal infrared surveys of Mount Rainier Volcano, Washington. *Bull. Volcanol.*, **38**, 929-943.

Le Guern, F., Carbonelle, J. and Tazieff, H. (1979), Erta 'Ale lava lake: Heat and gas transfer to the atmosphere. *J. Volcanol. Geotherm. Res.*, **6**, 27-48.

Lillesand T.M. and Kiefer, R.W. (1987), *Remote Sensing and Image Interpretation, 2nd edition.* (New York: John Wiley).

Llewellyn-Jones, D. T., Minnet, P. J., Saunders, R. W. and Zavody, A. M. (1984), Satellite multichannel infrared measurements of sea surface temperature of the N.E. Atlantic Ocean using AVHRR/2. Quarterly Journal of the Royal Meteorological Society, **110**, 613-631.

Malila, W.A. (1995), Comparison and cross-calibration of JERS-1 OPS and Landsat-5 TM multispectral data. *Proceedings of the Result Reporting Meeting of JERS-1 System Verification Program*, 29 November - 1 December 1994, Tokyo, Japan, pp. 161-170.

Markham, B.L. and Barker, J.L. (1987), Thematic Mapper bandpass solar exoatmospheric irradiances. *Int. J. Remote Sens.*, **8**, 517-523.

Mason, G. (1991), *Test and Calibration of the Along Track Scanning Radiometer, a Satellite-borne Infrared Radiometer Designed to Measure Sea Surface Temperature*, Ph.D. Thesis, Department of Atmospheric, Oceanic and Planetary Physics, University of Oxford.

Matson, M. (1984), The 1992 El Chichón volcano eruptions - a satellite perspective. *J. Volcanol. Geotherm. Res.*, **23**, 1-10.

Matson, M. and Dozier, J. (1981), Identification of subresolution high temperature sources using a thermal IR sensor. *Photogram. Eng. & Remote Sens.*, **47**, 1311-1318.

Matson, M. and Holben, B. (1987), Satellite detection of tropical burning in Brazil. *Int. J. of Remote Sens.*, **8**, 509-516.

Matthews, S.J., Gardeweg, M.C. and Sparks, R.S.J. (1997), Crater collapse and explosive eruptions as a result of magma degassing: the 1984 to 1996 cyclic activity of Lascar Volcano, Northern Chile. *Bull. Volcanol.*, **59**, 72-82.

McBirney, A.R. and Williams, H. (1969), *Geology and Petrology of the Galápagos Islands.* Geol. Soc. America Memoir 118, (Boulder, Colorado: Geol. Soc. of America).

McGuire, W., Kilburn, C. and Murray, J. (1995), *Monitoring Active Volcanoes: Strategies, Procedures and Techniques.* (London: UCL Press), 421pp.

McGuire, W.J., Norton, G.E., Sparks, R.S.J., Robertson, R. and Young, S.R. (1997), Report Of The Explosive Event Of September 17-18, 1996. *Monserrat Volcano Observatory Special Report 01*, 15pp.

Mouginis-Mark, P., Garbeil, H. and Flament, P. (1994), Effects of Viewing Geometry on AVHRR Observations of Volcanic Thermal Anomalies. *Remote Sens. Environ.*, **48**, 51-60.

Mouginis-Mark, P., Rowland, S. T. Garbeil, H., Flament, P. (1991a), AVHRR observations of the Kupianaha eruption, Hawaii. *EOS, Trans. American Geophys. Union,* 1991 Fall Meeting Program and Abstracts, pp. 562.

Mouginis-Mark, P., Rowland, S., Francis, P., Friedman, T. Garbeil, H., Gradie, J., Self, S., Wilson, L., Crisp, J., Glaze, L., Jones, K., Kahle, A., Pieri, D., Zebker, H., Kruger, A., Walter, L., Wood, C., Rose, W., Adams, J. and Wolff, R. (1991b), Analysis of active volcanoes from the Earth Observing System, *Remote Sens. Environ.,* **36**, 1-12.

Mouginis-Mark, P.J. (1995), Preliminary observations of volcanoes with the SIR-C radar. *IEEE Trans. Geosci. Remote Sens.*, **33**, 934-941.

Mouginis-Mark, P.J., Pieri, D.C., Francis, P.W., Wilson, L., Self, S., Rose, W.I., Wood, C.A. (1989), Remote sensing of volcanoes and volcanic terrains. *EOS Transactions of the American Geophysical Union*, **70**, pp. 1567-1575.

Moxham, R. (1970), Thermal features at some Cascade volcanoes as observed by aerial infrared surveys. *Bull. Volcanol.*, **34**, 77-106.

Moxham, R.M. (1971), Thermal surveillance of volcanoes. In *The Surveillance and Prediction of Volcanic Activity.* (Paris: UNESCO), pp. 103-124.

Moxham, R.M., Boynton, G.R. and Cote, C.E. (1972), Satellite telemetry of fumarole temperatures, Mount Rainier, Washington. *Bull. Volcanol.*, **36**, 191-199.

Munro, D.C. and Mouginis-Mark, P.J. (1990), Eruptive patterns and structure of Isla Fernandina, Galápagos Islands, from SPOT-1 HRV and large format camera images. *Int J. Remote Sens.*, **11,** 1501-1509.

Mutlow, C. T., Llewellyn-Jones, D. T., Závody, A. M. (1994), The Along Track Scanning Radiometer (ATSR), global validation results. *Proceedings of the Second ERS- 1 Symposium - Space at the Service of our Environment*, Hamburg, October 1993, pp. 1245-1249.

Nakada, S. (1992), Lava domes and pyroclastic flows of the 1991-1992 eruption at Unzen Volcano. In *Unzen Volcano the 1990-1992 Eruption*, editied by T. Yanagi, H. Okada, and K. Ohta, (Kyushu: Nishinippon and Kyushu University Press), pp. 56- 66.

Nakada, S. and Fujii, T. (1993), Preliminary report on the activity at Unzen Volcano (Japan), November 1990 - November 1991: dacite lava domes and pyroclastic flows. *J. Volcanol. Geotherm. Res.*, **54**, 319-333.

Nakada, S. and Shimizu, H. (1995), The 1991 - 1994 Activities of Unzendake Volcano. In *Report on volcanic activities and volcanological studies in Japan for the period from 1991 to 1994,* edited by H. Okada, Volcanol. Soc. Japan, Science Council of Japan, pp. 2-9.

Nakada, S., Myake, Y., Sato, H., Oshima, O. and Fujinawa, A., Endogenous growth of dacite dome and Unzen Volcano, Japan (1995), *Geology*, **23**, 157-160.

National Academy of Sciences (1987), *Confronting Natural Disasters: An International Decade for Natural Hazard Reduction.* (Washington, D.C.: National Academy of Sciences Press).

National Oceanic and Atmospheric Administration (1987), FAA consider volcano monitoring system. *Aviation Week & Space Technol.*, **127**, 30-31.

National Research Council (1995), *Earth Observations from Space, History, Promise, Reality*, (Washington D.C., Space Studies Board, NRC), 235pp.

Nishidai, T. (1993), Early results from 'Fuyo-1' Japan's Earth Resources Satellite (JERS-1). *Int. J. Remote Sens.*, **14**, 1825-1833.

Nishidai, T., Yoshie, T. and Tsu, H. (1994), Overall results of the Earth Resources Satellite 'Fuyo-1' Data Evaluation. *Proceedings of the Reporting Meeting of JERS-1 System Verification Program*, Tokyo, Japan, November 1994, pp. 31-39.

O'Brien, D.M. and Prata, A.J. (1990), Navigation of ERS-1 Along Track Scanning Radiometer (ATSR) images. *ESA Journal*, **14**, 448-465.

Ohta, K. (1984), *Unzen Volcano, Geography, Geology and Volcanic Phenomena.* (Nagasaki: Nagasaki Prefecture), 98 pp.

Oppenheimer, C. (1989), AVHRR volcano hotspot monitoring. *Proceedings of the 4th AVHRR Data Users Meeting*, Rothenburg, Germany, 5 - 8 August 1989, (Darmstadt-Eberstadt: EUMETSAT), pp. 335-338.

Oppenheimer, C. (1991), Lava flow cooling estimated from Landsat Thematic Mapper in infrared data: the Lonquimay eruption (Chile, 1989). *J. Geophys. Res.*, **96**, 21865-21878.

Oppenhiemer, C. (1993), Thermal distribution of hot volcanic surfaces constrained using three infrared bands of remote sensing data. *Geophys Res. Lett.*, **20**, 431-434.

Oppenhiemer, C. (1997), Remote sensing the colour and temperature of volcanic crater lakes. *Int. J. Remote Sens.*, **18**, 5-37.

Oppenheimer, C. and Francis, P. (1997), Remote sensing of heat, lava and fumarole emissions from Erta 'Ale volcano, Ethiopia. *Int. J. Remote Sens.*, **18**, 1661-1692.

Oppenheimer, C., Francis, P.W., Rothery, D.A. and Carlton, R.W.T. (1993), Infrared image analysis of volcanic thermal features: Lascar volcano, Chile 1984-1992. *J. Geophys. Res.*, **98**, 4269-4286.

Oppenhiemer, C. and Rothery, D.A. (1989), Infrared remote sensing of hot volcanoes assessed by field observations. *Proceedings of the 15th Annual Conference of the Remote Sensing Society*, University of Bristol, 13-15 September 1989, pp. 317-322.

Perry, W.J. and Crick, I.H. (1976), Aerial thermal infrared survey Rabaul area, Papua New Guinea. In *Volcanism in Australia,* edited by R.W. Johnson, (Oxford: Elsevier), pp. 211-221.

Pieri, D.C., Crisp, J. and Kahle, A.B. (1995), Observing volcanism and other transient phenomena with ASTER. *J. Remote Sens. Soc. Japan*, **15,** 56-61.

Pieri, D.C. and Glaze, L.S. (1989), Orbiting volcano observatory: a new small mission ? (absract). *EOS, Trans. American Geophys. Union*, **70**, pp. 1410.

Pieri, D.C., Glaze, L.S., Abrams, M.J. (1990), Thermal radiance observations of an active lava flow during the June 1984 eruption of Mount Etna. *Geology*, **18**, 1018-1022.

Pitts, D.R. and Sissom, L.E. (1977), *Theory and Problems of Heat Transfer.* (New York, McGraw-Hill), pp77.

Prata, A.J. (1989), Observations of Volcanic Ash Clouds in the 10-12 μm Window Using AVHRR/2 Data. *Int. J. Remote Sens.*, **10,** 751-761.

Prata, A.J.F., Cechet, R.P., Barton, I.J. and Llewellyn-Jones, D.T. (1990), The Along Track Scanning Radiometer for ERS-1 Scan Geometry and Data Simulation. *IEEE Trans. Geosci. Remote Sens.*, **28**, 3-13.

RAL (in press), *ATSR 1.6 μm Channel Data Calibration Report - Results of User Studies.* (Didcot : Rutherford Appleton Laboratory Space Science Department).

Read, P., Hardie, A., Magraw, J. Taylor, H. and Jelly, J. (1992), A calibration system, using an opal diffuser, for the visual channels of the along track scanning radiometer, ATSR-2. *Proceedings of Institute of Physics Conference on Photoelectronic Image Devices*, London, UK, September 1991, pp. 207-213.

Realmuto, V.J., Hon, K., Kahle, A.B., Abbot, E.A. and Pieri, D.C. (1992), Multispectral thermal infrared mapping of the 1 October 1988 Kupaianaha flow field, Kilauea Volcano, Hawaii, *Bull. Volcanol.*, **55**, pp. 33-44.

Rees, J.D. (1979), Effects of the eruption of Parícutin volcano on landforms, vegetation and human occupancy. In *Volcanic Activity and Human Ecology*, edited by P.D. Payson and D.K. Grayson, (New York: Academic Press), pp. 293-338.

Roberts, E. and Petkovc, M. (1993), The infrared focal plane array of the Along Track Scanning Radiometer; assembly, integration and test. *J. Electrical and Electronics Eng.*, **13**, 303-309.

Robinson, J.M. (1991), Fire from space: Global fire evaluation using infrared remote sensing. *Int. J. Remote Sens.*, **12**, 3-24.

Rothery, D.A. (1992), Monitoring and warning of volcanic eruptions by remote sensing. In *Geohazards Natural and Man-made,* edited by H.J.H. McHall and D.J. Laming, (London: Chapman-Hall), pp.25-32.

Rothery, D.A., Borgia, A., Carlton, R.W. and Oppenheimer, C. (1992), The 1992 Etna lava flow imaged by Landsat TM. *Int J. Remote Sens.*, **13**, 2759-2763.

Rothery, D.A. and Pieri, D.C. (1993), Remote sensing of active lava. In *Active Lavas* edited by C.R.J. Kilburn and G.Luongo, (London: UCL Press), pp. 203-231.

Rothery, D.A., Francis, P.W. and Wood, C.A. (1988), Volcano monitoring using short wavelength infrared data from satellites. *J. Geophys. Res.*, **93,** 7993-8008.

Rowland, S.K. (1996), Slopes, lava flow volumes and vent distribution of Volcán Fernandina, Gápagos Islands. *J. Geophys. Res.*, **101**, 27657-27672.

Rowland, S.K. and Munro, D.C. (1992), The Caldera of Volcán Fernandina: a remote sensing study of its structure and recent activity. *Bull. Volcanol.*, **55**, 97-109.

Salisbury, J.W. and D'Aria, D.M. (1992), Emissivity of terrestrial materials in the 8-14 μm atmospheric window. *Remote Sens. Environ.*, **42**, 83-106.

Salisbury, J.W. and D'Aria, D.M. (1994), Emissivity of Terrestrial Materials in the 3-5 μm Atmospheric Window. *Remote Sens. Environ.*, **47**, 345-361.

Salomonson, V.V., Barnes, W.L., Maymon, P.W., Montgomery, H.E. and Ostrow, H. (1989), MODIS: Advanced facility instrument for studies of the Earth as a system. *IEEE Trans. Geosci. Remote Sens.*, **27,** 145-153.

Sato, H., Fujii, T. and Nakada, S. (1992), Crumbling of dacite dome lava and generation of pyroclastic flows at Unzen Volcano. *Nature,* **360**, 664-666.

Saunders, R.W. (1986), An automated scheme for the removal of cloud contaminations from AVHRR radiances over Western Europe. *Int. J. Remote Sens.*, 7, 867-886.

Scorer, R.S. (1986), Etna: The eruption of Christmas 1985 as seen by meteorological satellite. *Weather*, **41**, 378-34.

Scorer, R.S. (1987), Hotspots and plumes: Observation by meteorological satellite. *Atm. Environ.*, **21**, 1427 -1435.

SEAN (1979), Sierra negra. *SEAN Bulletin*, **4**, 3-6.

Setzer, A.W. and Verstraete, M.M. (1994), Fire and glint in AVHRR's channel 3: a possible reason for the non-saturation mystery. *Int. J. Remote Sens.*, **15**, 711-718.

Shilin, B.V. and Komarov, V.B. (1968), Application of infrared aerial recording techniques to studies of volcanoes and thermal activities of Kamchatka Peninsula.

Proceedings of the 5th Symposium of Remote Sensing, University of Michigan (addendum), pp. 1-8.

Shimada, M. and Nakai, M. (1993), *Conversion formula for OPS DN to input radiance.* NASDA Document No. HE-93066, Earth Observing Centre/National Space Development Agency of Japan, Saitama-Ken, Japan.

Short, N.M. (1982), Landsat: A worldwide Perspective. In *The Landsat Tutorial Workbook*, (Washington D.C., National Aeronautics and Space Administration), pp. 455-475.

Shin, D., Pollard, J. K. and Muller, J-P. (1997), Accurate geometric correction of ATSR images. *IEEE Trans. Geosci. Remote Sens.*, ***35***, 997-1005.

Simkin T. and Howard K.A. (1970), Caldera collapse in the Galápagos Islands, 1968. *Science*, **169**, 429-437.

Simkin, T. (1984), Geology of the Gálapagos Islands. In *Galápagos Key Environments*, (Oxford: Pergammon Press), pp.15-41.

Simkin, T. and Kreuger, A.F. (1977), Skylab 4 observations of volcanoes. Part B. Summit eruption of Fernandina Caldera, Galápagos Islands, Ecuador. In *Skylab Explores the Earth*, NASA Special Publication No. 380, pp.171-172.

Simkin, T. and Siebert, L. (1994), *Volcanoes of the World.* (Tuscon: Geoscience Press), 229pp.

Smith, A., Saunders, R. and Zavody, A. (1994), The validation of ATSR using aircraft radiometer data over the tropical Atlantic. *J. Atmos. & Oceanic Technol.*, **11**, 789-800.

Smithsonian Institution (1992a), Etna. *GVN Bulletin,* **17**, 2, 12-16.

Smithsonian Institution (1992b), Lascar. *GVN Bulletin*, **17**, 5, 12-13.

Smithsonian Institution (1992c), Lascar. *GVN Bulletin,* **17**, 6, 10-11.

Smithsonian Institution (1993a), Lascar. *GVN Bulletin*, **18**, 4, 2-6.

Smithsonian Institution (1993b), Lascar. *GVN Bulletin,* **18**, 8, 3-4.

Smithsonian Institution (1993c), Lascar. *GVN Bulletin,* **18,** 11, 11-12.

Smithsonian Institution (1994a), Lascar. *GVN Bulletin,* **19**, 3, 7-8.

Smithsonian Institution (1994b), Unzen. *GVN Bulletin*, **19**, 5, 15-16.

Smithsonian Institution (1994c), Lascar. *GVN Bulletin*, **19,** 11, 7.

Smithsonian Institution (1995a), Fernandina. *GVN Bulletin,* **20**, 1, 2-3.

Smithsonian Institution (1995b), Fernandina. *GVN Bulletin,* **20**, 2,11-14.

Smithsonian Institution (1995c), Fernandina. *GVN Bulletin,* **20**, 3, 13-14.

Smithsonian Institution (1995d), Fernandina. *GVN Bulletin,* **20**, 5, 4.

Smithsonian Institution (1995e), Fernandina. *GVN Bulletin*, **20**, 8, 4-5

Smithsonian Institution (1995f), Lascar. *GVN Bulletin,* **20,** 3, 14-15.

Smithsonian Institution (1995g), Lascar. *GVN Bulletin,* **20**, 6, 11-12.

Sobrino, J.A., Li, Z.-L., Stoll, M.P. and Becker, F. (1994), Improvements in the split-window technique for land surface temperature determination. *IEEE Trans. Geosci. Remote Sens.*, **32**, 243-253.

Stephens, G. (1993), Mt. Spurr Ash Plume. *Int. J. Remote Sens.*, **14**, 2905-2906.

Stevens, N. F., Murray, J. B., Wadge, G. (1997), The volume and shape of the 1991-1993 lava flow field at Mount Etna, Sicily. *Bull. Volcanol.*, **58**, 449-454.

Stoiber, R.E. and Williams, S.N. (1990), Monitoring active volcanoes and mitigating volcanic hazards: the case for including simple approaches. *J. Volcanol. Geotherm. Res.*, **42**, 129-149.

Stricker, N.C.M., Hahne, A., Smith, D.L., Delderfield, J., Oliver, M.B. and Edwards, T. (1995), ATSR-2: The evolution in it's design from ERS-1 to ERS-2. *ESA Bulletin*, **83**, 32-37.

Suwa, A. and Tanaka, Y. (1959), The changes in the temperature of the fumaroles in the crater of Miharayama, Oshima, in connection with the activities of the volcano. *Bull. Volcanol. Soc. Japan*, **3**, 107-118.

Tanguy, J.C. and Biquand, D. (1967), Quelques propriétés physiques du magma actuel de Etna. *C. R. Acad. Sci. Paris*, **264D**, 699-702.

Tinker, D., Pick, D.R., Stringer, S.J. and Woods, C.G. (1985), The design of the focal plane assembly for the Along Track Scanning Radiometer. *Proceedings of SPIE 'Instrumentation for Optical Remote Sensing from Space'*, **589**, pp. 129-136.

Turcotte, D. L. and Schubert, G., *Geodynamics.* (New York, John Wiley and Sons), pp449.

Umakoshi, K., Shimuzu, H., Matsumo, N. and Ohta, K. (1992), Temperature measurements of lava domes and pyroclastic flows by infrared thermal video system. In *Unzen Volcano the 1990-1992 Eruption*, editied by T. Yanagi, H. Okada, and K. Ohta, (Kyushu: Nishinippon and Kyushu University Press), pp. 44-48

Urai, M. and Isobe, I. (1995), Surface temperature change of Unzen Volcano with night-time Landsat data. *J. Remote Sens. Soc. of Japan*, **15**, 3-15.

Wen, S. and Rose, W.I. (1994), Retrieval of sizes and total masses of particles in volcanic clouds using AVHRR bands 4 and 5. *J. Geophys. Res.*, **99,** 5421-5431.

Wiesnet, D.R. and D'Aguanno, J. (1982), Thermal imagery of Mount Erebus from the NOAA 6 satellite. *Antarctic J. U.S.*, **17**, 32-34.

Williams, H. (1932), The history and character of volcanic domes. *Bull. Dept. Geol. Soc.*, University of California Publication 21, 51-146.

Woods, A.W. and Kienle, J. (1994), The dynamics and thermodynamics of volcanic clouds. *J. Volcanol. Geotherm. Res.*, **62,** 273-299.

Woods, A.W., Holasek, R.E. and Self, S. (1995), Wind-driven dispersal of volcanic ash plumes and its control on the thermal structure of the plume-top. *Bull. Volcanol.*, **57,** 283-292.

Wooster, M.J. (1996), In orbit calibration of the ATSR-1 1.6 μm channel using high resolution data from the JERS-1 (Fuyo-1) optical sensor. *Int J. Remote Sens.*, **17**, 1069-1074.

Wooster, M. J. and Kaneko, T. (in press), Time-series analysis of lava dome development at Unzen volcano, Japan using infrared data from the Along Track Scanning Radiometer. *J. Geophys. Res.*

Wooster, M. J., Richards, T. S. and Kidwell, K. (1995), NOAA-11 AVHRR/2 – thermal channel calibration update. *Int J. Remote Sens.*, **16**, 359-363.

Wooster, M. J., Sear, C. B., Patterson, G. and Haigh, J. (1994), Tropical lake surface temperatures from locally received NOAA 11 AVHRR data - comparison with *in situ* measurements. *Int J. Remote Sens.*, **15**, 183-189.

Wooster, M.J. and Rothery, D.A. (1997a), Time-series analysis of effusive volcanic activity using the ERS Along Track Scanning Radiometer : the 1995 eruption of Fernandina Volcano, Galápagos Islands. *Remote Sens. Environ.*, **62**, 109-117.

Wooster, M. J. and Rothery, D. A. (1997b). Thermal monitoring of Lascar Volcano, Chile using infrared data from the Along Track Scanning Radiometer: a 1992-1995 time-series, *Bull. Volcanol.*, **58**, 566-579.

Wooster, M.J., Rothery, D.A., Sear, C.B. and Carlton, R.W.T. (in press), Monitoring the development of active lava domes using data from the ERS-1 Along Track Scanning Radiometer. *Adv. Space Res.*

Zavody, A.M., Gorman, M.R., Lee, D.J., Eccles, D., Mutlow, C.T. and Llewellyn-Jones, D.T. (1994), The ATSR data processing scheme developed for the EODC, *Int. J. Remote Sens.*, **15,** 827-843.

Appendix A.

Example IDL routine: extraction of volcanic hotspots

A.1. Details

This routine, written in Interactive Data Language (IDL), extracts relevant data from a set of ATSR-1 BT data products containing a volcanic hotspot. A version for use with ATSR-2 BT data products has also been produced. The set of data products is listed in an ASCII text file to which the IDL routine refers. For each scene the actual volcano location is selected as the pixel with the greatest 1.6 μm signal within a 10 x 10 pixel box surrounding the input volcano latitude/longitude location. This methodology was chosen to account for any inaccuracies associated with the ATSR geocoding operations, these being enhanced by the general high elevation of volcanic terrains. For each scene a window of data is extracted surrounding the identified volcano location, with additional statistics taken from non-volcanic areas in order to identify the level of background variation. The extracted time-series statistics can then be passed to other IDL routines and/or PC-based spreadsheets for further analysis.

A.2. Program listing

```
;; ---------------------------------------------------------------------------------------------- ;;
;; THIS PROGRAM ANALYSES A SPECIFIC (VOLCANIC) AREA IN A SET OF ATSR-1 BT PRODUCTS AND EXTRACTS THE STATISTICS OF ANY HOTSPOTS WITH A 1.6 µm SIGNAL.
;; ---------------------------------------------------------------------------------------------- ;;
;; SET UP INITIAL VARIABLES
pointlat=0.0 & pointlon=0.0
xsize = 0
ysize = 0
directory = ''
output_filename = ''
;; ---------------------------------------------------------------------------------------------- ;;
;;  ASK USER TO INPUT VARIABLES (E.G. VOLCANO LOCATION & WINDOW SIZE)
print, 'Please input the approx. latitude of the volcano (to 3 significant figures)'
read, pointlat
print, 'Please input the approx. longitude of the point (to 3 significant figures)'
read, pointlon
print, 'Input X pixel size of window either side of this (e.g. 2 gives a total of 5 pixels).'
read, xsize
print, 'Input Y pixel size of window either side of this (e.g. 2 gives a total of 5 pixels).'
read, ysize
print, 'Please type in the directory the products are in.'
read, directory
print, 'Please type in the filename to save the answer as.'
read, output_filename
;; ---------------------------------------------------------------------------------------------- ;;
;; THE LIST OF ATSR-1 BT DATA PRODUCTS TO BE ANALYSED MUST BE CONTAINED WITHIN A SEPARATE *.TXT FILE - THE USER NOW IDENTIFIES THAT FILE TO THE PROGRAM.
print, 'Now pick the *.txt file that you have listed the names to'
;/* Open the product file and read/display the contentsfilename=pickfile(/read,filter='*.bt')
list=pickfile(/read,filter='*.txt*')
;; ---------------------------------------------------------------------------------------------- ;;
;; DIMENSION A VARIABLE TO STORE UP TO 500 FILENAMES FROM THE IDENTIFIED LIST
temp = ''
```

```
names = strarr(500)
number = 0
openr, 1, list
repeat begin
        readf, 1, temp
        names(number) = temp
        number = number + 1
endrep until names(number-1) eq 'end'
close,1
number = number - 1
;; ---------- ;;
;; NOW DIMENSION ARRAYS TO STORE THE IMPORTED ATSR-1 DATA (THIS SECTION ADAPTED FROM THE ATSR-1 BT PRODUCT READER SUPPLIED IN BAILEY [1995]).
primary_head = {file_name: bytarr(46), node_time: bytarr(15), node_x_coord: bytarr(12), node_y_coord: bytarr(12), node_z_coord: bytarr(12),$
node_x_velocity: bytarr(10), node_y_velocity: bytarr(10), node_z_velocity: bytarr(10), image_time: bytarr(21), node_time_text: bytarr(21), ssp_lat: bytarr(10), ssp_lon: bytarr(10), asc_node_lon: bytarr(10), along_track_distance : bytarr(6), state_vector_source: bytarr(20),$
nad_elevs: bytarr(8,11),$
nad_elev_diff: bytarr (8,11), nad_azim_diff: bytarr(8,11), frw_elevs: bytarr(8, 11), frw_elev_diff: bytarr (8,11), frw_azim_diff: bytarr(8,11), geoloc_present: bytarr(2), nad_1_present: bytarr(2), nad_2_present: bytarr(2), nad_3_present: bytarr(2), for_1_present: bytarr(2),$
for_2_present: bytarr(2), for_3_present: bytarr(2), cooler_tip_temp: bytarr(8), detector_temps: bytarr(8,4), unused : bytarr(217) }
secondary_head = bytarr(1024)
nad_chan_1 = intarr(512, 512)
nad_chan_2 = intarr(512, 512)
nad_chan_3 = intarr(512, 512)
for_chan_1 = intarr(512, 512)
for_chan_2 = intarr(512, 512)
for_chan_3 = intarr(512, 512)
grid_line =lonarr(256)
offsets_line = bytarr(1024)
temp_line = intarr(512)
```

```
lat_grid = fltarr(512,512)
lon_grid = fltarr(512,512)
;; ---------------------------------------------------------------------------------------------- ;;
;; NOW DIMENSION ARRAYS TO STORE THE EXTRACTED HOTSPOT AREA DATA
xloc = intarr(number)
yloc = intarr(number)
lats = fltarr(number, (xsize*2+1),(ysize*2+1))
lons = fltarr(number, (xsize*2+1),(ysize*2+1))
n16 = intarr(number,  (xsize*2+1),(ysize*2+1))
f16 = intarr(number,  (xsize*2+1),(ysize*2+1))
n37 = intarr(number,  (xsize*2+1),(ysize*2+1))
f37 = intarr(number,  (xsize*2+1),(ysize*2+1))
n11 = intarr(number,  (xsize*2+1),(ysize*2+1))
f11 = intarr(number,  (xsize*2+1),(ysize*2+1))
n12 = intarr(number,  (xsize*2+1),(ysize*2+1))
f12 = intarr(number,  (xsize*2+1),(ysize*2+1))
julian_day = fltarr(number)
year = strarr(number)
month = strarr(number)
day = strarr(number)
nsat_zen=fltarr(number)
fsat_zen=fltarr(number)
sun_zen=fltarr(number)
meannoisen16=fltarr(number)
meannoisef16=fltarr(number)
sdnoisen16=fltarr(number)
sdnoisef16=fltarr(number)
;; ---------------------------------------------------------------------------------------------- ;;
;; NOW LOAD IN EACH BT PRODUCT IDENTIFIED IN THE *.TXT FILE AND EXTRACT THE
RELEVANT DATA(THIS SECTION ADAPTED FROM THE ATSR-1 BT PRODUCT READER SUPPLIED
IN BAILEY [199]).
for i = 0, (number-1) do begin
        openr, 1, directory+'/'+names(i), /fixed, 1024
        readu, 1, primary_head
```

```
        readu, 1, secondary_head
        if(fix(string(primary_head.geoloc_present)) eq 1) then begin
        for lat_loop = 0, 511 do begin
                readu, 1, grid_line
                byteorder, grid_line, /lswap
                lat_grid(0, lat_loop) = float(grid_line) / 1000.0
                readu, 1, grid_line
                byteorder, grid_line, /lswap
                lat_grid(256,lat_loop) = float(grid_line)/1000.0
         endfor
         for lon_loop = 0,511 do begin
                readu, 1, grid_line
                byteorder, grid_line, /lswap
                lon_grid(0,lon_loop) = float(grid_line)/1000.0
                readu, 1, grid_line
                byteorder, grid_line, /lswap
                lon_grid(256,lon_loop) = float(grid_line)/1000.0
         endfor
         for offsets_loop = 0, 511 do begin
                readu, 1, offsets_line
         endfor
endif
if (fix(string(primary_head.nad_1_present)) eq 1) then begin
         for temp_loop = 0,511 do begin
                readu, 1, temp_line
                byteorder, temp_line, /sswap
                nad_chan_1(0,temp_loop) = abs(temp_line)
       endfor
       endif
       if (fix(string(primary_head.nad_2_present)) eq 1) then begin
       for temp_loop = 0,511 do begin
                readu, 1, temp_line
                byteorder, temp_line, /sswap
                nad_chan_2(0,temp_loop) = abs(temp_line)
```

```
endfor
 endif
 if (fix(string(primary_head.nad_3_present)) eq 1) then begin
  for temp_loop = 0,511 do begin
          readu, 1, temp_line
           byteorder, temp_line, /sswap
           nad_chan_3(0,temp_loop) = abs(temp_line )
  endfor
  endif
  if (fix(string(primary_head.for_1_present)) eq 1) then begin
  for temp_loop = 0,511 do begin
          readu, 1, temp_line
          byteorder, temp_line, /sswap
          for_chan_1(0,temp_loop) = abs(temp_line)
  endfor
endif
if (fix(string(primary_head.for_2_present)) eq 1) then begin
for temp_loop = 0,511 do begin
          readu, 1, temp_line
          byteorder, temp_line, /sswap
         for_chan_2(0,temp_loop) = abs(temp_line)
endfor
endif
if (fix(string(primary_head.for_3_present)) eq 1) then begin
for temp_loop = 0,511 do begin
          readu, 1, temp_line
          byteorder, temp_line, /sswap
          for_chan_3(0,temp_loop) = abs(temp_line)
          endfor
          endif
;; ------------------------------------------------------------------------------------------ ;;
  ;; SEPARATE THE 1.6 AND 3.7 µM IMAGES
  nad_chan_4 = intarr(512,512)
  for_chan_4 = intarr(512,512)
```

```
chan_4nad_mask = where(nad_chan_3 lt 10001, count)
if (count gt 0) then nad_chan_4(chan_4nad_mask)=nad_chan_3(chan_4nad_mask)
if (count gt 0) then nad_chan_3(chan_4nad_mask)=0
chan_4for_mask = where(for_chan_3 lt 10001, count)
if (count gt 0) then for_chan_4(chan_4for_mask)=for_chan_3(chan_4for_mask)
if (count gt 0) then for_chan_3(chan_4for_mask) =0
;; ------------------------------------------------------------------------------------------ ;;
 ;; MAKE A COPY OF THE 1.6 MICRON CHANNEL IMAGE FOR THE NOISE ASSESSMENT
copy_nad_chan_4 = nad_chan_4
copy_for_chan_4 = for_chan_4
;; ------------------------------------------------------------------------------------------ ;;
;; SELECT THE CENTRE OF THE EXTRACTION WINDOW TO MATCH THE USERS CHOSEN
LOCATION TO WITHIN 0.001 DEGREES. IF IT DOES NOT THEN SEARCH IN 0.001
DEGREE STEPS.
latbox = 0.001
lonbox = 0.001
odd_even = 1
repeat begin
        lat_diff = lat_grid - pointlat
        lon_diff = lon_grid - pointlon
        lonloc = where(abs(lon_diff) lt lonbox, loncount) &
        latloc=where(abs(lat_diff) lt latbox, latcount)
        new=intarr(512,512)
        new2 = new
        if (latcount gt 0 ) then new(latloc) = 1
        if (loncount gt 0 ) then new2(lonloc)= 1
        new3=new*new2
        loc = where(new3 gt 0,final_count)
        ;; FINAL_COUNT SHOULD NOW = 1 - IF NOT INCREASE BOX AND TRY AGAIN
        odd_even = odd_even +1
        if (fix(odd_even/2.0) eq (odd_even/2.0)) then latbox = latbox + 0.001 else
        lonbox = lonbox + 0.001
endrep until final_count gt 0
;; IF FINALCOUNT IS > 1 (I.E.2 OR MORE PIXELS MATCH) THEN TAKE THE 1ST ONE
 a = loc(0) & loc = a
```

```
;; ------------------------------------------------------------------------------------------ ;;
    ;; CONVERT THIS 1D SUBSCRIPT INTO AN X AND Y LOCATION
    chosen_xlocation = fix(loc - (fix(loc/512.00)*512.00))
    chosen_ylocation  = fix(loc/512.00)
    ;;NOW EXTRACT THE DATA FOR AN (+/XSIZE,+/-YSIZE) WINDOW CENTRED ON THE
    POINT OF MAXIMUM 1.6 µM RADIANCE WITHIN THE CHOSEN AREA
    centrex = chosen_xlocation(0)-xsize(0)
    centrey = chosen_ylocation(0)-ysize(0)
    extrac_n16 = extrac(nad_chan_4 ,centrex, centrey,(xsize*2+1),(ysize*2+1) )
    extrac_f16 = extrac(for_chan_4 ,centrex, centrey,(xsize*2+1),(ysize*2+1) )
    extrac_n37 = extrac(nad_chan_3 ,centrex, centrey,(xsize*2+1),(ysize*2+1) )
    extrac_f37 = extrac(nad_chan_3 ,centrex, centrey,(xsize*2+1),(ysize*2+1) )
    extrac_n11 = extrac(nad_chan_2 ,centrex, centrey,(xsize*2+1),(ysize*2+1) )
    extrac_f11 = extrac(for_chan_2 ,centrex, centrey,(xsize*2+1),(ysize*2+1) )
    extrac_n12 = extrac(nad_chan_1 ,centrex, centrey,(xsize*2+1),(ysize*2+1) )
    extrac_f12 = extrac(nad_chan_1 ,centrex, centrey,(xsize*2+1),(ysize*2+1) )
    extrac_lats= extrac(lat_grid ,centrex, centrey,(xsize*2+1),(ysize*2+1) )
    extrac_lons= extrac(lon_grid ,centrex, centrey,(xsize*2+1),(ysize*2+1) )
;; ------------------------------------------------------------------------------------------ ;;
    ;; NOW SET THE STRORAGE VARIABLES TO THE EXTRACTED ARRAYS
    ;; FIRST THE DATE OF THE PRODUCT
    ;; FIND THE LOCATION OF THE $ IN THE FILENAME - THE DATE IS AFTER THIS
    dollar_location = strpos(string(primary_head.file_name),'$')
    year(i) = strmid(string(primary_head.file_name),dollar_location+1,1)
    month(i) = strmid(string(primary_head.file_name),dollar_location+2,2)
    day(i) = strmid(string(primary_head.file_name),dollar_location+4,2)
    julian_day(i) = julday(month(i),day(i),(1990+year(i)))
    n16(i,*,*) = extrac_n16
    f16(i,*,*) = extrac_f16
    n37(i,*,*) = extrac_n37
    f37(i,*,*) = extrac_f37
    n11(i,*,*) = extrac_n11
    f11(i,*,*) = extrac_f11
    n12(i,*,*) = extrac_n12
```

```
f12(i,*,*) = extrac_f12
lats(i,*,*) = extrac_lats
lons(i,*,*) = extrac_lons
xloc(i,*,*) = chosen_xlocation
yloc(i,*,*) = chosen_ylocation
;; ------------------------------------------------------------------------------------------ ;;
;; GET THE 1.6 MICRON NOISE FROM A 50 X 50 WINDOW;
xn16 =  extrac(copy_nad_chan_4,(chosen_xlocation(0)-25),(chosen_ylocation(0)-
25),50,50)
xf16 =  extrac(copy_for_chan_4,(chosen_xlocation(0)-25),(chosen_ylocation(0)-
25),50,50)
;; SET ANY ANOMALOUSLY HIGH VALUES TO THE MEAN OF THE 50 X 50 WINDOW
highn16 = where(xn16 gt 10, tempcountn)
highf16 = where(xf16 gt 10, tempcountf)
;; NOW SET 1ST PIXEL TO 3 SO THAT VARIANCE >0 -AFFECTS THE MOMENT
MINIMALLY
xn16(0,0) = 3
xf16(0,0) = 3
momentn16 = moment(xn16)
momentf16 = moment(xf16)
if (tempcountn gt 0) then xn16(highn16) = fix(momentn16(0))
if (tempcountf gt 0) then xf16(highf16) = fix(momentf16(0))
xn16(0,0) = 3
xf16(0,0) = 3
momentn16 = moment(xn16)
momentf16 = moment(xf16)
meannoisen16(i) = momentn16(0)
meannoisef16(i) = momentn16(0)
sdnoisen16(i) = sqrt(momentn16(1))
sdnoisef16(i) = sqrt(momentf16(1))
;; ------------------------------------------------------------------------------------------ ;;
;; TO GET THE SATELLITE ZENITH ANGLES
;; NADIR VIEW
pri_sun_elev = fltarr(1)
pri_sun_elev(0) = string(primary_head.nad_elevs(*,((chosen_xlocation/51))))
```

```
subs_sun_elev = fltarr(1)
subs_sun_elev(0) = string(primary_head.nad_elevs(*,(1+(chosen_xlocation/51))))
pri_sun_sat_elev_diff = fltarr(1)
pri_sun_sat_elev_diff(0)=
string(primary_head.nad_elev_diff(*,((chosen_xlocation/51))))
subs_sun_sat_elev_diff = fltarr(1)
subs_sun_sat_elev_diff(0)=
string(primary_head.nad_elev_diff(*,(1+(chosen_xlocation/51))))
nsun_elev = pri_sun_elev(0)+ ((subs_sun_elev(0)-
pri_sun_elev(0))/51)*(chosen_xlocation-(51*fix(chosen_xlocation/51)))
nsun_sat_elev_diff = pri_sun_sat_elev_diff(0)+ ((subs_sun_sat_elev_diff(0)-
pri_sun_sat_elev_diff(0))/51)*(chosen_xlocation-(51*fix(chosen_xlocation/51)))
nsat_zen(i) = 90 -( nsun_elev + nsun_sat_elev_diff)
sun_zen(i) = 90 - nsun_elev
pri_sun_elev = fltarr(1)
;; FORWARD VIEW
pri_sun_elev(0) = string(primary_head.frw_elevs(*,((chosen_xlocation/51))))
subs_sun_elev = fltarr(1)
subs_sun_elev(0) = string(primary_head.frw_elevs(*,(1+(chosen_xlocation/51))))
pri_sun_sat_elev_diff = fltarr(1)
pri_sun_sat_elev_diff(0) =
string(primary_head.frw_elev_diff(*,((chosen_xlocation/51))))
subs_sun_sat_elev_diff = fltarr(1)
subs_sun_sat_elev_diff(0) =
string(primary_head.frw_elev_diff(*,(1+(chosen_xlocation/51))))
fsun_elev = pri_sun_elev(0)+ ((subs_sun_elev(0)-
pri_sun_elev(0))/51)*(chosen_xlocation-(51*fix(chosen_xlocation/51)))
fsun_sat_elev_diff = pri_sun_sat_elev_diff(0)+ ((subs_sun_sat_elev_diff(0)-
pri_sun_sat_elev_diff(0))/51)*(chosen_xlocation-(51*fix(chosen_xlocation/51)))
fsat_zen(i) = 90 -(fsun_elev + fsun_sat_elev_diff)
;; ------------------------------------------------------------------------------------------ ;;
;; PRINT EXTRACTED DATA AND LOOP BACK TO LOAD THE NEXT BT FILE IN THE LIST
close,1
print, 'Processing Image Number ',i, ' Central 16 DN =', n16(i,xsize,ysize)
print, 'Got in +/- ', latbox,lonbox, ' degs and pixel no. = ', final_count
print, ' '
```

```
        print, ' '
endfor
;; ---------------------------------------------------------------------------------------------- ;;
;; OUTPUT THE WHOLE DATASET TO AN ASCII FILE
mean16 = intarr(11)
sd16 = intarr(11)
max16 = intarr(11) & for i=0,10 do max16(i) = max(n16(i,*,*))
min16 = intarr(11) & for i=0,10 do min16(i) = min(n16(i,*,*))
for i = 0,10 do mean16(i) = total(n16(i,*,*))/9
        for i = 0,10 do begin &  temp =  moment(n16(i,*,*), sdev=sd) & sd16(i) = sd &
endfor
openw,1, output_filename
for i = 0,10 do printf,1, names(i),',', n16(i,1,1), ',',min16(i),',', max16(i),',', n11(i,1,1),',',
nsat_zen(i),',',sun_zen(i),',',xloc(i), ',',yloc(i),',', lats(i,1,1), ',',lons(i,1,1),',', julian_day(i),',',
day(i),',', month(i),',', year(i), ',',mean16(i), ',',sd16(i)
close,1
stop
end
;; ---------------------------------------------------------------------------------------------- ;;
```

Appendix B.

The Split Window Variance Ratio technique

B.1 Background

The split window variance ratio (SWVR) technique was developed by Jedlovec (1990) and Sobrino *et al.* (1994) for the remote estimation of atmospheric transmittance in the longwave infrared (11 and 12 μm) wavebands of the AVHRR and ATSR instruments. The technique is based on the assumption that, over an appropriately sized portion of the Earth's surface, the atmosphere is spatially invariant whilst the surface temperature is spatially varying. If N pixels cover such an area, then Jedlovec (1990) shows that the atmospheric transmittance at 11 μm (τ_{11}) can be calculated from the covariance and variance of the 11 and 12 μm brightness temperatures (Equation B.1). The requirement for a constant emissivity can be met by using data collected over a water surface.

$$\left(\tau_{11}\right)^{b} = \frac{\sum_{k=1}^{N}(T_{11}-\overline{T_{11}})(T_{12}-\overline{T_{12}})}{\sum_{k=1}^{N}(T_{11}-\overline{T_{11}})^{2}} \qquad \text{(B.1)}$$

where τ_{11} is the atmospheric transmission in the 11 μm waveband

T_{11} is the 11μm brightness temperature (K)

T_{12} is the 12 μm brightness temperature (K)

b is a constant dependant upon the band-averaged absorption coefficients for water vapour and other gases (B= 2.09 for the ATSR nadir view)

Since atmospheric transmittances at 11 and 12 μm are well related (Llewellyn Jones *et al.*, 1984), the calculated value of τ_{11} can then be used to estimate T_{12} if required.

B.2. Application

I meet the requirement for a spatially varying temperature surface, of uniform emissivity, by taking a 25 x 25 pixel subscene of ATSR nadir-view data, obtained near a sea surface temperature front. Using these data, τ_{11} is then estimated from application of Equation B.1.

At any particular pixel, the radiance measured by the ATSR 11 μm channel is well approximated by Equation B.2 which, due to the high emissivity of water, neglects the effect of reflected downwelling atmospheric radiation.

$$R_{11} = \varepsilon_{11}\tau_{11}L_{11}(T_{sst}) + Ra_{11}^{\uparrow} \qquad \text{(B.2)}$$

where R_{11} is the spectral radiance reaching ATSR in the 11 μm waveband (W/m²/sr/μm)

$L_{11}(T)$ is the 11 μm Plank function (W/m²/sr/μm)

T is the blackbody temperature (K)

T_{sst} is the sea surface temperature

ε_{11} is the emissivity of water at 11 μm

τ_{11} is the atmospheric transmission at 11 μm

$Ra_{11}{}^{\uparrow}$ is the upwelling atmospheric radiation at 11 μm (W/m²/sr/μm)

With knowledge of the atmospheric transmission and the sea surface temperature, Equation B.2 can be used to estimate the upwelling atmospheric radiance ($Ra_{11}{}^{\uparrow}$) arriving at the sensor. Knowledge of τ_{11} can be gained from use of Equation B.1 and, since the surface temperature gradient of large water bodies is negligible at spatial scales of around 1 km (Mason, 1991), an appropriate sea surface temperature (T_{sst}) value can be gained from the ATSR sea surface temperature product described in Mutlow *et al.* (1994). Rearrangement of Equation B.2 then provides an estimate of $Ra_{11}{}^{\uparrow}$ and, with knowledge of this parameter and of τ_{11}, the atmospheric effects on the longwave infrared thermal flux emitted from the volcanic surface can be estimated.

B.3. References

Jedlovec, G.R. (1990), Precipitable water estimation from high-resolution split-window radiance measurements, *J. Appl. Meteorol.*, **29**, 863-876.

Sobrino, J.A., Li, Z.-L., Stoll, M.P. and Becker, F. (1994), Improvements in the split-window technique for land surface temperature determination. *IEEE Trans. Geosci. Remote Sens.*, **32**, 243-253.

Appendix C.

Estimating radiative losses using low spatial resolution infrared radiance data

---

3.1. Introduction

As outlined in Chapter 1, the so-called dualband technique of Rothery *et al.* (1988) has been widely used to quantify the subpixel surface temperature structure of active lava surfaces. Chapter 7 includes details of methodologies used to adapt this technique to estimate the proportion of high- and low-temperature surface material within an ATSR pixel and in Chaper 7, Equations 7.2 and 7.3 are derived from Equation 7.1 which, given ATSR infrared spectral radiance measurements of an active lava surface, can be used to provide estimates of the proportion of the ATSR ground resolution element (GRE) covered by active crust (assumed to have a temperature between 70 and 400 °C) and exposed magmatic temperature material (assumed to have a temperature between 950 and 1050 °C). Here I briefly discuss a sensitivity analysis for this technique, and go onto describe how these proportion estimates can be used to estimate the radiative power loss from the upper flow surface.

C.2. Sensitivity analysis

A sensitivity analysis was carried out with respect to the estimated maximum error present in the parameters of Equations 7.2 and 7.3. The results showed that a ±5 °C error in the assumed background temperature (T_b) has a negligible effect on results, as does the ±5 % uncertainty in basalt emissivity found by Realmuto *et al.* (1992). The methodology is more sensitive to the value of assumed atmospheric transmission and, for the minimum 11 μm spectral radiance value expected over an active lava flow surface, a ± 15% uncertainty in the 11 μm atmospheric transmission (τ_{11}) leads to an uncertainty of ± 30% in the estimated area of active crust. Although the magnitude of this error diminishes at higher radiance values (i.e. when the flows are most active), this observation highlights the need to accurately constrain the estimate of atmospheric transmission. This can be done using appropriate atmospheric profile data with a radiative transfer model (e.g. LOWTRAN 7) or by use of the Split Window Variance Ratio technique (Appendix B).

3.3. Estimating radiative power loss

Chapter 1 described how previous volcanological studies have used TM and AVHRR dualband solutions within the Stefan-Boltzman relationship (Equation 1.4), in order to estimate the total radiative power loss (Q_{rad}) from a lava flow surface (e.g. Pieri *et al.,* 1990; Oppenheimer, 1991; Flynn *et al.,* 1994; Harris *et al.*, 1997; Oppenheimer and Francis, 1997). This methodology can similarly be used with the ATSR dualband solutions obtained from Equations 7.2 and 7.3 :

$$Q_c = \sigma \varepsilon A_{GRE} \left(P_c T_c^4 \right) \tag{C.1}$$

$$Q_h = \sigma \varepsilon A_{GRE} \left(P_h T_h^4 \right) \tag{C.2}$$

$$Q_{rad} = Q_h + Q_c \tag{C.3}$$

Where Q_h is the radiative power loss from the exposed core surface (watts)

Q_c is the radiative power loss from the chilled crust surface (watts)

Q_{rad} is the radiative power loss from the entire flow surface (watts)

ε is the emissivity

A_{GRE} is the area of the ATSR ground resolution element (m^2)

σ is the Stefan-Boltzman constant (5.67×10^{-8} W/m^2)

P_c is the proportion of the GRE covered by active crust

T_c is the temperature of the crust (K)

P_h is the proportion of the GRE covered by exposed hot core

T_h is the temperature of the exposed hot core (K)

As discussed in Chapter 7, with information in only two spectral bands the indeterminacy of Equations 7.2 and 7.3 requires that temperatures T_h and T_c must be assumed for the equations to be solvable. In order to minimise the effect of incorrect temperature assumptions, a range of T_h and T_c values is assumed, and Equations 7.2 and 7.3 solved using all temperature values within this range. For both the crust and exposed core, the maximum assumed temperatures (400 °C and 1050 °C respectively) give rise to the minimum estimated areas, and the minimum assumed temperature (70 °C and 950 °C respectively) give rise to the maximum estimated areas. Use of the entire temperature range (at, say, a temperature resolution of 25 °C) results in a set of (T_h, P_h) and (T_c, P_c) data pairs within which the true proportions of crust and exposed core proportion should lie.

Once the set of dualband solutions has been obtained, any calculation of Q_{rad} must make use of the full set of (T_h, P_h) and (T_c, P_c) solutions in order to ensure that the calculated range of radiative power losses also spans the true values. Figure C.1 shows the situation with regard to the crustal solutions. For a particular value of recorded 11μm spectral radiance (R_{11}) and ambient background temperature (T_b), Figure C.1 shows the

range of crustal fractions (P_c) obtained using Equation 7.2, and the range of radiative power losses (Q_c) calculated using Equation C.1.

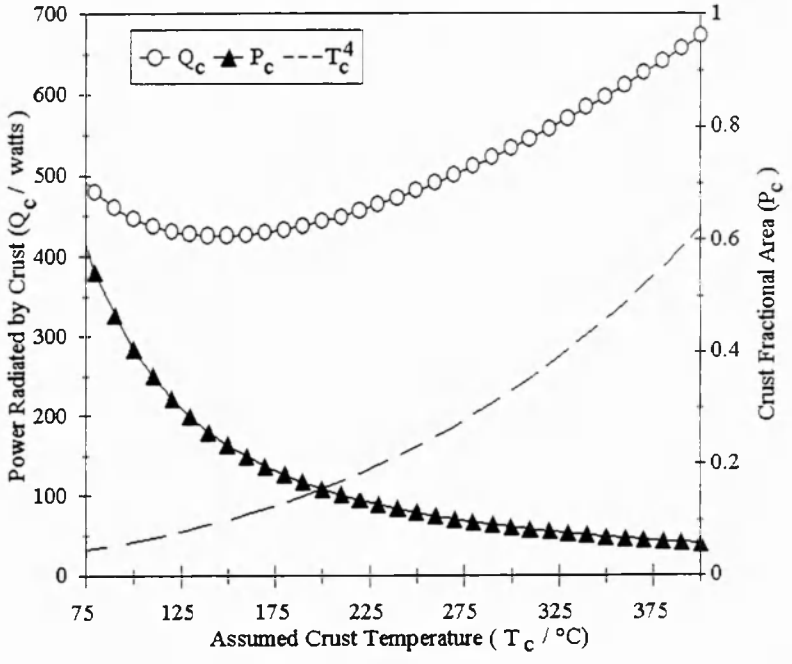

Figure C.1. The range of crustal fraction (P_c) and radiative power loss (Q_c) solutions, calculated using Equations 7.2 and C.1. A recorded 11μm spectral radiance value of 13.6 W/m²/sr/μm is assumed for the pixel, with an ambient background temperature of 10 °C. A Stefan-Boltzman T_c^4 curve is superimposed.

From the data shown in Figure C.1 it can be seen that the gradients of the P_c and T^4_c curves are opposite in sign and that the minimum Q_c value does not occur at the minimum assumed T_c, but rather at a T_c of 150 °C. Differentiation of Equation C.1 with respect to T_c gives :

$$\frac{dQ_c}{dT_c} = \sigma\varepsilon A_{GRE}\left(\frac{dP_c}{dT_c} T_c^4 + 4T_c^3 Pc \right) \qquad \text{(C.4)}$$

At the turning point of the Q_c curve dQ_c/dT_c is zero :

$$0 = \sigma \varepsilon A_{GRE} T_c^3 \left(\frac{dP_c}{dT_c} T + 4Pc \right) \qquad \text{(C.5)}$$

Giving :

$$T_C = \frac{-4P_C}{\left(\frac{dP_C}{dT_C} \right)} \qquad \text{(C.6).}$$

Equation C.6. gives the value of assumed T_c at which the radiative power loss (Q_c) is a minimum. As already stated, for the data of Figure C.1, this minimum occurs at T_c = 150 °C. Along with the corresponding P_c value (found by use of Equation 7.2 with T_c = 150 °C) this value can be used in Equation C.1 to calculate the minimum value of Q_c for these data. Figure C.4 additionally shows that Q_c is greatest at the maximum assumed value of T_c, i.e. 400 °C. Along with the corresponding P_c value (found by use of Equation C.2 with T_c = 400 °C) this value can be used in Equation C.1 to calculate the minimum Q_c value for these data.

With regard to the exposed core solutions, Figure C.2 shows the exposed core fractions (P_h) and radiative losses (Q_h) calculated by solving Equations 7.3 and C.4 for a particular value of recorded 1.6 µm spectral radiance ($R_{1.6}$). It is clear that the radiative power loss (Q_h) is inversely proportional to the assumed core temperature (T_h) since over the full range of assumed core temperatures, the magnitude of the gradient of the P_c curve is consistently greater than that of the T_h^4 curve.

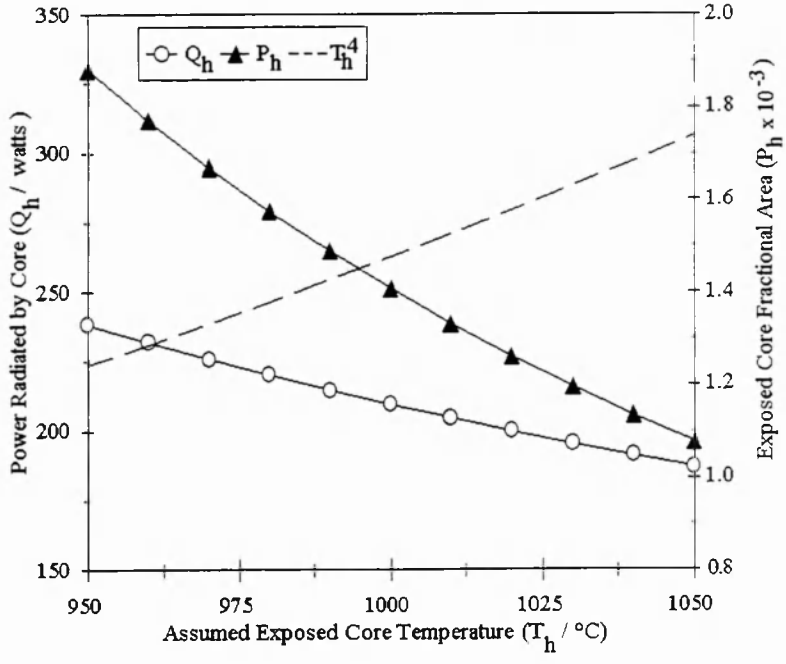

Figure C.2. The range of exposed core fractions (P_h) and values of radiative power loss (Q_h) for a value of recorded 1.6μm spectral radiance of 13.7 W/m²/sr/μm, calculated using Equations 7.3 and C.2. A Stefan-Boltzman T_c^4 curve is superimposed.

An important characteristic of the fractional area and radiative power loss solutions is that the relative uncertainty in the estimates of power loss (Q_c and Q_h) is much lower than that in the corresponding values of proportion (P_c and P_h respectively). This is a direct result of the opposing gradients of the proportion solution and Stefan-Boltzman (T^4) curves and is illustrated clearly by the data of Figure C.1 since the P_c solutions are seen to vary by an order of magnitude, whilst the Q_c solutions vary by only ± 50%.

The smaller variation in the estimates of radiative power loss, when compared to those of pixel proportion, can be further demonstrated using ATSR data from the 1995 Fernandina eruption (Chapter 7). Figures C.3 and C.4 repeat the proportion solution graphs of Chapter 7, whilst Figure C.5 shows the radiative power losses obtained using Equation C.3 with these data and with the full range of crust (T_c) and exposed core (T_h) temperatures previously described.

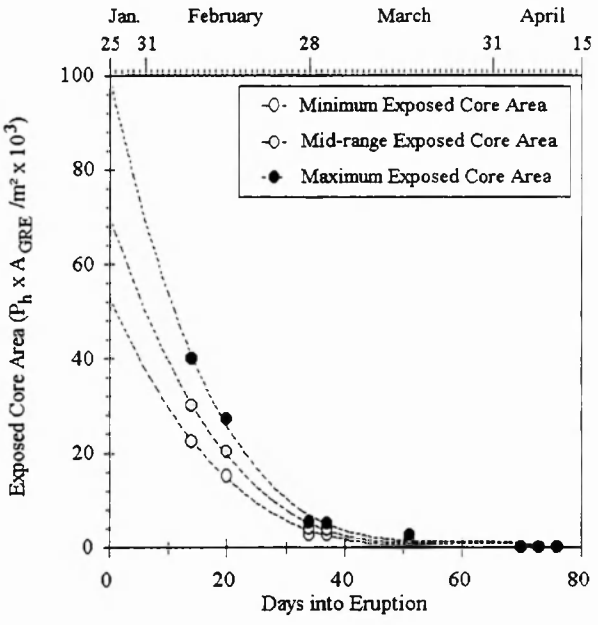

Figure C.3. The area of exposed hot core derived from the eight nighttime, cloud-free ATSR scenes of the 1995 Fernandina eruption used in Chapter 7.

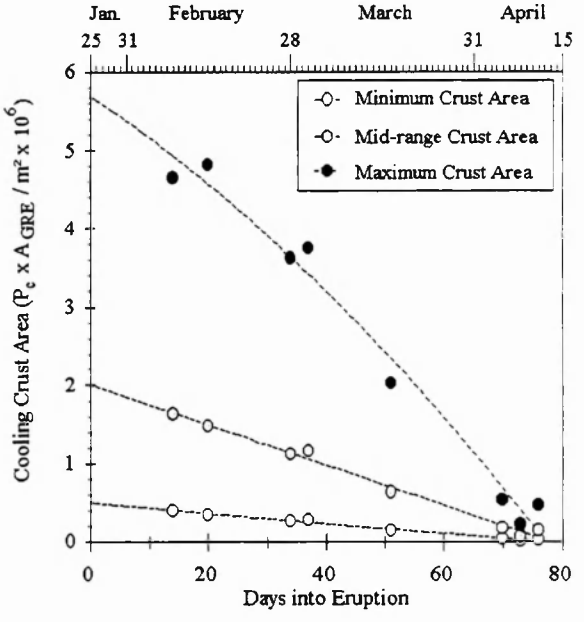

Figure C.4. The area of cooling lava crust derived from the eight nighttime, cloud-free ATSR scenes of the 1995 Fernandina eruption used in Chapter 7.

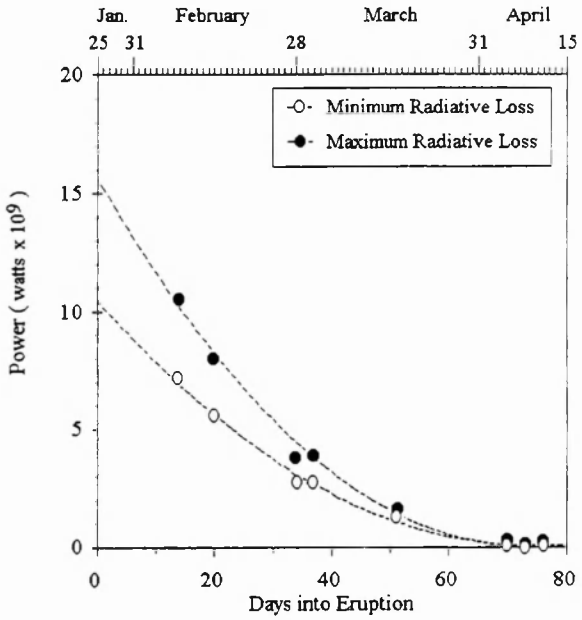

Figure C.5. The radiative power less from the lava flow surface, derived from the eight nighttime, cloud-free ATSR scenes of the 1995 Fernandina eruption used in Chapter 7.

Comparing the minimum and maximum solutions in Figures C.4 and C.5 it can clearly be seen that the solutions of radiative power loss cover a significantly narrower range than do the solutions of crustal proportion. Therefore, on this basis, dualband solutions of radiative power loss can be constrained significantly more tightly than can the corresponding lava flow area estimates. This is a useful finding since the rate of heat loss has important implications for flow longevity (Crisp and Baloga, 1990) and, as Chapter 9 discusses, this heat loss is highly dependent upon radiation from the upper flow surface. Provided that the lava flow thermal components conform to the assumptions made in the dualband technique, radiative power loss appears to be a more tightly constrained and potentially more useful parameter than active lava flow area.

3.3. References

Crisp, J. and Baloga, S. (1990), A model for lava flows with two thermal components.

J. Geophys. Res., **95**, 1255-1270.

Flynn, L. P., Mouginis-Mark, P. J. and Horton, K. A (1994), Distribution of thermal areas on an active lava flow field: Landsat observations of Kilauea, Hawaii, July 1991. *Bull. Volcanol.*, **56**, 284-296.

Harris, A. J. L, Blake, S., Rothery, D. A. and Stevens, N. F. (1997), A chronology of the 1991 to 1993 Etna eruption using AVHRR data: implications for real time thermal volcano monitoring. *J. Geophys. Res.*, **102**, 7985-8003.

Head, J. W. and Wilson, L. (1986), Volcanic processes and landforms on Venus, theory, predictions and observations, *J. Geophys. Res.*, ***91***, 9407-9446.

Oppenhiemer, C. (1993), Thermal distribution of hot volcanic surfaces constrained using three infrared bands of remote sensing data. *Geophys Res. Lett.*, **20**, 431-434.

Oppenheimer, C. and Francis, P. (1997), Remote sensing of heat, lava and fumarole emissions from Erta 'Ale volcano, Ethiopia. *Int. J. Remote Sens.*, **18**, 1661-1692.

Pieri, D.C., Glaze, L.S., Abrams, M.J. (1990), Thermal radiance observations of an active lava flow during the June 1984 eruption of Mount Etna. *Geology*, **18**, 1018-1022.

Realmuto, V.J., Hon, K., Kahle, A.B., Abbot, E.A. and Pieri, D.C. (1992), Multispectral thermal infrared mapping of the 1 October 1988 Kupaianaha flow field, Kilauea Volcano, Hawaii, *Bull. Volcanol.*, **55**, pp. 33-44.

Rothery, D.A., Francis, P.W. and Wood, C.A. (1988), Volcano monitoring using short wavelength infrared data from satellites. *J. Geophys. Res.*, **93,** 7993-8008.

Appendix D.

Indonesian fires observed using AVHRR

M. J. Wooster, P. Ceccato and S. Flasse

Accepted for publication in the International Journal of Remote Sensing (Nov. 1998)

D.1. Introduction

As in many countries world wide, a 'burning season' occurs every year in Indonesia, primarily to prepare agricultural land for plantation before the rains, but also as a "slash and burn" practice at the forest edge in order to extend the area available for agriculture. In 1997 however, the rains arrived late and the drought conditions allowed the burning activity to become more intense than in non-drought years. The 1997 fires produced dense layers of smoke that reportedly blanketed the Indonesian Islands of Borneo and Sumatra, as well as large sections of Malaysia, Singapore, Brunei, the Philippines and Thailand. The scale of the fires, and the associated haze, was such that the activity was widely reported around the world.

D.2 The haze

Haze from tropical burning is known to contain, amongst other constituents, large concentrations of carbon monoxide, carbon dioxide, nitrogen monoxide and ozone. Though smoke from the fires initially rises to a few kilometres altitude, convective activity ultimately mixes material from the haze layers down into the boundary layer, forming a ground level smog (Andreae *et al.*, 1988). The World Health Organisation reported that longer term inhalation of the Indonesian smog may have serious health implications, particularly for those already suffering from respiratory conditions such as asthma (Reuters, 1997). At the height of the burning activity, poor breathing conditions were reported cities and rural areas throughout southeast Asia.

D.3. Satellite observations of the activity

Active fires can be located using infrared data from the Advanced Very High Resolution Radiometer (AVHRR), carried onboard the NOAA Polar Orbiting Environmental Satellites (Robinson, 1991). The principal underlying the technique is that hot fires radiate intensely at middle infrared wavelengths, but less so at longwave infrared wavelengths. Active fires are therefore identified by locating AVHRR pixels where the middle infrared (3.7 μm) and longwave infrared (11 μm) signals appear widely divergent.

AVHRR High Resolution Picture Transmission (HRPT) data, transmitted direct from the NOAA satellites, has previously been used to investigate the extent of biomass burning activity in many individual regions of the tropics (e.g. Matson and Holben, 1987; Kennedy *et al.*, 1994). AVHRR Global Area Coverage (GAC) data has also been used for the same purpose, primarily where full resolution HRPT data were not conveniently available (e.g. Malingreau *et al.*, 1985). Because of the subsampling process used to

derive GAC data from the original AVHRR measurements (Kidwell, 1995), GAC data are of questionable value for individual fire identification (Belward *et al.*, 1994). GAC data can, however, provide information on the general spatial and temporal distribution of biomass burning activity, and they are freely and readily available from the NOAA Satellite Active Archive (Kidwell, 1995). We obtained AVHRR GAC data of western Indonesia throughout the summer of 1997, in order to remotely observe the extent of the burning activity and the associated atmospheric effects.

Figure D.1 shows one such GAC image, obtained near the reported peak of haze activity on September 11, 1997. The data are displayed with the AVHRR 'red' (0.58 - 0.68 μm) and 'near-infrared' (0.73 - 1.10 μm) channels combined to form a greyscale image. With appropriate contrast stretching this method of display shows clouds as white and the smoke and haze associated with the fires as grey. The smoke is most dense over the islands of Borneo and Sumatra. The figure also indicates as black dots the location of pixels believed to contain active fires. These were identified by first calibrating the GAC data according to Wooster *et al.* (1995), and then locating pixels with a widely divergent 3.7 μm and 11 μm brightness temperature. This methodology is similar to that used in the contextual fire detection algorithm of Flasse and Ceccato (1996). Most fires are concentrated around the southern coast of Kalimantan, the Indonesian sector of Borneo, and in southern Sumatra. At this time winds appear to be transporting the smoke towards mainland Malaysia and Singapore, which explains the poor breathing conditions reported in these non-burning regions.

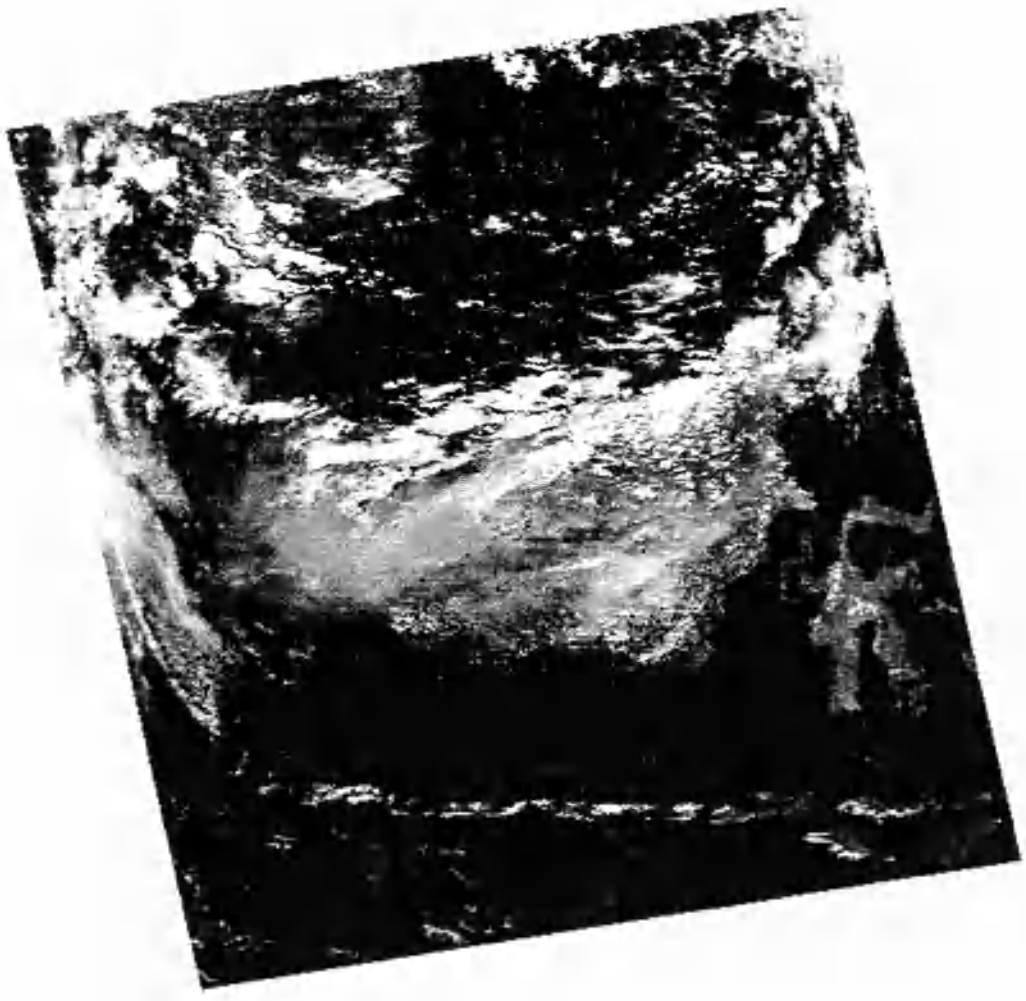

Figure D.1. AVHRR Global Area Coverage (GAC) data of southeast Asia (11 September 1997), with the island of Borneo at the centre of the scene. Pixels identified as containing active fires are highlighted in black.

D.4. Fire monitoring from space in Indonesia

For several years now a network of local receiving stations, supported by development projects (Flasse *et al.*, 1997), has enabled full resolution AVHRR HRPT data to be received directly in departments of the Indonesian Ministry of Forestry in Palembang (Sumatra), Jakarta (Java) and Palangka Raya (Kalimantan). Figure D.2 displays a part of a full spatial resolution HRPT image captured in Palembang during the summer 1997 burning season. This subscene shows south Sumatra, where individual smoke plumes are

clearly visible. The plumes are orientated north-west due to the dominant easterly wind. The grey shade east of Sumatra corresponds to the smoke resulting from fires on Kalimantan. As well as information on active fires, data on vegetation status, which is useful for fire risk assessment, is also available from the HRPT imagery. It is planned that these locally-derived earth observation products will be increasingly used to analyse fire issues within the local context and to draw up, and assess the success of, national fire prevention policies.

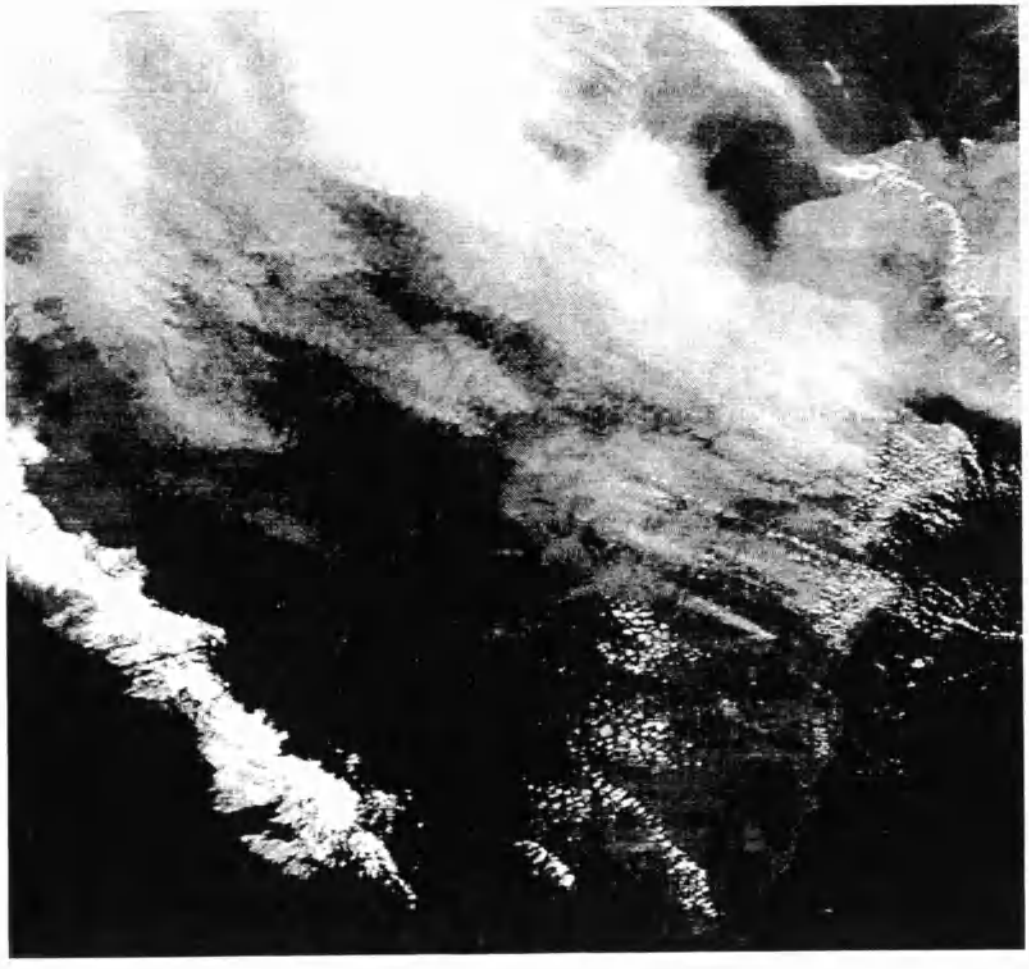

Figure D.2. AVHRR HRPT subscene showing smoke plumes in southern Sumatra (September 1997). The plumes are being driven in a westerly direction by the prevailing wind.

D.5 References

Andreae, M. O., Browell, E. V., Garstang, M., Gregory, G. L., Harriss, R. C., Hill, G. F., Jacob, D. J., Pereira, M. C., Sachse, G. W., Setzer, A. W., Dias, P. L. S., Talbot, R. W., Torres, A. L. and Wofsy, S. C. (1988), Biomass burning emissions and associated haze layers over Amozonia. *J. Geophys. Res.*, **93**, 1509-1527.

Belward, A. S., Kennedy P. J. and Grégoire, J.-M. (1994), The limitations of AVHRR GAC data for continental scale fire studies. *Int. J. Remote Sens.*, **15**, 2215-2234.

Flasse, S. P. and Ceccato, P. (1996), A contextual algorithm for AVHRR fire detection. *Int. J. Remote Sens.*, **17**, 419-424.

Flasse, S. P., Ceccato, P., Downey, I. D., Raimadoya, M. A. and Navarro, P. (1997), Remote sensing and GIS tools to support vegetation fire management in developing countries. *Proceedings of IGARSS'97*, 03-08 August 1997, Singapore, pp. 1569-1572.

Kennedy, P. J., Belward, A. S. and Grégoire, J.-M. (1994), An improved approach to fire monitoring in West Africa using AVHRR data. *Int J. Remote Sens.*, **15**, 2235-2255.

Kidwell, K. (1995), *NOAA Polar Orbiter Data Users Guide.* (Washington D.C.: National Oceanic and Atmospheric Adminstration, National Environmental Satellite Data Information Service, Satellite Data Services Division).

Reuters (1997), U.N. concerned about the smog in S.E. Asia. *Reuters Reports,* 10:51 GMT, 23 September 1997.

Robinson, J.M. (1991), Fire from space: Global fire evaluation using infrared remote sensing. *Int. J. Remote Sens.*, **12**, 3-24.

Malingreau, J. P., Stephens, G. and Fellows, L. (1985), Remote sensing of forest fires: Kalimantan and North Borneo in 1982-3. *Ambio*, **14**, 314-315.

Matson, M. and Holben, B. (1987), Satellite detection of tropical burning in Brazil. *Int. J. of Remote Sens.*, **8**, 509-516.

Appendix E.

Possibilities for automatically discriminating Earth surface hotspots using nighttime ATSR infrared radiance data

---

E.1. Introduction

One of the specified aims of the NASA Earth Observing System (EOS) Volcanology project is to determine techniques by which Earth surface hotspots can be automatically identified and classified using remote observations from satellites, thus acting as an 'eruption' alarm for unmonitored volcanic sites (Mouginis-Mark *et al.*, 1991b). The Moderate Resolution Imaging Spectrometer (MODIS) is to be the principal EOS instrument used in this effort, and this instrument will make daily observations of all Earth surface locations. It has also been mooted that it may be desirable to implement a European version of such a system, working from observations made by the ATSR and/or Advanced ATSR (AATSR) instruments. This is feasible since a near 'real-time' processing chain for downlinked ATSR data currently exists at the Tromsϕ satellite station in Norway (Guneriussen, 1990). This processing chain is currently used only for the

production of global sea surface temperature datasets, however it would be possible to adapt the system to include a hotspot detection and classification algorithm.

Discounting industrial flares and persistently active geothermal features, which are easily identified on the basis of their known and unvarying locations, vegetation fires and newly erupting volcanoes comprise the main potential source of hotspot activity. The purpose of this appendix is to make use of existing ATSR datasets to outline potential methods by which new hotspots may be detected and classified as either volcanic or fire-related. The ability to classify in this way is clearly of importance to an eruption alarm system since, due to their fertile volcanic soils, many volcanoes are surrounded by lush forests and agricultural land in which natural and anthropogenic vegetation fires are a relatively frequent occurrence.

E.2. The remote detection of hotspots

Many techniques have been proposed for the remote detection of Earth surface hotspots, principally those relating to vegetation fires. The vast majority of these have used data from the Advanced Very High Resolution Radiometer (AVHRR), and they are commonly based upon sensitivity of the AVHRR 3.7 μm channel to hotspots of subpixel resolution (Figures 1.2 and 1.3). Since both the ATSR-2 and Advanced ATSR (AATSR) instruments possess a continuously operating 3.7 μm channel that is nearly identical to that of the AVHRR (Holdaway, 1993; Stricker *et al.*, 1995), hotspot detection techniques developed for the AVHRR are also applicable for use with ATSR data. Amongst others, Robinson (1991), Justice and Dowty (1994) and Langaas (1995) have comprehensively reviewed the various ways that data from the AVHRR 3.7 μm channel have been used to detect hotspots and so only a short summary will be provided here.

All AVHRR-based hotspot detection techniques make use of the increased 3.7 μm channel brightness temperatures obtained when the sensor views even a very small subpixel sized high temperature heat source. In this case the 3.7 μm brightness temperature of the hotspot pixel becomes significantly elevated over those of the surrounding non-hotspot pixels. Additionally, since the 3.7 μm channel is highly sensitive to the presence of a small high temperature heat source whilst the 11 μm channel is not (Figure 1.2), the 3.7 μm and 11 μm brightness temperatures of hotspot pixels are also widely divergent (Figure 1.3). Figure E.1 shows examples of these phenomena, taken from ATSR-2 data containing active fires.

Due to the phenomena demonstrated in Figure E.1, most AVHRR hotspot detection algorithms have worked by placing a simple threshold on either the 3.7 μm brightness temperature ($T_{3.7}$) and/or on the difference between the 3.7 μm and 11 μm brightness temperatures ($\Delta T_{3.7\text{-}11}$). Pixels having $T_{3.7}$ or $\Delta T_{37\text{-}11}$ values above these thresholds are then classified as hotspots (Langass, 1995). The detection thresholds have most often been manually determined for a particular scene of interest. Appendix D details use of this technique in the monitoring of the widespread biomass burning activity that occurred in Indonesia throughout the summer of 1997. This manual procedure is especially suited to analysis of nighttime data, where the brightness temperatures of non-hotspot pixels are more uniform than during the day and where solar contamination of the 3.7 μm signal is not an issue (Langaas, 1993). However, such manual techniques are inefficient when attempting to detect hotspots in very large datasets covering a wide variety of different ecosystems and/or seasons.

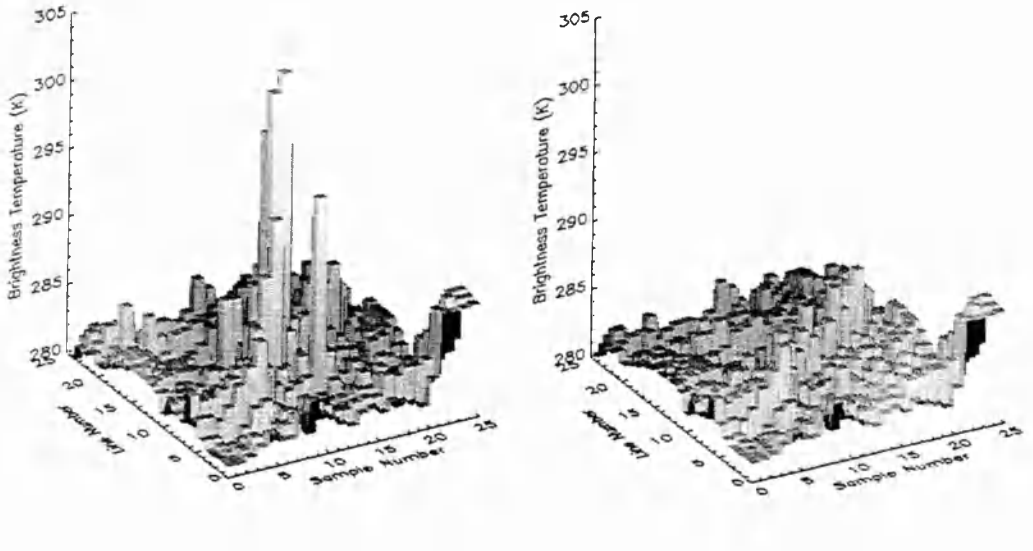

(a) (b)

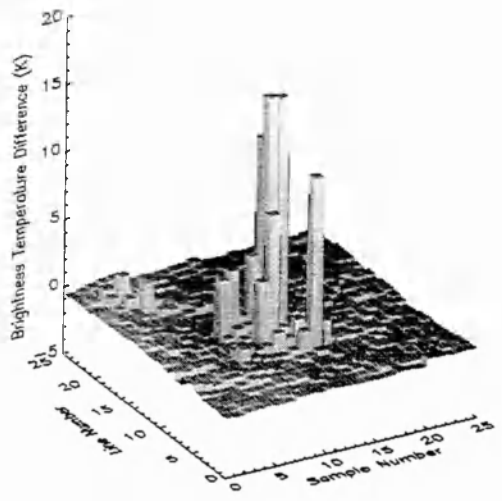

(c)

Figure E.1. Nighttime brightness temperature data of a forest fire event, extracted from an ATSR-2 BT product covering a region of the Canadian boreal forests (04:05 GMT, 3 June 1995). (a) The 3.7 μm channel data, showing the fire affected pixels as having an increased brightness temperature, (b) the 11 μm channel data, showing the pixel brightness temperatures as being relatively unaffected by the presence of the fires, and (c) the brightness temperature difference between the 3.7 and 11 μm channel data, which identifies the fire affected pixels very clearly.

Whilst reviewing techniques for potential use in a global hotspot detection methodology, Justice and Dowty (1994) cited a so-called 'contextual' approach whereby the $T_{3.7}$ and/or $\Delta T_{3.7\text{-}11}$ detection thresholds are automatically set according to the level of background (non-hotspot) brightness temperature variation within that particular area of the scene. Implementation of the contextual approach requires three stages, (i) select all 'potential' hotspot pixels on the basis of fixed $T_{3.7}$ and/or $T_{3.7\text{-}11}$ thresholds that are set low to avoid any errors of omission, (ii) use the mean and variance of the surrounding non-hotspot pixels to automatically determine a new locally-optimised $T_{3.7}$ and/or $T_{3.7\text{-}11}$ threshold for more accurate hotspot detection and, (ii) keep or discard each 'potential' hotspot by testing with these new localised detection thresholds.

Flasse and Ceccato (1996) developed the contextual algorithm further and the resulting methodology was subsequently successfully applied to a global AVHRR dataset for the purpose of world-wide fire distribution mapping (Stuttard *et al.*, 1995). Harris *et al.* (1995a) also used the 'contextual' approach to detect thermally anomalous AVHRR pixels associated with the 1991 - 1993 Mount Etna lava flow, thus showing the algorithm's value for the detection of volcanic as well as fire-based hotspots. Finally, a variation of the Flasse and Ceccato (1996) contextual algorithm has recently been employed to detect hotpots in multi-date, multi-ecosystem ATSR-2 thermal channel data, thus proving that the approach is valid for use with these data as well as those from the AVHRR (Matthew Perrin, personal communication 1997). Whilst additional studies would most likely be required to 'fine tune' the contextual approach for use with global ATSR datasets, it is clear that this technique offers a likely method of accurately locating ATSR hotspots of both fire and volcanic origin.

E.3. Example of a newly detected volcanic thermal feature

An example of a new volcanic feature detected by ATSR is the 1991 lava dome at Galeras Volcano, Columbia. Galeras had shown no major activity since 1977 and, in 1991, around 4000 people were believed to live within the high-hazard zone that had previously been affected by short (<5 km) pyroclastic flows of hot ash, rock and volcanic gases (Smithsonian Institution, 1991). In February 1989 fumerolic and ash emissions began at Galeras and, sometime in early October 1991, a lava dome emerged within the active crater, being noticed during an aircraft overflight. On 16 July 1992 an explosive eruption, presumably related to the preceding dome development, destroyed 90% of the dome and ejected 1 m diameter blocks up to 1.3 km from the volcano, though no pyroclastic flows were produced.

Figure E.2 shows the ATSR 3.7 μm and 1.6 μm nighttime spectral radiances obtained for Galeras' location for the two months surrounding the proposed appearance date of the 1991 dome. In 5 of the 6 cloud-free scenes, the volcano was characterised by a significant radiance anomaly in the nadir-view 3.7 μm channel data. However, on the 12 October 1991 scene the thermal emittance from the volcano was intense enough to turn on recording of ATSR-1's 1.6 μm channel, suggesting that this scene falls closest to the initial appearance of fresh lava within the active crater. Therefore, from the ATSR data alone, it is possible to conclude that new lava emerged within Galeras' crater sometime between 30 September and 12 October 1991. The relative decrease in 3.7 μm signal after this date is consistent with rapid cooling of the dome surface.

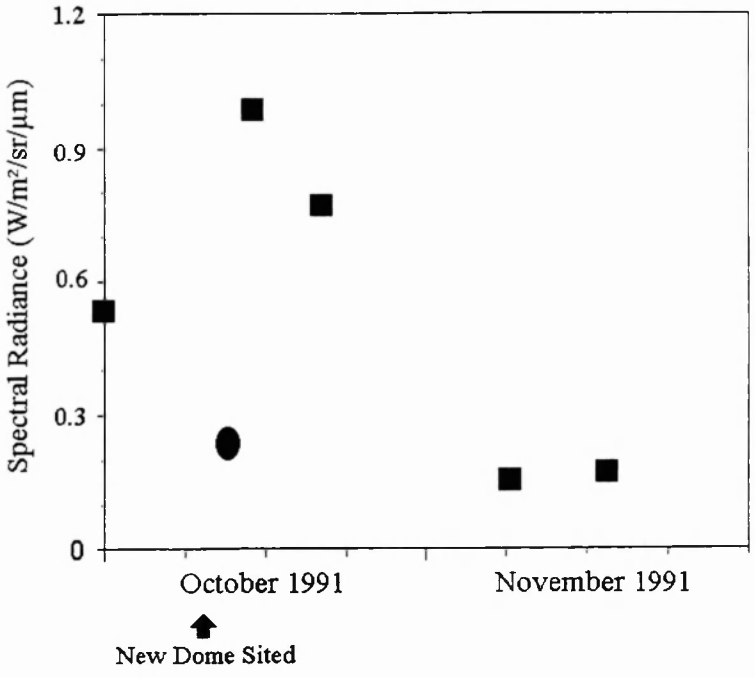

Fig. 2. The 3.7 µm (■) and 1.6 µm (●) spectral radiance time-series for Galeras Volcano (Columbia), obtained from ATSR-1 nadir-view data. The proposed date of dome appearance was identified during an aircraft overflight and is taken from Smithsonian Institution (1991).

E.4. Discriminating fire and volcanic hotspots

The methods outlined in Section E.2 provide no clue as to the cause of any detected hotspot feature except that, due to the widely differing 3.7 and 11 µm brightness temperature signature, it is likely to be subpixel in origin. However, to be most useful, an eruption alarm system based on satellite-derived thermal data must be capable of attempting to discriminate volcanic hotspots from those caused by vegetation fires. Such a discrimination process might make use of spatial, temporal and/or spectral information since the radiative patterns of fires and volcanoes may differ in respect of each of these parameters. I will now go onto document some potential methods, which may use information collected in each of these domains, for the discrimination of fire and volcanic

hotpots. Following the other studies presented in this thesis, these discriminatory techniques will be aimed at the analysis of nighttime data since accurate use of 1.6 μm channel thermal observations is restricted to this situation. Alternative eruption alarm techniques based upon infrared observations of volcanic clouds (e.g. Prata, 1989) will not be considered here.

E.4.1. Spatial discrimination

An example of a basic discriminatory process based upon spatial data would be a check between the location of the detected hotspot and a database of known volcanic locations. Figure E.2 shows the approximate spatial distribution of the areas of the world having the greatest density of historically active volcanoes. Information on the exact latitude and longitude of each of these 600+ volcanoes, and of the even more numerous volcanoes that are believed to have erupted in geological recent times, is readily available in a database held by the Smithsonian Institution Global Volcanism Project (Simkin and Siebert (1994) at *http://www-volcano.si.edu/gvp.*

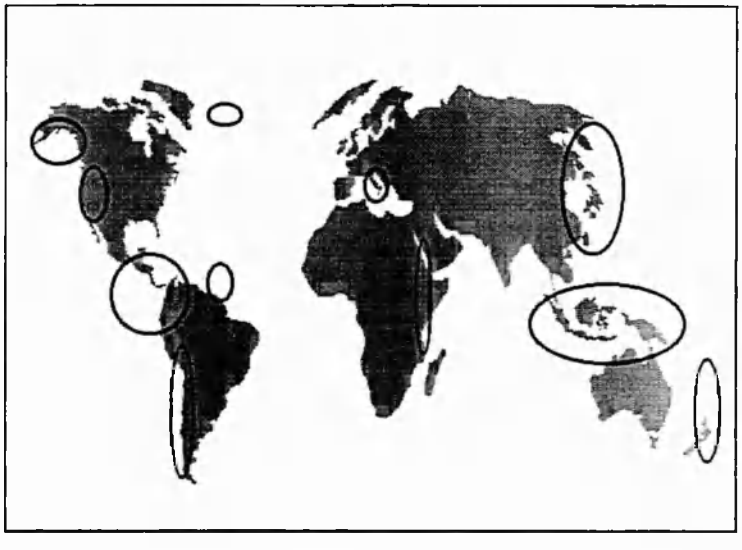

Figure E.3. The spatial distribution of areas having the highest density of historically active volcanoes, adapted from data in Simkin and Siebert (1994).

Allowing for small residual errors in the geocorrection procedure used in processing the ATSR data (Shin *et al.*, 1997), it would be a simple matter to check the latitude and longitude of the detected hotspot against a database containing the location of all known volcanoes. If a match were found then it is clearly possible that the detected hotspot may be due to volcanic activity. However, if no such match existed it might not be wise to completely disregard the possibility of volcanic origin since eruptions have occurred at sites not previously considered to be volcanoes, most recently at Parícutin, Mexico (Rees, 1979) and Mount Lamington, New Guinea (Fisher, 1958). The Mount Lamington eruption proved particularly devastating, with pyroclastic flows killing almost 3000 local inhabitants (Taylor, 1958). For this reason the best course of action would be to downgrade the likelihood of volcanic origin if the hotspot location is not known to be the site of a historically active volcano, but to disregard volcanism completely only if the hotspot is located in a totally non-volcanically active region.

A further spatially-based discrimination technique could perhaps make use of the spatial distribution of thermally anomalous pixels. Flynn and Mouginis-Mark (1995) used high spatial resolution Landsat TM data to investigate this possibility. Their analysis concluded that the most radiant pixels covering an active lava flow are usually located near the centre of the thermally anomalous region, whilst for a vegetation fire they are more likely to be at the edge of the still-warm burn scar. Unfortunately analysis shows that such clear spatial signatures do not appear to be relevant to lower resolution nighttime data, though burn scars are relatively easy to detect using daytime reflectance data (Cahoon *et al.*, 1992).

E.4.2. Temporal discrimination

Fires burn combustible material at a rapid rate. Once an area is denuded of such material any flames die out and the surfaces cool quite rapidly, though the fire may of course have spread to neighbouring locations (Flynn and Mouginis-Mark, 1995). In contrast, the inner core of an active lava flow is generally at a near magmatic temperature for many days or weeks after emplacement. With such a high temperature interior, conduction of heat also keeps the surface crust at temperatures tens or hundreds of degrees above ambient (Flynn *et al.*, 1994). Additionally, cracks or ruptures in the crustal surface may continue to expose the inner core itself. For this reason, if a hotspot is detectable by ATSR in the same location on two consecutive ERS passes, spaced three days apart, then the phenomena is much more likely to be of volcanic origin than to be associated with biomass burning. This temporal information could clearly be useful as a part of a discriminatory process.

E.4.3. Spectral discrimination

The temperature of an active fire, upon which the fires spectral signature is highly dependent, is highly variable both spatially and temporally. However a number of threshold temperatures have relevance to the different phases of biomass burning activity (Robinson, 1991). In cellulose-rich fuels, exothermic reactions are sustained at temperatures above about 200 - 300 °C, flaming combustion requires temperatures in excess of about 300 - 350 °C and thick flames normally burn at around 1000 °C. The nature of the burning activity generally changes from smouldering to flaming around the 300 - 350 °C threshold, whilst the maximum possible temperature of a vegetation fire is around 1400 - 1500 °C. These figures indicate that the overall temperature range associated with the majority of vegetation fire activity is of a similar magnitude to that

characterising active lava, so it may be expected that the spectral characteristics of fires and active lava are quite similar. However, the size of the hot features associated with these two phenomena may differ markedly, leading to large differences in the radiant emittance. Additionally, whilst active lavas have spectral emissivities fairly close to those of blackbodies (Rothery *et al.*, 1988), fires behave as greybodies whose emissivity is dependent upon the depth of the flames in the viewing direction (Langaas, 1995). Following Tien *et al.* (1988), Langaas (1995) cites Equation E.1, which indicates that a fire having depth significantly less than 6 m will possess an emissivity far below that of a blackbody (Figure E.3). Langaas (1995) reports that the majority of field-observed fires he observed did not approach 6 m height, suggesting that such fires emit significantly less thermal radiation than an active lava surface of the same planimetric size and thermodynamic temperature.

$$\varepsilon_T = (1 - \exp(-k_s S) \qquad \text{(E.1)}$$

where ε_T is the fire emissivity over all wavelengths

k_s is the effective Planck absorption coefficient of the soot

S is the fire depth in the sensor view direction

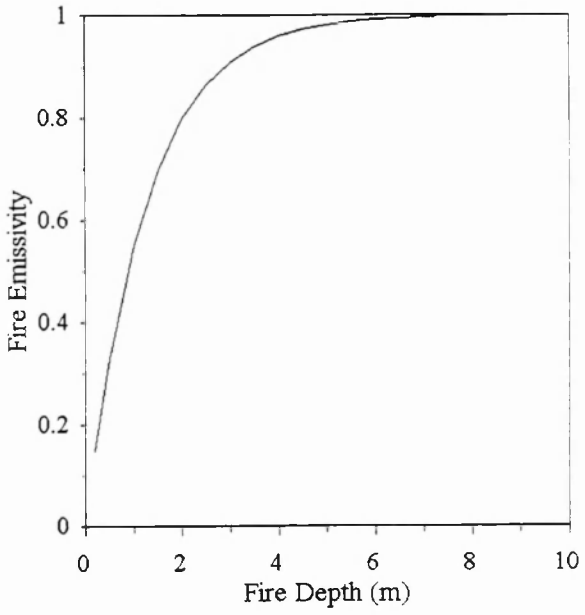

Figure E.4. The relationship between fire emissivity and fire depth in the viewing direction (which is vertical assuming nadir observations), calculated according to Equation E.1. The effective Planck absorption coefficient (k_s) has been set to 0.8 m^{-1} since this is the value that has been determined from soot derived from wood, dry grasses and other cellulose-rich material (Langaas, 1995).

To compare the actual spectral signatures of vegetation fires and active lava, ATSR data containing examples of these phenomena were obtained. Cloud free nighttime ATSR-2 scenes covering (i) the Brazilian tropical forest, and (ii) the Canadian boreal forest ecosystems were first used to evaluate the spectral signature of vegetation fires. These ecosystems experience large numbers of such events, particularly near the boundary of cleared and uncleared forest. These land cover classes are also quite similar to those surrounding many active volcanoes.

Following the many techniques cited in Robinson (1991), Justice and Dowty (1994) and Langaas (1995), hotspot detection was carried out using a $\Delta T_{37\text{-}11}$ threshold. Since only a single ecosystem type was present in each scene, a threshold value of 5 K was chosen by manual iteration. When hotspot detection was attempted on the basis of an

identifiable 1.6 μm signal, far fewer fire pixels were located than with the $\Delta T_{37\text{-}11}$ threshold technique. For this reason it was found to be essential to utilise ATSR-2 data during this study, ATSR-2 possessing simultaneously operating 3.7 μm and 1.6 μm channels. At each identified hotspot pixel the 1.6, 3.7 and 11 μm signals were extracted and stored, along with those of the immediately surrounding non-hotspot pixels.

The fire signatures were compared to volcanic hotspot data extracted from the previously used ATSR-1 scenes of Mount Etna (Sicily) and Fernandina Volcano (Galápagos Islands). For the Fernandina location the entire cloud-free dataset described in Chapter 7 was used so that large numbers of thermally anomalous pixels were available for analysis. For the Etna scenes the first two months of the full dataset described in Chapter 9 was used for the same reason. Since these data were obtained from the ATSR-1 sensor, 3.7 μm channel measurements were not available. Hotspot pixels in the Fernandina and Etna scenes were identified on the basis that they showed a 1.6 μm signal above that of the background noise level, or were thermally anomalous at 11 μm when compared to the surrounding pixels. To ensure that no hotspot pixels were omitted by this procedure, a manual check was made on the data extracted from each scene.

Figure E.4 shows the 1.6 μm spectral radiance and 11 μm brightness temperature anomalies associated with each pixel identified as a hotspot in the fire or volcanic datasets. The 3.7 μm signal is not shown since this exists for the ATSR-2 data only, and was in fact saturated at many hotspot locations. Such saturation would also be present over the majority of active lava pixels, making data from this channel of little use in discrimination procedures.

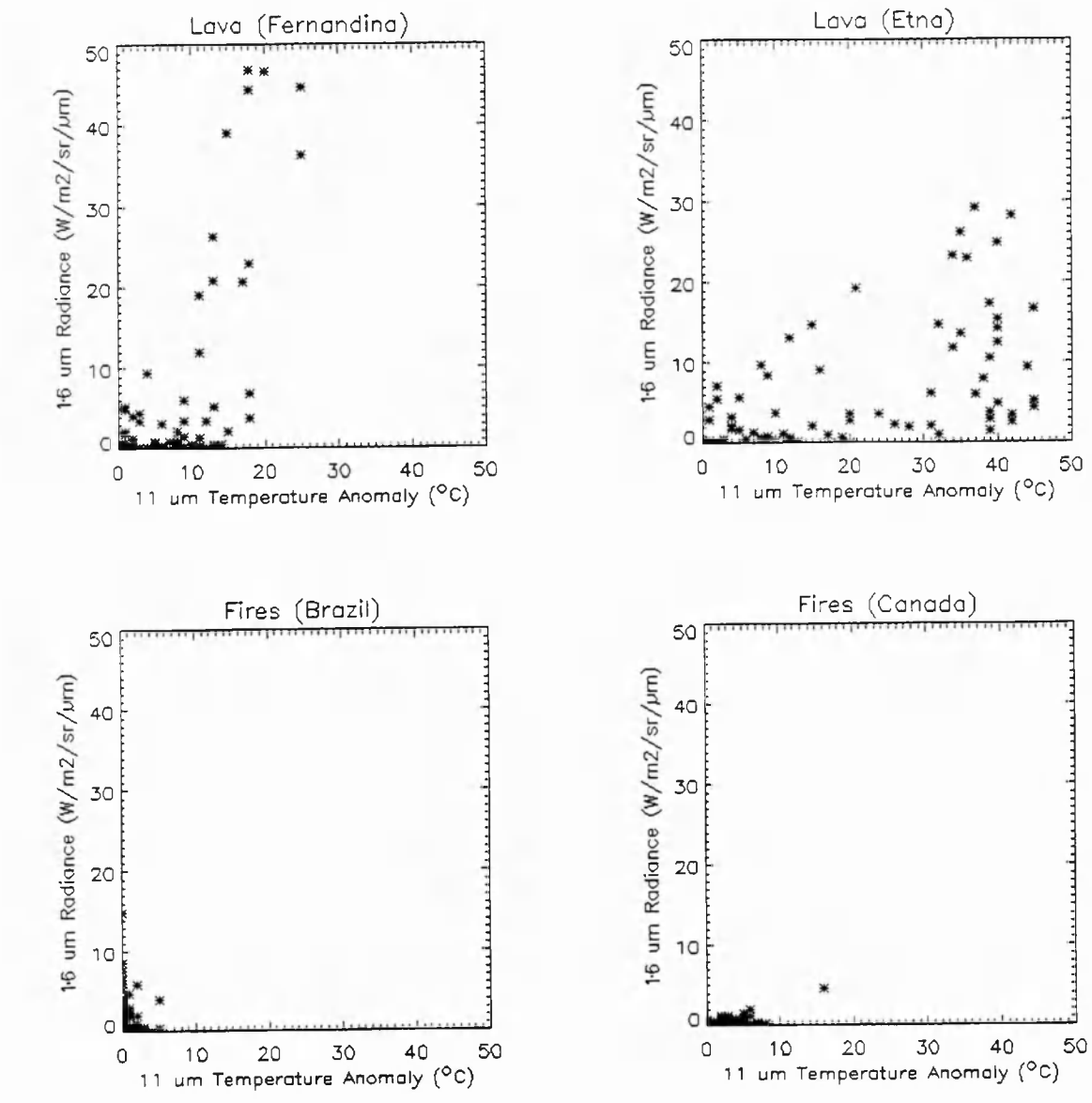

Figure E.5. The 1.6 and 11 μm spectral signature of ATSR pixels containing part of an active lava flow (top row), or a vegetation fire (bottom row).

The data in Figure E.4 clearly show that the shortwave and longwave infrared anomalies associated with pixels containing active lavas are generally (but not always) much larger than those associated with pixels containing active fires. A pre-set radiance and/or brightness temperature threshold could be set on these data which, when exceeded, would indicate that the hotspot is unambiguously due to an active lava flow and not to a

vegetation fire. Additional analysis of the ATSR time-series shows that the 1.6 and 11 μm signals associated with active lavas are greatest at or near the start of the eruptive activity. Therefore, it is these early volcanic observations that show the strongest 1.6 μm and 11 μm anomalies in the data of Figure E.4 (top row), and which are thus most clearly differentiated from the anomalies associated with the active fires (bottom row). Unless cloud cover at the volcano is highly persistent during the initial stages of the eruption, the first image of any newly active flow is likely to be obtained relatively close to the initial appearance of the lava. The volcanic activity should thus be easily distinguished from biomass burning on the basis of the stronger thermal anomalies associated with at least some of the affected pixels. Observations of pyroclastic flows and fumarolically active lava domes at Mount Unzen and Lascar Volcano (Figure E.5) indicate that it may also be possible to spectrally discriminate between certain of these features. Unlike the other volcanic or fire phenomena, the pyroclastic surfaces are consistently too cold to emit at 1.6 μm, and so should be readily identifiable on this basis. The active lava dome hotspots are more difficult to discriminate since, unlike the other volcanic phenomena, they usually cause only one or two pixels to be thermally anomalous in each scene. This provides a poor statistical sample for any analysis. Furthermore the majority of the lava dome hotspots are in a region of the plot that is also heavily populated by the fire pixels, suggesting that these two phenomena would be difficult to discriminate on the basis of spectral information. It is true that certain of the lava dome pixels show a significantly larger 11 μm temperature anomaly than do the fire pixels, but this is not generally the case. It thus seems unlikely that such lava domes can routinely be spectrally discriminated from vegetation fire activity using 1.6 and 11 μm spectral information alone.

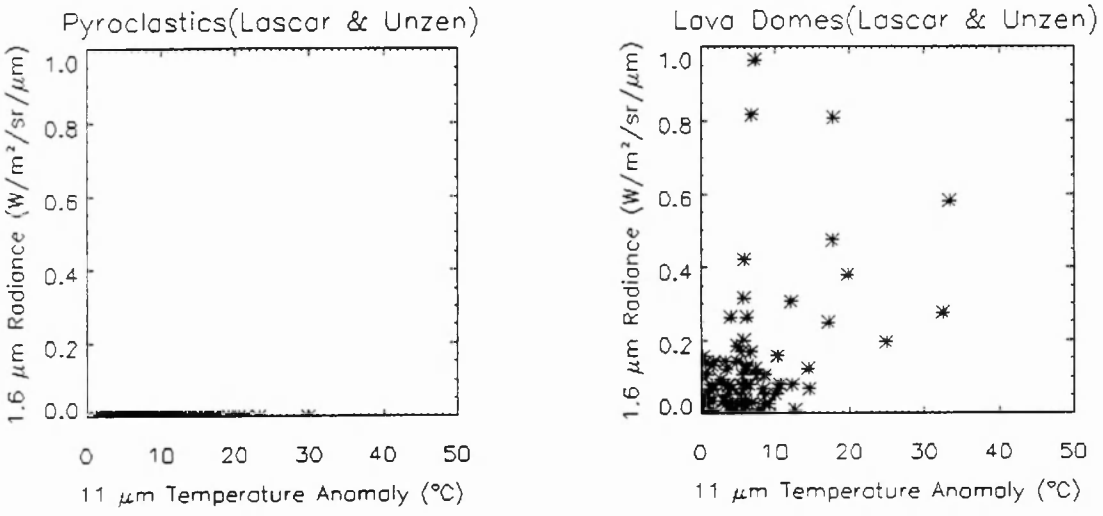

Figure E.6. The 1.6 and 11 μm spectral signature of ATSR pixels containing pyroclastic flows (left) and fumarolically active lava domes (right). Note the reduced scale of the y-axis in comparison to Figure E.4.

E.5. Conclusion

It is clear that fire and volcanic hotspots can be readily identified in ATSR-2 data using techniques initially developed for use with the AVHRR. The most successful such techniques generally make use of the widely divergent 3.7 and 11 μm channel brightness temperatures obtained when the sensor views a subpixel hotspot. A contextual approach to hotspot detection (Justice and Dowty, 1994), whereby the detection thresholds placed upon the channel brightness temperatures are automatically varied on the basis of the general brightness temperature variance in the scene, appear most suited to analysis of global ATSR datasets.

Discrimination between fire and volcanic hotspots is an important consideration in any eruption alarm system utilising satellite-derived infrared radiance data. Multispectral information appears invaluable to such a discriminatory process. The 1.6 and 11 μm thermal anomalies associated with active lava flows appear much larger than those

associated with vegetation fires, making spectral information a likely discriminator of these phenomena. Pyroclastic flow surfaces appear too cool to emit at 1.6 μm, making these phenomena readily identifiable. Fumarolically active lava domes appear less distinct, with spectral signatures that may be readily confused with those of vegetation fires. However it seems likely that a combination of spatial and temporal information could discriminate these types of activity.

These detection and discriminatory processes have been discussed in relation to data from the ATSR instruments of the ERS satellites. Any eruption alarm system utilising data from MODIS will, most likely, also make use of information collected in the spatial, temporal and spectral domains. It is hoped that further studies using ATSR can highlight some of the potential techniques involved in the operation of any MODIS based system, prior to the operation of the MODIS instrument.

E.6. References

Cahoon, D. R., Stocks, B. J., Kevine, J. S., Cofer III, W. R. and Chung, C. C. (1992), Evaluation of a technique for satellite-derived area estimation of forest fires, *J. Geophys. Res.*, **97**, 3805-3814.

Fisher, N.H. (1957), Melanesia, *Catalogue of Active Volcanoes of the Word: part V.*, (Naples: Int. Volcanol. Assoc.), 105pp.

Flasse, S. P. and Ceccato, P. (1996), A contextual algorithm for AVHRR fire detection. *Int. J. Remote Sens.*, **17**, 419-424.

Flynn, L.P. and Mouginis-Mark, P.J. (1995), A comparison of the thermal characteristics of active lava flows and forest fires. *Geophys Res. Lett.*, **22**, 2577-2580.

Guneriussen, T. (1997), Processing of ERS-1 ATSR data into averaged sea surface temperature (ASST) map at Tromsϕ ERS-1 satellite station (TERS). *Proceedings of Remote Sensing Science for the Ninties*, **3,** pp. 1817-1820.

Holdaway, R. (1993), U.K. Instruments for Mission to Planet Earth. *Space Technol.*, **13**, 561-567.

Justice, C. O. and Dowty, P. (1994), IGBP-DIS satellite fire detection algorithm workshop technical report, *IGBP-DIS Working Paper*, **9**,. February NASA/GSFC, Greenbelt, Maryland, USA, 88pp.

Langass, S. (1993), A parameterised bispectral model for savanna fire detection using AVHRR night images. *Int J. Remote Sens.*, **14**, 2245-2262.

Langass, S. (1995), *Nighttime Observations of West-African Bushfires from Space: Studies on Methods and Applications of Thermal NOAA/AVHRR Satellite Data from Senegal and the Gambia.* Ph.D. Thesis, Department of Geography, Unisversity of Oslo.

Mouginis-Mark, P., Rowland, S., Francis, P., Friedman, T. Garbeil, H., Gradie, J., Self, S., Wilson, L., Crisp, J., Glaze, L., Jones, K., Kahle, A., Pieri, D., Zebker, H., Kruger, A., Walter, L., Wood, C., Rose, W., Adams, J. and Wolff, R. (1991b), Analysis of active volcanoes from the Earth Observing System, *Remote Sens. Environ.*, **36**, 1-12.

Prata, A.J. (1989), Observations of Volcanic Ash Clouds in the 10-12 μm Window Using AVHRR/2 Data. *Int. J. Remote Sens.*, **10,** 751-761.

Rees, J.D. (1979), Effects of the eruption of Parícutin volcano on landforms, vegetation and human occupancy. In *Volcanic Activity and Human Ecology*, edited by P.D. Payson and D.K. Grayson, (New York: Academic Press), pp. 293-338.

Robinson, J.M. (1991), Fire from space: Global fire evaluation using infrared remote sensing. *Int. J. Remote Sens.*, **12**, 3-24.

Rothery, D.A., Francis, P.W. and Wood, C.A. (1988), Volcano monitoring using short wavelength infrared data from satellites. *J. Geophys. Res.*, **93**, 7993-8008.

Simkin, T. and Siebert, L. (1994), *Volcanoes of the World.* (Tuscon: Geoscience Press), 229pp.

Smithsonian Institution (1991), Galeras. *GVN Bulletin,* **16**, 10, 6.

Stricker, N.C.M., Hahne, A., Smith, D.L., Delderfield, J., Oliver, M.B. and Edwards, T. (1995), ATSR-2: The evolution in it's design from ERS-1 to ERS-2. *ESA Bulletin*, **83**, 32-37.

Stuttard, M., Boardman, S., Ceccato, P., Downey, I., Flasse, S., Gooding, R. and Muirhead, K. (1995*), Global Vegetation Fire Product Final Report for Joint Research Centre*, Contract 10444-94-09-FIEP ISP GB, Ispra, Italy.

Taylor, G.A.M. (1958), The 1951 eruption of Mount Lamington, Papua. *Bulletin of the Autralian Bureau of Mineral Resources, Ecology and Geophysics, Australia*, **38**.

Tien, C.L., Lee, K.Y. and Stretton, A.J. (1988), Fundamentals of radiation heat transfer. In *Handbook of Fire Protection Engineering*, The Society of Fire Protection Engineers.